The Dissertation Committee for Kenneth Teh-Yong Liao
certifies that this is the approved version of the following dissertation:

Helium Charge Exchange Recombination Spectroscopy on Alcator C-Mod Tokamak

Committee:

Kenneth W. Gentle, Supervisor

William L. Rowan, Co-Supervisor

Wendell Horton

Herb Berk

Gary Hallock

Richard Fitzpatrick

Helium Charge Exchange Recombination Spectroscopy on Alcator C-Mod Tokamak

by

Kenneth Teh-Yong Liao, B.A.

DISSERTATION

Presented to the Faculty of the Graduate School of

The University of Texas at Austin

in Partial Fulfillment

of the Requirements

for the Degree of

DOCTOR OF PHILOSOPHY

THE UNIVERSITY OF TEXAS AT AUSTIN

May 2014

Acknowledgments

I have been very fortunate to have regularly interacted with researchers and staff at two institutions, and therefore there is a very long list of people who have benefitted me. Regretably, I cannot include everybody here.

I owe the greatest thanks to my advisor, Dr. William Rowan, for his patience and dedication in guiding me along this journey, supporting me financially by securing grants, for mentoring me, and for his encouragement and strategy when things seemed to go all wrong. He has been a devoted leader of the experimental fusion group at the University of Texas and He has given me valuable insight in the ways of the experimentalist. I would also like to thank Professor Ken Gentle, for introducing me to the world of fusion and giving me the opportunity to work in this research group, and for patiently reviewing my thesis. I also thank the other members of my thesis committee, Professors Wendell Horton (who also kept me informed on new transport research), Gary Hollock, Richard Fitzpatrick, and Herb Berk.

I would like to thank my colleague, Igor Bespamyatnov, for showing me the ropes and for valuable advice and explanations; Robert Granetz for support and endless troubleshooting of the DNB; Robert Mumgaard for his extensive help with in-vessel calibration and assorted beam analyses; Aaron Bader for his friendly advice and company and and for teaching me how to

run AORSA and CQL3D; Michael Churchill for fruitful talks, helping with in-vessel work, and lending me various Edge CXRS equipment; David Hatch for guiding me through the GENE code; Nathan Howard for teaching me to run STRAHL; and Steve Wukitch for his personal concern and helping with ICRF experiment design.

I'd like to thank the entire staff at Alcator C-Mod; so much occurs under the hood of which I barely have a surface knowledge of, yet my work fully depends on, and you have all pulled through year after year. I specifically call out Dave Terry, Edgar Rollins, and Morris Chung for their DNB work; Alan Binus and Yijun Lin for ICRF work; Josh Stillerman and Tom Fredian for MDSplus and the computer system; Tom Toland; and Paul Lienard. Thanks to Maria Silveira for devoting many hours as a confined space attendant. Thanks to Steve Wolfe and Syun'ichi Shiraiwa for their roles as PhysOp.

At FRC, I'd like to thank Teresa Garza for administrative support, and Keith Carter for technical support including reviewing my hardware designs and getting them built.

Many data used in my analysis were taken by other people. I am grateful to Jerry Hughes, Yunxing Ma, and John Walk for Thomson data; Matt Reinke for HIREX data (and keeping me on my toes); Amanda Hubbard, Perry Phillips, Michael Brookman (with whom I also shared an office and had useful conversations) for ECE data; Naoto Tsujii and Mark Evans for PCI data; and Ted Golfinopoulos (with whom there is no better person to commiserate) for Magnetics data.

I'd also like to thank Oleksandr Marchuk, Yuri Ralchenko, Bill Heidbrink, Max Austin, Xiangrong Fu, Paul Bonoli, Steve Scott, Catherine Fiore, Fred Jaeger, Carol Noriega, David Pace, Brent Covele, Chad Williams, Kevin Lee, Martin Greenwald, Earl Marmar, Cathy Rapinett, and Roger Bengtson.

Finally, I thank my mom and dad, who have sacrificed so much so that I could be here today.

Helium Charge Exchange Recombination Spectroscopy on Alcator C-Mod Tokamak

Kenneth Teh-Yong Liao, Ph.D.
The University of Texas at Austin, 2014

Supervisors: Kenneth W. Gentle
William L. Rowan

The Wide-View Charge Exchange Recombination Spectroscopy (CXRS) diagnostic at Alcator C-Mod, originally designed for measurement of boron, has been modified to fit several different roles. By measuring the He^{1+}(n = 4 $\longrightarrow$ 3) emission line at 4686 Å and surrounding spectra, we can measure ^{4}He and ^{3}He density, temperature, and velocity profiles and use this information to study turbulent impurity transport. The transport is characterized using a standard ansatz for the radial particle flux:

$$\langle \Gamma_{s,r} \rangle = -D(r,t)\frac{\partial n_s}{\partial r} + v(r,t)n_s$$

where D and v are flux-averaged anomalous diffusion and convection coefficients, respectively. This effort is designated He CXRS. Also, direct measurement of ^{3}He are used to test models of Ion Cyclotron Resonance Heating (ICRH). We look for evidence of fast ion production and the effect of the minority ion profile on fast wave heating.

Several modifications were made to the hardware. Light is collected via two optical arrays: poloidal and toroidal. The toroidal array has been

upgraded to increase throughput and spatial resolution, increasing the number of toroidal channels from 10 to 22. A new protective shroud was installed on the poloidal array. Additional diagnostics (a 11 channel beam duct view, neutralizer view, duct pressure monitor) were added to the Diagnostic Neutral Beam to improve DNB modeling for CXRS.

This work includes investigation of plasmas where helium is at low concentration ($< 1\,\%$), acting passively, as well as scenarios with a large fraction ($\gtrsim 20\%$). Using the STRAHL code, time-dependent helium density profiles are used to obtain anomalous transport parameters. Thermodiffusion and curvature pinch terms are also estimated from experimental scaling studies. Results are compared with neoclassical results from the NCLASS code and calculations by the GENE gyrokinetic code.

Another focus is verification of power deposition models which are crucially dependent on minority ion density, for which ^{3}He is used. At low ^{3}He fraction, direct absorption by ^{3}He generates fast ions with anisotropic velocity-space distribution functions. At high ^{3}He fraction, mode conversion heating of electrons is dominant. The minority distribution function and predicted wave deposition are simulated using AORSA and CQL3D.

This work provides the first measurements of helium transport on C-Mod and expands our understanding of helium transport and fast wave heating.

Table of Contents

Chapter 1

Introduction

Energy use has been associated with human development and prosperity. In the past two centuries, large improvements in automation have allowed people to harness external sources of energy to produce vastly more output with less effort, freeing up time for leisure, technology, and scholarly pursuit, allowing increases in literacy, wealth, and well-being. However, these benefits have relied on plentiful sources of easily-harnessed energy. Fossil fuels have filled this role, as they are energy-dense and large deposits have been discovered within the earth. Today, most electricity generation comes from combustion of fossil fuels.

Due to an increasing global population and higher levels of industrial development, human civilization is demanding progressively higher levels of energy production. The human population has increased by 79% from 1972 to 2010, and the global energy consumption has increases at a even greater rate, by 114% over the same interval[93]. Given the current situation, we come to grips with the fact that fossil fuels are finite and nonrenewable, and the Earth's reserves are rapidly dwindling. At the same time, pollution from fossil fuel combustion is threatening us with dire global consequences. In addition,

the cost of petroleum is rapidly increasing, and rising costs are contributing to widespread economic and political instability. Therefore, one of the most important problems concerning the prosperity of future generations is development of alternative sources of energy.

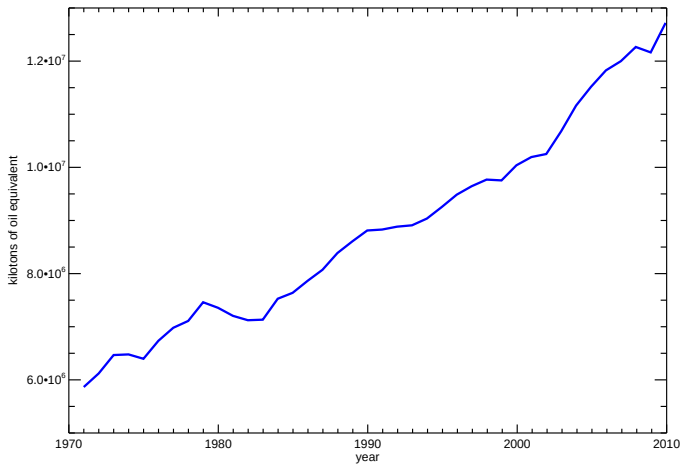

Figure 1.1: Growth in global energy production (kilotons of oil equivalent) estimated by the International Energy Agency[93]

Mature renewable energy sources such as hydroelectric and geothermal are relatively clean and reliable; however, good locations are very limited and mostly already utilized. Solar and wind can be placed much more flexibly, but are subject to large diurnal and seasonal variation and low energy density. Nuclear fission energy is a proven technology already widely used; however, it has several problems: long-lived radioactive waste, proliferation risk for nuclear weapons, and risk of a catostrophic meltdown. Unfortunately, none of the currently existing technologies is fully satisfactory for the energy requirements of today or the future.

One of the most promising energy sources for the future is nuclear fusion. Fusion offers high power density, base-load capability[1], and virtually inexhaustible fuel supply, with much less radioactivity and risk of a catostrophic radiation release than fission power. There is no proliferation risk and no chance for a runaway reaction. These properties have made fusion a very enticing prospect and it has been a subject of global research since the 1950s. Since that time, a large amount of progress has been made, and the international community is finally now constructing a full scale experimental reactor, called ITER[100].

Much of the progress in magnetically confined fusion research during the last 20 years has been made at the Alcator C-Mod tokamak, at the Plasma Sciences and Fusion Center, MIT. This thesis covers just a facet of the research conducted on this device: the measurement and physical understanding of helium transport in a tokamak using the charge exchange recombination spectroscopy (CXRS) diagnostic. Understanding light impurity transport is important to controlling fuel dilution among other effects, but helium has a very special importance as the final product of the fusion reaction, as well as having a role in ICRF minority heating.

[1]Base-load capability refers to a highly reliable source whose output can be varied to meet the fluctuating energy demand

1.1 Fusion Energy

Fusion reactions are nuclear reactions in which two or more light nuclei react to form a heavier nucleus and perhaps other light nuclei, neutrons, or neutrinos.[2] The binding energy of a nucleon is the difference in mass between the nucleon and a reference mass (typically m_{proton}), expressed in energy units using the equivalence $E = mc^2$. When the combined mass of the products is lower than the combined mass of the reactants, energy is released as kinetic energy in the reactants. Isotopes of hydrogen have the lowest binding energy per nucleon of all common nuclei, so fusion reactions involving these nuclei tend to be strongly exothermic. The nuclear binding energies are several orders of magnitude higher than any chemical binding energies, and fusion of these light nuclei offers more energy per mass of available fuel than any other energy source.

In order to achieve fusion in the laboratory, some means is necessary for overcoming the Coulomb repulsion between nuclei. This can be achieved with particle accelerators, or by raising the fuel to a very high temperature, so some fraction of the nuclei will collide with enough energy to react. Fusion is relatively easily accomplished with particle accelerator based systems, and devices such as the fusor[51, 79] have brought fusion within the range of hobbyists[89]. Though these devices do achieve fusion, they probably cannot

[2]Some fusion reactions, such as $^{1}\text{H} + {}^{11}\text{B} \longrightarrow 3\,{}^{4}\text{He}$ generate nuclei which are *lighter* than one of the reactants but heavier than another reactant. The low binding energy of hydrogen allows this reaction to be exothermic.

be used for fusion energy. It can be shown that the energy required to accelerate the fuel exceeds the fusion yield; the cross sections for fusion are too small relative to the cross sections for scattering, so the majority of the fuel is scattered into a loss region before fusing. This is a general problem for fusion concepts which rely on a non-thermal fuel distribution. On the other hand, if the fuel is allowed to thermalize and can be sufficiently confined, the temperature of the fuel can become hot enough for fusion to occur, and efficient fusion is possible. This is the basic concept of thermonuclear fusion. At these high temperatures or energies, the fuel will be in the plasma state, so fusion physics is a part of plasma physics.

The study of thermonuclear fusion has followed a few divergent strategies for confining the fusion plasma. The most prominent are magnetic confinement, inertial confinement, and (to a much lesser degree) inertial electrostatic confinement. Magnetic confinement involves using magnetic fields to trap a plasma and includes all work on tokamaks, stellerators, reverse field pinches, and mirror machines. Inertial confinement involves rapidly heating and compressing a fuel target with lasers or heavy ion beams so fusion occurs before the fuel can break apart. Inertial electrostatic confinement confines a population of electrons in a region and uses the electrostatic potential of the electrons to confine fusion ions. This latter concept has had some early successes but currently faces some severe physical barriers[157]. Currently, magnetic confinement schemes, in particular tokamaks, seems to be the most promising technique for future power generation.

Natural fusion occuring in the Sun is primarily based on the proton-proton chain, of which the rate determining reaction is $\mathrm{H} + \mathrm{H} \longrightarrow {}^{2}\mathrm{He}$. Although the Sun has been a long-time inspiration for the fusion energy effort, the solar fusion rate is far too slow to be of practical use in any terrestrial application[3]. Here, we must focus on reactions which are many orders of magnitude faster. The most important nuclear reactions relevant to a fusion reactor are shown in table 1.1.

	Q(MeV)	$\sigma_{\max}$(barn)	$\epsilon_{\max}$(keV)
$\mathrm{D} + \mathrm{T} \longrightarrow \alpha + \mathrm{n}$	17.59	5.0	64
$\mathrm{D} + \mathrm{D} \longrightarrow \mathrm{T} + \mathrm{p}$	4.04	0.096	1250
$\mathrm{D} + \mathrm{D} \longrightarrow {}^{3}\mathrm{He} + \mathrm{n}$	3.27	0.11	1750
$\mathrm{T} + \mathrm{T} \longrightarrow \alpha + 2\,\mathrm{n}$	11.33	0.16	1000
$\mathrm{D} + {}^{3}\mathrm{He} \longrightarrow \alpha + \mathrm{p}$	18.35	0.9	250
$\mathrm{n} + {}^{6}\mathrm{Li} \longrightarrow \mathrm{T} + \alpha$	4.8	3.4	250

Table 1.1: Fusion relevant nuclear reactions from [4] and [154]. Q is the fusion yield per reaction; $\sigma_{\max}$ is the maximum cross section, which occurs at a collision energy of $\epsilon_{\max}$.

First generation fusion devices will most likely be based on the DT reaction, because it has the highest reactivity at temperatures which are attainable by current and near future devices. A major drawback of the DT reaction is that tritium is a rare, radioactive resource. Tritium decays by beta decay into helium-3 with a half-life of 12.32 years, so natural deposits of tritium do not exist. Therefore, any credible plan for DT fusion must include a

[3]The power density from the Sun has oft been compared to power generated in a compost heap. The reason the Sun puts out so much energy is becaus it is so big!

mechanism for breeding tritium. A lithium blanket surrounding the reaction chamber has been proposed for this purpose, utilizing the last reaction in table 1.1. The blanket will serve a double duty of absorbing some of the neutrons generated by the DT reaction and producing tritium for use in the reactor after some reprocessing. Neutrons which are not absorbed by the blanket can cause activation and embrittlement of the vessel walls as well as damage of nearby equipment and coils and also pose a risk to personnel. Certain other reactions, such as boron-hydrogen, have been envisioned for use in fusion reactors of the (distant) future. These other reactions do not require rare fuel and may also have the benefit of not producing neutrons. These advanced fusion scenarios require even higher temperatures and higher confinement, which may prove to be impossible to achieve due to bremsstrahlung losses. Even reaching temperatures required for DT fusion has proven to be a great scientific and engineering challenge.

The reactivity is

$$\langle \sigma \mathbf{v}_{\mathrm{rel}} \rangle = \int \sigma(|\mathbf{v}_1 - \mathbf{v}_2|)\, |\mathbf{v}_1 - \mathbf{v}_2|\, f(\mathbf{v}_1) f(\mathbf{v}_2)\ \mathrm{d}^3\mathbf{v}_1\, \mathrm{d}^3\mathbf{v}_2 \tag{1.1}$$

For a Maxwellian population of reactants, DT fusion reaches a maximum reactivity at $T_1 = T_2 = 68.6\,\mathrm{keV}$[24]. This temperature is still out of reach of current devices[4]. ITER is projected to run at 15 keV, where the DT reactivity is 31% of the maximum value. ICRF or neutral beam heating can generate a non-Maxwellian population of ions, including high energy *fast ions*, which

[4]Record ion temperature of 50 keV was achieved on TFTR with neutral beam heating.

can have beneficial effects on the reactivity. The DT, DD, and D^{3}He fusion

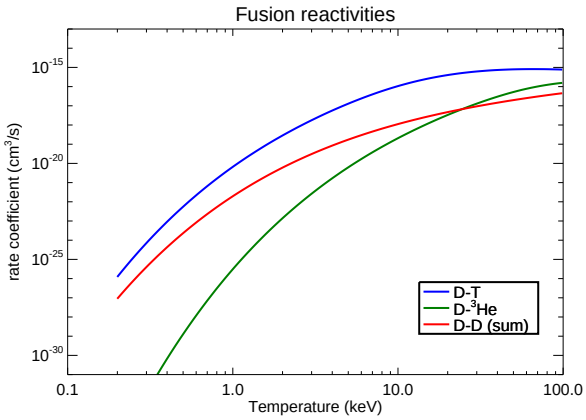

Figure 1.2: Fusion reactivities for selected fusion reactions[24]

reactivities are plotted in figure 1.1.

The DT reaction produces 3.5 MeV alpha particles, or helium-4 nuclei, as a product. Because this is far in excess of the plasma temperature, these are known as *fast ions* or *energetic particles*. If the alpha particles are sufficiently confined, they will slow down via collisons and eventually thermalize, raising the average temperature of the plasma. This reduces the amount of input heating power needed to maintain thermonuclear temperatures and improves the efficiency of the reactor. If the conditions are right, the alpha particles can supply all of the heating power and the reaction becomes self-sustaining. We call this condition *ignition*, and call the plasma a *burning* plasma. However, as the reaction progresses, accumulation of helium "ash" will begin to dilute the fuel, slowing the reaction, as well as increasing the effective Z, increasing bremsstrahlung losses. Therefore, understanding and controlling the trans-

port of helium is of grave importance in a steady-state reactor. We face the interesting problem of confining fast helium long enough to thermalize, but allowing helium ash to eventually be expelled.

There are two figures of merit for the efficiency of a fusion reactor, Q_{phy} and Q_{eng}. Q_{phy} is the ratio of power released by the fusion reaction to input heating power reaching the fuel. Q_{eng} is the ratio of electrical power generated to total input power used by the reactor. Clearly, Q_{eng} is the more stringent metric, because it includes every source of inefficiency in the process chain. Currently, most literature focuses on Q_{phy} because the details of the process chain are not fully developed yet. A *burning* plasma is equivalent to $Q_{\text{phy}} = \infty$. A Q_{phy} of 10 is believed to be the minimum necessary for a practical power generation reactor, and this value has been set as a target and prediction for ITER.

1.2 Magnetic Confinement of Plasma

Charged particles moving through a magnetic field experience the Lorentz force:

$$\mathbf{F} = q(\mathbf{E} + \mathbf{v} \times \mathbf{B}) \tag{1.2}$$

The magnetic part of the force is perpendicular to motion of the charged particle and the magnetic field, so the trajectory of a charged particle will be bent by the magnetic field. For a uniform magnetic field, with no other forces present, the trajectories will be helices, winding around a magnetic field line. In other words, the charged particles are confined to the magnetic field line in

two dimensions, and free to travel in the direction of the magnetic field. The motion is typically decomposed into a fast circular motion (referred to by the prefix *gyro-*, e.g. gyro-orbit, gyro-motion, gyro-radius, gyro-kinetic) about a guiding center, where the guiding center moves in a straight line parallel to the magnetic field.

The radius of the helical orbit is called the gyroradius, and is

$$\rho_s = \frac{m_s v_\perp}{|q_s| B} \tag{1.3}$$

where m_s, q_s, and $v_\perp$ are the mass, charge, and perpendicular velocity of the charged particle, and B is the magnetic field magnitude. Magnetic confinement devices use strong values of magnetic field such that the typical gyroradius is small compared to the dimensions of the device. In this limit, the particle guiding centers approximately follow the field lines.

A homogeneous magnetic field will confine a plasma in two dimensions, but the plasma will quickly escape in the remaining direction because the parallel motion of particles is unaffected. One way of getting around this is to wrap the magnetic field lines into a torus, so parallel motion never leaves the device[5]. In this device[6], one finds that the plasma quickly escapes due to particle drifts caused by the magnetic nonuniformity.

[5]Another method, using the magnetic mirror effect to reflect particles reaching the ends won't be discussed here, but see [163, 151]

[6]An example is the Texas Helimak[66], when the vertical field is turned off. It is an experimental realization of the cylindrical slab geometry.

The guiding center of the charged particle orbit does not exactly follow the magnetic field because of the presence of particle drifts. The most important of these are the grad B drift and curvature drifts, equal to

$$v_{\nabla B} = \frac{m v_\perp^2}{2qB} \frac{\mathbf{B} \times \nabla B}{B^2} \tag{1.4}$$

$$v_{\text{curv}} = \frac{m v_\parallel^2}{qB} \mathbf{b} \times (\mathbf{b} \cdot \nabla) \mathbf{b} \tag{1.5}$$

For a toroidal magnetic field, the drifts are parallel to the axis of symmetry (assumed to be vertical), with a direction depending on the sign of the charge and the direction of the magnetic field. Since electrons and ions have opposite charge sign, the drifts create a vertical current, which creates a charge imbalance between the top and bottom of the device. This charge imbalance creates an electric field which leads to loss of confinement due to an outward $\mathbf{E} \times \mathbf{B}$ drift. To remedy this effect, if a poloidal[7] field component is added to the magnetic field, the particles execute larger orbits in which the drifts cancel out. This mechanism is explained further in section 1.3. Now, the magnetic field lines do not wrap around and close on themselves (except in special cases, rational surfaces), but rather they wrap around over and over, missing themselves, eventually filling a two dimensional surface called a *flux surface*. These flux surfaces are nested like a (toroidal) onion, and transport between them is slow.

[7] In a toroidal geometry, the poloidal direction is the angle coordinate in the circular cross section normally called θ.

A tokamak is a type of magnetic confinement fusion reactor design with an axisymmetric magnetic configuration, and the combination of a strong externally-driven toroidal field and a weaker poloidal field which is generated by a current flowing through the plasma itself. Some of the essential components of a tokamak are shown in figure 1.3. A thorough introduction to tokamaks can be found in [111]. The work presented in this thesis was conducted on a specific tokamak, Alcator C-Mod, which is operated by the Plasma Sciences Fusion Center at MIT.

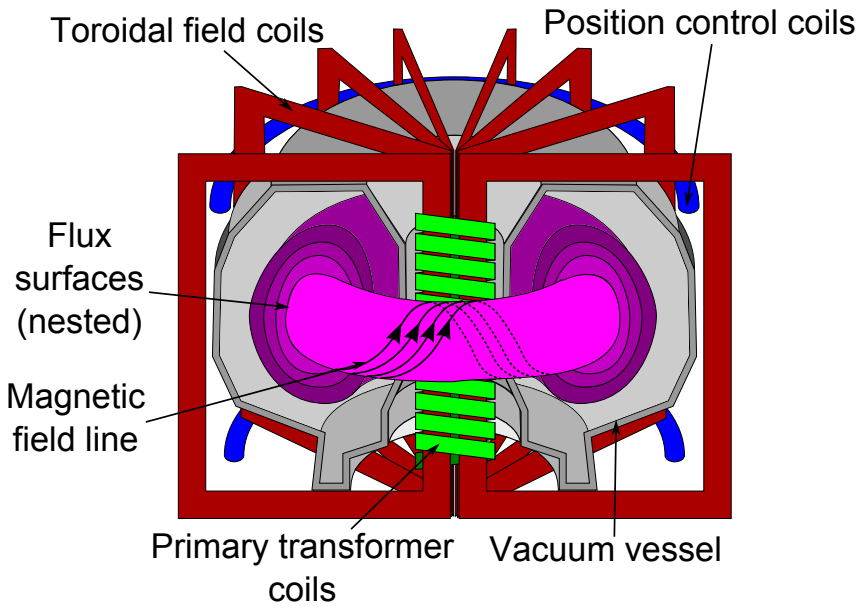

Figure 1.3: Essential components of a tokamak

One of the advantages of a tokamak is that the plasma is essentially 2D, because the dimension around the axis of symmetry can be removed. Therefore, the steady-state plasma equilibrium (from ideal MHD) is given by the Grad-Shrafanov equation[68, 161]. It can be shown that an MHD

stable solution exists. However, a standard tokamak can't run in continuously because in order to generate a steady plasma current, the primary transformer must continually ramp up its voltage[8]. Steady-state only exists insofar as the shot durations in present day tokamaks exceeds many confinement times.

Even after canceling out the magnetic drifts, the plasma confinement is not perfect. Some particles and energy leak across flux surfaces, due to the effects of collisions, turbulence, or some kind of equilibrium activity. This phenomenon is called transport, which is the topic of chapter 3. Understanding and controlling different types of transport remains one of the foremost challenges existing in fusion energy research.

1.3 Particle orbits in a Tokamak

The charged particles in a tokamak (in the absence of collisions) have orbits which fall into three main categories

trapped These are particles trapped in a region of poloidal angles by magnetic mirroring at the turning points, and so they continually change direction in parallel velocity. This includes banana orbits and potato orbits. Usually, they are also trapped to a small region in poloidal space, as well.

[8]An advanced tokamak could potentially run continously by taking advantage of various techniques for generating current without relying on the transfomer, such as neutral beam injection, electron cyclotron current drive, lower hybrid current drive, and bootstrap current.

passing These are particles which monotonically increase or decrease in toroidal and poloidal angle; the parallel velocity never changes sign. If the sign of the parallel velocity is the same as the sign of the magnetic field, then it is a co-passing particle; otherwise, it is counter-passing.

loss Loss orbits are orbits that intersect the tokamak walls. Most particles outside the last closed flux surface (separatrix) will fall into this category, but some particles inside the separatrix will also be lost because the gyroradius or banana width is too big.

Some depictions of different orbits are shown in figure 1.4. Collisions can take a particle from one orbit to another, but if the collision frequency is higher than the orbit frequency, then the orbits lose meaning.

The primary governing parameter for trapped/passing is the velocity pitch angle, $\arctan(v_\perp/v_\parallel)$ when the particle passes the midplane on the low field side of the tokamak. Particles are trapped because of conservation of energy and conservation of the magnetic moment $\mu = \frac{mv_\perp^2}{2B}$, which is an adiabatic invariant[156]. As particles move into higher magnetic field, the parallel energy decreases and the perpendicular energy increases. Trapped particles do not have enough parallel energy to reach the high field side midplane. Using the approximations $B \propto 1/R$ and circular flux surfaces, the condition for trapping is

$$v_{0\parallel} < \varepsilon^{1/2} v_{0\perp} \tag{1.6}$$

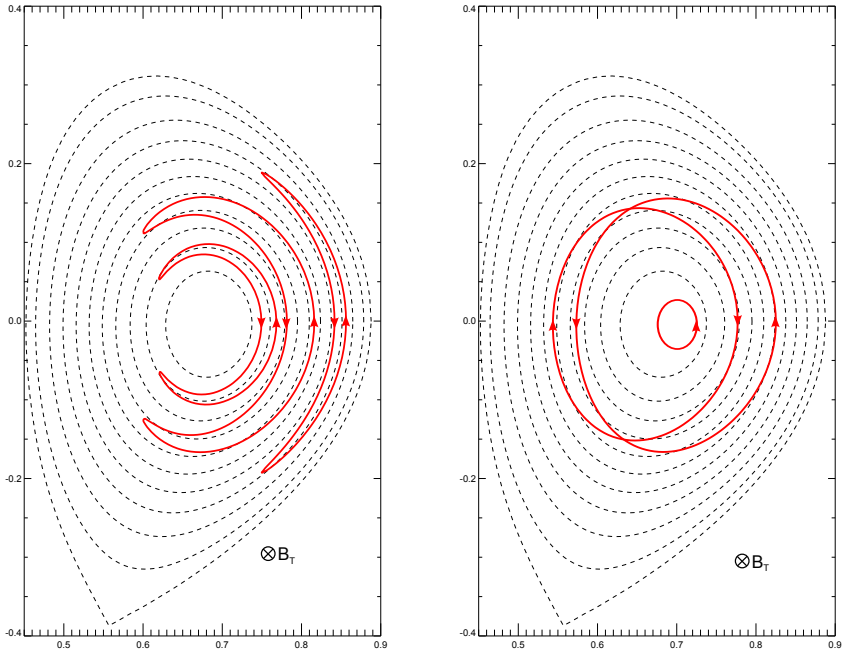

(a) banana orbits (b) passing orbits

Figure 1.4: Particle orbits. Arrow direction shown for ions

where $\varepsilon = r/R_{\text{axis}}$ is the *local* inverse aspect ratio. Therefore, if the particles have an isotropic velocity distribution, the trapped fraction is

$$f = \left(\frac{2r}{R_0 + r}\right)^{1/2} \tag{1.7}$$

This has important consequences for transport, as discussed in chapter 3.

1.4 Alcator C-Mod

Alcator C-Mod is a tokamak that is operating at the MIT Plasma Sciences Fusion Center (PSFC). The name Alcator is an acronym of the Italian words *Alto Campo Torus*, which translates to high field torus, so named

because the Alcator series of tokamaks have operated with some of the highest magnetic fields seen in any tokamak. C-Mod (1991–present) is the third machine in the series, and it actually has a lower toroidal field than its predecessors, Alcator A (1973–1979) (9 T) and Alcator C (1978–1987) (13 T)[146], but it still has a higher toroidal field than any other tokamak currently in operation. The high magnetic field has allowed C-Mod has to achieve record values for tokamak plasma pressure.

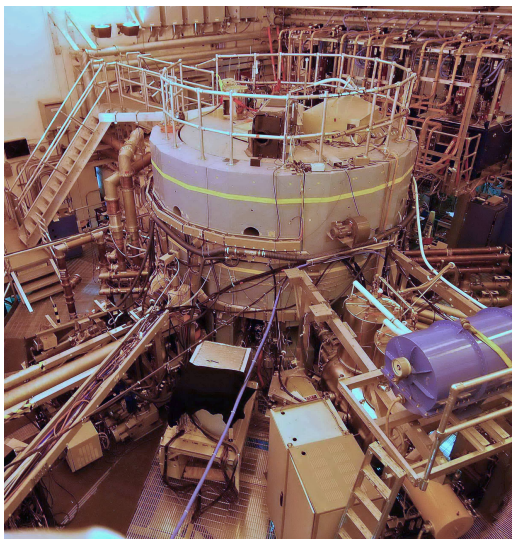

Figure 1.5: Alcator C-Mod Tokamak photo. The vacuum vessel is completely surrounded by a cryostat and a cylindrical concrete neutron barrier.

Alcator C-Mod is one of the premier tokamak research facilities in the United States. Although the plasma volume is smaller than most operating tokamaks ($\lesssim 1\,\mathrm{m}^3$), its unique parameters (see table 1.2) allow exploration of many reactor-relevant phenomena and it is equipped with a powerful suite of modern diagnostics and systems. A partial list of systems can be found on the

alcator facility webpage[9]. The systems which are most relevant to this thesis work are listed in table 1.3. A photo of the tokamak is shown in figure 1.5.

Table 1.2: Alcator C-Mod Parameters

parameter	value
major radius of plasma geometric center (R_0)	0.67 m
minor radius (a)	0.22 m
toroidal field on axis (B_T)	2 T to 8.11 T
plasma current (I_p)	0.6 A to 2.0 A
pulse duration	1 s to 3 s
core electron density ($n_e(0)$)	$0.8 \times 10^{14}\,\mathrm{cm}^{-3}$ to $3 \times 10^{14}\,\mathrm{cm}^{-3}$
core electron temperature ($T_e(0)$)	1 keV to 8 keV
elongation (κ)	1.6 (0.95–1.85)
triangularity (δ)	0.35,0.55
ICRF heating power (P_{ICRF})	0 MW to 5 MW
LH heating power (P_{LH})	0 MW to 2.5 MW
first wall material	Mo
diverter material	W, Mo, and TZM
shots per day of operation	about 33[a]

[a] For 5.3 T operation. At 8 T, the TF coils require additional time to cool, reducing shots to about 16.

The C-Mod vacuum vessel is constructed from type 304L stainless steel by welding cylindrical and annular components. It is nearly[10] 10-fold radially symmetric, with 10 horizontal ports, 10 top ports, and 10 bottom ports, shown in 1.6. The ports are labeled (clockwise from top) A through K, skipping the letter I, with the suffix -Hor, -Top, or -Bot to designate the toroidal and vertical location. The toroidal magnetic field is generated by a set of 20 copper

[9] `https://www.psfc.mit.edu/research/alcator/facility/system_availability/index.php`

[10] A-port is smaller and shorter than others to accomodate the TF bus between A and K.

Table 1.3: C-Mod Systems relevant to this work

system	remark
Diagnostic Neutral Beam (DNB)	needed for CXRS, BES, MSE
Core CXRS	n_s, v_s, T_s
ICRF	
Thomson Scattering	n_e, T_e
Electron Cyclotron Emission[a]	T_e, $\langle T_e \rangle$
Magnetics	I_p, q, $\langle B \rangle$
BES	n_B, E_b
Phase Contrast Imaging	$\langle \tilde{n}_e \rangle$
Motional Stark Effect	I_p, q
HIREX	T_i, v_i

[a] 4 ECE systems named GPC, GPC2, FRCECE, and CECE

toroidal field (TF) coils which wrap around the vacuum vessel. The tokamak also possesses five pairs of equilibrium field coils (EF1, EF2, EF3, EF4, EFC) and two ohmic heating coils (OH1, OH2) as well as 8 asymmetric field coils (A-coils). EF1, EF2, EF3, and EFC fit snugly into the space between the TF coils and the vacuum vessel and the center stack is occupied by the TF and OH coils. The space within the envelope of the TF coils is extremely compact and nearly every space is used. The ports and outer wall are nearly fully occupied by diagnostics and systems.

The TF coils are surrounded by a stainless steel cylinder and massive stainless steel domes, which are held together by 96 large INCONEL drawbars. These structures resist the extreme forces (up to 110 MN) generated by an 8 T magnetic field. The whole assembly is fully encased in a cryostat (filled with evaporated nitrogen) and actively cooled with a network of liquid nitrogen

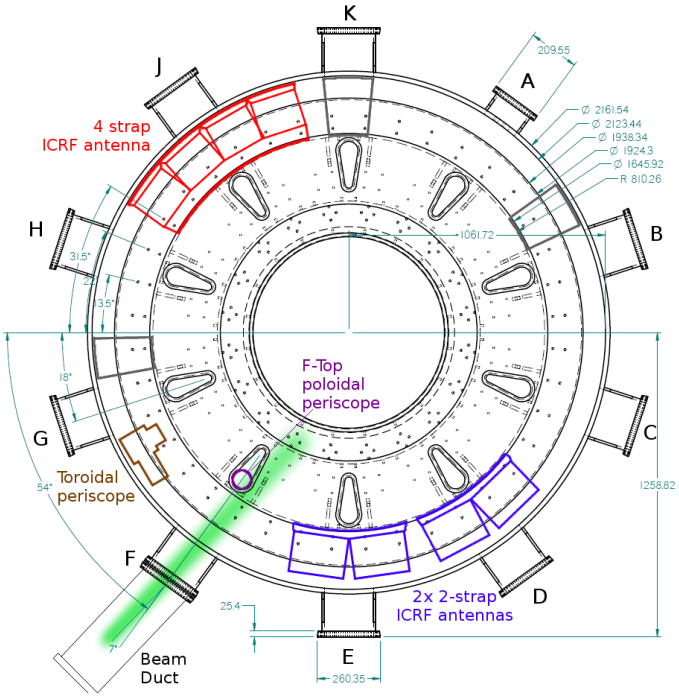

Figure 1.6: C-Mod ports, CXRS periscopes, and ICRF antennas. The neutral beam duct is attached to F-Hor and rotated by 7° to the port centerline.

channels.[11] In turn, the cryostat is surrounded by a boron loaded concrete radiation shield known as the "igloo" which serves to slow and absorb most of the neutrons emitted. The igloo is 6.63 m tall and has a diameter of 4.9 m. Many of the engineering aspects of the core design are covered in [94].

The inner wall, divertors, and limiters are covered with molybdenum and tungsten tiles to protect the vacuum vessel walls from the high heat flux ($\lesssim 500\,\mathrm{MW/m^2}$) from the plasma. These tiles typically show extensive melt

[11]The shot cycle time is largely bottlenecked by the time to cool the TF coils, which are resistively heated.

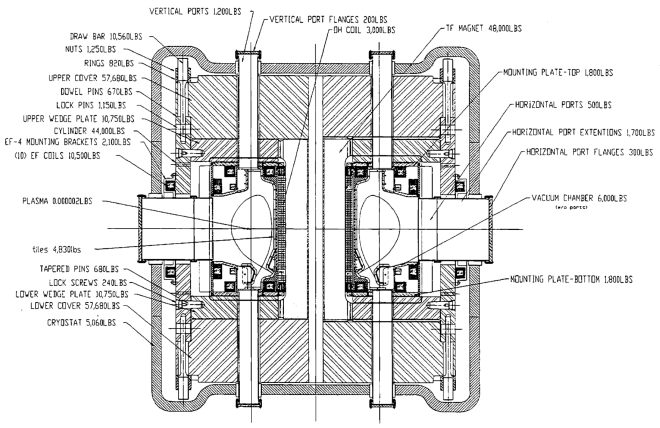

Figure 1.7: C-Mod cross section

damage after a run campaign, and require regular maintenance. In order to reduce the amount of high Z impurities (primarily Mo, W, Fe) that is sputtered into the plasma and improve performance, the plasma facing surfaces are covered with boron through a process of *boronization*. In boronization, a low temperature plasma is used to ionize diborane and deposit boron on all plasma facing surfaces. This process must be repeated every few run days if high performance plasma is required. Unfortunately, boronization is responsible for much of the degradation of optical signal due to partial coating of the optics, so various techniques are needed to protect the optics (see 2.4).

Alcator C-Mod is capable of operating in several different plasma equilibria and different confinement modes. It is capable of inner wall or limiter limited plasmas, or diverted plasmas with lower null, upper null, or double null. Lower null plasmas are preferred because the lower diverter is shaped to withstand higher power loads than the upper diverter. Shown in figure 1.8 is

the output of an equilibrium reconstruction by the EFIT[118, 91] code. C-Mod can run in L-mode (LOC and SOC), H-mode (ELMy, ELM-free, and EDA), ITB, and I-mode. A very short description of these modes is given.

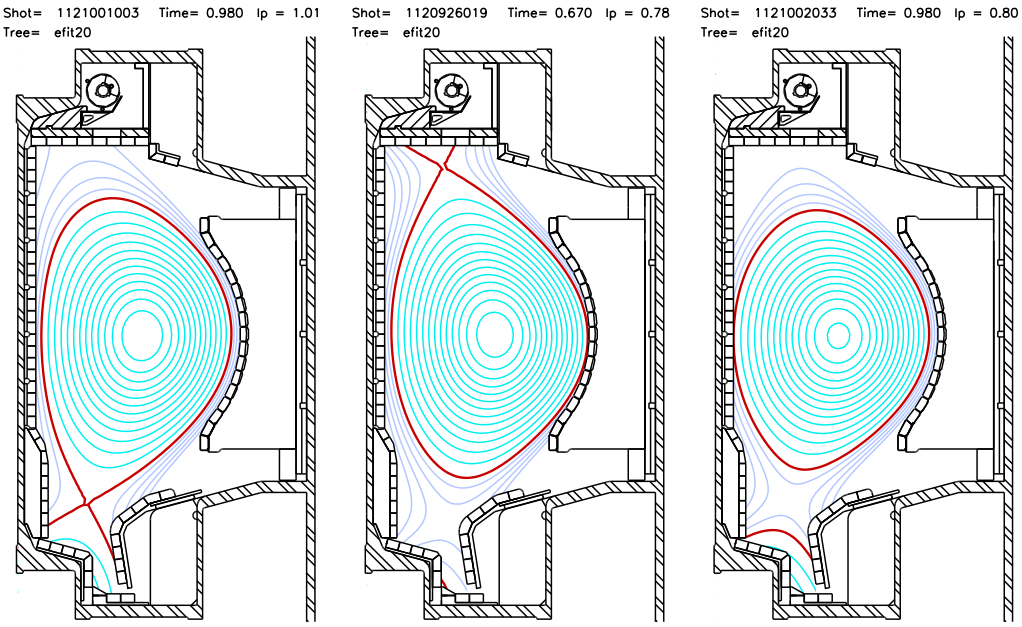

(a) lower single null (b) upper single null (c) inner wall limited

Figure 1.8: EFIT equilibrium reconstruction for three plasma shapes

L-mode The standard plasma without transport barriers was named L-mode after the discovery of H-mode. Density and temperature gradually increase from the edge to the core of the plasma.

Linear Ohmic Confinement In low density plasmas, the confinement time τ_E increases with density, following a Neo-Alcator scaling[155]

Saturated Ohmic Confinement At higher densities, the confinement time stops increasing with density.

H-mode A regime of substantially higher energy and particle confinement characterized by the presence of an edge transport barrier and an edge pedestal, first discovered on ASDEX[188]. Transition from L-mode to H-mode is sudden and shows hysteresis.

ELMy During H-mode, the edge pressure gradient grows to the point that a peeling-ballooning instability develops, which leads to periodic *Edge Localized Modes* (ELMs) which expel heat and particles from the edge at regular intervals.

ELM-free This is a transient H-mode where ELMs don't occur and the density continues to rise until some instability causes the plasma to drop out of H-mode.

EDA Enhanced D_α H-mode is a steady state H-mode where the ELMs are replaced by a quasi-coherent mode which generates some edge transport which prevents the edge pressure gradient from reaching a level where ELMs occur.

Internal Transport Barrier This is a regime with sharply reduced transport near the core of the plasma. It is usually triggered by off-axis ICRF heating[53].

I-mode Discovered on C-Mod[191], this is a regime with an edge temperature pedestal but not an edge density pedestal, with a so-called weakly coherent mode present near the edge.

C-Mod has been operating since 1991 and has generated a great deal of research during its time. However, the future of C-Mod is currently threatened

by budget cuts to domestic fusion research. At the time of this writing, Alcator C-Mod has secured funding for an additional run campaign, following a period of uncertain shutdown. It is not clear how long operation will continue.

1.5 Purpose and Structure of This Thesis

The purpose of this thesis is to document my work in the measurement of helium detection and transport on Alcator C-Mod tokamak, as well as some work in understanding helium's role as a fast ion and an element for ICRF heating. Despite concentrated effort by the fusion community, impurity transport, and in particular, helium transport, is still an open problem. This work allows us to test current turbulent transport theories and identify areas where more work is needed.

The helium results on Alcator C-Mod will contribute to an International Tokamak Physics Activity (ITPA)[101] database of impurity transport results which spans multiple machines, including ASDEX-Upgrade, DIII-D, JET, and C-Mod. The database allows a study of transport scalings and sensitivities to various plasma parameters, guided by theoretical models. Since both ^{4}He and ^{3}He are measured, it is possible to look for a mass dependence in transport.

This thesis is organized in the following way. Chapter 1 serves as an introduction to fusion research on Alcator C-Mod and lays out the structure of the thesis. Chapter 2 explains the helium CXRS diagnostic and describes how it has been implemented on C-Mod. Chapter 3 delves into the physics of impurity transport and efforts to advance our understanding of transport

through measurement. Chapter 4 is about the role of helium minority ions in ICRF minority heating and mode conversion heating. Chapter 5 summarizes the results and expounds on what has been learned, as well as what work remains to be conducted.

Chapter 2

Charge Exchange Recombination Spectroscopy on C-Mod

2.1 Introduction

Charge Exchange Recombination Spectroscopy (CXRS) is one of the standard ion diagnostic techniques for high temperature plasmas. CXRS systems have been installed on a large number of magnetic confinement devices, including D-IIID[183], JET[186], TEXTOR[33], TFTR[134], and C-Mod[158]. CXRS provides local measurements of the densities, velocities, and temperatures of a specific light ion species. It can also provide a projection of the velocity-space distribution function and be used to detect fast ions[75, 74][1]. By choosing the wavelength window of the spectroscopic measurement (using an appropriate diffraction grating), the diagnostic can be tuned for a particular ion species. CXRS measurements have been conducted for several low Z ions such as carbon, boron, helium, oxygen, deuterium, and lithium. The primary focus of this thesis is helium measurement on C-Mod, labeled He CXRS.

CXRS solves a particular difficulty in plasma spectroscopy, due to the

[1]Fast ions are ions with energy much greater than the ion temperature, with a density far in excess of what is expected from a Maxwell-Boltzmann distribution. They can be generated by neutral beam injection or ICRF heating. See 4.5.1.2

fact that fusion devices are at high temperature and low density. Low Z ions, including the fueling ions and light impurities, are completely ionized everywhere in the plasma except near the edge. The fully ionized nuclei do not have atomic line emission and only emit through free-free bremsstrahlung emission. This broadband signal is difficult to analyze because different species cannot be separated, whereas atomic line emission contains a unique signature for each species. It was observed that when a beam of neutral atoms is injected into the plasma, line emission from light impurities is increased[97]. This is due to electron transfer (deemed charge exchange or electron capture) from the neutral beam atoms to the light impurity directly into an excited state, allowing the newly formed hydrogenic ion to emit[99]. This is the basis for active CXRS. Following the discovery of charge exchange, it was determined that line emission modeling needed to take into account charge exchange from neutrals naturally present near the plasma edge[98]. This passive CXRS may also provide some useful information. Alternatively, neutral gas may be puffed at the edge to provide another source for active CXRS[178].

On Alcator C-mod, there are two CXRS systems, referred to as the Edge CXRS system and the Core CXRS system. The Edge CXRS system measures a small region at the plasma edge, and is covered elsewhere[133]. The Core CXRS system, also known as the Wide-View CXRS system, covers a wide spatial view encompassing the entire minor radius of the plasma on the low field side. Experiments on this system are the focus of this work. The Core CXRS system has been used for measurement of boron impurity and

now helium as an impurity or as the main ion. In order to switch between boron measurement and helium measurement, it is necessary to change the diffraction grating within the spectrometer. The basic components of the diagnostic are shown in figure 2.1. The spectrometer is located far from the

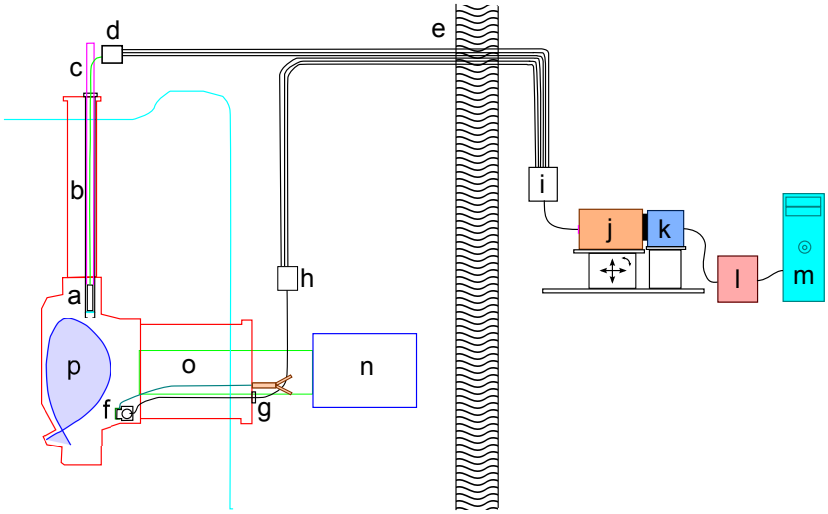

Figure 2.1: Core CXRS components diagram, not to scale. (a) Poloidal optics cartridge, periscope window (cyan), shroud; (b) poloidal periscope, stalk (magenta), fiber bundle (green); (c) top of stalk (magenta); (d) poloidal breakout box, transfer fibers; (e) transfer fiber bus, wall separating C-Mod cell and diagnostics lab; (f) toroidal periscope, shutter; (g) toroidal fiber bundle and vacuum feedthrough (black), push-pull shutter control (brown); (h) toroidal breakout box, transfer fibers; (i) spectrometer breakout box; (j) Holospec spectrometer atop 6 axis stage; (k) MicroMAX CCD; (l) CCD control unit; (m) computer; (n) diagnostic neutral beam (smaller than scale); (o) F-Hor port, beam duct (green), push-pull cables (teal); (p) C-Mod plasma

collecting optics, outside the *cell* (the room that houses the tokamak), and the light is conducted through optical fibers. This arrangement allows convenient

access to the spectrometer during an experiment (for calibration, insertion of filters, or changing the setup), and also reduces the noise induced by vibrations, magnetic fields, neutrons and x-rays. The disadvantage of this is that optical fibers lose some transmission when damaged or exposed to too much radiation and the fibers are expensive and difficult to replace.

The design of the diagnostic hardware has been driven by the requirements of diagnostic and the constraints imposed by the project. High étendue optics and high efficiency detector are needed to improve the photon statistics of the line fitting, but the collecting optics must be compact enough to fit in the C-Mod vacuum vessel. The diagnostic neutral beam uses an energy near the peak of the charge exchange cross section for light impurities while still getting beam penetration to the core.

Core He CXRS is based on the He II $n = 4 \rightarrow n = 3$ transition[2], which emits at a wavelength near 4686 Å. The primary He CXRS channel is shown here, if a hydrogen neutral beam is used.

$$\mathrm{He}^{+2} + \mathrm{H}^{0}_{\mathrm{beam}} \longrightarrow \mathrm{He}^{+1*} + \mathrm{H}^{+}_{\mathrm{fast}} \tag{2.1}$$

$$\mathrm{He}^{+1}(\mathrm{n} = 4\,) \longrightarrow \mathrm{He}^{+1}(\mathrm{n} = 3\,) + \gamma(4686\,\text{Å}) \tag{2.2}$$

Other pathways (such as CX to higher excitation levels followed by cascade, or excitation from lower levels) have smaller contributions to the effective cross section. The diagnostic cannot distinguish between the two isotopes of helium,

[2]In spectroscopic notation, He II refers to singly ionized helium.

^{4}He and ^{3}He. These isotopes have different center wavelengths: 4685.7 Å and 4685.9 Å, but the separation between the two is much less than the widths of the lines from Doppler broadening and the Zeeman effect+fine structure. On the other hand, 0.2 Å corresponds to a Doppler velocity of about 130 km/s, so accounting for the isotope shift is important for ion velocities. Typically, in helium experiments, we puff either ^{4}He or ^{3}He into the plasma, but not both during the same run day, so helium isotopes can be studied separately in the plasma.

The signal reaching the detector is the sum of the active charge exchange induced emission and various background emission contributions, which have detrimental effects on the measurement. The main background contributions are bremsstrahlung (or free-free emission), cold edge emission, and interfering spectral lines of other impurities. Cold edge emission is usually the dominant background, and it typically exceeds the active CXRS emission by an order of magnitude. Figure 2.2 shows the spectrum in a small region around 4686 Å, measured by the CXRS diagnostic, with some of the contributions fitted and identified. This particular shot has good conditions for CXRS. In more difficult situations, the active CXRS can be hard to fit. Unfortunately, the active CXRS signal for He CXRS is small, since the main pathway relies on a non-resonant charge exchange process (see 2.2.1). The problem is exacerbated on C-Mod because the high plasma density creates a lot of bremsstrahlung and also results in strong beam attenuation. This combination makes the He CXRS analysis challenging and imposes various requirements on the diagnostic

design. The specific analysis protocol will be detailed in section 2.6.

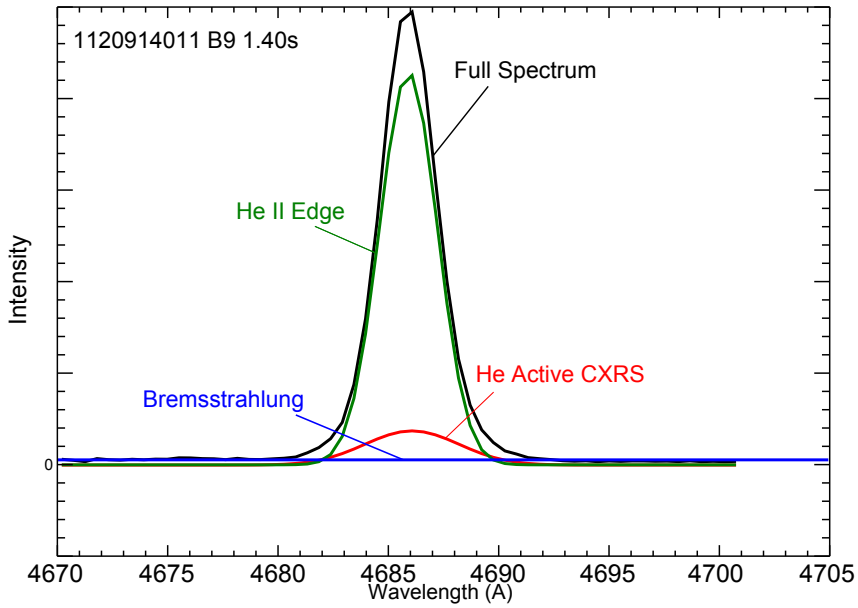

Figure 2.2: Fitted spectrum near 4686 Å, with the He II active CXRS emission, He II passive edge emission, and bremsstrahlung marked.

If we look at a larger spectral region, a variety of impurity lines become visible, as seen in figure 2.3. Some effort was undertaken to identify these lines (see table 2.1).

The diagnostic uses time-slice background subtraction using a modulated beam. The main background contributions are independent of the neutral beam, so the difference between a spectrum taken with beam on and beam off is dominated by the CXRS signal. The effectiveness of the background subtraction depends on how large the background is compared with the foreground, how the background is varying over time, and whether there are other impurity lines which also charge exchange with the beam. Once the

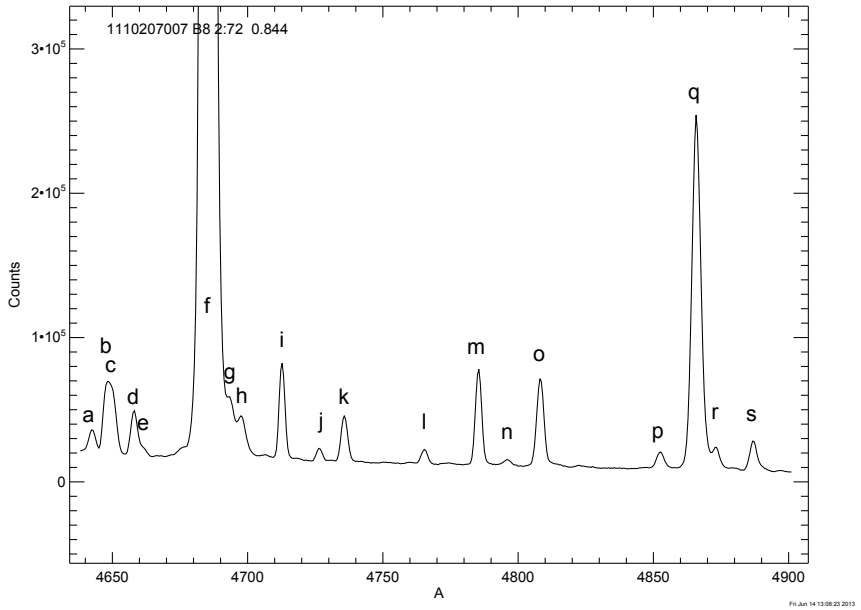

Figure 2.3: Impurity lines in spectrum in a wider range around 4686 Å. The plot has been zoomed in so that the He II line, marked f, is above the scale, so that impurity lines in this wider region are more easily visible.

background is subtracted out, the components of the emission spectrum are close to Gaussians at a common temperature and can be fitted. The area of the Gaussians gives a measurement of the fully ionized density. The center of the Gaussians gives a measurement of the ion velocity component along the viewing direction. The width of the Gaussians gives a measurement of the ion temperature along the viewing direction.

Table 2.1: Impurity line identification with low dispersion helium grating

	observed	identification
a	4643.2398	Ar I 4642.137
b	4648.5	C III 4647.42, B IV 4647.13, Ar I 4647.489
c	4650.9	C III 4650.25, C III 4651.47, Ar 4652.3
d	4658.8362	C IV 4658.30, B IV 4658.15, Ar II 4657.901
e	4662	C III 4663.642
f	4686	He II 4685.8, B IV 4685.00, C IV 4658.30 (6h-5g), Ar II 4682.2759
g	4694.1	
h	4698.4	
i	4713.2090	He I 4713.1457, Ar II 4710.8230
j	4726.8542	Ar II 4726.868
k	4735.9279	Ar II 4735.906, C IV 4736, C II 4735.464, C I 4735.163
l	4764.8574	Ar II 4764.865
m	4784.3007	B II 4784.206
n	4794.5101	
o	4806.2516	Ar II 4806.020
p	4848.2331	Ar II 4847.810
q	4860.6078	D 4860, C II 4862.580
r	4867.5	Ar II 4865.910
s	4880.0746	Ar II 4879.864

2.2 Emission Model

The CXRS spectral photon emissivity is given by

$$\varepsilon\left(\mathbf{r},\Omega,\lambda\right)\mathrm{d}V\,\mathrm{d}\Omega\,\mathrm{d}\lambda=\frac{1}{4\pi}\iint f_n\left(\mathbf{r},\mathbf{v}_n\right)f\left(\mathbf{r},\mathbf{v}\right)q_{\mathrm{em}}\left(\left|\mathbf{v}_r\right|\right)\epsilon(\mathbf{v},\hat{\mathbf{s}},\Omega,\lambda)\,\mathrm{d}^3\mathbf{v}\,\mathrm{d}^3\mathbf{v}_n \tag{2.3}$$

where $f\left(\mathbf{r},\mathbf{v}\right)$ and $f_n\left(\mathbf{r},\mathbf{v}_n\right)$ are the distribution functions for the ions and fast neutrals respectively, $\mathbf{v}_r\equiv\mathbf{v}-\mathbf{v}_n$, q_{em} is an effective rate coefficient for photon emission within a transition of interest (e.g. $\mathrm{n}=4\longrightarrow 3$), and ϵ contains the Doppler shifted atomic emission model. q_{em} combines the cross

section for charge exchange into various states with cascade probabilities, Stark and collisional mixing, excitation, and ionization, and therefore also depends on n_e, T_i, B, and Z_{eff} to a small degree. It will be examined more closely in section 2.2.1.

When a neutral beam is used as a source of neutrals, the neutral velocity distribution approximately occupies just a few discrete values[3], so the equation can be written

$$\varepsilon\left(\mathbf{r},\Omega,\lambda\right)\mathrm{d}V\,\mathrm{d}\Omega\,\mathrm{d}\lambda=\frac{1}{4\pi}\int\sum_{k}n_{k}f\left(\mathbf{r},\mathbf{v}\right)q_{\text{em}}\left(\left|\mathbf{v}_{r}\right|\right)\epsilon(\mathbf{v},\hat{\mathbf{s}},\Omega,\lambda)\,\mathrm{d}^{3}\mathbf{v} \tag{2.4}$$

where k is an index for a small number of beam energy components.

All of the wavelength and angular dependence is contained within ϵ, given by

$$\epsilon(\mathbf{v},\hat{\mathbf{s}},\mathbf{B},\lambda)=\sum_{n}a_{n}(\Omega)\delta\left[\lambda-\lambda_{n}\left(1+\frac{\mathbf{v}\cdot\hat{\mathbf{s}}}{c}\right)\right] \tag{2.5}$$

The summation over n is a summation over all lines within the transition array. This flexibility allows us to include the effects of fine structure and Stark-Zeeman splitting. a_n and λ_n are the normalized amplitude and wavelength of the nth (sub)line. We require that $\frac{1}{4\pi}\iint\epsilon(\mathbf{v},\hat{\mathbf{s}},\Omega,\lambda)\,d\Omega\,d\lambda=1$. If this level of resolution is not needed (as in the case of high temperature and low magnetic field), then only a single line is required, and the expression is greatly simplified:

$$\epsilon(\mathbf{v},\hat{\mathbf{s}},\lambda)\approx\delta\left[\lambda-\lambda_{0}\left(1+\frac{\mathbf{v}\cdot\hat{\mathbf{s}}}{c}\right)\right]$$

[3]For positive ion extraction beams, the kinetic energy of the output atoms fall on integer fractions of the extraction energy. See 2.4.2

The term in parentheses in equation 2.5, $1+\frac{\mathbf{v}\cdot\hat{\mathbf{s}}}{c}$, is the non-relativistic Doppler shift of the line, given by the velocity of the newly formed ion projected on to the viewing direction $\hat{\mathbf{s}}$. As we typically cannot resolve ions with relativistic energies using CXRS, this approximation is appropriate. The full atomic line model is examined in section 2.2.3.

There are two grades of emission model which are applicable to the CXRS diagnostic:

synthetic diagnostic A synthetic diagnostic attempts to reproduce the signals exactly as measured by the detector using an emission model based on an estimated plasma state.

fitting model Instead of knowing the plasma state beforehand, the emission model is fitted to produce values for the plasma state (e.g. n_i, T_i, v_i).

Clearly, the second application is more useful, since it is a much more direct way of acquiring information. However, the second application requires inverting the emission model, and this requires use of a substantially simplified emission model. The synthetic model uses a more complete emission model which includes more physics. It is valuable for checking the validity of the fitting model and for seeing effects which are difficult to fit, such as the effect of finite beam width or non-Gaussian instrument function. Both models are used. Transport results are based on measurements from the simpler fitting model, and checked with the synthetic diagnostic. For fast ion studies with ICRF deposition, synthetic diagnostics were primarily used.

Equation 2.4 gives the spectral photon emissivity at just a single point in space. The actual detector signal contains contributions from the entire volume of a viewing chord. Due to the fairly large width of the beam (about 14 cm in the plasma) compared to the plasma size and the finite width of the chords, the detector signal for a single channel has contributions from many flux surfaces, limiting the radial resolution of the measurement. This effect is shown in figure 2.4 and the effect on resolution is calculated in 2.6.1.4.

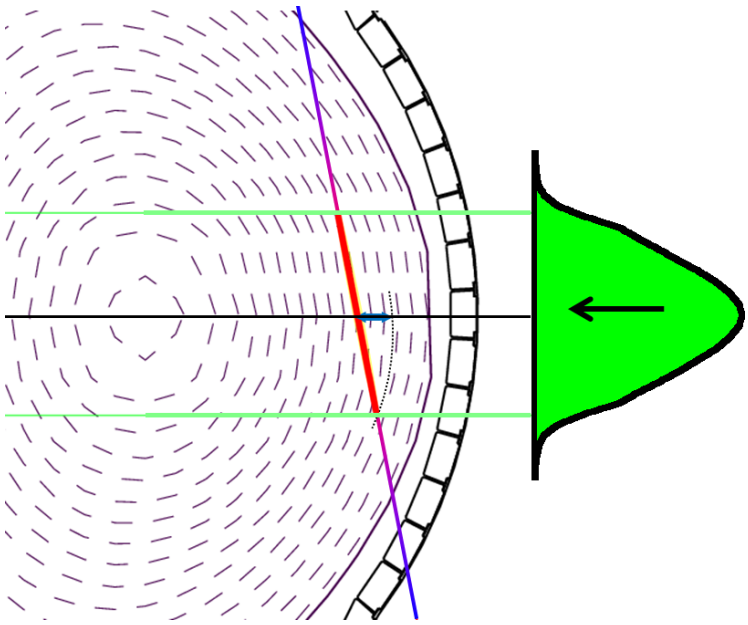

Figure 2.4: Explanation of emission localization. The viewing chord (vertical slanted line) passes through several plasma flux surfaces (purple dashed curves). The beam density is plotted on the right side. CXRS emission occurs along the intersection (shown in thick red) between the beam and viewing chord. This intersection spans several flux surfaces which are indicated by a short teal line at the midplane.

The synthetic diagnostic numerically integrates the emissivity over sev-

eral points along the viewing chord to give the detector signal.

$$I_j(\lambda)\,\mathrm{d}\lambda = X_j \int_{\text{chord}} \varepsilon\left(\mathbf{r}(s), \Omega_j, \lambda\right) \mathrm{d}s \tag{2.6}$$

Here, j is an index for a CXRS channel. I_j is the measured spectral intensity. X_j is a calibration factor which depends on the geometry and throughput of the optics. Section 2.5.2 explains how X_j is obtained. s is a position along the viewing chord. The full equation is

$$I_j \lambda\,\mathrm{d}\lambda = \frac{X_j}{4\pi} \int_{\text{chord}} \int_{\mathbf{v}} \sum_k n_k f\left(\mathbf{r}, \mathbf{v}\right) q_{\text{em}}\left(|\mathbf{v}_r|\right) \epsilon(\mathbf{v}, \hat{\mathbf{s}}, \Omega, \lambda)\,\mathrm{d}^3\mathbf{v}\,\mathrm{d}s \tag{2.7}$$

q_{em} only very weakly depends on local plasma parameters (other than collision velocity) (see 2.2.1), so both emission models use a value for q_{em} that was computed with typical C-Mod plasma conditions, so it is treated as a function of only the collision velocity.

For the fitting model, several additional approximations are made. The relative speed $|\mathbf{v}_r|$ in q_{em} is replaced by the beam velocity. This introduces some errors in the fit parameters which are examined in section 2.2.2. Except when specifically looking for fast ions, the impurity ions are assumed to have a thermal distribution (with mean flow). Finally, the impurity distribution is assumed to have the same value along the entire beam/chord intersection. In other words, f is given by

$$f(\mathbf{r}, \mathbf{v}) \approx n(\mathbf{r}_j) \left(\frac{m}{2\pi T(\mathbf{r}_j)}\right)^{3/2} \exp\left[-\frac{m(\mathbf{v} - \mathbf{v}_{\text{rot}}(\mathbf{r}_j))^2}{2T(\mathbf{r}_j)}\right] \tag{2.8}$$

where $\mathbf{r}_j$ is taken to be some representative radial position for the channel, close to the intersection between the midplane and the viewing chord (see

2.6.1.4), and m is the measured ion mass. With these assumptions, the emission spectrum takes a simple form:

$$I_j \lambda \, \mathrm{d}\lambda \approx K_j n_j \sum_n a_n(\Omega) \sqrt{\frac{mc^2}{2\pi T_j \lambda_j^2}} \exp\left(-\frac{mc^2 \left[\lambda - \lambda_n(1 + v_j/c)\right]^2}{2T_j \lambda_j^2} \right) \mathrm{d}\lambda \tag{2.9}$$

$$K_j \equiv \frac{1}{4\pi} \left(\sum_k q_{\mathrm{em}}(v_k) \int n_k \, \mathrm{d}s \right) \tag{2.10}$$

where n_j, v_j, and T_j are the approximate ion density, velocity component (parallel to chord), and temperature for the chord.

The CXRS analysis code searches for a weighted nonlinear least squares best fit of this model to the measured spectrum minus background by varying n_j, v_j, and T_j using a Levenberg-Marquardt routine called MPFIT [131] based on the MINPACK algorithm [137].

2.2.1 Charge exchange cross section and effective emission rate

Accurate cross sections for charge exchange from a hydrogen neutral beam to a bare nucleus are vitally important for CXRS measurements, both directly in analyzing the emission and indirectly in modeling the beam penetration. For the first task, it is necessary to know the distribution of final energy states following a charge exchange reaction in order to calculate the effective rate coefficient for photon emission q_{em}.

q_{em} is a combination of all possible reaction pathways that produce a photon of the transition of interest. This is somewhat less than the cross section for charge exchange into an excited state because the excited state

can take several different decay paths which may not include the transition of interest. For the most part, only charge exchange into the upper state of the transition of interest or a more excited state can contribute to the spectroscopic signal. For the helium diagnostic, we are viewing the transition $He^{+1}(n = 4)$ to $(n = 3)$, emitting a photon near 4686 Å, so we are most interested in state selective cross sections into $(n = 4)$ or above.

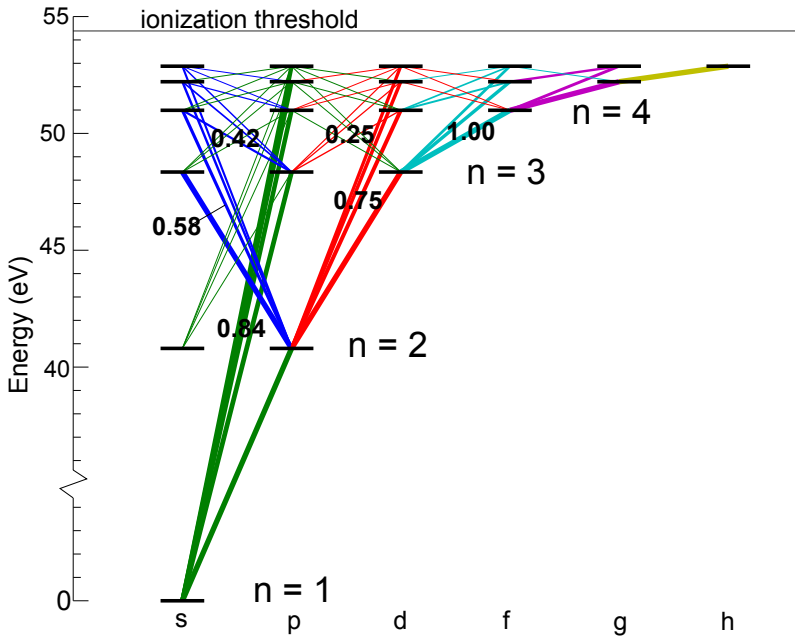

Figure 2.5: Helium Grotrian diagram. Allowable radiative transitions are shown by diagonal lines, with the thickness of the line scaled by the branching ratio from the upper state. A few branching ratios for the $n = 4$ upper state are printed.

Figure 2.5 shows the radiative transitions for He II. The transition probabilities are extremely well known. For excited states with maximal angular momentum for a given energy level, $\ell = n - 1$, the only allowable transi-

tion is $\Delta n = -1$, $\Delta \ell = -1$. But for other excited states, the most probable transitions jump multiple principle quantum numbers, to the lowest n state allowable by ℓ selection. Due to this ℓ asymmetry in radiation rates, state selective charge exchange cross sections with full $n\ell$ resolution are needed.

Some heuristics can aid in understanding the distribution of energy levels following an electron transfer. Consider that the mass of the electron is much less than the mass of the nuclei, so the electron cannot impart much momentum from the beam to the impurity ion, so the motion of the projectile atom and target ion are largely unchanged by the charge exchange process. Conservation of electron energy suggests that the initial electron binding energy should be about equal to the final binding energy. The energy levels of a hydrogenic ion are

$$E_n = -hcR_\infty \frac{Z^2}{n^2} \tag{2.11}$$

where R_∞ is the Rydberg constant. This gives the resonant transfer condition $n_f = Zn_i$. Charge exchange cross sections tend to reach a maximum at collision velocities $v \approx v_e$ where v_e is the orbital velocity of the bound electron. The virial theorem gives

$$\langle v_e \rangle = \sqrt{-E_n/m_e} \tag{2.12}$$

By time symmetry, we can expect that cross section is larger when the orbital velocity of the final state is roughly equal to the orbital velocity. However, this gives a different resonant transfer condition $n_f = Z^{0.5} n_i$. Classical Trajectory Monte Carlo simulations[159, 143] have established that the dominant transfer condition is somewhere in the middle, $n_f \approx Z^{0.75} n_i$. These calculations are

most likely to be valid for high excitation stages, where the correspondence principle holds.

For helium, the dominant state after charge exchange is $(n = 2)$. For collision energies $E < 13\,\mathrm{keV}$, $(n = 2)$ accounts for over 90% of the total charge exchange cross section[81], although the ratio decreases at higher beam energies. The reason the CXRS diagnostic makes use of the $(4 \rightarrow 3)$ transition rather than the $(2 \rightarrow 1)$ transition is that the Lyman emission at 303.8 Å is at the end of the extreme ultraviolet range which restricts the use of optical hardware, including lenses and port windows. In addition, the relative line shifts and widths are much more difficult to resolve at smaller wavelength.

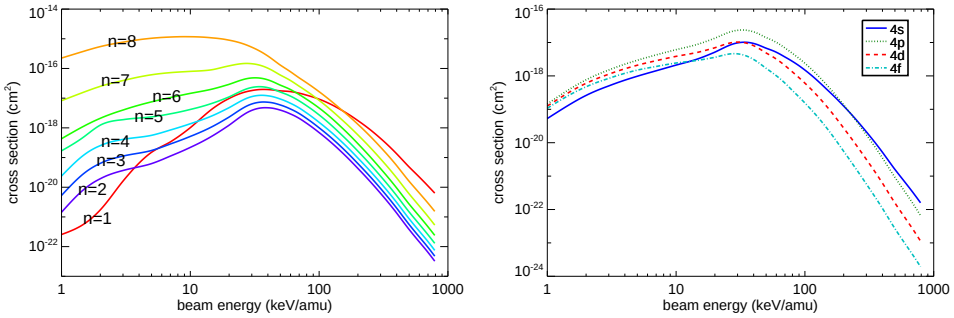

Figure 2.6: CX $He^{2+} + H^0 \longrightarrow He^+[nl] + H^+$ cross sections from [168]. left: summed over ℓ. right: $n\ell$-resolved.

Charge exchange cross sections for helium have been the subject of many theoretical[59, 11, 182, 193, 84, 136] and experimental[81, 58, 72] efforts. This reaction has been regarded as an important benchmark of quantum methods as one of the simplest cases of an asymmetric three body atomic problem. Recommended cross sections have previously been assessed in the

ORNL Redbook[7] and IAEA APID series[107] but are lacking some of the necessary high $n\ell$-resolved states. The most complete set of recommended cross sections was found in the ADAS database[168]. The ADAS dataset `qcx#h0_old#he2.dat` was manually assembled largely from data from Fritsch[59], Belkić[11], and Hoekstra[81] and last updated in 1995, and contains data for $n \leq 6$, as well as scalings for extrapolating to higher n. The ADAS dataset was used for the CXRS results in this thesis. Minami et al[136] (2008) have published newer theoretical cross sections based on a lattice time dependent Schrödinger equation method, and have done a broad comparison with previous experimental and theoretical results. These results have not yet been incorporated into the CXRS analysis. The cross sections of Minami *et al* differ from the ADAS dataset by up to 50 % for energies near 50 keV.

The simplest estimate of the emission rate coefficient is

$$q_{\rm em}(|\mathbf{v}_r|) = |\mathbf{v}_r| \sum_{\ell} \sigma_{{\rm cx},4\ell} B_{4\ell} \tag{2.13}$$

where $\sigma_{{\rm cx},4\ell}$ is the cross section for charge exchange into the $n\ell = 4\ell$ state and $B_{4\ell}$ is the radiative branching factor

$$B_\ell = \frac{A_{4\ell\to 3}}{\sum\limits_{n<4} A_{4\ell\to n}} \tag{2.14}$$

A more complete calculation of $q_{\rm em}$ includes collisional and Stark partial mixing of ℓ states as well as effects of charge exchange to higher energy levels, which can cascade to the $(n = 4)$ state and significantly increase the emission rate. Partial mixing of the ℓ states at $n = 4$ causes a moderate reduction in

the emission because some He^{1+} $(4f)$ (which has a branching factor of 1 for transitions to $(n = 3)$) convert to other states with lower branching factor (such as $4p$, which has a branching factor of 0.04). At higher energy levels, the ℓ-mixing increases because the energy levels are more closely spaced, the rate of collisions increases, and the rate of radiative decay decreases. Above $n \gtrsim 6$, the ℓ states can be treated as statistically populated within an n level. The effective emission rate coefficient has been calculated using ADAS 309[168], including contributions from charge exchange to all states $4 \leq n \leq 20$ and taking into account branching factors and collisional mixing. Excitations from lower states are not included. The code solves the following equation

$$\sum_{\ell''} M_{(n)ell,\ell''} N_{n\ell''} = N_b N^+ q_{n\ell}^{(CX)} + \sum_{n' \geq n+1} A_{n\ell,n'\ell'} N_{n'\ell'} \tag{2.15}$$

where $M_{(n)\ell,\ell''}$ is a matrix for collisional mixing between ℓ states, $q_{n\ell}^{(CX)}$ is the charge exchange rate to the $n\ell$ state, N_b is the beam population, and N^+ is the fully ionized He population. The radiative cascade is handled by solving each n level iteratively, starting at $n = 20$ and moving down. Figure 2.7 shows the results of the code, compared to other estimates. The present calculation differs from a previous calculation [185] which was performed for JET parameters by less than 2 %.

In principle, lower states can contribute to the effective emission rate because the ion can undergo collisional excitation from a lower state to the $(n = 4)$ state. This creates an effect called plume (see 2.3.4). In addition, collisional deëxcitation and ionization can reduce the effective emission by

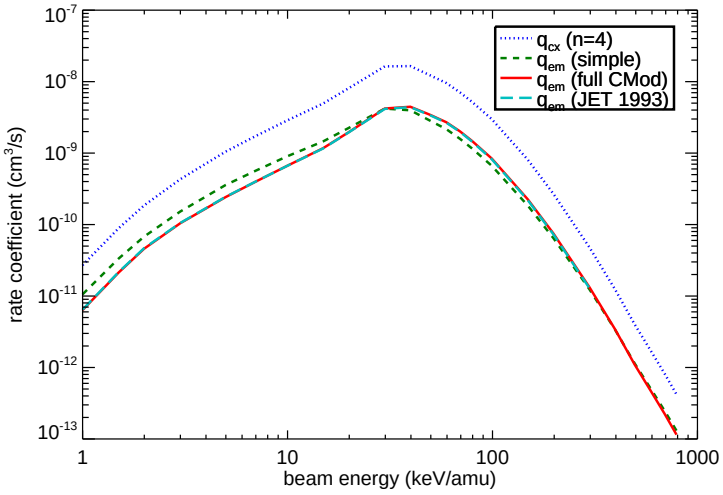

Figure 2.7: Computed charge exchange photon emission rate coefficient for He $4 \rightarrow 3$. The new Alcator C-Mod calculation is shown as a solid red line. The JET result [185] is shown in a dashed cyan line. The simple calculation based on 2.13 is shown as a dashed green line. The cross section to the n=4 state is shown as a dotted line.

reducing the effective branching factor. Since electrons move much faster than the ions, electron collisions dominate these collisional processes. To check if these processes can be safely neglected, it is useful to compare the rates of collisional processes with the radiative transition probabilities. Table 2.2 shows typical values for the C-Mod core plasma, with statistical average taken over ℓ.

Fusion plasmas are generally optically thin to visible wavelengths, so we can ignore the effects of stimulated emission and absorption. Passive recombination is not included here because it is not an active process (proportional to beam density); however, it will contribute to the background signal. For

Table 2.2: Approximate Rates of Atomic Processes[a]

atomic process	rate per atom $(s^{-1})^1$
CX from beam to He (n=4)	1.20
CX from beam to He (all n)	14.2
spontaneous emission A_{43}	1.44E8
spontaneous emission A_{42}	1.34E8
spontaneous emission A_{41}	1.09E9
spontaneous emission A_{54}	4.32E7
spontaneous emission $\sum_{n<5} A_{5n}$	1.85E8
collisional excitation C_{34}	2.58E7
collisional deëxcitation C_{43}	1.46E7
collisional excitation C_{24}	9.28E5
collisional deëxcitation C_{42}	2.34E5
collisional excitation C_{45}	7.80E7
collisional deëxcitation C_{54}	5.00E7
collisional excitation C_{14}	2.77E4
collisional deëxcitation C_{41}	1.82E3
ionization of He (n=1) by e^-	3.9E5
ionization of He (n=2) by e^-	1.6E6
ionization of He (n=3) by e^-	3.7E6
ionization of He (n=4) by e^-	6.6E6
ionization of He (n=5) by e^-	1.0E7

[a] ($T_e = 1\,\mathrm{keV}$,$n_e = 1 \times 10^{14}\,\mathrm{cm}^{-3}$,$E_b = 40\,\mathrm{keV}$,$n_b = 1 \times 10^{8}\,\mathrm{cm}^{-3}$)

[1] numerals after E denote multiplication by powers of 10

states $n \leq 4$, spontaneous emission is the dominant process, but collisional processes become more important at higher n. The threshold at which collisional processes largly take over is around $n = 5$. At higher n numbers, the collisional excitation exceeds the deëxcitation. Therefore, charge exchange to higher states are not really contributing to the $4 \rightarrow 3$ emission rate, and we can cut off the calculation beyond a certain collisional limit.

2.2.2 Cross section effects

When a Gaussian fitting model is used to fit the Doppler-broadened CXRS spectrum, the velocity dependence of the cross sections and effective rate coefficient cause some error in the inferred density, temperature, and velocity. The effect has been studied in [184], where the effect is calculated for several species, including ^{3}He and ^{4}He, and three beam angles. The cross-section effects are small when $T \ll E_{\text{beam}}$ but grow rapidly as T becomes closer to E_{beam}. For ^{4}He, $T = 2\,\text{keV}$, and $E_b = 40\,\text{keV}$, the deviations between true and apparent values are approximately

$$n_{\text{true}}/n_{\text{app}} \sim 0.95 \tag{2.16}$$

$$\left|T_{\text{true}} - T_{\text{app}}\right| < 0.05\,\text{keV} \tag{2.17}$$

$$v_{\text{true}} - v_{\text{app}} \sim -10\,\text{km/sec} \tag{2.18}$$

where the apparent value is a naïve estimate obtained by using the beam velocity instead of the relative velocity in the effective emission cross section.

To verify the results, I have run simulations for the 2 keV case, for both ^{4}He and ^{3}He CXRS. The cross-section effects depend on the angle θ between the viewing chord and the beam. Some results are shown in figure 2.8. The velocity error scales approximately with $\cos(\theta)$, and reaches zero when the viewing chord and beam are perpendicular, by symmetry. The temperature error is very small when $\theta = 90^\circ$ but grows as θ is reduced or increased. On the other hand, the density error is insensitive to the angle between the viewing

chord and beam. The effects for ^{3}He are larger than ^{4}He because the thermal velocity for ^{3}He is greater. The simulations agree with previous results.

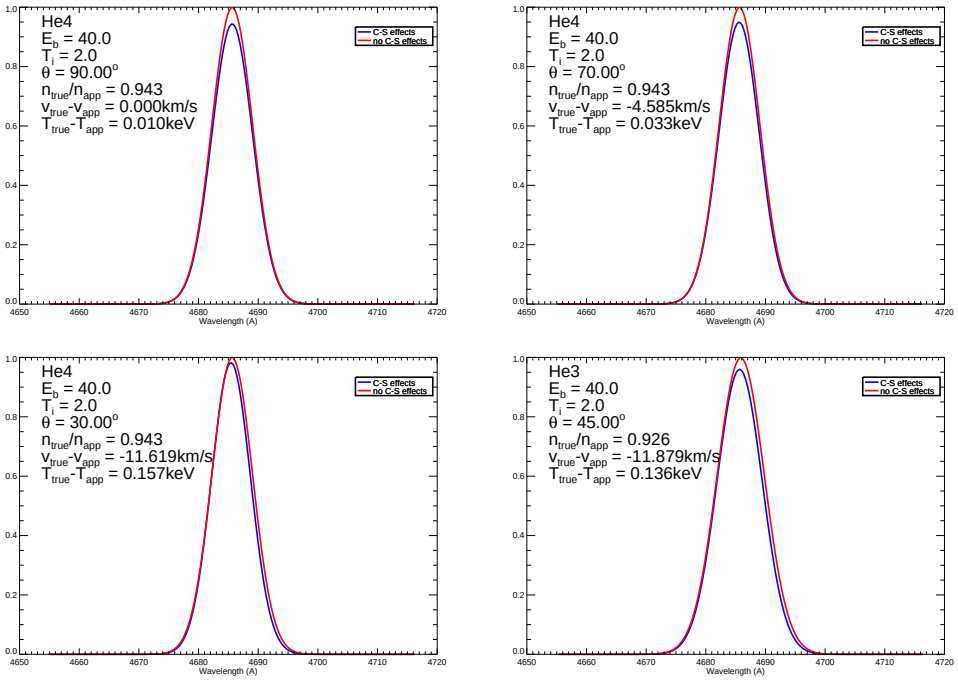

Figure 2.8: A comparison between synthetic CXRS spectra with cross section effects, and without cross section effects. A single component line was used for the atomic model.

The deviations are small compared to our measurement errors, but the analytical correction factors are included in the most recent analysis. The correction factors for density and velocity depend on the true temperature. Because the experimental error in the CXRS temperature measurement is large, it doesn't make sense to use the experimental temperature to calculate the correction factor for the density and velocity. Instead, the electron temperature from Thomson scattering was used for the purpose of calculating the

correction factors, which are small anyways. The impact on the helium profiles can be seen in figure 2.9.

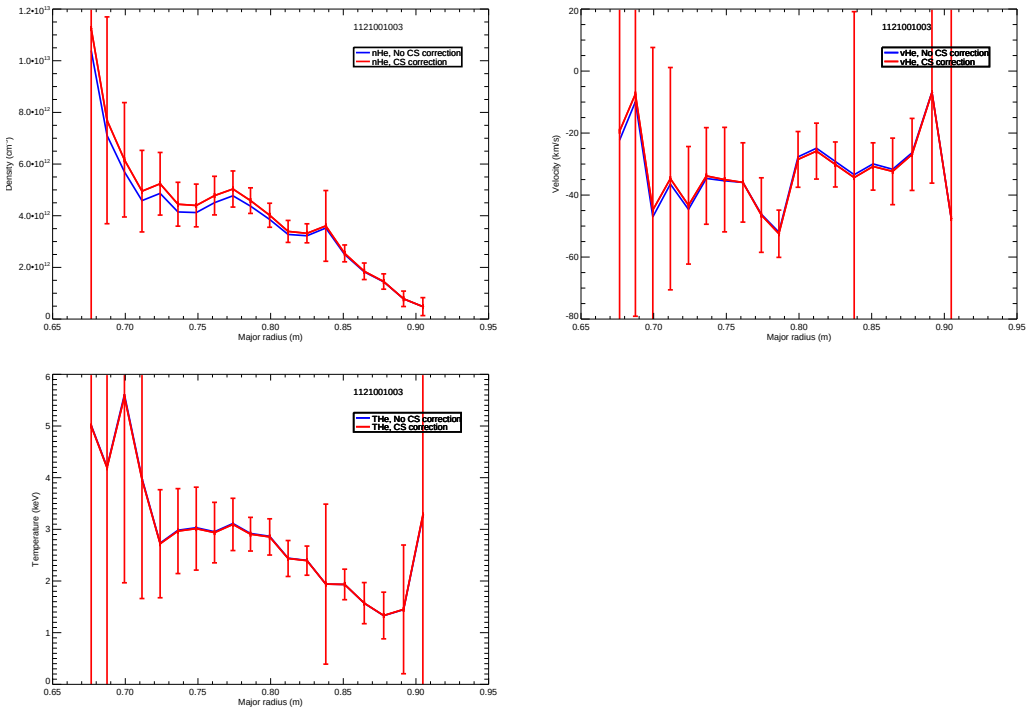

Figure 2.9: Cross section effect corrections to ^{3}He profiles for shot 1121001003

2.2.3 Zeeman Effect and Fine Structure

When an atom[4] is in a magnetic field, the degeneracy is broken between states with the same m quantum number, and the line emission is split into many components. Traditionally, the term Zeeman effect is used to decribe the splitting when the coupling to the external field is small compared to the

[4]taken to include ions with bound electrons

fine structure (weak field limit), and the magnetic coupling can be treated as a perterbation. When the coupling is large compared to the fine structure (but small compared to the gross structure), it is known as the Paschen-Back effect (strong field limit). However, in a tokamak plasma, the magnetic field has an intermediate strength such that neither limit is appropriate, and eigenstates for the full Hamiltonian should be used to describe the atom. This includes the combined effect of the fine structure and an arbitrary magnetic field. This general case is still usually referred to as the Zeeman effect.

For ^{4}He, which has no nuclear magnetic moment, this describes the fully resolved splitting of the energy levels. For ^{3}He, additional splitting exists due to interaction between the magnetic field and the nuclear magnetic moment.

The Zeeman effect is analogous to the Stark effect, which describes splitting due to an external electric field. In the plasma rest frame, the electric field is negligible. However, relativity states that an atom moving through a magnetic field experiences an electric field in its own rest frame. Therefore, fast moving atoms experience a so-called motional Stark effect in a magnetic field. This effect can be used to diagnose the plasma (for example, [86]). In general, a combination of Stark and Zeeman effects is present, resulting in a complicated spectrum. The Stark-Zeeman effect has been studied in [96] and [25] for H_α and H_β in the high-field limit (neglecting fine structure) for the purpose of characterizing beam emission. However, for CXRS emission, it is not appropriate to neglect the fine structure and instead the motional Stark effect can be neglected, as it is smaller than the fine structure and Zeeman

splitting for typical thermal velocities for $T_i \sim 1\,\mathrm{keV}$. Table 2.3 compares the sizes of splittings in C-Mod CXRS relevant conditions.

Table 2.3: Comparison of Stark, Zeeman, and Spin-Orbit coupling[a]

type	magnitude	approximate splitting energy
Zeeman	$\mu_\mathrm{B} B_T$	$3 \times 10^{-4}\,\mathrm{eV}$
Spin-Orbit	$\frac{m_e c^2 (Z\alpha)^4}{3n^3}$	$3 \times 10^{-4}\,\mathrm{eV}$
Stark (1 keV)	$\frac{3ea_0 v_\perp B_T}{Zc}$	$9 \times 10^{-5}\,\mathrm{eV}$
Stark (10 keV)	$\frac{3ea_0 v_\perp B_T}{Zc}$	$3 \times 10^{-4}\,\mathrm{eV}$

[a] hydrogenic helium, $Z = 2$, $A = 4$, $B_T = 5.3\,\mathrm{T}$

The total Hamiltonian of a hydrogenic atom, including fine structure and the Zeeman effect, but not the Stark effect, is

$$H = H_0 + H_\mathrm{kinetic} + H_{LS} + H_\mathrm{Darwin} + H_\mathrm{Zeeman} \tag{2.19}$$

where H_0 is the Hamiltonian for a basic non-relativistic spinless atom (Schrödinger atom), H_kinetic is the first order relativistic correction to the kinetic energy, H_{LS} is the spin-orbit coupling, H_Darwin is the Darwin term[39], and H_Zeeman is the coupling between the atomic magnetic moment and the external field. These

terms are expanded as:

$$H_0 = \frac{\mathbf{p}^2}{2m} - \frac{Ze^2}{r} \tag{2.20}$$

$$H_{\text{kinetic}} = -\frac{\mathbf{p}^4}{8m^3c^2} \tag{2.21}$$

$$H_{LS} = \frac{Z\alpha\hbar}{m^2c}\frac{\mathbf{L}\cdot\mathbf{S}}{r^3} = \frac{Z\alpha\hbar}{2m^2c}\frac{\mathbf{J}^2 - \mathbf{L}^2 - \mathbf{S}^2}{r^3} \tag{2.22}$$

$$H_{\text{Darwin}} = \frac{\pi}{2}\frac{Z\alpha\hbar^3}{m^2c}\delta^3(r) \tag{2.23}$$

$$H_{\text{Zeeman}} = \boldsymbol{\mu}\cdot\mathbf{B} = \boldsymbol{\mu}_\ell\cdot\mathbf{B} + \boldsymbol{\mu}_s\cdot\mathbf{B} \tag{2.24}$$

where m is the reduced mass and $\boldsymbol{\mu}$ is the total magnetic moment, which is the sum of the orbital magnetic moment and the electron spin magnetic moment[5].

This is analytically solvable, but there are many lines in the resulting spectrum. There are $2n^2$ sublevels within every principle energy level, which are all non-degenerate in the full Hamiltonian. Thus, there are $32 \times 18 = 576$ potential transitions for the $n : 4 \to 3$ group; however, only 146 of these are allowed by the dipole selection rules ($\Delta j \in -1, 0, 1$, $\Delta m_j \in -1, 0, 1$).

The calulation for the Zeeman+fine structure line energies and amplitudes builds upon the solution to the fine structure Hamiltonian $H_{fs} = H_{\text{kin}} + H_{LS} + H_{\text{Dar}}$, so the fine structure solution is given first.

In the fine-structure-only case, good quantum numbers are n, ℓ, j, and m (and of course s, which is always 1/2). The resulting energy levels are

[5]The nuclear magnetic moment is about 1000 times smaller due to the larger mass and has been neglected in the present discussion.

dependent on n and j only[6]. The energy shifts relative to the Rydberg energy levels are given by

$$\Delta E_{nj} = -R_m \frac{\alpha^2 Z^4}{n^3} \left(\frac{1}{j+1/2} - \frac{3}{4n} \right) \tag{2.25}$$

where $R_m = \frac{m_e m_i}{m_e+m_i} \frac{e^4}{8\varepsilon_0^2 h^3 c}$ is the reduced mass Rydberg constant and α is the fine structure constant.

An abbreviated derivation of the fine structure energy levels is given here, based on [115]. We note that H_{kin} and H_{Dar} are invariant under rotation of $\mathbf{r}$, and H_{LS} is invariant when rotating $\mathbf{r}$ and $\mathbf{s}$ simultaneously. Therefore, the sum $\mathbf{J} = \mathbf{L} + \mathbf{s}$ commutes with H_{fs}, confirming that j is a good quantum number. Therefore, we need to compute the values of H_{kin}, H_{LS}, and H_{Dar} in an $n\ell j$ eigenstate.

Starting with H_{kin}, note that

$$H_{kin} = -\frac{1}{2mc^2} \left(H_0 + \frac{Ze^2}{r} \right)^2 \tag{2.26}$$

Then, we can replace the H_0 with the Schrödinger atom solution, taking advantage of energy conservation. We require the radial expectation values

$$\left\langle \frac{Ze^2}{r} \right\rangle_{n\ell} = 2E_0 = \frac{Z^2\alpha^2 mc^2}{n^2} \tag{2.27}$$

$$\left\langle \frac{Z^2e^4}{r^2} \right\rangle_{n\ell} = \frac{Z^4\alpha^4 m^2 c^4}{n^3(\ell+1/2)} \tag{2.28}$$

[6]There is an additional effect from quantum electrodynamics called the Lamb shift which is responsible for a small energy dependence on ℓ, but it is safely neglected here.

The first one can be obtained from the virial theorem which states that the average potential energy is twice the total energy, using the H_0 solution. The second one can be obtained[54] by applying the Hellmann-Feynman theorem to the H_0 solution. Therefore, the result is

$$E_{kin} = -\frac{Z^4\alpha^4 mc^2}{2}\left(\frac{3}{4n^4} + \frac{1}{n^3(\ell+1/2)}\right) \tag{2.29}$$

H_{LS} is put into diagonal form by noting that

$$\mathbf{L}\cdot\mathbf{s} = \frac{1}{2}\left(J^2 - L^2 - s^2\right) = \frac{\hbar^2}{2}\left[j(j+1) - \ell(\ell+1) - \frac{3}{4}\right] \tag{2.30}$$

We also need the radial expectation

$$\left\langle \frac{1}{r^3} \right\rangle_{n\ell} = \frac{Z^3}{n^3(\ell+1)(\ell+\frac{1}{2})\ell a_0^3} \tag{2.31}$$

This expression is only valid for $\ell > 0$, but there is no LS coupling for the case when $\ell = 0$, so we can ignore it. This gives us

$$E_{LS} = \frac{Z^4\alpha^4 mc^2}{2}\frac{\left[j(j+1) - \ell(\ell+1) - \frac{3}{4}\right]\hbar^2}{2n^3(\ell+1)(\ell+\frac{1}{2})\ell} \tag{2.32}$$

The Darwin term is only non-zero for the $\ell = 0$ states because only s orbitals have non-zero radial wavefunction at the origin.

$$\left\langle \delta^3 r \right\rangle_{\ell=0} = \frac{1}{4\pi}\left|R_{n0}(0)\right|^2 = \frac{Z^3}{\pi n^3 a_0^3} \tag{2.33}$$

This gives

$$E_{\mathrm{Dar}} = \frac{Z^4\alpha^4 mc^2}{2}\frac{1}{n^3} \tag{2.34}$$

Adding the terms together, we get a magical cancellation of ℓ, and result in 2.25 above.

In the presence of a weak magnetic field, the Zeeman effect can be treated as a first order perturbation, such that the $n\ell jm$ eigenstates are still approximately valid. In this case, the magnetic moment is usually written in terms of the Landé g-factor which is defined such that

$$H_{\text{Zeeman}} = \mu_B g_j \mathbf{J}/\hbar \cdot \mathbf{B} = \mu_B g_j m_j B \tag{2.35}$$

$$g_j = g_\ell \frac{j(l+1) - s(s+1) + \ell(\ell+1)}{2j(j+1)} + g_s \frac{j(j+1) + s(s+1) - \ell(\ell+1)}{2j(j+1)} \tag{2.36}$$

The first term is the orbital contribution, proportional to the orbital g-factor g_ℓ, and the second term is the electron spin contribution, proportional to the electron g-factor g_s. These g-factors have values

$$g_\ell = 1/\left(1 + m_e/m_i\right) \tag{2.37}$$

$$g_s = 2.0023193043622 \tag{2.38}$$

where a reduced mass correction was inserted into the orbital g-factor. The Landé g-factor purposely avoids writing the magnetic moment in terms of m_ℓ and m_s, so the energy shifts for the $n\ell jm$ states can be read right off of the Hamiltonian.

When an external magnetic field is added, the eigenstates of the full Hamiltonian are modified from the fine structure case. If the magnetic field is large enough that $H_{\text{Zeeman}} \gtrsim H_{fs}$, but not so large that H_{Zeeman} becomes comparable to the splitting between principle energy levels[7], then j is no longer

[7]This puts a limit $B \ll \frac{Z^2}{2n^4} 10^6\, T$

a good quantum number, but n and ℓ are still perfectly good. m is still good because H_{Zeeman} is invariant under rotation about $\mathbf{B}$. The magnetic field will mix states of different j which have the same n, ℓ and m. The exception is when $|m| = \ell + 1/2$. This is the case when $\mathbf{L}$ and $\mathbf{S}$ are maximally aligned in the z direction and $m = m_\ell + m_s$ can only be satisfied in one way.

j may take up to two values, $j = \ell - 1/2$ and $j = \ell + 1/2$, (but only $j = \ell + 1/2$ if $\ell = 0$), so we require a new quantum number which can take two values to fully specify an electron state. Let us define a new quantum number o, which can take the values $-1/2$ and $+1/2$[8]. Each o state represents a mixture of the $j = \ell - 1/2$ and $j = \ell + 1/2$ states. In the weak field limit, the $o = -1/2$ state corresponds to the $j = \ell - 1/2$ state and the $o = +1/2$ state corresponds to the $j = \ell + 1/2$ state. In the high field limit, the o state corresponds to the m_s state in the Paschen-Back description.

The method for solving the Zeeman eigenstates follows [115] and [19]. The fact that the Zeeman and fine structure share the same n, ℓ, and m states means that the new eigenstates can be obtained by diagonalizing a 2×2 transition matrix for $H_{fs} + H_{\text{Zeeman}}$, including just the two j states. We can set the zero of energy wherever we want, so we can write the matrix as

$$\begin{pmatrix} \Delta + H_{\text{Zeeman00}} & H_{\text{Zeeman01}} \\ H_{\text{Zeeman10}} & H_{\text{Zeeman11}} \end{pmatrix} \tag{2.39}$$

with $\Delta = E_{fs}(j = \ell + 1/2) - E_{fs}(j = \ell - 1/2)$ being the difference in energy between the two fine structure lines which share the same n, ℓ, and m. The

[8]The values are simply labels and can be arbitrarily defined

upper-left element represents the $j = \ell + 1/2$ state and the lower right the $j = \ell - 1/2$ state. We need to compute

$$\left\langle \ell j m \,\middle|\, H_{\text{Zeeman}} \,\middle|\, \ell j' m \right\rangle \tag{2.40}$$

If we use $g_\ell = 1$ and $g_s = 2$,

$$H_{\text{Zeeman}} \approx \mu_B \left\langle \ell_z + 2 s_z \right\rangle B = \mu_B \left\langle j_z + s_z \right\rangle B \tag{2.41}$$

The $\langle j_z \rangle = m$ is already diagonal, so what is needed is

$$\left\langle \ell j m \,\middle|\, s_z \,\middle|\, \ell j' m \right\rangle = \sum_{m_s=-1/2}^{1/2} \langle \ell j m \,|\, \ell m_\ell s m_s \rangle \, m_s \left\langle \ell m_\ell s m_s \,\middle|\, \ell j' m \right\rangle \tag{2.42}$$

These are sums of products of Clebsch-Gordan coefficients. Useful specific forms for the Clebsch-Gordan coefficients are

$$\left\langle (\ell + 1/2), m \,\middle|\, \ell, m_\ell, s, (\pm 1/2) \right\rangle = + \sqrt{\frac{(2\ell \pm 2m + 1)}{2(2\ell + 1)}} \tag{2.43}$$

$$\left\langle (\ell - 1/2), m \,\middle|\, \ell, m_\ell, s, (\pm 1/2) \right\rangle = \mp \sqrt{\frac{2\ell \mp 2m + 1}{2(2\ell + 1)}} \tag{2.44}$$

Evaluating 2.42 with 2.43 and 2.44 gives

$$\langle s_z \rangle = \begin{pmatrix} \frac{m}{2\ell+1} & -\frac{\sqrt{(2\ell+1)^2 - 4m^2}}{2(2\ell+1)} \\ -\frac{\sqrt{(2\ell+1)^2 - 4m^2}}{2(2\ell+1)} & -\frac{m}{2\ell+1} \end{pmatrix} \tag{2.45}$$

So, the transition matrix is

$$\langle H_{fs} + H_{\text{Zeeman}} \rangle = \begin{pmatrix} \Delta + m\left(1 + \frac{1}{2\ell+1}\right)\beta & -\frac{\sqrt{(2\ell+1)^2 - 4m^2}}{2(2\ell+1)}\beta \\ -\frac{\sqrt{(2\ell+1)^2 - 4m^2}}{2(2\ell+1)}\beta & m\left(1 - \frac{1}{2\ell+1}\right)\beta \end{pmatrix} \tag{2.46}$$

where $\beta = \mu_B B$.

Diagonalizing this matrix gives the energy levels

$$E_\pm = \frac{1}{2}\Delta + m\beta \pm \frac{1}{2}\sqrt{\Delta^2 + 4\Delta\beta\frac{m}{2\ell+1} + \beta^2} \tag{2.47}$$

The transformation matrix from the j states to the o states is

$$|n\ell om\rangle \langle n\ell jm| = \begin{pmatrix} -\sqrt{(1-\gamma)/2} & \sqrt{(1+\gamma)/2} \\ \sqrt{(1+\gamma)/2} & \sqrt{(1-\gamma)/2} \end{pmatrix} \tag{2.48}$$

$$\gamma = \frac{\Delta + 2\beta\frac{m}{2\ell+1}}{\sqrt{\Delta^2 + 4\Delta\beta\frac{m}{2\ell+1} + \beta^2}} \tag{2.49}$$

This procedure can be repeated for every multiplet to give the spectrum.

The transformation matrix can be used to obtain the amplitudes of the lines. It is assumed that the magnetic field has negligible effect on the dipole transition matrix, so one can simply take the field-free solution and transform it to the new basis. The line amplitudes in the $n\ell om$ basis are weighted sums of one or two lines in the $n\ell jm$ basis. The $n\ell j$ resolved transition probabilities can be found in NIST, and the Wigner-Eckart theorem can be used to obtain the m dependence.

The radiative transition rate is given by

$$A = \frac{32\alpha\pi^3 c}{3\lambda^3}\left|\langle n\ell jm \,|\, \mathbf{r} \,|\, n\ell jm\rangle\right|^2 \tag{2.50}$$

$$|n\ell jm\rangle = R_{n\ell}(r)Y_{\ell m} \tag{2.51}$$

The radial wavefunctions are given by

$$R_{n\ell}(r) = \sqrt{\left(\frac{2Z}{na_0}\right)^3 \frac{(n-\ell-1)!}{2n(n+\ell)!}} \exp -\rho/2\rho^\ell L^{2\ell+1}_{n-\ell-1}(\rho) \tag{2.52}$$

where $\rho = \frac{2r}{na_0}$, a_0 is the Bohr radius, and $L^{2\ell+1}_{n-\ell-1}$ is the generalized Laguerre polynomial of degree $n-\ell-1$. This has been evaluated for $n=3$ and $n=4$.

$$R_{30}(r) = \frac{1}{9\sqrt{(3)}}\sqrt{\frac{Z^3}{a_0^3}}\exp -\rho/2\left(6-6\rho+\rho^2\right) \tag{2.53}$$

$$R_{31}(r) = \frac{1}{9\sqrt{(6)}}\sqrt{\frac{Z^3}{a_0^3}}\exp -\rho/2\left(4\rho-\rho^2\right) \tag{2.54}$$

$$R_{32}(r) = \frac{1}{9\sqrt{(30)}}\sqrt{\frac{Z^3}{a_0^3}}\exp -\rho/2\left(\rho^2\right) \tag{2.55}$$

$$R_{40}(r) = \frac{1}{96}\sqrt{\frac{Z^3}{a_0^3}}\exp -\rho/2\left(24-36\rho+12\rho^2-\rho^3\right) \tag{2.56}$$

$$R_{41}(r) = \frac{1}{32\sqrt{(15)}}\sqrt{\frac{Z^3}{a_0^3}}\exp -\rho/2\left(20\rho-10\rho^2+\rho^3\right) \tag{2.57}$$

$$R_{42}(r) = \frac{1}{96\sqrt{(5)}}\sqrt{\frac{Z^3}{a_0^3}}\exp -\rho/2\left(6\rho^2-\rho^3\right) \tag{2.58}$$

$$R_{43}(r) = \frac{1}{96\sqrt{(35)}}\sqrt{\frac{Z^3}{a_0^3}}\exp -\rho/2\left(\rho^3\right) \tag{2.59}$$

The radial integral is $R_{n\ell n'\ell'} = \int_0^\infty R_{n\ell}(r) r R_{n'\ell'}(r) r^2\,\mathrm{d}r$. Values for the $4 \to 3$ transitions have been directly calculated from 2.52 with the aid of the computer

algebra system Mathematica[132].

$$R_{4332} = \frac{63700992}{5764801}\sqrt{\frac{6}{7}}\frac{a_0}{Z} \approx 26.16a_0 \quad (2.60)$$

$$R_{4231} = \frac{7962524\sqrt{30}}{5764801}\frac{a_0}{Z} \approx 14.31a_0 \quad (2.61)$$

$$R_{4132} = \frac{5308416\sqrt{2}}{5764801}\frac{a_0}{Z} \approx 0.424a_0 \quad (2.62)$$

$$R_{4130} = \frac{14100480\sqrt{5}}{5764801}\frac{a_0}{Z} \approx 7.478a_0 \quad (2.63)$$

$$R_{4031} = \frac{5750784\sqrt{6}}{5764801}\frac{a_0}{Z} \approx 1.493a_0 \quad (2.64)$$

The Zeeman lines are polarized based on the change in m in the transition that makes up the line. The transitions with $\Delta m = 0$ create a group of lines called the π component, because the emission is linearly polarized in the direction of the magnetic field, projected perpendicular to the propagation. The $\Delta m = \pm 1$ lines make up the $\sigma_\pm$ lines[9], and the lines are elliptically polarized depending on the projected image of a circle lying perpendicular to the magnetic field.

The Zeeman splitting has been computed with an IDL program. Results are shown in figures 2.10 and 2.11. At zero magnetic field, the Zeeman effect coincides with the fine structure lines. At zero field, the top and bottom multiplets vanish because they correspond to transitions with $\Delta j = 2$, which is forbidden, but they may appear at higher field, where j ceases to have any meaning. Despite the complex Zeeman structure, the individual Zeeman components are never visible in a fusion plasma due to Doppler and instrumental

[9]after "senkrecht", the German word for perpendicular

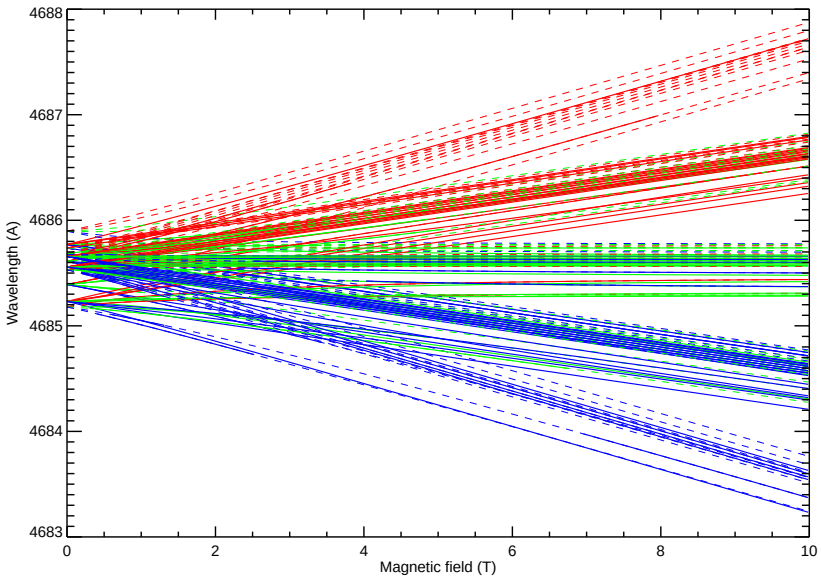

Figure 2.10: Zeeman splitting of the He II $4 \rightarrow 3$ lines versus magnetic field strength. The dashed lines represent very weak components. The red, green, and blue lines represent σ_+, π, and σ_- components. Typical tokamak fields are 3 to 9 tesla.

broadening. Nevertheless, the Zeeman effect has a small effect on the fitted line width and center.

2.2.4 Halo

Halo, in the context of neutral beam spectroscopy, refers to a population of thermal neutral atoms which surround the neutral beam within the plasma[27]. This population is formed by charge exchange from the beam atoms to a hydrogen isotope, usually the main ion deuterium. The halo neutrals are unconfined by the magnetic field and may travel a short distance before being ionized or undergoing charge exchange. By repeated charge ex-

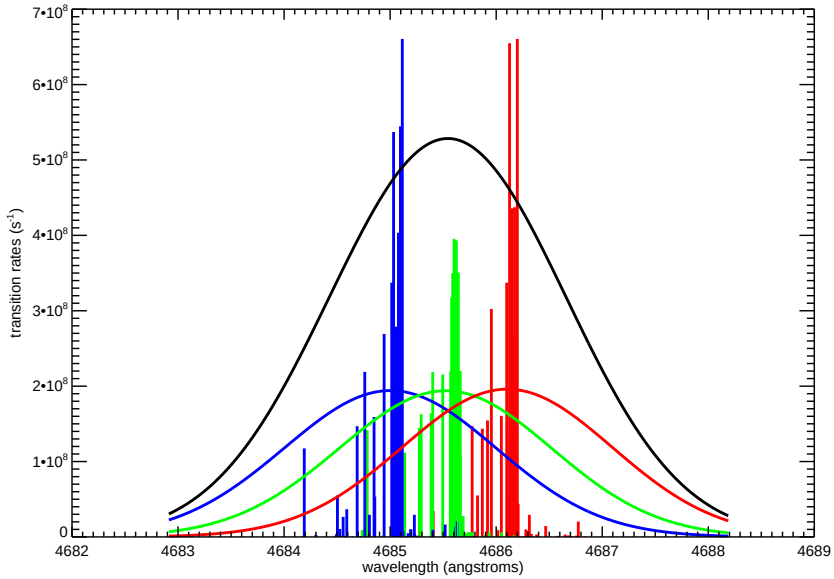

Figure 2.11: Zeeman spectrum for the He II $4 \rightarrow 3$ lines at 5.3 T. The vertical lines are the Zeeman components, and the smooth lines are spectra which have been convolved by a 1.39 Å Gaussian instrument function. The red, green, and blue lines represent σ_+, π, and σ_- components, viewed at an angle of 45° from the magnetic field.

change to other main ions, the neutral can do a random walk and travel some distance from the beam. The halo neutral population quickly decays when the beam is off. For the purpose of the CXRS diagnostic, the halo acts as another beam energy component, except the beam energy is replaced by the deuterium thermal energy.

A simple estimate puts the halo neutral density as similar to the beam density. The halo population is in an equilibrium between generation from the beam and loss from collisional ionization. If we initially ignore transport, the halo density is determined by a competition between the generation rate from

the beam and ionization by collisions:

$$n_{\text{halo}}/n_{\text{beam}} \sim \sum_k \frac{\langle \sigma_{\text{cx}} v_b \rangle_k \, f_k}{\langle \sigma_{ei} v_e \rangle + \langle \sigma_{ii} v_i \rangle} \tag{2.65}$$

If we evaluate 2.65 for typical values for C-Mod plasmas ($T_e \sim 1300\,\text{keV}$, $n_e \sim 1 \times 10^{14}\,\text{cm}^{-3}$, $E_b = [50, 25, 16.7, 2.8]\text{keV}$, $n_b = [2.26, 0.70, 3.22, 0.64] \times 10^8\text{cm}^{-3}$), we obtain $n_{\text{halo}}/n_{\text{beam}} \sim 3.6$. The cross sections were taken from [107]. Transport will spread out the halo distribution, and it will make the central density correspondingly lower. The width of the beam is about 14 cm in the plasma (FWHM). The width of the halo is estimated by

$$d_{\text{step}} = \frac{v_{Ti}}{n_e \langle \sigma_{\text{cx}} v_e \rangle} \sim 7.5\,\text{cm} \tag{2.66}$$

$$N_{\text{step}} = \frac{\langle \sigma_{\text{cx}} \rangle}{\langle \sigma_{ei} \rangle + \langle \sigma_{ii} \rangle} \sim 4.5 \tag{2.67}$$

$$\lambda_{\text{halo}} = d_{\text{step}} \sqrt{N_{\text{step}}} \sim 16\,\text{cm} \tag{2.68}$$

$$w_{\text{halo}} = \sqrt{w_{\text{beam}}^2 + \lambda_{\text{halo}}^2} \sim 21\,\text{cm} \tag{2.69}$$

If the shape of the beam is Gaussian, the shape of the halo is the convolution of a Gaussian and a Laplace distribution, which is very close to a Gaussian.

Now that we know the halo width, we can obtain a new estimate of the halo density at the beam axis by spreading the same total population over a larger width (in two dimensions). This gives the estimate $n_{\text{halo},ax}/n_{b,ax} \sim 3.6\frac{14^2}{21^2} \sim 1.6$. The results of this estimate agree with Tang's estimate [176, p.82].

The halo has strong effects on the deuterium and hydrogen emission and charge exchange, and is an important consideration for the BES, MSE,

FIDA, FICX and NPA diagnostics[10]. But for helium CXRS, the halo has a negligible effect, because the effective emission rate (see 2.2.1) is small at thermal collision energies. For 1 keV collision energy, the effective rate is only 0.17 % of the value at 50 keV. For this reason, it is not necessary to make a detailed numerical calculation of the halo taking into account the plasma geometry.

2.3 Background Emission

2.3.1 Interfering lines

A quick look at the NIST atomic spectral database shows a plethora of spectral lines which exist in the vicinity of the 4686 Å He II line. Fortunately, the plasma is quite clean and only a few elements have a chance of getting into the plasma.

Ar II lines are clearly visible in figure 2.3 at many wavelengths. There is also an Ar II line at 4682.2759 Å, but it cannot be resolved because it is in the wing of the He II 4686 Å line. To judge if this line is a problem, we need to estimate the intensity of the line. The line comes from the transition $3s^2 3p^4(^1D)4p[^2F_{7/2}] \rightarrow 3s^2 3p^4(^3P)3d[^2F_{7/2}]$. Unfortunately, no other lines from the same upper state are within range, but Ar II 4657.901 Å comes from a similar starting state $3s^2 3p^4(^3P)4p[^2P_{1/2}]$. The transition probabilities given in NIST are $8 \times 10^5\,\mathrm{s}^{-1}$ and $8.92 \times 10^7\,\mathrm{s}^{-1}$ for the 4682.2759 Å line and the

[10]Beam Emission Spectroscopy, Motional Stark Effect, Fast Ion D Alpha, Fast Ion Charge Exchange, Neutral Particle Analyzer

4657.901 Å line. Taking into account the degeneracy, the latter line is about 30 times brighter. The He II 4686 Å line is at least 100 times brighter than the 4657.901 Å line, so I estimate it is 3000 times brighter than the interfering 4682.2759 Å line.

C VI ($n = 12 \rightarrow 9$) 4685 Å is a potential interfering line, since it is nearly indistinguishable from helium. C-Mod does not use carbon in plasma facing tiles, but it may be present in trace amounts in SS 304 or SS 316 or oil residue, and can be degased from metal components. Griem's boundary[174] is a condition for the density at which the spontaneous emission rates and collisional excitation and deëxcitation rates are similar in magnitude.

$$n_e^{\text{Griem}} \approx \frac{1.5 \times 10^{24}\,\text{m}^{-3}}{n^8.5} \left(\frac{T_e}{Z^2 \text{Ry}}\right)^{1/2} Z^7 \tag{2.70}$$

For $n = 12, Z = 6$, $n_e^{\text{Griem}} \approx 4.9 \times 10^{20}\,\text{m}^{-3}$ which is a few times higher than typical C-Mod density, so spontaneous emission is still a possibility. However, the $n = 12$ excited population is very small. A very good reason for neglecting the C VI 4686 Å line comes from the fact that it is not observed in the CXRS diagnostics at JET in the He II 4686 Å spectral range, despite clearly measuring C VI at 5290.5 Å[187].

During some past experiments, calcium was introduced into the plasma using a laser blowoff system for the purpose of studying moderate mass impurity transport. It was observed that the Ca II 4685.27 Å line is detectable on our system and interferes with the helium measurement. Fortunately, calcium does not recycle so the line is short lived (∼20 ms).

Beryllium has not been used in C-Mod; however it is important in the fusion program because it is a favored material for plasma facing components due to a low Z of 4. It has been used in JET tiles and evaporators since 1988[147], and the Be IV $n = 8 \rightarrow 6$ 4685 Å line was a serious source of background for the helium CXRS measurement[187].

2.3.2 Bremsstrahlung

Bremsstrahlung, from the German word for braking radiation, is electromagnetic radiation emitted when charged particles are deflected and decelerated by collisions with other charged particles. Multi-species hot plasmas (i.e. electrons and ions) are continuously emitting (thermal) bremsstrahlung emission because the particles in thermal motion are constantly scattering off each other in microscopic Coulomb interactions. Thermal bremsstrahlung is a major cooling mechanism for fusion plasmas, and a physical limitation to the thermal confinement achievable in a fusion device. The emission spectrum is continuous and spans microwave to x-ray wavelengths. Therefore, it is a source of background to all spectroscopic measurements. Bremsstrahlung is particularly strong on Alcator C-Mod due to the quadratic density scaling.

Bremsstrahlung emission is proportional to the electron-ion collision rate and therefore scales with $n_e n_i$, and $T^{-1/2}$. The collisions between like species (electron-electron or ion-same-ion) do not contribute to bremsstrahlung because the Larmor emission from both bodies accelerating in opposite directions destructively cancels. In electron-ion collisions, electrons are deflected to

a much greater degree than the ions, and therefore, the dominant emission is from electrons. The bremsstrahlung spectral emissivity is given (in SI units) by[113]

$$\frac{\mathrm{d}W}{\mathrm{d}V\,\mathrm{d}t\,\mathrm{d}\nu\,\mathrm{d}\Omega} = \frac{e^6}{6\pi^2\epsilon_0^3 mc^3}\sqrt{\frac{2\pi}{3mk_BT}}Z^2 n_e n_i \exp\left(-h\nu/k_BT\right)\overline{g}_{ff} \tag{2.71}$$

Converting from energy to photon count and from frequency space to wavelength space, we get

$$\frac{\mathrm{d}N_\gamma}{\mathrm{d}V\,\mathrm{d}t\,\mathrm{d}\lambda\,\mathrm{d}\Omega} = \frac{e^6}{6\pi^2\epsilon_0^3 mc^3}\sqrt{\frac{2\pi}{3mk_BT}}Z^2 n_e n_i \exp\left(-h\nu/k_BT\right)\overline{g}_{ff}\frac{1}{\lambda h} \tag{2.72}$$

$\overline{g}_{ff}$ is the free-free Gaunt factor averaged over a Maxwell-Boltzmann distribution. It is a unitless number which contains the logarithmic dependence on the impact factor b, with quantum mechanical corrections. An approximate value is[57]

$$\overline{g}_{ff} = \frac{\sqrt{3}}{\pi}\log\left((1.81\times10^{-4}\,\text{Å}^{-1}\,\text{eV}^{-1})\lambda T_e\right) \tag{2.73}$$

The emissivity has a 1/wavelength dependence when written in wavelength space. Since the CXRS diagnostic only views a small wavelength range, the bremsstrahlung emission is approximately flat (see figure 2.2).

Since the bremsstrahlung emission can be estimated using other diagnostics, it can also used as an absolute intensity calibration (see 2.5.2.2).

2.3.3 He II edge emission

Although helium is fully ionized throughout most of the C-mod plasma, at the edge of the plasma, the temperature becomes low enough that partially

ionized He^{+1} is present in significant quantities. Passive charge exchange from neutral gas penetrating into the edge of the plasma also contributes to the He^{+1} population. This edge population emits at the same wavelength as the core CXRS emission and is a dominant source of background, since every viewing chord passes through the edge in two places. As seen in figure 2.2, the edge He II 4686 Å emission is much stronger than the core emission, sometimes obscuring the core emission completely in the case of some core channels in high density discharges.

When the beam is off, the edge emission can be measured and used to provide the edge He^{+1} population. This technique is utilized in 3.5.3.2 in order to determine the helium recycling needed to calculate He^{+2} transport coefficients.

The 4686 Å emission is proportional to the $n = 4$ excited population and given by

$$\epsilon_{\mathrm{Pa}\alpha} = \frac{1}{4\pi} n_{\mathrm{He}^{+2}} f_{n=4} A_{4\to 3} \tag{2.74}$$

where $f_{n=4}$ is the fraction of He II that is in the $n = 4$ state. This fraction can be calculated with a collisional-radiative-recombination model if the electron, ion, and neutral densities are known, and the electron temperature is known. The ADAS205 code[168] is used to calculate the excited state fractions.

2.3.4 Plume

In the helium CXRS measurement, the actively generated He^{+} can travel along field lines between the time they are formed (by charge exchange)

and when they are ultimately ionized. Most of the 4868 Å emission occurs within a small distance (0.6 cm) from the charge exchange point, because the charge exchange leaves the ion in an excited state. But a small fraction of the emission comes from collisionally excited ions, which occurs over a much longer distance. The collisionally excited emission is called plume, and it is treated as a source of background because the spatial localization of the signal is too poor to be treated as foreground. The plume has been studied previously in PDX and TFTR[56] and DIII-D[52] and found to be a source of significant contamination for helium measurement.

We divide the 4686 Å emission into two categories. Prompt emission is due to charge exchange directly into the $n \geq 4$ states, which emit promptly. The timescale associated with prompt emission is the lifetime of the $n = 4$ state, which is primarily determined by the spontaneous emission coefficients. Plume emission comes from a He^+ ion which is collisionally excited from any $n < 4$ state. The timescale for plume is the lifetime of the hydrogenic ion, which is primarily determined by the ionization rate from the $n = 1$ state.

The prompt travel distance is

$$d_{\text{prompt}} = \frac{v_{T,He}}{\sum_{k<4} (A_{4k} + C_{4k}) + S_4} \tag{2.75}$$

If we plug in values from table 2.2 and the thermal speed $v_{T,He} \sim 2.5 \times 10^7$ cm/s, we get $d_{\text{prompt}} \sim 0.02$ cm. Therefore, the prompt emission can be treated as coming from the beam-chord intersection. On the other hand, the plume travel

distance is

$$d_{\text{plume}} = \frac{v_{T,He}}{S_1} \sim 64\,\text{cm} \tag{2.76}$$

This is roughly 1/6 of the circumference of the torus.

Due to the geometry of the tokamak, plume only affects toroidal channels. Figure 2.12 shows how the plume confuses the radial location of a signal. On our system, because our toroidal views are tilted upward by about 36°, the effects of plume are greatly reduced. The plume emission is only visible a short distance from the beam (about $w_{\text{beam}} \cot(36°)$ from the beam center) because otherwise it misses the chord vertically.

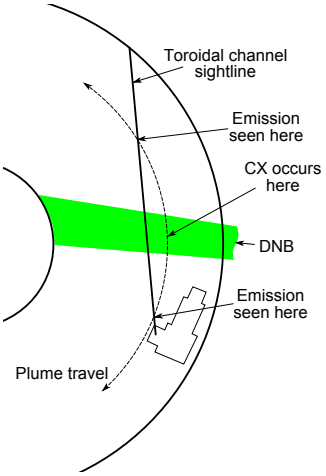

Figure 2.12: Plume effect. Plume emission from all $\rho > \rho_{\text{chan}}$ will contribute to signal

There is no effective way of separating the plume emission from the foreground emission, so all we can do is estimate the magnitude of the effect.

The ratio of the plume emission to the prompt emission is given by

$$I_{\text{plume}}/I_{\text{prompt}} = q_{\text{plume}}/q_{\text{em}} \tag{2.77}$$

$$q_{\text{plume}} \approx \left(|\mathbf{v}_r|\,\sigma_{\text{cx,all}}\right)\left(\sum_{\ell}\frac{C_{1s4\ell}B_{4\ell}}{S_1}\right)G \sim 1.0\times10^{-9}\,\text{cm}^3/\text{s}G \tag{2.78}$$

where the first factor is the He^+ generation rate, the second factor is how much an ion emits before being destroyed, and the third factor G has to do with the geometry, which is only crudely estimated.

$$G \sim \frac{w_{\text{beam}}\cot\alpha_{\text{tor}}}{d_{\text{plume}}} \sim 0.15 \tag{2.79}$$

Using typical values, the ratio of plume to prompt signal for toroidal channels is about 6 %. In machines with more toroidally oriented views, the plume is much larger (perhaps 20 % of the main signal) and a much more sophisticated estimate is needed.

2.4 Core CXRS Diagnostic Hardware

A basic layout of the top level components was shown in figure 2.1. The components can be divided into several categories: the diagnostic neutral beam, which is a complex and large device in its own right, with its own suite of diagnostics; the detection system which includes the spectrometer, CCD, computer, and camac modules; the 20 channel poloidal optical system, which rests above the plasma; the 22 channel toroidal optical system which rests on the vacuum vessel near the outer wall; and the transfer fibers linking the poloidal and toroidal systems to the detector. The design and construction of

each of these systems will be described, as well as techniques for testing and calibrating the systems.

In both the poloidal and toroidal optical systems, the optics direct light into an array of optical fibers, so each fiber carries the light for one view. These fibers end at either the poloidal or toroidal breakout box, where 35 m long transfer fibers are attached, which carry the light from the tokamak to the detector in another room. The transfer fibers do not attach directly to the spectrometer; there is another breakout box which contains fibers which attach to the spectrometer. The connections between the fibers are made with SMA905 connectors. All of the optical fibers in the system have 400 µm core diameter, excepting patch cables used for calibration, which have a variety of sizes.

There are currently 30 transfer fibers, fewer than the number of poloidal plus toroidal channels. This limits the channels available for an experiment. Each transfer fiber is labeled with a number and depending on the experiment, the connections between view channels and transfer fibers can vary. (This information is stored in the MDSplus database.)

2.4.1 Optical Design

The optical design is a tradeoff between optical throughput and spatial resolution, with a fairly stringent space constraint, both in the vacuum vessel and also with respect to access ports. The highest signal is achieved by placing the proximal optical components as close to the plasma as possible, but some

margin of safety is required as the periscopes are not allowed to face the plasma directly. High throughput is necessary in order to reduce the noise in the measurement. Generally, the photon shot noise increases as the square root of the intensity, so the signal to noise ratio increases with intensity. The measurement error is covered more fully in section 2.6.1.

The throughput in an optical system can be characterized by a photon efficiency and a geometric factor known as the étendue. Étendue comes from the French *étendue géométrique*, which means geometrical extent. Before giving the definition of étendue, it is useful to understand the motivation of the concept. Generally speaking, in a homogenous medium, the flux of light passing through a surface is proportional to $A\cos(\theta)$, where A is the area and θ is the angle of the light to the surface normal. It doesn't matter if we are talking about the source or the target because the geometry is equivalent. The étendue goes a step further by including the angles of acceptance (or emittance) into the definition. Usually, this has the shape of an acceptance (or emittance) cone. If the source is Lambertian[11], the photon transmission rate is proportional to the solid angle of the acceptance (or emittance) cone. Therefore, the étendue is given by

$$G = \int_S \int_\Omega n^2 \, \mathrm{d}^2 S \cos\theta \, \mathrm{d}^2 \Omega \tag{2.80}$$

where n is the index of refraction of the surrounding medium. Some lenses are capable of transmitting light over a large angle, but if a lens is used to focus

[11] A Lambertian source appears equally bright from all directions. This is usually a good approximation for a plasma, especially over a small angle range.

light on a target (such as a fiber, or another lens), then the distance and size of the target will determine the acceptance angle used to calculate the étendue. Photons entering from outside this angle will miss the target and don't count.

The important characteristic of the étendue is that étendue of the whole optical system is the minimum étendue across all of the elements. Any excess étendue in an element is wasted, as in the example of the lens above. Therefore, a wisely designed system has matching étendue to minimize waste of resources. In our case, the whole optical system contains the viewing chord, the prisms (for the poloidal system) or mirrors (for the toroidal system), lenses, optical fibers, spectrometer, and CCD. The étendue between two elements can be approximated as

$$G_{S\Sigma} \approx \frac{n^2}{d^2} S \cos\theta_S \Sigma \cos\theta_\Sigma \tag{2.81}$$

where S and Σ are the areas of the apertures of the elements, θ_S and θ_Σ are the angles relative to the line connecting the centers two elements, and d is the distance between the elements.

The geometric specification of many optical elements is given by the f-number, or focal ratio, which is the ratio of the focal length to the diameter of the entrance pupil. This number is used instead of the étendue because the nature of the target is not known to the manufacturer. The f-number can be used to calculate the étendue if the magnification is known. The numerical aperture is a related quantity. It is a measure of the angles over which an

optical element can accept or emit light, given by

$$\mathrm{NA} = n \sin(\theta) \tag{2.82}$$

where θ is the half-angle of the acceptance cone. Therefore, it is related to the étendue by

$$G = \pi S \mathrm{NA}^2 \tag{2.83}$$

where S is the area of the optical surface or entrance pupil. For an infinity-focused aberration corrected lens, the f-number N is $N \approx \frac{1}{2\mathrm{NA}}$. Confusingly, f-numbers are usually written in the notation $f/\#$, where $\#$ is replaced by the numeral value for N, i.e. $f/4$ means $N = 4$. A $f/8$ part has 1/4 the throughput of a $f/4$ part used to generate the same magnification.

Table 2.4: Étendue summary

source	target	A_{src} cm^2	A_{tgt} cm^2	d_{st} cm	étendue cm^2
plasma[a]	poloidal prism 1	0.785	2.85	42	0.0013
plasma	poloidal prism 2	0.785	2.85	43	0.0012
plasma	video lens	0.785	0.196	44	7.5×10^{-5}
video lens	fiber	0.196	0.00126		2.47×10^{-4}
400 µm fiber	Holospec $f/1.8$	0.00126			
Holospec $f/1.8$	MicroMAX CCD				7.5×10^{-5}

[a] 1 cm spot size
[1] Large prism is necessary to cover all channels

The étendue of the system is set by the optical fibers that are used. Note that a single fiber will not fill the Fujinon video lens, but the video lens must be large enough to accomodate 20 fibers arranged in a line. Basically,

this means that the video lens must capture light to fill an imaginary fiber that is 20 times the diameter, plus about 6.5° to account for space between fibers.

2.4.2 Diagnostic Neutral Beam

The C-Mod Diagnostic Neutral Beam Injector (DNB) provides the active charge exchange for the CXRS diagnostic. It was designed and built by the Budker Institute of Nuclear Physics (BINP) in Novosibirsk, and installed at Alcator C-Mod in 2005[8]. It is capable of an acceleration voltage up to 50 kV and extracted current up to 7 A. It uses a hollow cathode with a LaB_6 emitter which allows long pulses of up to 3 s[43], although C-mod plasma discharges are generally shorter than 2 s. Some properties of the DNB are listed in table 2.5.

The principal responsibility for all aspects of the DNB at C-Mod is held by Dr. R. S. Granetz. Details are reported here mainly to support the understanding of the CXRS diagnostic.

The beam is typically modulated with a duty cycle of 60 ms on, 40 ms off, but other timings are sometimes used. Modulation allows for time-slice subtraction of the background signal and extends the limit on pulse length to 3 s. However, the beam requires about 20 ms to stabilize following the start of each on cycle, putting limits on the modulation time and limiting the total signal (since unstable frames are removed from the analysis). Note that background subtraction is necessary on C-mod as the background intensity is

Table 2.5: Diagnostic Neutral Beam Parameters

parameter	value
acceleration energy	up to 55 keV
extracted current	up to 7.5 A
pulse length	3 s
E:E/2:E/3[1]	75%:5%:14%
beam divergence	0.7°
beam power[a]	200 kW
neutralization efficiency	48%
beam shape	circular
grid diameter	14 cm
FWHM at $\rho = 0$	10 cm
pressure in beam tank	~ 0.5 mtorr
pressure in beam duct	~ 0.1 mtorr

[a] power reaching plasma
[1] fraction of source current giving rise to energy components

larger than the active signal.

The DNB injector is fairly large when compared to the size of the tokamak itself. From the end of the source to the end of the calorimeter, it is about 220 cm long, and it connects to the tokamak "F-port" by means of a 160 cm duct (including the length of aperture block). A gate valve near the end of the duct allows the DNB to be pumped down or up separately from the main torus for maintenance or testing, and a set of rails allows the DNB be to pulled back away from the torus when the DNB is brought to air pressure. A schematic view of the DNB is presented in figure 2.14.

Major components of the DNB are the ion source, neutralizer tube, vacuum tank, bending magnet, ion dump, twin cryopumps, and retractable

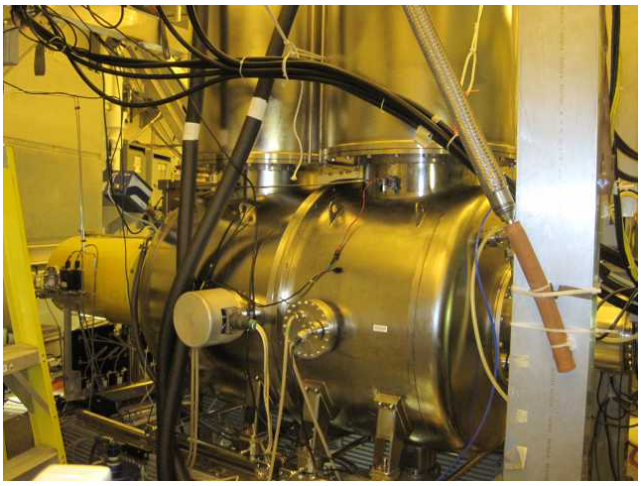

Figure 2.13: Photograph of the DNB at Alcator C-Mod

calorimeter. The ion source contains a lanthanum hexaboride hollow cathode, anode orifice, plasma chamber, accelerator grids, and a neutralizer tube. The LaB_6 emitter is actively heated to 1700 °C to reduce cathode sputtering, greatly increasing the lifespan beyond that of a cold cathode. The entire ion source is water cooled. The cryopumps operate with liquid helium. This is one of the major limiting resources for beam operation. A programmable logic controller (PLC) located in the cell[12] controls all of the major functions of beam and is connected to a PC in the control room.

The DNB operates by forming an arc between the hollow cathode and anode orifice. Fast electrons stream from the cathode through the anode and ionize the input hydrogen gas, generating a plasma in the expansion chamber. The walls of the expansion chamber are also shorted to the orifice and serve

[12]The cell is an access-controlled and shielded room containing the C-Mod tokamak.

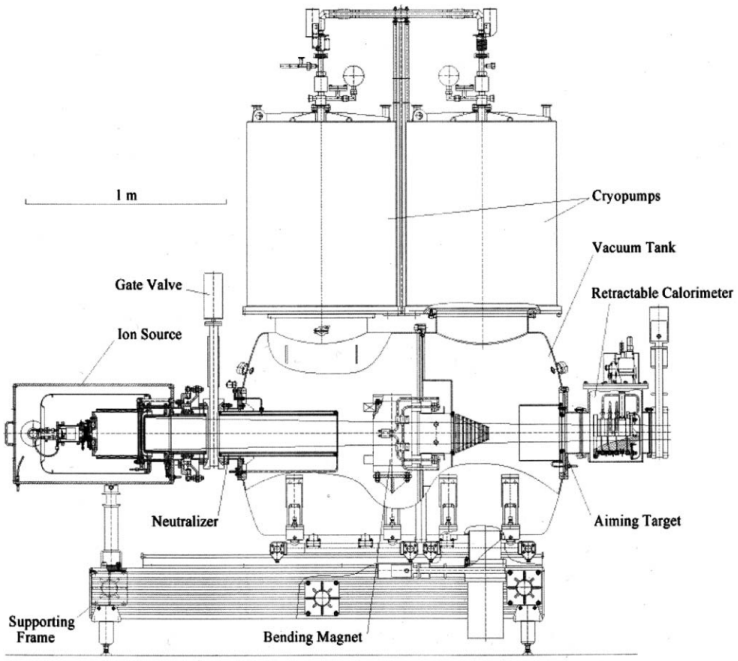

Figure 2.14: DNB general layout. Reprinted with permission from [43]. Copyright 2006, AIP Publishing LLC.

as part of the anode. The collisional processes generate several species of ions (H^+, H_2^+, H_3^+, H_2O^+, CH_3^+) which are responsible for the discrete energy components seen in the beam output. Proper optimization of the beam parameters allows for a high fraction of H^+ ions, which contribute to the full energy component of the beam, which contributes most strongly to the charge exchange signal. The multipole fields provide partial confinement of the plasma in the expansion chamber by magnetic mirroring[103], increasing the plasma density and uniformity for ion-beam extraction by the ion-optical[13] accelerating

[13]The term ion-optical refers to the use of curved acceleration grids, which generates a focal point in the tokamak 3.4 m from the accelerating grid. The propagation of ion rays is analogous to light rays in geometric optics.

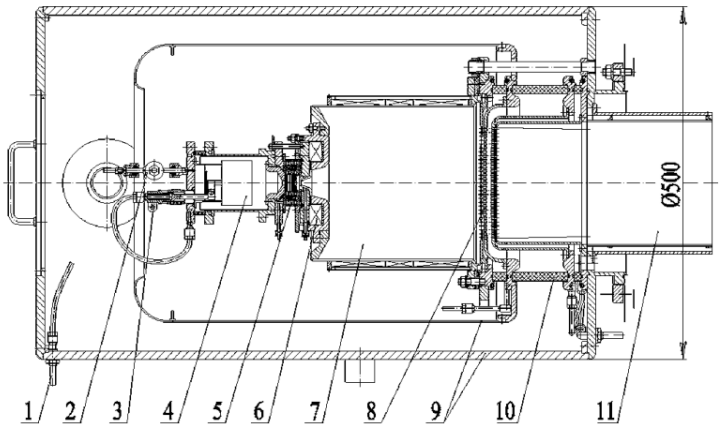

Figure 2.15: DNB ion source schematic. 1. cooling water. 2. gas valve. 3. filament contact. 4. LaB_6 cathode module. 5. arc channel. 6. magnetic insulation coil. 7. $Nd_{15}Fe_{77}B_8$ permanent magnets. 8. the grids of the ion-optical system. 9. magnetic screens. 10. HV insulator. 11. neutralizer tube. Reprinted with permission from [43]. Copyright 2006, AIP Publishing LLC.

grids[102]. Four closely-spaced biased grids accelerate a stream of ions to a velocity dependent on the charge to mass ratio of the ions. The grids direct the ion beam through the neutralizer, which is a tube filled with cold H_2 gas. The beam ions interact with the gas through charge exchange and other atomic processes[192]. About 50% of the ions are converted to neutrals in this way. The molecular ions are broken up during neutralization, primarily into neutral atomic hydrogen, but the atoms keep the ion velocities and the beam energy is distributed among simple fractions of e times the grid voltage. The beam passes by a bending magnet and the remaining ions are directed out of the beam path into a beam dump. The neutral beam travels down the beam duct into the tokamak, where it can interact with the plasma.

A few tools exist for diagnosing the beam performance. Power status, vacuum status, pressure logging, faults, LN_2 level, and other values are logged. A retractable segmented calorimeter can be put in the beam path in order to measure the shape of the power distribution of the beam. It also allows test shots to be taken without firing the beam into the tokamak, by absorbing the beam power before it reaches the gate valve. In addition, two new diagnostics have been implemented on the DNB: an 11-channel beam duct view and a single channel neutralizer view. These new systems are described in the appendix.

The beam energy fractions (the population fractions of the different energy components) are measured by Doppler spectroscopy, using a viewing chord within the beam tank oriented at 35 degrees to the beam. A spectrum is shown in figure 2.16. The spectrum clearly shows at least four Doppler-shifted H-alpha lines, corresponding to different energy components of the beam. An unshifted H-alpha line (656.28 Å) is also present, due to excitation of the tank gas by the beam. A program automatically analyzes the spectral data for beam energies and energy fractions after each beam shot. Results of the fitting are stored in MDSplus[14].

The line fits, combined with cross sections for photon emission, gives the beam energy fractions. Table 2.6 shows the energy fractions for two different

[14]MDSplus is a database and set of data analysis tools for scientific data (particularly fusion). `http://www.mdsplus.org/`. It was largely developed around the C-Mod program and serves as a database for most of the C-Mod data.

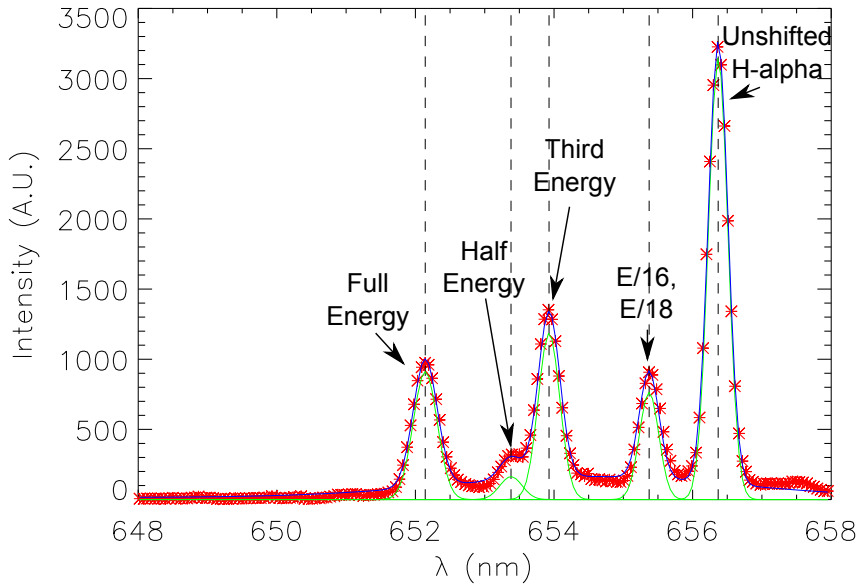

Figure 2.16: DNB spectrum measured in beam tank during shot 1121001003, t=0.72 s.

beam conditions. We can see that only a minority of the hydrogen atoms have the full beam energy. The energy component with the highest population is the one third-energy component, with a population much higher than the one-half component. ITER will use a beam based on negative ion extraction[5], which will avoid the problem of fractional beam energies.

The nominal full beam energy is 50 keV. This is slightly higher than the peak energy in the effective emission rate function, but somewhat better for the 1/2 and 1/3 energy components. In addition, running at lower beam energies decreases the beam penetration and increases the beam divergence. During the 2012 campaign, the beam was forced to run at lower than nominal beam energy because several of the high voltage inverters had failed. By the

Table 2.6: DNB energy fractions with respect to H^0 density

Component	responsible ion	fraction I[a]	fraction II[1]
E_0	H^+	0.275	0.246
$E_0/2$	H_2^+	0.053	0.081
$E_0/3$	H_3^+	0.416	0.502
E_0/x[2]	$H_2O_C^+H_3^+$	0.256[3]	0.170[3]

[a] Shot 1121001003 0.72 s: $E_0 = 34\,\mathrm{keV}$, $I_b = 4.7\,\mathrm{A}$
[1] Shot 1110323006 1.31 s: $E_0 = 50\,\mathrm{keV}$, $I_b = 7.5\,\mathrm{A}$
[2] Unresolvable combination of $E_0/16$ and $E_0/18$
[3] Calculation assumes H_2O^+

end of the campaign, four of the eight invertors had failed, which limited the beam voltage and current to 33.5 keV and 4.2 A. This resulted in lower beam penetration and a smaller beam density in the plasma, although beam signals were still adequate for some measurements to be undertaken.

2.4.2.1 Beam Modeling

Modeling the CXRS emission critically depends on knowing the beam density at many locations within the plasma. In particular, density measurements are inversely proportional to the assumed beam density, and the beam density varies quite dramatically across the plasma due to effects of beam stopping and divergence. The CXRS diagnostic must rely on extensive beam simulation, backed up by direct measurements of the beam emission, to provide the full 3D[15] profile of the beam density. Beam emission spectroscopy

[15]This is needed because the beam is angled relative to the tokamak radius, and the viewing chords also intersect the beam at an angle

can be used provide chord integrated beam densities[129]; however, measurements of beam emission are only available at a few locations in the C-Mod plasma. Neutral beam modeling was done using ALCBEAM[16], a three spatial dimensional neutral beam propagation and formation code developed to simulate the C-Mod beam, which has also recently been applied to beams at EAST and W7-X.

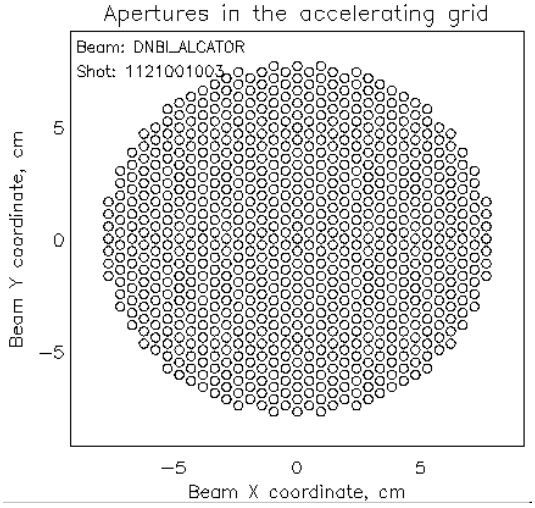

Figure 2.17: Beam grid apertures

The C-Mod beam has four acceleration grids each containing 745 holes which are laid out in a hexagonal packing arrangement filling a circle (figure 2.17). The grids are curved so that the beam is converging as it exits the front of the beam. The output beam can be treated as a superposition of 745 beamlets which emerge from each hole which are directed towards the focal point of the grids. Each beamlet can be treated as a Gaussian beam that diverges as it propagates along the beamlet axis[102]. Since the beam

is converging and the beamlets are diverging, the minimum of beam width occurs at a point in front of the focal point of the grid (see figure 2.18). The

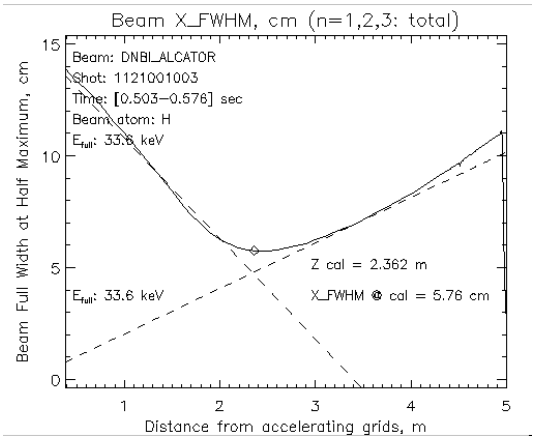

Figure 2.18: Beam width versus distance from accelerating grids. The solid line shows the beam FWHM density of all beam components. The dashed line with negative slope shows the envelope of the beamlet centers which reaches a minimum at 3.4 m due to the curvature of the grid. The upward sloping dashed line shows the effect of beamlet divergence on the width.

plasma edge is located about 4.5 m from the accelerating grids, which means that beam reaches a minimum width well before reaching the plasma. This appears to be a very suboptimal design since the beam diagnostics benefit from a tightly collimated beam within the plasma, which suggests moving the grid focus farther out, to $R_c \approx 4.7$ m which would put the grid focus deep within the plasma.

The angular divergence of each beamlet is due to a space charge effect in the vicinity of the accelerating grids and has a dependence on the ion

current[41]. The dependence can be approximated by[40]

$$\alpha(j) \approx \alpha_0 \left[1 + \gamma \left(1 - j/j_0\right)^2\right] \tag{2.84}$$

where $\alpha(j)$ is the angular dispersion at current j, α_0 is the angular dispersion at optimal beam extraction conditions, j_0 is the optimal beam current, and $\gamma = (1/2)\sqrt{\alpha''(j_0)/\alpha_0} j_0^2 \approx 30$. The values for α_0, j_0, and γ are taken as input parameters to ALCBEAM[16]. Measurements of the beam width had been undertaken[15] to find appropriate values for the angular divergence parameters. The following values provide a good match to experiment.

$$\alpha_0 = 0.7^\circ$$

$$j_0 = 5.6\,\mathrm{A}$$

$$\gamma = 0$$

Each beamlet is attenuated as it traverses through the gas filling the beam duct or through the plasma through collisions between beam atoms and gas molecules or plasma ions and electrons. The gas attenuation is dominated by ionizing collisions. Ionized beam atoms are effectively lost because they are bent by the strong tokamak fields. Within the plasma, the beam attenuation is calculated using an effective beam stopping cross section which combines the various physical processes which will stop the beam. The main processes are charge exchange from the beam to plasma ions (mainly resonant transfer to deuterium), collisional excitation, and collisional ionization. Since the beam velocity is close to the orbital velocity of the bound electron v_e, collisions with

ions are both important and should be included. Charge exchange is dominant below 40 keV/amu and ion impact ionization above 40 keV/amu[44].

As the beam atoms pass through the plasma, they may be excited to various energy levels. Although the excited population is small compared to the ground state ($\lesssim 1\%$), the excited states contribute significantly to the effective beam stopping cross section because the excited states have higher ionization and charge exchange cross sections[22, 108, 90]. The excited state contribution increases with beam energy and plasma density, making up $\approx 20\%$ of the the stopping cross section in JET-like beams (50 keV/amu, $n_e = 5 \times 10^{19}\,\mathrm{m}^{-3}$) and $\approx 45\%$ in ITER beams (500 keV/amu, $n_e = 1 \times 10^{20}\,\mathrm{m}^{-3}$)[44]. Understanding excited state populations is also critical to interpreting beam emission measurements (typically based around the Balmer-α line) for validating the beam modeling. The beam emission is not simply proportional to the beam density times the plasma density as the coronal model would predict.

In the plasma, ALCBEAM uses beam excitation and beam stopping cross sections which have been computed with a version of ADAS[168] which includes corrections made by Delabie[44, 50] to the excited state charge exchange computation, as well as Delabie's recommended cross sections which are used as input to the collisional radiative model. The recommended cross sections are based on the Janev and Smith's review [107], but with corrections to the ion impact energies for excited states. The results of Delabie are close to those of Hutchinson[90] and resolve the discrepancy seen in ADAS modeling by Anderson *et al*[2]. In the gas, ALCBEAM bases the beam stopping

cross section on the stripping cross section $H + H_2 \longrightarrow H^+ + H_2 + e$, where Oak Ridge Redbook vol 1. recommended values were used[7]. Figure 2.19

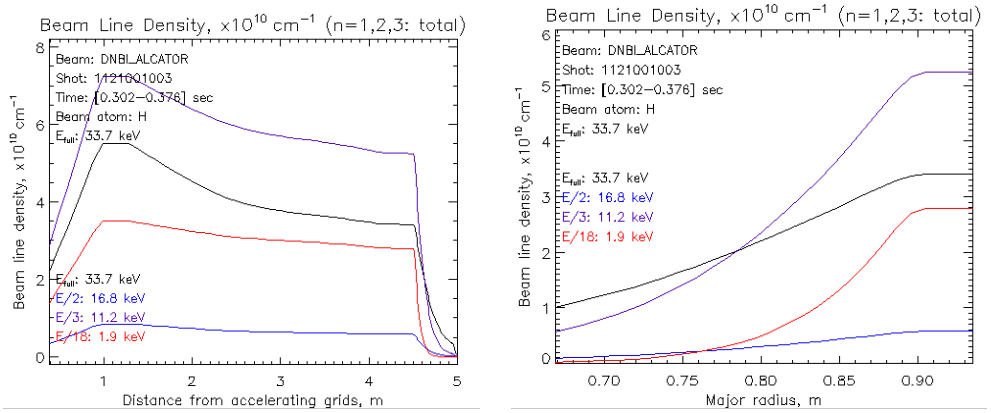

Figure 2.19: Beam line density calculated by ALCBEAM for shot 1121001003, 0.302–0.376 s.

shows the neutral density integrated over the beam width versus distance in front of the accelerating grids. Starting from the grids, the density increases as ions are neutralized in the neutralizer. The beam density reaches a maximum and begins to decrease due to ionization by collision with residual tank gas. At 4.5 m from the grids, the attenuation sharply increases because the plasma beam stopping is much greater. Although the one-third component density is larger initially, the higher energy components can penetrate farther into the plasma.

ALCBEAM uses ray tracing to solve the beam distribution. For each grid point, rays are drawn to each grid pore such that the density at each grid point contains a contribution from each Gaussian beamlet. The beamlets are attenuated by the effective beam stopping cross section along each intervening

grid block on the way to the target. ALCBEAM uses a quasi-steady-state approximation for the excitation, which neglects time of flight effects, which is adequate for regions where the plasma gradients are small, but incorrect at the edge of the plasma, where the output shows a step increase in excitation when the beam enters the plasma.

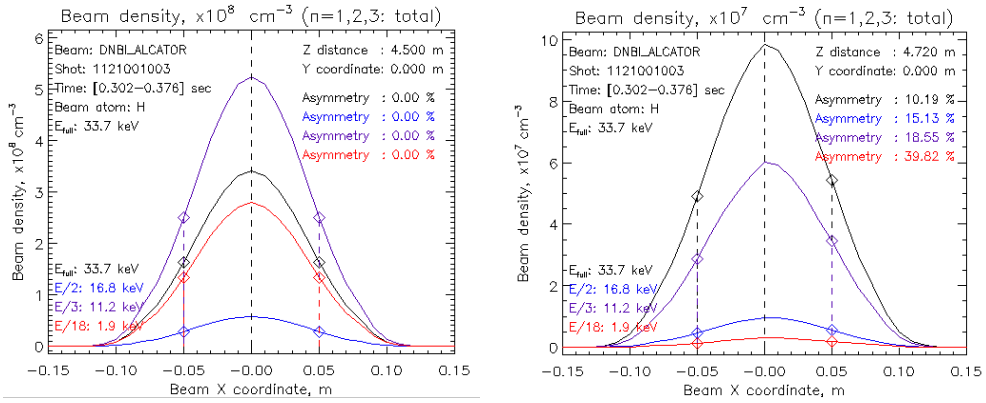

Figure 2.20: Beam density profile perpendicular to beamline. *left*: just outside of edge of plasma. *right*: near core of plasma

Beam penetration calculations can only be accurate to a maximum penetration depth, because small errors in plasma parameters or stopping cross sections can accumulate into large errors in beam densities in regions where the beam is strongly attenuated. A discussion is given in section 2.6.1.

2.4.3 Periscope Views

The components of an optical system within the tokamak vacuum vessel are arranged in assemblages called periscopes, because they allow oriented views of the interior of the vessel from a distant location. The Core CXRS

diagnostic has two dedicated periscopes: the poloidal and toroidal periscopes. An overview of the views of the periscopes is shown in figure 2.21. There are 20 channels in the poloidal persicope and 22 channels in the toroidal periscope.

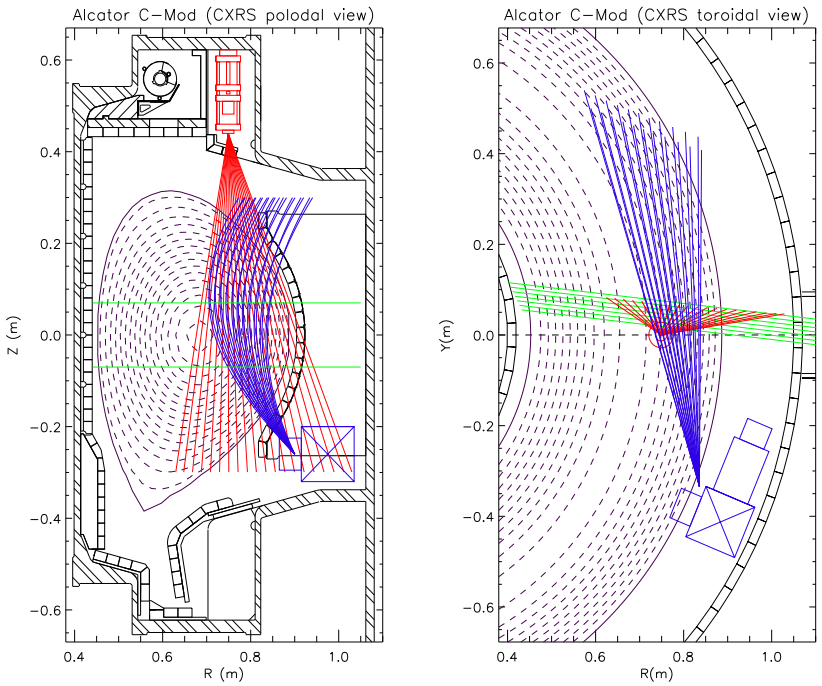

(a) poloidal (R,Z) cross section (b) toroidal (X,Y) cross section

Figure 2.21: CXRS periscope views. The red lines show the chords of the 20 poloidal channels, emanating from the poloidal optical cartridge. The blue lines show the chords of the 22 toroidal channels, emanating from the toroidal periscope. Typical plasma flux surfaces are shown in purple. The beam is represented by green lines.

2.4.3.1 Poloidal Periscope and Views

The poloidal periscope is a tube descending from the F-top port at the top of the C-Mod vacuum vessel to a position close above the plasma.

Inside the tube are the poloidal optics and a long mounting structure that we call the stalk. The periscope tube is designed to hold a vacuum; the poloidal optics and stalk actually remain at atmospheric pressure, allowing for easier maintenance of the optics. Figure 2.22 shows the layout and composition of the "P1" poloidal optics. The "P1" optics are the second iteration of the CXRS poloidal optics, succeeding the "P" optics. The "P1" optics increases the size of the fiber from 200 µm to 400 µm, increasing the throughput by a factor of four.

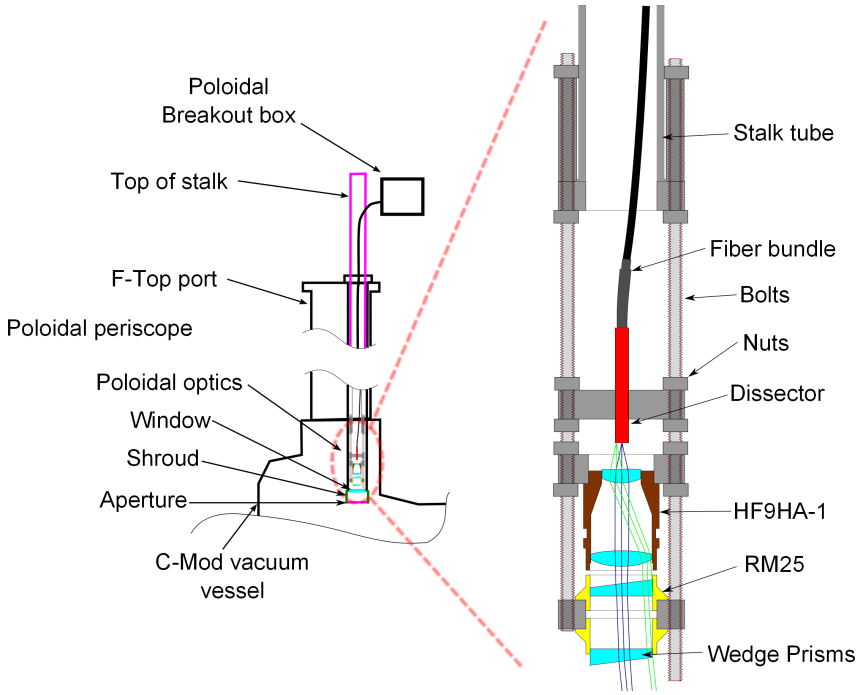

Figure 2.22: "P1" Poloidal optics. The wedge prisms have been rotated for clarity.

Part definitions:

Breakout box The fiber bundle from the poloidal optics goes to this aluminum box, located on top of the C-Mod igloo, which has 20 SMA905 interconnects on the front face, to which the transfer fibers are attached.

Stalk A long aluminum tube which holds the poloidal optics on one end. It mounts to the top of the poloidal periscope and extends upward and carries the fibers to the breakout box.

Dissector The dissector is a rigid mount which holds the 20 fibers in a closely packed linear array in front of the video lens. The dissector has extremely tight geometric tolerances because it is the pre-image of the viewing chords.

HF9HA-1 Fujinon HF9HA-1B video lens, 9 mm focal length, f/1.4 lens for 2/3 in CCD camera.

RM25 Newport Polarizer Rotation Mount. Two of these were taken apart to obtain the circular dials that are used to hold the wedge prisms

Wedge prisms Edmund optics NT45-560 (VIS-NIR), 4 deg wedge prism. Two of these together allows steering of the chords within an 8 degree circle, to allow the channels to be lined up with the beam axis. These are affixed to the rotation mounts with epoxy.

Shroud A sheet of metal around the circumference of the vacuum window that protects it from fast particles and boronization coating.

Aperture An improvement to the shroud which more completely envelops the window, leaving only a small slot for chords to pass through.

The poloidal periscope is located directly above the F-port axis. However, the DNB is rotated by 7° relative to the F-port axis, so the wedge prisms are necessary to for the chords to intersect the center of the beam. The angle of the wedge prisms is adjusted during pre-run calibration to optimize the positions of the chords.

The poloidal chords intersect the midplane over a range of major radii (0.67 m – 0.92 m). Since the fibers are 400 µm in diameter, a magnification of 31.25 is needed.

The aperture was built and installed in mid-2011 to reduce the coating of the vacuum window, which led to gradual and serious signal degradation. Figure 2.23 shows a photo of it.

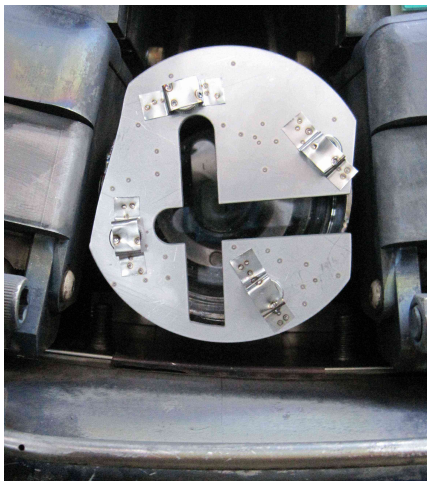

Figure 2.23: Aperture installed on poloidal shroud. Slots allow two orientations of the poloidal optics.

2.4.3.2 Toroidal Periscope and Views

The toroidal periscope is the housing for the toroidal optics, consisting of a cylindrical section which holds the dissector and lenses, a cuboid section which holds stainless steel mirrors, a shutter designed to protect the optics from boronization. The toroidal periscope is located on bottom ledge between F and G ports, on an region of the vacuum vessel near the outer wall not exposed to plasma. It is located about 22.5 cm below the tokamak midplane, and the viewing chords are aimed upward at the beamline at about a 36° angle, so there is a very substantial poloidal component to the views. Nevertheless, it is called the toroidal periscope and the associated views are called the toroidal channels. The toroidal channels are somewhat more closely aligned to the magnetic field during "reverse field" operation than "forward field" operation. Unlike the poloidal optics, the toroidal optics are exposed to vacuum, so the fibers must traverse a specially designed vacuum feedthrough to get from the toroidal dissector to the external breakout box. A diagram of the toroidal periscope and optics is shown in figure 2.24.

The "L2" toroidal optics are the third iteration of the toroidal optics, after the "L" and the "L1" designations. They were designed to improve the light throughput and spatial resolution over the "L1" optics. The "L2" optics has 22 channels and uses a single 400 µm fiber to carry each channels. The "L1" optics had 10 channels and used an array of 64 200 µm fibers for each channel. It may seem that the older system had greater throughput due to higher fiber area, but all that extra fiber area was actually wasted since each fiber array

was attached to just a single 400 µm transfer fiber. Practically speaking, this meant that only one fiber in each channel was being utilized. Obtaining 640 transfer fibers and setting up the necessary junctions was impractical, so the optics were redesigned. The "L2" optics actually provide about 4 times greater throughput. The new optics were designed in 2009 and installed in May 2010.

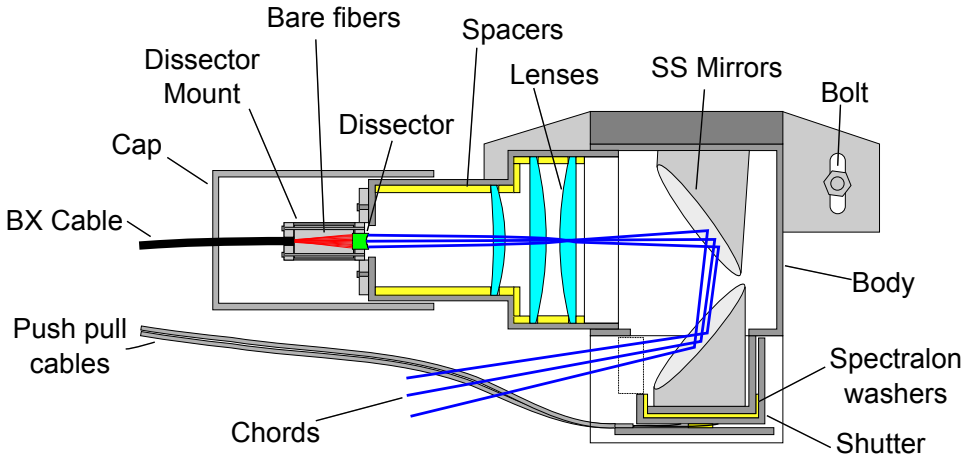

Figure 2.24: "L2" toroidal optics, top view

Part definitions:

BX Cable Armored BX cable is a flexible ribbed metal sheath commonly used for protecting electrical wiring. Stainless steel, 5/8 in. Here it is used to house and protect the toroidal fibers all the way to the toroidal feedthrough, which is located at F-port. The BX cable has a minimum bend radius of about 3 in.

Cap This stainless steel tube is threaded on the inside and screws on to the periscope body. The other end has a hole in it through which the BX

cable passes. The hole is covered with shim stock after installation to form a close seal around the BX cable to protect the dissector.

Dissector A rigid stainless steel mount which holds the 22 toroidal fibers in a staggered arrangement (see below).

Dissector Mount Several stainless steel pieces which hold the dissector and BX Cable and protect the fragile fibers.

Bare fibers 400 µm fibers with minimal jacketing

Spacers Spectralon pieces cut into tubes to hold the lenses in the correct position

Lenses Melles-Griot 50 mm meniscus lens, $R_1 = 110.72\,\text{mm}$, $R_2 = 235.0\,\text{mm}$, $n = 1.52$. 2 Oriel 41980 76.3 mm plano-convex lenses $f = 200\,\text{mm}$.

SS Mirrors 2 cylindrical polished stainless steel mirrors cut at 45°.

Bolt 3 bolts (2 obscured) mount the periscope to the C-Mod vacuum vessel. The bolts are welded to the vacuum vessel, and nuts hold the periscope in place.

Body The stainless steel body and cap fully enclose the toroidal optics except for the outer mirror, protecting them from plasma ions and boronization.

Shutter The shutter is a cylindrical cover for the exposed toroidal window. It has a window on one side and an aperture on another side, and it can swivel on its axis to bring the aperture (open position) or window (closed position) in front of the outer SS mirror. It is manually controlled with push-pull cables which can exert a torque on the shutter.

Push-pull cables There are two cables so that the shutter can be closed or

opened with a pulling motion for either direction. The force is transmitted by flexible braided stainless steel wire within a semi-rigid nylon inner coated stainless steel tube. It is a type of Bowden cable. The push-pull cables connect to push-pull pistons which are located at F-port.

A photo of the toroidal periscope, with shutter removed, is shown in figure 2.25.

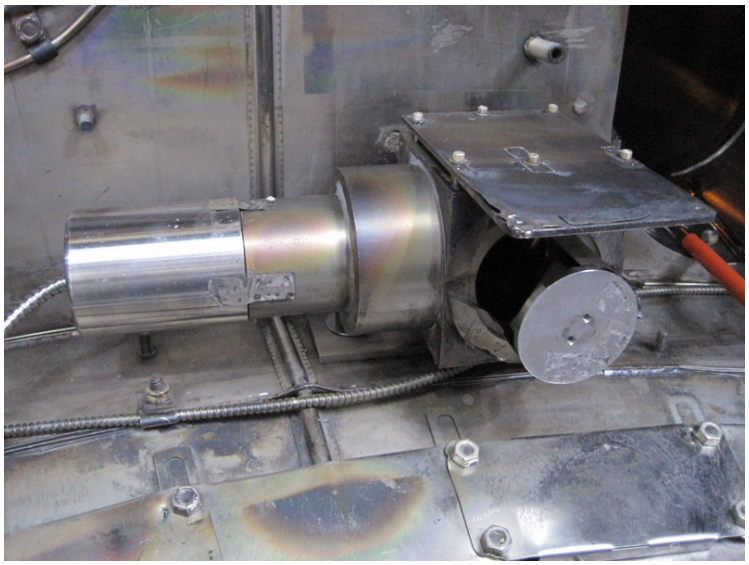

Figure 2.25: Toroidal periscope installed in vessel, with shutter removed

Since the light is reflected off two mirrors, the toroidal signals are considerably polarized. This effect is measured in 2.5.4

All of the screws are secured with welded shim stock to prevent loosening during vibration.

2.4.3.3 Design and installation of the new toroidal dissector and feedthrough

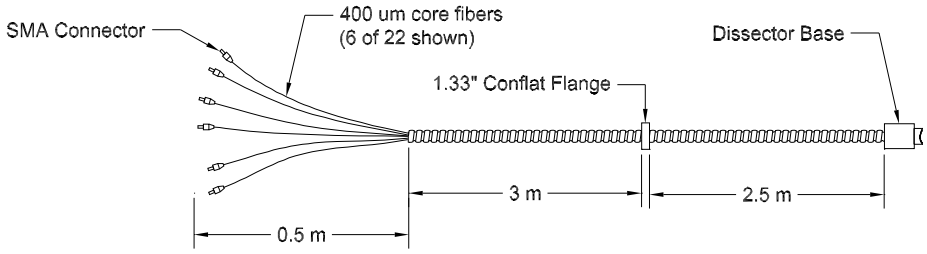

Figure 2.26: Toroidal fiber optics feedthrough and dissector

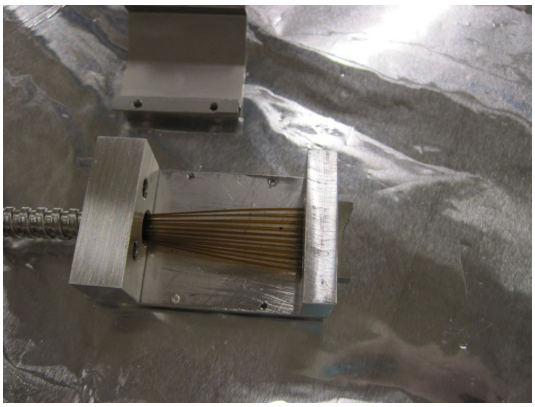

Figure 2.27: Toroidal dissector mount with cover removed

The "L2" optics uses a curved dissector to compensate for the curved focal plane of the toroidal optics. The dissector is a small and extremely complicated piece. Each fiber is placed at a different focal distance by using a stair-stepped surface. Also, the fibers are staggered vertically to allow a minimum distance between holes for structural integrity.

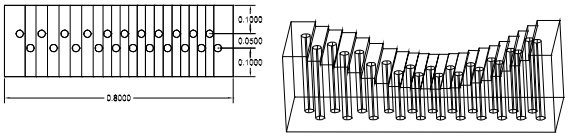

Figure 2.28: Dissector

2.4.4 Detector

The detector consists of the spectrometer, the CCD, camac digitizers for the trigger signals, and a data acquisition computer.

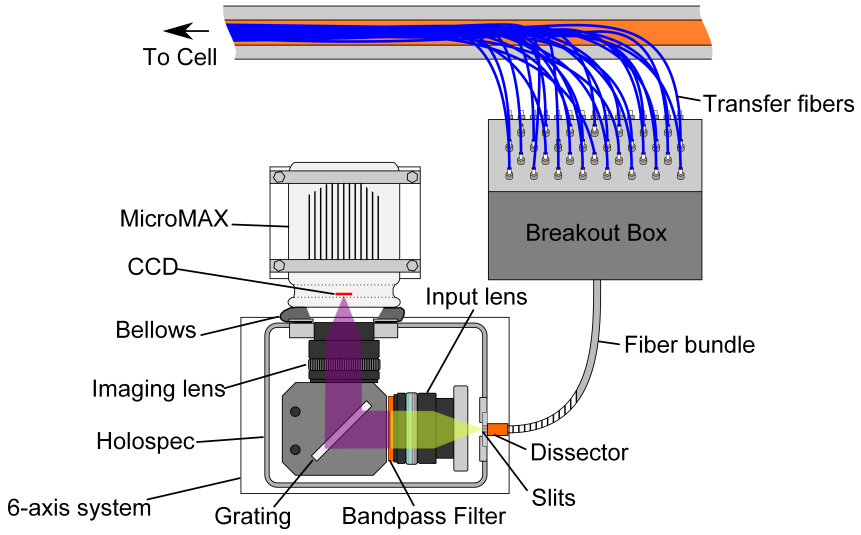

Figure 2.29: The CXRS detector subsystem. Not shown are the camac digitizers or computer or Avantes lamp.

Part definitions:

Table 2.7: Dissector hole positions. x influences radial location of chord. y influences vertical location of chord. z influences focal distance

Channel	x	y	z
1	-0.3464736	0.0250000	0.2445650
2	-0.3092201	-0.0250000	0.2292260
3	-0.2697701	0.0250000	0.2175957
4	-0.2280638	-0.0250000	0.2097756
5	-0.1894193	0.0250000	0.1919402
6	-0.1500815	-0.0250000	0.1744138
7	-0.1098409	0.0250000	0.1574697
8	-0.0697862	-0.0250000	0.1476236
9	-0.0398398	0.0250000	0.1438807
10	-0.0098143	-0.0250000	0.1414961
11	0.0202473	0.0250000	0.1397276
12	0.0498626	-0.0250000	0.1395665
13	0.0789587	0.0250000	0.1412780
14	0.1083976	-0.0250000	0.1439736
15	0.1396287	0.0250000	0.1517815
16	0.1708598	-0.0250000	0.1595894
17	0.2020913	0.0250000	0.1673972
18	0.2317161	-0.0250000	0.1811461
19	0.2604051	0.0250000	0.1983591
20	0.2890953	-0.0250000	0.2155732
21	0.3177843	0.0250000	0.2327870
22	0.3464732	-0.0250000	0.2500000

Holospec Kaiser Optical Systems Holospec f/1.8 imaging spectrograph. It is marketed for Raman spectroscopy and features high throughput.

MicroMAX Roper Scientific/Princeton Instruments MicroMAX, high-speed, low-noise CCD with 512×512 resolution. It (optionally) takes an external framing trigger as input and outputs a NOT(SCAN) signal which

indicates when a readout is occuring.

Slits A few different sizes of slits can be installed to trade off between resolution and signal strength. 90 µm slits were used for helium measurements in the 2012 campaign. For helium, background signal is very bright and reducing signal strength in favor of resolution is beneficial.

Input lens Nikon Nikkor AF 85 mm f/1.8. This gives the Holospec an overall f/1.8.

Imaging lens Nikon Nikkor AF 50 mm f/1.4

Bandpass filter Andover optics bandpass 2-cavity interference filter.

Grating Kaiser Optical Systems HSG 468.6-SA s/n HSG 45471[16]

Transfer fibers 400 µm

Camac timing module 221L timing module is used to generate the external trigger signal for the MicroMAX.

Camac digitizer 2812 8 channel analog input digitizer. Two channels are used to monitor the external trigger signal and the NOT(SCAN) signal.

Avantes neon lamp Avantes lamp with AvaLight-CAL-NEON-B bulb, used as a shot to shot wavelength calibration.

Typical traditional spectrometers have used a long path length between the diffraction grating and the slits in order to increase the linear dispersion. In the common Czerny-Turner design[127], the focusing element is two concave mirrors which are located some distance from the slit. These devices are

[16]The grating has frequently been swapped out in order to configure the system to measure boron or hydrogen

usually optimized for low abberation rather than optical throughput, and so the f-number is large—perhaps $f/4$–$f/9$. Typical optical fibers have f-numbers of $\sim f/2$, so inefficient expanding optics and a very large slit size are needed to prevent loss of light. The development of short focal length spectrometers overcomes this obstacle[12]. The commercially available Holospec $f/1.8$ imaging spectrograph was chosen for this role because similar models have been successfully used in TFTR[13] and NSTX[21]. The high f-number allows optical fibers to be directly mounted at the slit plane. In addition, the angle of the transmission grating allows for full selection of the $m = 1$ order diffraction, optimizing the photon efficiency. The image preserving capability of the Holospec allows multiple channels to be dispersed with a single spectrometer and CCD.

The detector is set up to handle 45 channels simultaneously, with the image on the CCD organized into 15 rows and 3 columns. The columns are displaced in the spectral direction and spectrally separated using a bandpass filter which selects a small region around the 4686 Å line. The fiber dissector arranges the fibers behind a slit plate which has three laser cut slits which each encompass 15 channels stacked vertically.

The geometry of spectrometer introduces a strong curvature in the image of the slits. This effect can be corrected by use of curved slits[12]; suitable choice of radius of curvature will give a flat slit image at the CCD.

For a transmission diffraction grating

$$R_{slit} = \left(\frac{\lambda_0}{\lambda}\right) \frac{f_1 \cos(\theta_1 + \phi_1)}{\sin(\theta_1) + \sin(\theta_2)} \tag{2.85}$$

where θ_1 is the angle of the incoming ray to the grating normal, θ_2 is the angle of the outgoing ray to the opposite grating normal, $\phi_1 = x_1/f_1$ is the angle of the ray from the slit to the center of the nodal plane of the lens, and λ_0 is the central wavelength of the grating.

For the helium grating HSG 468.6-SA s/n HSG 45471, the value for the central slit is $R_{slit} = 1.746\,\text{in}$. The slits and dissector in the CXRS system (figure 2.30) were designed for the boron grating (HDG 494.3nm s/n 39445), and so they were designed with a different curvature, with $R_{\text{slit}} = 1.4674\,\text{in}$. Since the radii are very similar, it was decided to use the same slits and dissector for both measurements. The residual curvature introduces less than a pixel shift in the helium measurement (although shifted up to 17 pixels for hydrogen measurement with the HFG-700-39.0 s/n HFG-19070).

The MicroMAX is configured with a 16-bit ADC and the CCD has a well capacity of 100000 electrons; however it has been observed that the output is extremely nonlinear for signals greater 45000 counts, so these signals are avoided. Each channel spans about 19 vertical pixels on the CCD, and about 150 pixels in the horizontal spectral direction. These pixels are vertically binned[17] to increase the frame rate, forming an effective 512×15 pixel array,

[17]Binning combines several pixels into larger effective pixels. The combined charge is simultaneously read out to the ADC.

Figure 2.30: CXRS 90 µm slits and dissector. The fibers have been backlit from the breakout box.

or a 512×10 pixel array. The minimum integration time is 12.5 ms for 15 rows (enough for 45 channels) or 10 ms if 10 rows are used (30 channels). The faster frame rate is useful for time-dependent transport measurements. The CCD is cooled by a TEC to $-40\,^{\circ}\mathrm{C}$ to bring the dark current noise to about 40 counts per bin at 20 ms integration time.

The MicroMAX has a built in fast frame shutter, but it has been removed for this diagnostic. In normal acquisition mode, the CCD is exposed for an interval and must be closed by the shutter while the charge is read out to prevent tearing of the signal. The MicroMAX features a special mode called "frame transfer operation", used by this diagnostic, in which half the CCD is used for sensing light and half for storage and readout, so the system can collect light and readout simultaneously. In this mode, the shutter is not needed and the integration time is determined by the time between triggers.

The beginning of each actual exposure time is slightly delayed from the trigger, and the falling edge of the NOT(SCAN) output of the CCD is synchronized to the start of each exposure. A timing diagram is shown in figure 2.31.

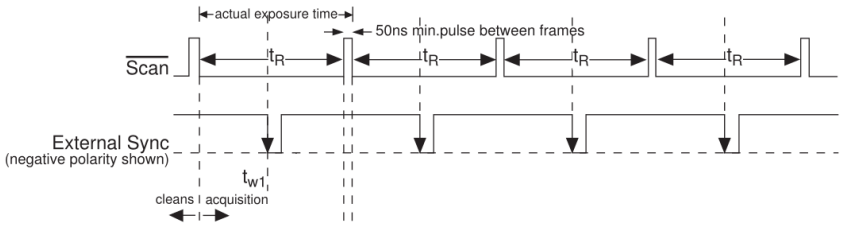

Figure 2.31: MicroMAX CCD timing diagram for frame transfer operation with external triggering, adapted from MicroMAX System User Manual version 5.A

When using this CCD configuration, the first frame of every shot is saturated because the shutter has been open for an indeterminate long time. In practice, the first two frames are discarded in every data shot.

External triggering is used to allow synchronization with the beam and all other C-Mod diagnostics. A C-Mod shot trigger is input to the 221L camac timing module which generates a pulse train to act as the external trigger for the CCD. The external trigger is connected to both the CCD control unit and the 2812 camac digitizer. The NOT(SCAN) signal is connected to the 2812 camac digitizer and the digitizer signal is analyzed after each shot to give precise frame times for the experiment.

2.5 Calibration

A tokamak in operation is a stressful and trying environment for any diagnostic. Equipment regularly experiences extreme magnetic fields, temperature swings, pressure changes, vibrations, neutron irradiation, halo currents, energetic particle bombardment, electromagnetic waves, boronization, and in some cases, direct plasma exposure. Even the most robust diagnostics must be calibrated and maintained on a regular basis.

Calibrations are usually performed before and after a run campaign (which lasts about 8 months during a maintenance period in which the vacuum vessel is vented (brought up to air). Detector calibrations are also performed any time the grating is changed, which may happen frequently during the run campaign. Pre-run calibrations occur after optimizing the viewing geometry and cleaning the optics during the vent, so they represent the fresh state of the system. On the other hand, the post-run calibrations occur immediately after the run before any adjustments are made.

Spatial, radiometric, and polarization calibration require in-vessel access and are only available during a vent. Confined space training is required to perform in-vessel calibrations and upgrades.

2.5.1 Spatial calibration

Spatial calibration is done by backlighting the channels from the poloidal or toroidal breakout box and measuring the chord positions on a screen placed in the vessel. The screen containing graph paper is placed in the path of the

beam, and the position of the screen is carefully measured so the 3D position of where each chord intersects the beam is known.

Backlighting is done with a lab bright halogen lamp. Chromatic aberration is negligible compared to spatial measurement uncertainties, so no color filter is necessary. A special table is installed at F-port during calibration to support the screen. The table mounts to F-port and locks in the toroidal angle. The table position and orientation are carefully measured, using a ruler, digital level, and alignment laser.

For poloidal channels, the screen is oriented with normal pointed up and raised to the beam centerline (Figure 2.32). A photograph of the screen is taken, and the channel positions are graphically obtained from the photograph and geometric measurements of the table.

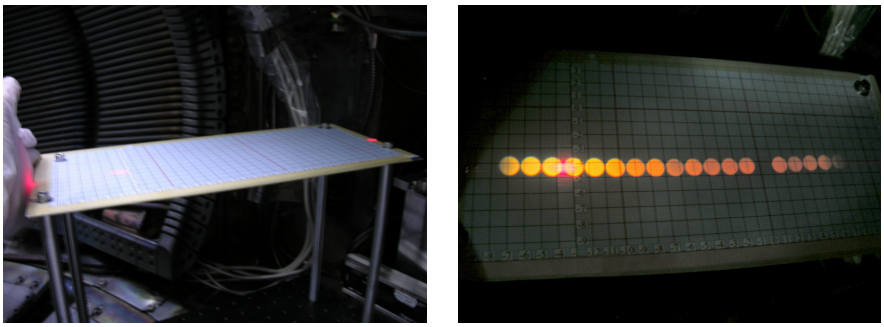

Figure 2.32: Poloidal calibration. *left*: Viewing calibration table from G-port, looking toward F-port. *right*: Backlit channels. Channel 14 is dark because a fiber is broken. Right maps to the positive radial direction, Up maps to the positive toroidal direction.

For toroidal channels, the screen is a box placed on the calibration table oriented with normal perpendicular to the beam, with grid mostly oriented

in the R, Z plane. Figure 2.33 shows the measurement. This photo also shows backlit channels from the Edge CXRS diagnostic for comparison, and some cross calibration efforts were undertaken to check consistency between diagnostics.

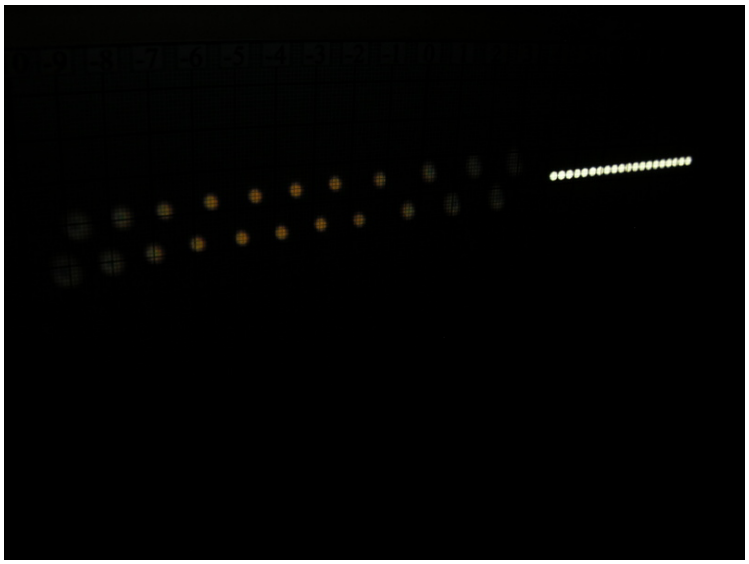

Figure 2.33: Toroidal calibration. The 22 Core CXRS channels are visible on the left. 20 Edge CXRS channels are visible on the right

It takes two points to define a viewing chord. One point is measured by the screen projection. The other is the optical nodal point. The optical nodal point is the point where the chords for one view intersect inside the periscope. The poloidal nodal point is directly below F-top port, and the height is estimated from measurements of the window height and measurement of the distance from the optical elements to the window. The toroidal nodal point is estimated from mechanical drawings of the vessel bolt position and toroidal periscope.

Figure 2.21 above shows results of a spatial calibration. Results for the chord locations and widths are stored in the MDSplus database.

2.5.2 Intensity calibration

Several methods exist for absolute calibration of intensity of each channel:

- In-vessel radiometric calibration
- Bremsstrahlung calibration
- Quasineutrality calibration
- Beam-into-gas calibration

Each has advantages and disadvantages. Of these, the in-vessel radiometric calibration is the most straightforward and foolproof. However, it can only be performed during a vent, and the throughput of the optics can undergo dramatic change (losing as much as an order of magnitude) over the span of a run campaign. Therefore, the radiometric calibration is less viable for experiments in the middle of a run campaign or after several boronizations. The other methods can be performed during a run campaign but rely on accurate modeling of physical parameters.

The units for the intensity calibration are $\mathrm{cm}^2\,\mathrm{sr}$. This unit is required for comparing the spectral radiance measured along an idealized zero-width chord (in units of $1/(\mathrm{cm}^2\,\mathrm{s}\,\text{Å})$) to a number of counts in a detector (unitless) times the frame rate (in s^{-1}).

The throughput of the system is wavelength dependent. For simplicity, it is assumed that the entire wavelength dependence is in the detector, and not in the vessel optics. The wavelength dependence of the detector is measured separately, and can be combined with the intensity calibration to give the full wavelength dependence of the system.

2.5.2.1 Radiometric calibration

A Labsphere calibrated integrating sphere light source is brought into the vacuum vessel and placed in the path of each channel while the detector captures the signal using exactly the same optics as the experiment. Figure 2.34 shows preparation for the radiometric calibration. During radiometric calibration, vessel lighting is turned off.

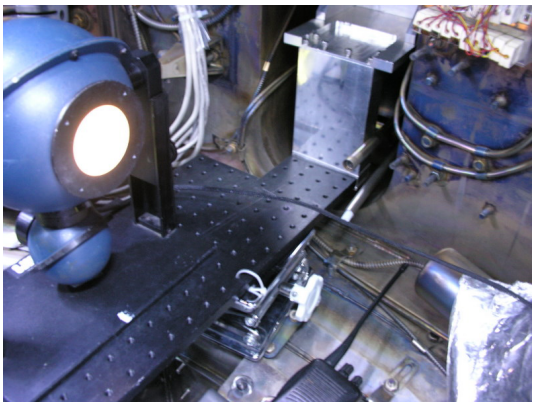

Figure 2.34: Preparing for radiometric calibration

An integrating sphere is a hollow cavity with an inner surface covered with highly Lambertian and reflective material, intended to produce a very uniform brightness across all interior surfaces. As a light source this is conve-

nient for illuminating a channel because the illumination is nearly independent of distance and angle, so accurate alignment to the lamp is unnecessary, as long as the chord completely enters the mouth of the cavity approximately straight in.

Three people are needed to perform the radiometric calibration: one person in the vacuum vessel, one person at the vessel entrance required for safety compliance (the "babysitter"), and one person at the spectrometer breakout box in the diagnostics lab. A labsphere is taken into the vacuum vessel. Each channel must be backlit from the detector side in order to align the mouth of the Labsphere to the channel. For each channel, the transfer fiber is separated from the spectrometer breakout box and placed in front of a lamp, shining a beam in the tokamak. Once the labsphere is aligned, the transfer fiber is reattached to the spectrometer breakout box and a test shot is taken and the spectrum is saved to the MDSplus database. An appropriate integration time is chosen to get adequate signal and not saturate the detector (usually 200 ms for toroidal channels and 500 ms for poloidal channels). Another test shot is taken with the transfer fibers disconnected to serve as a detector background shot, in order to subtract the dark current counts from the final result. This shot is taken with the same integration time as the other test shots.

We have performed this procedure with the labsphere near the midplane, and with the labsphere placed close to the optical node, with identical results.

The labsphere is absolutely calibrated by cross calibrating to another labsphere with a built-in calibrated photodetector.

2.5.2.2 Bremsstrahlung calibration

Bremsstrahlung calibration is achieved by using the continuum part of the measured spectrum and finding a scalefactor that will bring the continuum level to the predicted levels of free-free bremsstrahlung emission. The physics of bremsstrahlung emission was discussed in section 2.3.2.

When other calibrations are not available, bremsstrahlung calibration frequently is. Bremstrahlung calibration can normally be run in the background, without any special program needed for the experimental run. However, it is most accurate if high density H-mode shots are available. During H-mode, density is increased, giving higher bremsstrahlung, and density and temperature profiles are generally flatter across flux surfaces, so the calibration is less sensitive to equilibrium fitting errors.

The bremsstrahlung equation 2.71 has the numerical value

$$\frac{\mathrm{d}N_\gamma}{\mathrm{d}V\,\mathrm{d}t\,\mathrm{d}\lambda\,\mathrm{d}\Omega} = \frac{n_e^2 Z_{\mathrm{eff}} \overline{g}_{ff}}{\sqrt{T_e}\lambda} \exp\left(\frac{-12398.4 T_e}{\lambda}\right) \left(7.62742 \times 10^{-15} \frac{\mathrm{ph}}{\text{Å}\mathrm{cm}^3\ \mathrm{s}\ \mathrm{sr}}\right) \tag{2.86}$$

where λ is measured in angstroms, T_e in electron volts, n_e in cm^{-3}, Z_{eff} is the effective ion charge. Since these quantities are all approximately flux functions, the bremsstrahlung is also a flux function.

The bremsstrahlung emissivity is calculated over the full range of flux

surfaces, and the emissivity is integrated along the length of each viewing chord to provide the expected bremsstrahlung contribution. This is compared to the measured bremsstrahlung contribution in a region of the spectrum which is clean and free from impurity emission.

T_e and n_e are provided by the Core and Edge Thomson Scattering diagnostics[138, 87, 88]. The flux surface mapping is obtained from the standard EFIT equilibrium solver[118, 91], which has been run on the same timebase as the Thomson Scattering diagnostic. It is difficult to get a good measurement of Z_{eff}. The Dalsa diagnostic for visible bremsstrahlung has suffered from reflection issues which made the measurement unreliable, and it has been out of commision since 2011. Single channel Z_meter is not sufficient because Z_{eff} is known to vary with radius.

Z_{eff} is estimated using the `z_neo_profile` code by I. O. Bespamyatnov. The code computes the Z_{eff} necessary to match the EFIT fitted current to the modeled current. The modeled current consists of the bootstrap current plus the inductive current generated by the primary transformer, which depends on the resistivity of the plasma which is assumed to be neoclassical.[18] The neoclassical resistivity is a function of Z_{eff}.

An example calculation is given for shot 1120913029, frame 68, channel L2 $R = 0.767\,\text{m}$. Figure 2.35 shows the n_e, T_e, Z_{eff}, and local bremsstrahlung profiles. Figure 2.36 shows the measured bremsstrahlung level. Although the

[18]The calculation is invalid when other sources of current exist, such as lower hybrid current drive or mode conversion current drive.

density is highest in the core of the plasma, the bremsstrahlung emissivity for this shot has a peak just inside the pedestal. This shot has a large effective Z near the edge due to impurity puffing and sputtering of tiles.

The chord integration is done by breaking the chord into a large number of discrete steps. The (R,Z) value of each position is mapped to a flux surface and the bremsstrahlung value at this flux surface is multiplied by the step length and accumulated. Figure 2.37 shows this process.

The ratio between the measured bremsstrahlung (in detector counts) and the calculated bremsstrahlung radiance gives an estimate of the calibration constant. A better estimate is gotten by averaging the estimates from about 80 or more time points from one or more nearby shots. Typically, several higher density shots are chosen from each group of shots (divided by boronization events) to serve as calibration shots for that group.

2.5.2.3 Quasineutrality calibration

The idea of quasineutrality calibration is very simple. Helium has an ionic charge of 2, so in a plasma that is fully comprised of helium, the quasineutrality condition gives $n_e = 2n_i = 2n_{\mathrm{He}}$. We can cross calibrate the helium density to one of the electron density diagnostics such as Thomson Scattering or Two-Color Interferometry. The throughput can be calculated from the inferred helium density, the effective emission rate, and the modeled beam density. This calibration is available any time helium is used as the main ion species, which usually happens for a few runs a year.

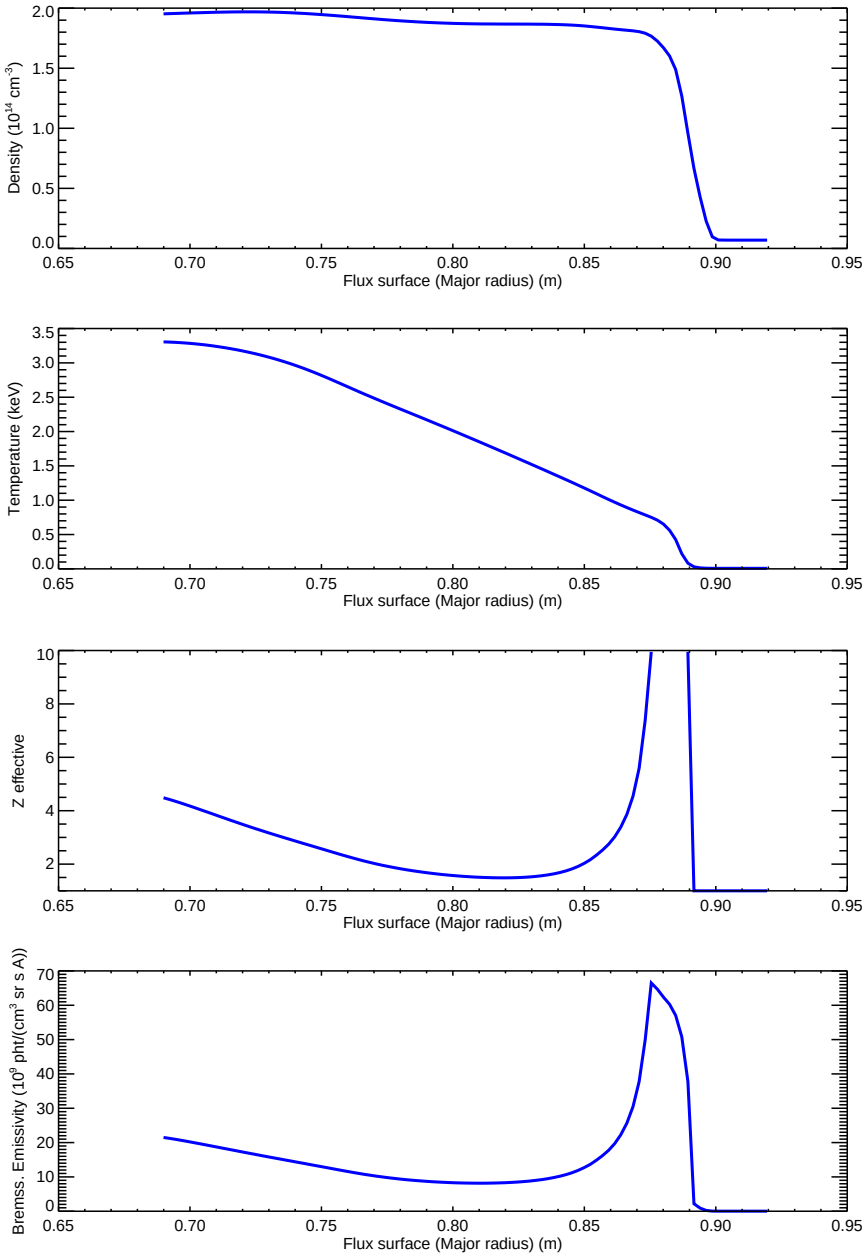

Figure 2.35: n_e, T_e, Z_{eff}, and bremsstrahlung profiles for 1120913029, frame 68, for channel L2 $R = 0.767\,\text{m}$

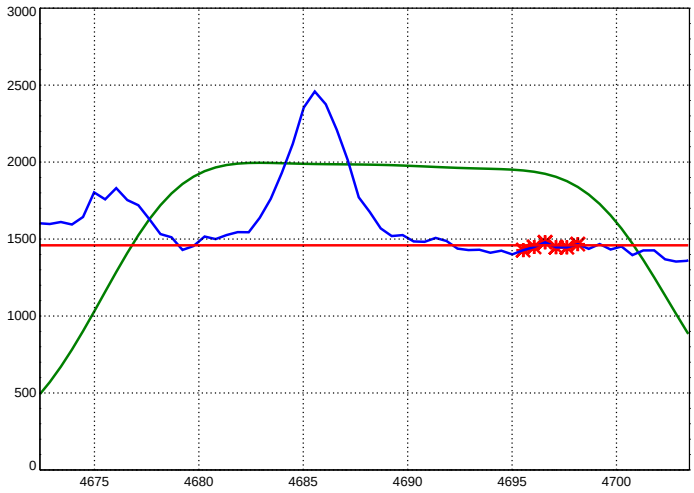

Figure 2.36: Measured bremsstrahlung level. The green line shows the envelope function for the bandpass filter. The blue line shows the measured spectrum, divided by the envelope function. The red symbols show the points between 4695 Å and 4698 Å which are clear of interference and used to fit the bremsstrahlung level, shown by the red line.

It turns out that the beam penetration into a helium plasma is similar to the beam penetration in a deuterium plasma of equal electron density, and the effective photon emission rate for the 4686 Å is mostly insensitive to plasma composition.

A disadvantage of the quasineutrality calibration is that it requires about 20 experiment shots for the plasma to clear out the residual and adsorbed helium when the main plenum is switched from helium to deuterium.

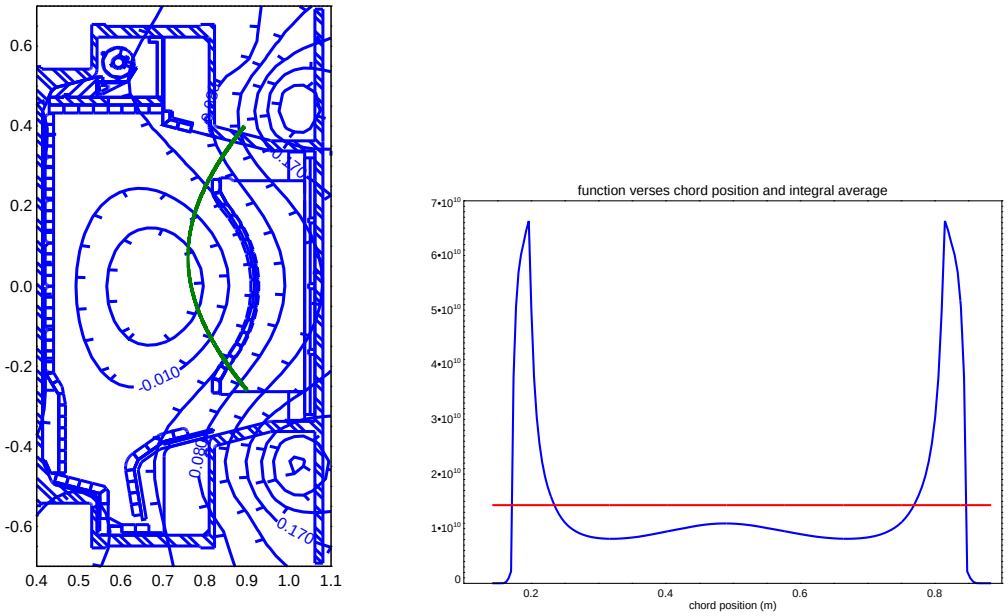

Figure 2.37: Bremsstrahlung chord integration, shot 1120913029

2.5.2.4 Beam into gas calibration

Another method for intensity calibration of the channels is by firing the neutral beam into the tokamak vessel filled with cold helium gas, with no plasma or magnetic fields present. This method was frequently used for calibrating the helium CXRS diagnostic on DIII-D[52]. Due to uncertainties in the atomic physics involved in the beam-gas interaction, this technique is only useful for providing channel-relative intensity calibrations, and another technique must be used to constrain the average throughput for the channels. Nevertheless, the technique naturally corrects for the beam shape without need for beam divergence modeling.

Either the He II 4686 Å line or the He I 4713 Å line can be used to calibrate the channels, although the latter is preferable because the line is brighter. The emission in the beam into gas shot is much weaker than from a plasma shot. A typical line area measured on the CXRS detection equipment is about 500 Å counts for the 4713 Å line and 60 Å counts for the 4686 Å line.

The line intensity scales with the helium concentration (and therefore helium fill pressure) in the vacuum vessel. At lower helium pressures, the scaling is linear, but at high pressures, the beam is attenuated by the gas and the line intensity begins to roll off. This is observed to be the case even when there is no magnetic field, although to a lesser extent (since collisionally stripped fast ions are not removed from the beam).[19] The local emission is

$$\varepsilon = n_{\mathrm{He}} \left(n_{\mathrm{H}^0} q_{\mathrm{exc}}(v_b)^{(0)} + n_{\mathrm{H}^+} q_{\mathrm{exc}}(v_b)^{(+)} \right) \tag{2.87}$$

The channel signal is assumed to take the simplified form

$$I_i = a_i I_{\mathrm{beam}} P_{\mathrm{torus}} \exp(-P_{\mathrm{torus}}/b_i) \tag{2.88}$$

where I_i is the area of the 4713 Å line measured on channel i, a_i is a calibration factor proportional to the channel throughput, I_{beam} is the beam extraction current measured by the DNB engineering sensors, P_{torus} is the torus pressure measured by the G-port MKS pressure gauge, and b_i is a beam penetration depth for the channel. It should be expected that b_i is greater for channels that

[19] The DIII-D measurements did not observe this effect because they used lower fill pressures.

intersect the beam toward the high field side, since the beam must traverse more gas.

Taking measurements at multiple torus pressures, a_i and b_i are obtained using a least squares fit. Figure 2.38 shows the area of the 4713 Å line measured at each channel during the course of one shot where the beam was modulated with 100 ms on–100 ms off timing. When the beam is off there is no emission. Figure 2.39 shows the fits to a_i and b_i using data from several shots using equation 2.88.

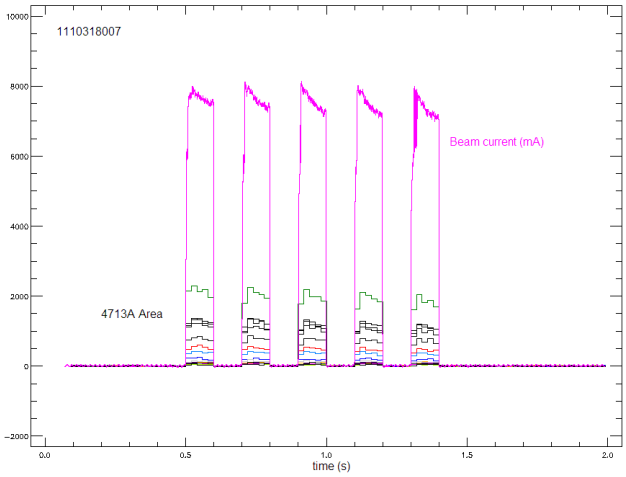

Figure 2.38: Line area versus beam current, shot 1110318007

2.5.2.5 Comparison of different absolute calibrations

Calibrations at different dates show wildly different throughputs. See figure 2.40. Therefore, comparison of different calibration methods only makes sense for temporally close measurements.

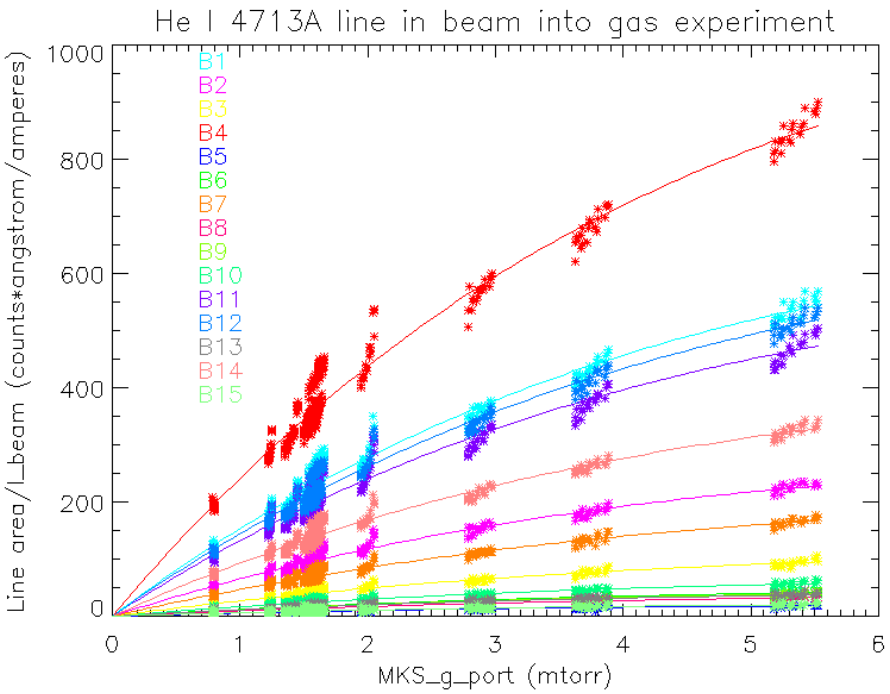

Figure 2.39: Beam into gas, least squares fitting. Each star is a fit to the 4713 Å line on a channel, and the smooth lines are to a linear times exponential model.

Figures 2.41 and 2.42 show calibrations taken during the 2011 campaign and at the end of the 2012 campaign. Since beam-into-gas calibration only provides relative calibration, it has been scaled to the other calibrations' average. No absolute calibration was available for mid-2011, and no quasineutrality calibration was available near end of 2012.

Bremsstrahlung calibration tends to overpredict the throughput of the system when compared with Labsphere measurements. This suggests that the bremsstrahlung model generally underpredicts the true background continuum

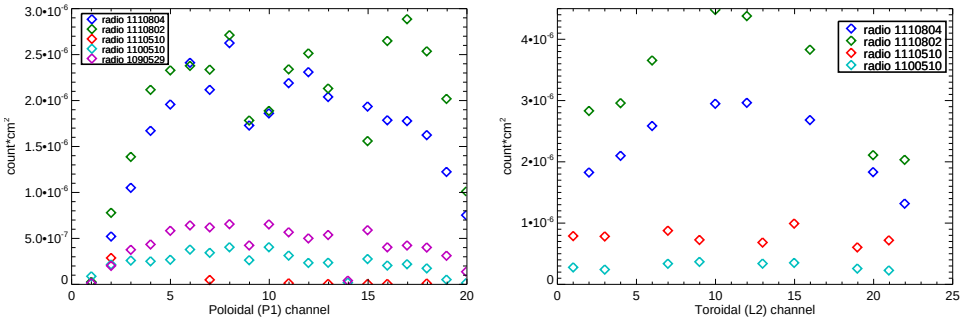

Figure 2.40: Comparison of radiometric calibration coefficients taken at different times

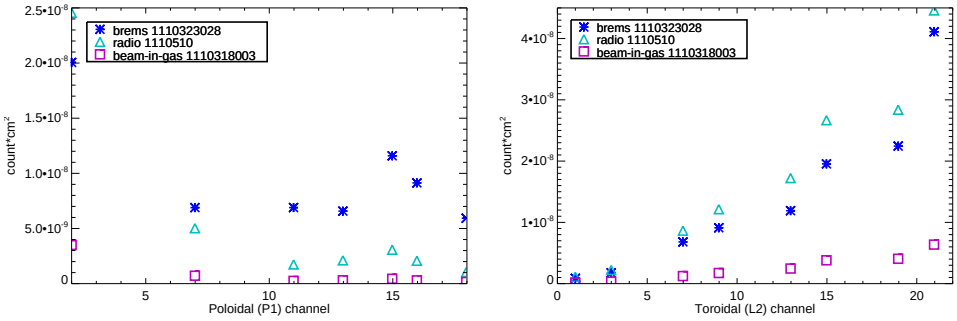

Figure 2.41: Comparison of absolute calibrations, middle of 2011 campaign.

emission.[20] One reason for this discrepancy is that tile reflection increases the background signal reaching the detector.

The amount of reflected emission depends on the exact geometry of the viewing chords and tiles, and the condition of the tiles, so it is impossible to model precisely. Measurements of molybdenum tile reflectivity at several wavelengths were conducted on D-IIID[82], but C-Mod uses tungsten tiles and

[20]This is corroborated by the fact that DALSA tends to overpredict effective Z, compared with other estimates. DALSA uses a similar bremsstrahlung model and treats Z_{eff} as the unknown.

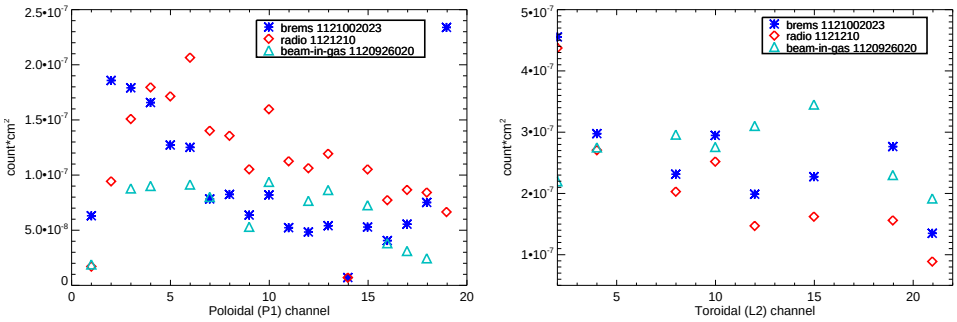

Figure 2.42: Comparison of intensity calibrations, end of 2012 campaign.

boronization, which could greatly affect results. Nevertheless, the D-IIID tile reflectivity near 4358 Å is roughly 0.25. If we allow for multiple reflections, this means that the ambient background is scaled by about 1.3. This puts the bremsstrahlung results closer to in-vessel measurements.

2.5.2.6 Optical loss budget

The throughput of the system is the étendue of system multiplied by the transmission of every optical component. From this, we can obtain an expected result for the absolute calibration, useful for identifying issues.

Transmission measurements were made to develop the optical loss budget.

1. Single fiber from calibrated light source to detector: 2500 counts
2. Two fibers attached to each other by SMA905 fiber connector: 2170 counts
3. Two fibers through 2 Nikon lenses: 1850 counts

4. Two fibers through 2 Nikon lenses and interference filter: 1600 counts.

Table 2.8: Optical Loss Budget

element	transmission
toroidal	
SS mirrors[a]	0.6^2
BK7 Lenses	0.92^3
Fiber face	0.95
Feedthrough	1
SMA905 connection (2)	0.868^2
Fiber losses[2]	0.96
Total toroidal	0.19
poloidal	
Periscope window[1]	0.8
Wedge prisms (2)	0.95^2
Video Lens	0.84
Fiber face	0.95
SMA905 connection (2)	0.868^2
Fiber losses[2]	0.96
Total poloidal	0.42
detector	
Fiber face	0.95
90 µm slit	90/400
Nikon lenses (2)	0.74
Interference filter	0.865
Grating efficiency	0.9
CCD efficiency	0.9
Total detector	0.11

[a] polarization dependent
[1] greatly varies due to coating by contaminants
[2] may vary due to radiation darkening or damage

2.5.3 Detector calibration

Detector calibration involves focusing the optics, wavelength calibration, spectral transmission function, and instrument function measurements. These measurements involve only the detector, and can be performed at any time during the run campaign. The calibration must be repeated any time the detector configuration is changed (slit change, grating change, insertion of the blocking bar[21].

In every detector measurement, the dark current counts are subtracted using dedicated background shots. For this subtraction, the frames are averaged together and the average dark counts for each pixel are subtracted from each data shot.

Focusing the optics involves adjusting the micrometer settings on the 6-axis position/orientation stage supporting the spectrometer so the image is well focused.

Wavelength calibration is performed by measuring the spectrum of an argon Geissler tube and matching the measured lines to tabulated line locations, shown in table 2.9. However, before making the measurements, the bandpass filter must be removed to improve the quality of the spectral fit. The spectrum is measured by mounting a 2 m patch fiber in front of a Geissler tube lamp and connecting the fiber to each channel in turn, measuring a single

[21]The blocking bar[121, 125] is a module that can be inserted between the spectrometer and detector to block specific ranges of wavelengths from reaching the detector that was developed for CXRS measurement of hydrogen fast ions.

channel at a time. Instrument function measurements are also obtained from the same measurements.

The mapping from pixel to wavelength is highly curved because of the short focal length, and it is fit using a cubic polynomial. The process is as follows:

1. Initial estimates for the mapping polynomial are entered.
2. A single manually selected line in the spectrum is fitted with a Gaussian to obtain a model line width and to adjust the initial estimate of the constant term in the polynomial.
3. A model spectrum is contructed as a sum of Gaussians with centers given in angstroms for each line in the table within an estimated window, where each amplitude is a free parameter.
4. The mapping polynomial is varied (using MPFIT[131]) to obtain a best fit between the model and the measured spectrum.

The model line width is stored to use as an estimate of the instrument function. A sample fitted spectrum is shown in figure 2.43. For the Helium HSG 468.6-SA s/n HSG 45471 grating, a typical fit polynomial is

$$\lambda = 4530.7076 + 0.57112704x - 7.223\,284\,4 \times 10^{-5}x^2 - 1.091\,030\,8 \times 10^{-8}x^3 \tag{2.89}$$

where x is the pixel column and λ is in angstroms.

The spectral transmission function gives the sensitivity of the detector as a function of the wavelength or, more accurately, pixel number. It is used in

Table 2.9: Ar I lines for calibration from the NIST atomic spectral database[140, 141]

wavelength (Å)	upper state[a]	lower state
4423.994	$(^2P^o_{3/2})5p^2[3/2]_1$	$(^2P^o_{1/2})4s^2[1/2]^o_0$
4510.733	$(^2P^o_{3/2})5p^2[1/2]_0$	$(^2P^o_{1/2})4s^2[1/2]^o_1$
4522.323	$(^2P^o_{3/2})5p^2[1/2]_1$	$(^2P^o_{1/2})4s^2[1/2]^o_0$
4544.746	$(^2P^o_{3/2})11d^2[1/2]^o_1$	$(^2P^o_{3/2})4p^2[1/2]_1$
4554.324	$(^2P^o_{1/2})7d^2[3/2]^o_2$	$(^2P^o_{3/2})4p^2[1/2]_1$
4589.289	$(^2P^o_{3/2})5p^2[3/2]_2$	$(^2P^o_{1/2})4s^2[1/2]^o_1$
4596.097	$(^2P^o_{3/2})5p^2[3/2]_1$	$(^2P^o_{1/2})4s^2[1/2]^o_1$
4628.441	$(^2P^o_{3/2})5p^2[5/2]_2$	$(^2P^o_{1/2})4s^2[1/2]^o_1$
4642.137	$(^2P^o_{3/2})9d^2[3/2]^o_2$	$(^2P^o_{3/2})4p^2[1/2]_1$
4647.489	$(^2P^o_{3/2})9d^2[1/2]^o_1$	$(^2P^o_{3/2})4p^2[1/2]_1$
4702.316	$(^2P^o_{3/2})5p^2[1/2]_1$	$(^2P^o_{1/2})4s^2[1/2]^o_1$
4746.821	$(^2P^o_{3/2})8d^2[1/2]^o_0$	$(^2P^o_{3/2})4p^2[1/2]_1$
4752.939	$(^2P^o_{3/2})8d^2[1/2]^o_1$	$(^2P^o_{3/2})4p^2[1/2]_1$
4768.673	$(^2P^o_{1/2})6d^2[3/2]^o_2$	$(^2P^o_{3/2})4p^2[1/2]_1$
4836.697	$(^2P^o_{3/2})9s^2[3/2]^o_2$	$(^2P^o_{3/2})4p^2[1/2]_1$
4876.261	$(^2P^o_{3/2})7d^2[3/2]^o_2$	$(^2P^o_{3/2})4p^2[1/2]_1$
4887.947	$(^2P^o_{3/2})7d^2[1/2]^o_1$	$(^2P^o_{3/2})4p^2[1/2]_1$

[a] Given in jl coupling notation [153]

conjunction with the intensity calibration measurement. By separating out the wavelength dependence in this way, the same intensity calibration can be used with multiple grating configurations of the detector. Transmission function measurements are done by reinserting the bandpass filter and measuring the spectrum of a broadband calibrated light source. The Ocean Optics LS-1-CAL, which uses a tungsten filament and connects directly to an optical fiber using an SMA905 connector, is used for this purpose. The light source has a

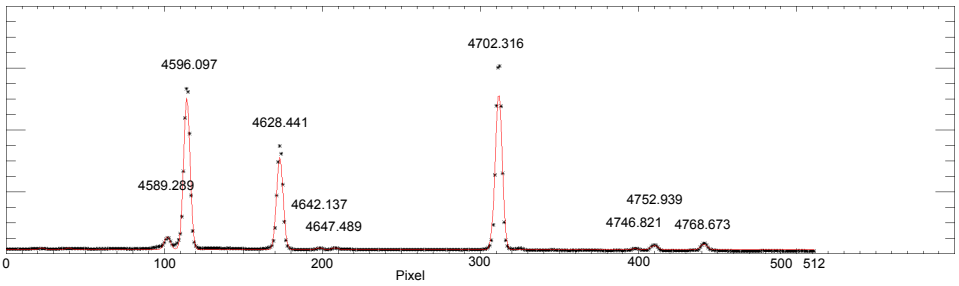

Figure 2.43: Wavelength calibration spectrum for column B using Argon geissler tube. Black is measured data. Red is model function.

known output spectrum from the equipment calibration documentation (see figure 2.44). A background shot is also taken with no lamp attached.

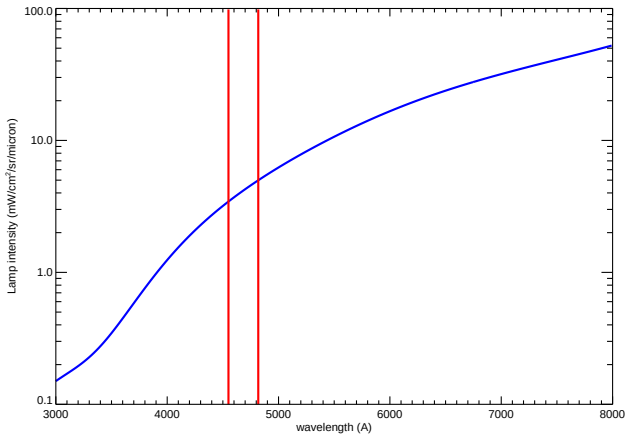

Figure 2.44: LS-CAL-1 output. Vertical lines show region relevant to the helium grating.

The transmission function of the detector is measured spectrum minus dark current counts in counts/second divided by the lamp output. A result is shown in figure 2.45. Due to the three vertical slits, the same wavelength region is projected three times on the same row, and we can see that the

bandpass filter isolates these regions on the CCD by suppressing transmission outside a narrow range of wavelengths.

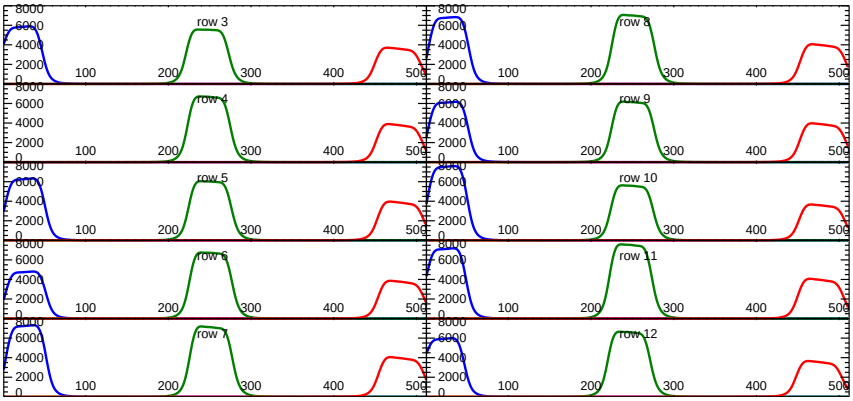

Figure 2.45: Spectral detector transmission functions for 30 channels on 10 rows (each graph is one row). The three peaks represent transmission of the same wavelength interval through the bandpass filter but imaged to different part of the CCD. The y-axis is counts $\mathrm{cm}^2\,\mathrm{sr}\,\mu\mathrm{m/mW}$. The blue, green, and red curves are associated with the "A", "B", and "C" columns.

2.5.4 Polarization calibration

Because angled stainless steel mirrors are used, the toroidal optics are polarizing. This has small effects on the measured spectrum because the Zeeman components have different polarizations. The polarization is measured by placing a polarized light source in front of each viewing chord and measuring the detector intensity as the source is rotated.

A polarized light source was borrowed from R. Mumgaard who has designed a rig for MSE calibration, for which polarization effects are much more important. The source contains a lamp and a linear polarizer both

mounted on a rotation stage equipped with a stepping motor. As the light source is rotated, we measure a sinusoidal variation in the intensity, shown in figure 2.46.

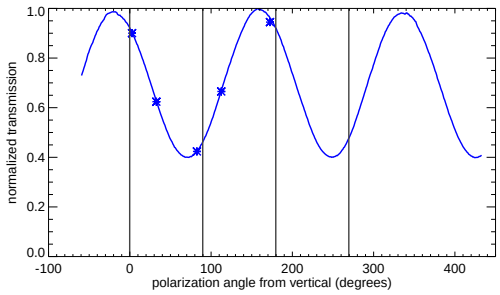

Figure 2.46: Polarization calibration measurements for toroidal channel L2:2.

The ratio of minimum to maximum intensity is roughly 40 %, demonstrating that the mirrors are indeed strongly polarizing. However, because the overall effect on the CXRS measurement is very small and not expected to vary, the calibration is performed infrequently.

2.6 Analysis of measurement

In addition to the plasma shots, one or more background shots are taken during each run day requiring the CXRS diagnostic. These shots are no light shots taken during the cooldown period between plasma shots and are used to subtract the dark current counts from the CCD signal. These background shots should not be confused with the background frames of a plasma shot, which are frames with no neutral beam.

So that proper background subtraction can be performed, the timing

of the CCD frames is synchronized to the timing of the DNB modulation. Typical combinations are shown in table 2.10.

Table 2.10: DNB and CCD timing combinations

beam on/off timing	frame timing
60 ms/40 ms	10 ms or 20 ms
60 ms/20 ms	10 ms or 20 ms
75 ms/25 ms	12.5 ms or 25 ms
100 ms/100 ms	10 ms, 12.5 ms, 20 ms, 25 ms

A shot may have about 80 to 150 frames of spectral data captured by the CCD, some of which were taken with beam on and some with beam off. These frames are partitioned into frame groups such that each group contains some beam on frames and some nearby beam off frames. This group of frames will be combined to form a single time point in the CXRS measurement. Figure 2.47 shows an IDL widget used for selection of frame groups for a shot. Only frames during or surrounding a beam pulse are used in the analysis. Frames without beam are used for background (aka ambient) measurement, and frames with beam contain background and CXRS emission. Not all frames are used: the first one or two frames of each beam pulse are thrown out because the beam takes about 10 ms to 20 ms to stabilize after the start of each pulse. Since both background and foreground frames are needed for the analysis, the beam modulation timing limits the time resolution of the CXRS measurement.

The CCD data $D(x, y, t)$ contains the number of counts in each bin for each frame time. The bin is given by horizontal pixel x and row y, and t is an

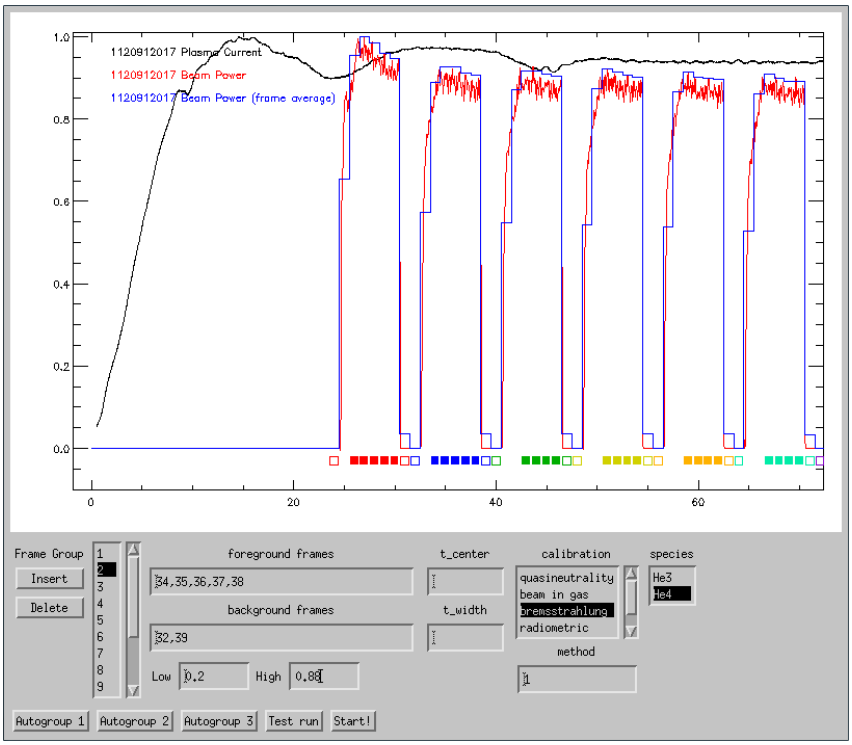

Figure 2.47: Analysis widget, selection of frames, using shot 1120912017. The plot has been zoomed in to the first half of the shot. The black line shows the plasma current. The red line shows beam output power, normalized to 1. The blue line is the beam output power averaged over the CXRS CCD frame times. Squares drawn under the lines show frames that are used by the analysis, color coded by frame group assignment. The solid squares represent CXRS (active) frames, and the empty squares represent background frames.

integer index for the frame. The dark count subtracted CCD data $\tilde{D}$ is

$$\tilde{D}(x,y,t) = D_{\mathrm{fg}}(x,y,t) - \frac{1}{N_t - 2}\sum_{i=2}^{N_t-1} D_{\mathrm{bg}}(x,y,i) \tag{2.90}$$

Note that the first two frames are discarded in the background shot averaging. Let $F_{j,k}(x)$ and $B_{j,k}(x)$ be the foreground and background frame-average

signals for channel j in frame group k.

$$F_{j,k}(x) = \frac{1}{N_k^{(\mathrm{fg})}} \sum_{t \in G_k^{(\mathrm{fg})}} \left[\tilde{D}(x, y_j, t)\right] / T_j(x), x \in X_j \tag{2.91}$$

$$B_{j,k}(x) = \frac{1}{N_k^{(\mathrm{bg})}} \sum_{t \in G_k^{(\mathrm{bg})}} \left[\tilde{D}(x, y_j, t)\right] / T_j(x), x \in X_j \tag{2.92}$$

where $G_k^{(\mathrm{fg})}$ and $G_k^{(\mathrm{bg})}$ are the foreground and background frames in frame group k, y_j is the row containing channel j, and $T_j(x)$ is the transmission function obtained in 2.5.3 for channel j. Since there are multiple channels in a row, there are multiple transmission functions for the same row, the signal is only valid in a pixel range where the transmission function is significant, given by X_j.

The shot noise is given (as variance) by

$$(\Delta\tilde{D}(x, y, t))^2 = D_{\mathrm{fg}}(x, y, t) + \frac{1}{(N_t - 2)^2} \sum_{i=2}^{N_t - 1} D_{\mathrm{bg}}(x, y, i) \tag{2.93}$$

$$(\Delta B_{j,k}(x))^2 = \frac{1}{(N_k^{(\mathrm{bg})})^2} \sum_{t \in G_k^{(\mathrm{bg})}} \left[\Delta\tilde{D}(x, y_j, t)\right]^2 / (T_j(x))^2 \tag{2.94}$$

The variances are needed for proper weighting of the least squares fit.

The atomic emission depends on the angle between the magnetic field and the viewing chord along every point in the viewing chord. The viewing chord geometry is available from calibration. The magnetic field is obtained from EFIT. EFIT gives the poloidal flux ψ and the poloidal current function

f_{pol} which have the following properties

$$B_r = -\frac{1}{r}\frac{\mathrm{d}\psi}{\mathrm{d}z} \tag{2.95}$$

$$B_z = \frac{1}{r}\frac{\mathrm{d}\psi}{\mathrm{d}r} \tag{2.96}$$

$$B_t = \frac{1}{r} f_{\text{pol}} \tag{2.97}$$

The ψ and f_{pol} are time averaged over the time span of the frame group. For simplicity, the angle is only calculated at a single point in space (two for ambient). For the active frames, the angle is calculated at the midpoint of the line of closest approach between the viewing chord and the beam axis (near the midplane). For the background frames, the angle is calculated at both intersections of the chord and edge of the plasma.

Both the foreground and background signals are fit with a fitting model restricted to a span of 59 pixels around the 4686 Å line. The background signal is fitted first, using the model

$$B_{j,k}(x) = A_0 \sum_n a_n(\Omega) \exp\left(-\frac{(\lambda - \lambda_n(1 + A_2/c))^2}{A_1}\right) + A_3 \tag{2.98}$$

The a_n are calculated from the Zeeman effect calculation based on the angle given above.

The background subtraction can be done by either subtracting the background signal $B_{j,k}$ from the foreground signal or by subtracting the fitted background signal from the foreground signal. (Another option is to fit $F_{j,k}$ with a fitting function that contains both the foreground and background fit functions.) It was found that the first method gave slightly better results,

which can be explained if the background (beam off) frame contains emission other than the helium line and flat background. The background subtracted signal (or CXRS signal) is

$$S_{j,k}(x) = F_{j,k}(x) - B_{j,k}(x) \tag{2.99}$$

By doing background subtraction in this way, the CXRS signal only contains signals which are enhanced by the beam and signals with second derivative time variation.

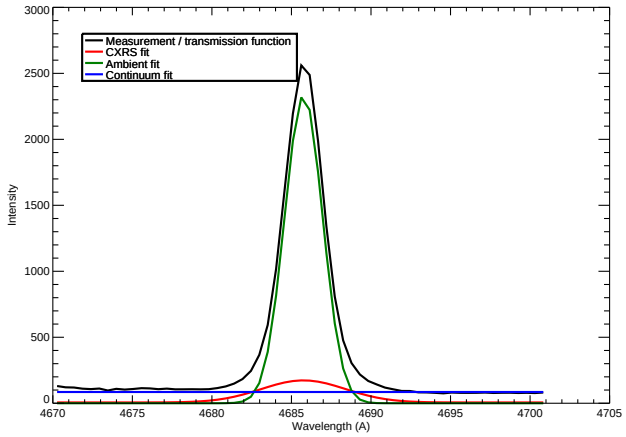

Figure 2.48: Analysis of shot 1120912017, B8, 0.3235–0.3859 s. The black curve shows the average signal (detector signal divided by wavelength transmission function) of the frames with beam on. The green line shows the ambient signal which was fitted from the beam off frames. The red line shows the fit of the CXRS data. The blue line shows a fit of the constant continuum.

The CXRS signal is fitted with the same model, but the a_n are different because the angle between the chord and magnetic field is different.

$$S_{j,k}(x) = C_0 \sum_n a_n(\Omega) \exp\left(-\frac{(\lambda - \lambda_n(1 + C_2/c))^2}{C_1}\right) + C_3 \tag{2.100}$$

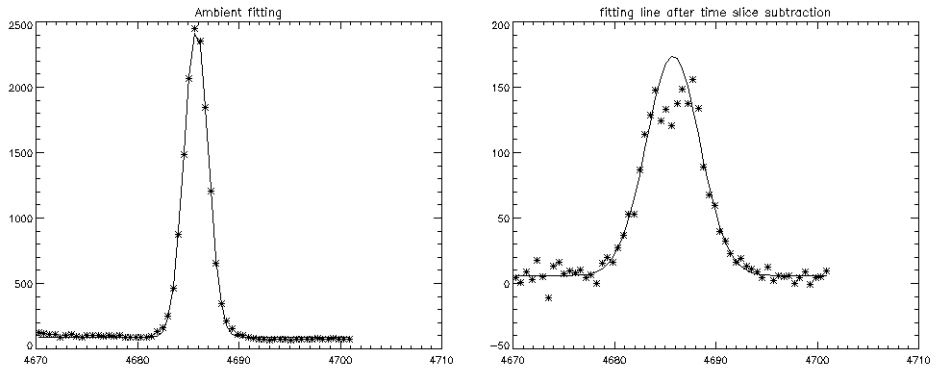

Figure 2.49: Background and foreground fitting

However, the error weighting is calculated differently.

The shot noise variance in the CXRS signal is

$$(\Delta S_{j,k}(x))^2_{(\mathrm{shot})} = \frac{1}{(N_k^{(\mathrm{fg})})^2} \sum_{t \in G_k^{(\mathrm{fg})}} \left[D(x, y_j, t)\right] / (T_j(x))^2 + \frac{1}{(N_k^{(\mathrm{bg})})^2} \sum_{t \in G_k^{(\mathrm{bg})}} \left[D(x, y_j, t)\right] / (T_j(x))^2 \tag{2.101}$$

D is used instead of $\tilde{D}$ because the background shot is the same for foreground and background frames and cancels. This shot error is not adequate for the CXRS measurement, because the time variation in the background line emission is a dominant source of error in the background subtraction. Therefore, we add another component to the error to get the full error. It is 3 % of the

fitted line model for the ambient line (without the continuum)[22].

$$(\Delta S_{j,k}(x))^2_{(\mathrm{tot})} = (\Delta S_{j,k}(x))^2_{(\mathrm{shot})} + 0.03 \times A_0 \sum_n a_n(\Omega) \exp\left(-\frac{(\lambda - \lambda_n(1 + A_2/c))^2}{A_1}\right) \tag{2.102}$$

This form of error strongly reduces the weight of the center of the line and correspondingly increases the weight of the wings. This, or a similar weighting, is necessary to get a proper fit[23]. The right side of figure 2.49 shows a fit of the CXRS signal. Note that the center of the line is a poor fit to a Gaussian after background subtraction. This is a typical result.

One channel has been dedicated to making measurements of a neon calibration lamp. This allows adjustment of the wavelength calibration to handle mechanical drift of optical components between full calibrations. The full wavelength calibration provides the wavelength mapping of each channel individually. This single channel measurement provides an estimated wavelength calibration shift for all channels, assuming the channels all move together.

Based on 2.9,

$$n_{\mathrm{He}} = C_0 \sqrt{\pi C_1} / X_j \tag{2.103}$$

$$X_j = 4\pi T_j (4686\,\text{Å}) \frac{\mathrm{d}\lambda}{\mathrm{d}x} t_{\mathrm{int}} \int_{\mathrm{chord}} \left(\sum_k q_{\mathrm{em}}(v_k) \int_{\mathrm{chord}} n_k \,\mathrm{d}s \right) \tag{2.104}$$

[22]This value was chosen by measuring several shots without beam, and looking at the typical variation between the intensity of the background He II line between frames

[23]Another possibility is to fit the sum of the CXRS signal and a residual background line which has the same width as the background line, but with the amplitude a free parameter around 3 % of the ambient line amplitude. This technique also works and provides results which are close to the same.

where T_j is the calibrated absolute transmission for channel j, $\frac{\mathrm{d}\lambda}{\mathrm{d}x}$ is the dispersion, t_{int} is the integration time, and the summation is over beam velocity components.

$$T_{\mathrm{He}} = \left(C_1 - w_{\mathrm{instr}}^2\right) \frac{mc^2}{\lambda_0^2} \tag{2.105}$$

where w_{instr} is the instrument width, measured during detector calibration.

$$v_{\mathrm{He}} = C_2 + \frac{\Delta\lambda_{\mathrm{Ne}}}{\lambda_{\mathrm{Ne}}} c \tag{2.106}$$

where the second term is an adjustment of the wavelength calibration using the neon lamp.

2.6.1 Measurement error

Measurement errors fall into two categories: random and systematic errors. The random errors are largely due to counting statistics and plasma evolution between time slices used for time-slice subtraction. Systematic errors are errors in calibration and in atomic cross sections, as well as radial smearing due to the finite beam width and finite chord width.

In plots of ion profiles, only the random error is included in the error bars.

2.6.1.1 Line fitting error (random)

The line fitting error was simulated using a Monte Carlo technique. 20000 pairs (beam off spectrum and beam on spectrum) of noisy spectra were randomly generated over a range of parameter values, using the Zeeman line models in 2.98 and 2.100. The generated lines were fit using MPFIT, and the differences between the fitted parameters and the initial parameters has been analyzed.

The error in the fit parameters of a line profile depends on the underlying error in the counts of each pixel. The CCD noise contains a shot noise component due to counting of individual electrons and a readout noise associated with the ADC and electronics. For our operating conditions, the shot noise is dominant, so the counts measured in each pixel follow a Poisson distribution, with variance equal to the mean value. When adding and subtracting[164] Poisson distributions, the variances add, so the pixel errors are given by 2.102.

About 5 % of the iterations failed to converge or the fit was very poor. These are thrown out as outliers. This problem exists in fitting of real data as well, and the data point will be marked as invalid.

We are interested in the standard deviation in the fitted area, width-squared, and velocity-shift as a function of the input parameters. Sensitivities to input parameters are checked by first choosing a parameter to study, sorting the 20000 points by that parameter and dividing them into 20 bins. The stan-

Table 2.11: Monte Carlo parameter ranges

Parameter	min	max	unit
A_0/C_0 [a]	30	60	
A_1	2.4	2.7	Å^2
A_2	-10	10	km/s
A_3	90	110	counts
C_0	20	3000	counts
C_1	1.5	25	Å^2
C_2	-10	10	km/s
C_3	-10	10	counts

[a] Parameter A_0 was generated as a random number times C_0

dard deviation of the differences between the initial parameters and the fitted parameters is calculated in each bin. It is observed that the most important parameters are C_0, A_0, and C_1. A_1 is not important because the width of the ambient He II line does not vary much in experiment, and the effects of A_3 and C_3 are small enough to be neglected in this analysis.

The parameter dependence of the error was found by fitting the Monte Carlo results with model functional forms to get partial dependencies, and combining the partial dependencies into a single derived scaling law. The area error is seen to scale with $\sqrt{C_0}$, $1/C_1$, and $\sqrt{A_0}$. The partial dependencies (plotted in red in figures 2.50 and 2.51) are

$$\Delta A = 4.712178\sqrt{9.8848740C_0} - 46.281389 + f(C_1, A_0) \tag{2.107}$$

$$\Delta A = \frac{1649.9413}{C_1} + 285.5582 + f(C_0, A_0) \tag{2.108}$$

$$\Delta A = 2.4965705\sqrt{0.74856499A_0} - 20.431885 + f(C_1, C_2) \tag{2.109}$$

and the derived fit (in count-Å) is

$$\Delta A = 2.3131381\sqrt{9.884874C_0} + 1.2255293\sqrt{0.74956499A_0} - 27.951239 \tag{2.110}$$

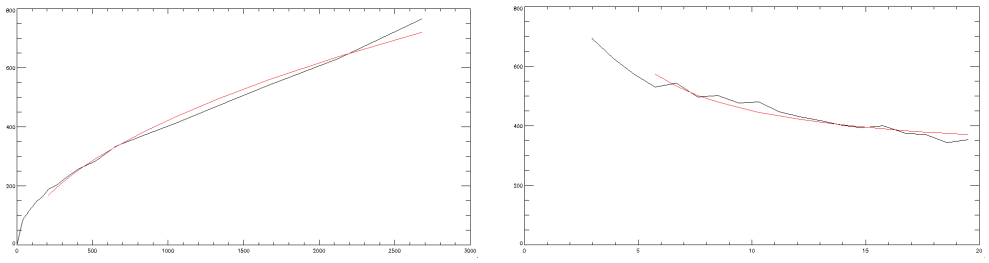

Figure 2.50: Area error versus C_0 *(left)* and C_1 *(right)* in count-Å. Black shows Monte Carlo results and red shows a parametric fit.

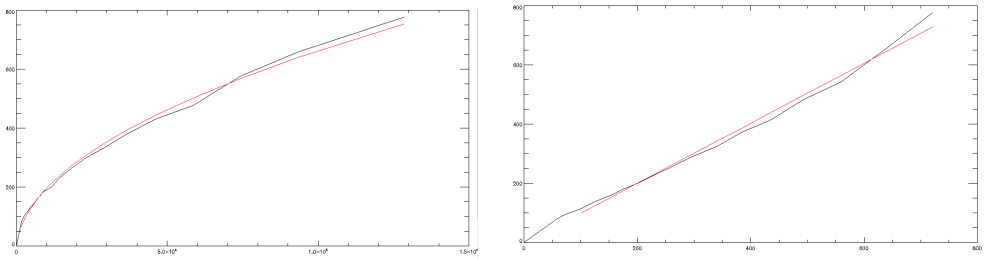

Figure 2.51: *(left)* Area error versus A_0 in count-Å. *(right)* Area error versus derived scaling law (should lie on y=x line).

Similarly, for width-squared ΔT (measured in Å^2), the partial sensitivities are

$$\Delta T = \frac{42.562073}{\sqrt{C_0}} - 0.52076323 + f(A_0) \tag{2.111}$$

$$\Delta T = \frac{341.65811}{\sqrt{A_0}} - 0.78996495 + f(C_0) \tag{2.112}$$

and the derived fit is

$$\Delta T = \frac{18.2727147}{\sqrt{C_0}} + \frac{146.67582}{\sqrt{A_0}} \tag{2.113}$$

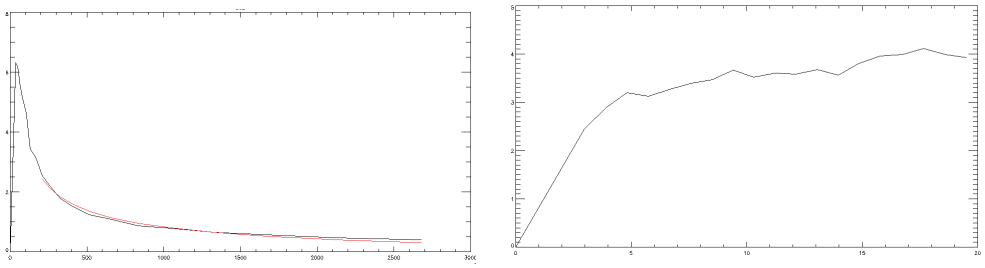

Figure 2.52: Width-squared error versus C_0 *(left)* and C_1 *(right)* in count-Å. Black shows Monte Carlo results and red shows a parametric fit. C_1 has a weak dependence and is neglected.

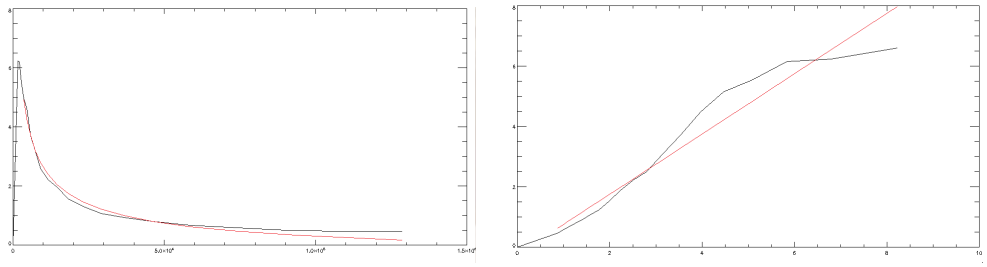

Figure 2.53: *(left)* Width-squared error versus A_0 in count-Å. *(right)* Width-squared error versus derived scaling law (should lie on y=x line).

Finally, for velocity fitting error (in km/s), partial sensitivities are

$$\Delta v = \frac{297.20907}{\sqrt{C_0}} - 2.5356724 + f(C_1, A_0) \tag{2.114}$$

$$\Delta v = \frac{67.866032}{C_1} + 16.880263 + f(C_0, A_0) \tag{2.115}$$

$$\Delta v = \frac{2158.0663}{\sqrt{A_1}} - 3.1226902 + f(C_0, C_1) \tag{2.116}$$

$$\tag{2.117}$$

and the derived fit is

$$\Delta v = \frac{131.08713}{\sqrt{C_0}} + \frac{951.83743}{\sqrt{A_0}} \tag{2.118}$$

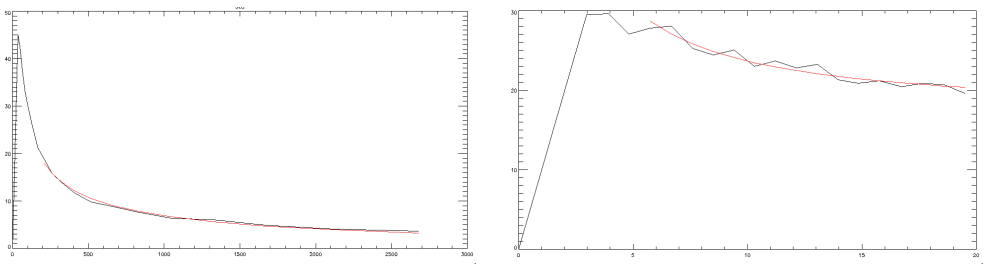

Figure 2.54: Velocity error versus C_0 *(left)* and C_1 *(right)* in count-Å. Black shows Monte Carlo results and red shows a parametric fit. C_1 has a weak dependence and is neglected.

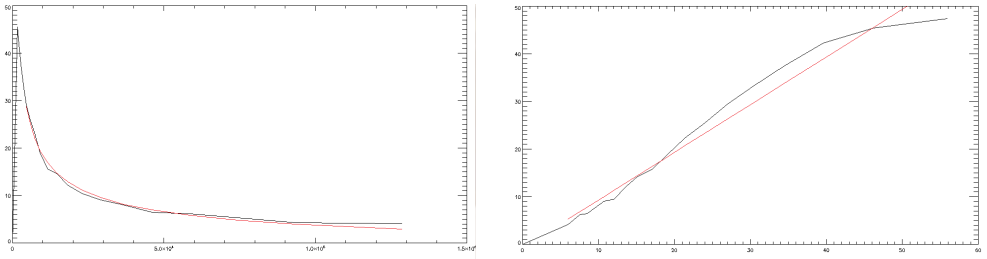

Figure 2.55: *(left)* Velocity error versus A_0 in count-Å. *(right)* Velocity error versus derived scaling law (should lie on y=x line).

The derived fits are not perfect, but they should be adequate for an error estimate for this range of parameter values.

MPFIT also provide estimates of uncertainty of the fit, based on an estimate of the covariance matrix. This estimate can sometimes give a larger or smaller error than the Monte Carlo parameter scaling, but usually gives results within a factor of 3 of the Monte Carlo result. The error is usually

larger in the case of a poor fit, but a smaller error does not guarantee a realistic fit. In practice, I use the maximum of the Monte Carlo derived error and the MPFIT covariance error to estimate the error in the calculated profiles.

2.6.1.2 Beam modeling error (systematic)

The accuracy of the beam density in regions of very strong beam attenuation is low, because even a small error in stopping cross sections of a few percent will convert into a large error in density. Therefore, the core channels suffer doubly from lower signal to noise and greater systematic uncertainty. Using a simple exponential decay model, $n_b = n_0 \exp(-sd)$, the relative error in n_b from a relative error in s, the inverse stopping distance, is easily obtained.

$$\frac{s}{n_b}\frac{\partial n_b}{\partial s} = -sd \tag{2.119}$$

Let $D \equiv sd$ be the beam depth. Therefore, at a beam attenuation of $1/e$, with $D = 1$, a 10 % error in s will translate into a 10 % error in n_b. The error in s contains contributions from the error in the stopping cross section and the errors in the ion and electron densities. The uncertainty in the ADAS calculated beam stopping cross sections depends on the uncertainties in the underlying atomic cross sections used in the collisional-radiative model. The proton impact ionization and from the ground state and charge exchange are the most important contributions[50] to the total uncertainty. The Janev and Smith 1993 review[107] has assigned an uncertainty of 10–25% for the ionization cross section and 10–50% for the charge exchange cross sections. This is comparable to the uncertainties in the plasma density.

From ALCBEAM simulations, the beam depth is typically about 0.7 at the edge and 1.4–2.5 at the core, n_{e0} 1.0 cm^{-3} to 1.7 cm^{-3}. Therefore, the uncertainty due to beam modeling is perhaps around 7% at the edge to 100% in the core.

2.6.1.3 q_{eff} uncertainty (systematic)

The transition probabilities and resulting branching factors are very well known. Therefore, the uncertainty comes primarily the charge exchange cross sections. The ADAS dataset `qcx#h0_old#he2.dat` is primarily influenced by Fritsch[59] at energies of 50 keV. It is hard to assess an accuracy of the close-coupling calculations. The main calculation is at most 15 % larger than the purely atomic orbital expansion calculation, so 15 % is taken as the cross section uncertainty.

2.6.1.4 Radial uncertainty (systematic)

A goal of the CXRS diagnostic is to obtain 1D radial profiles of the impurity density, temperature, and velocity along the midplane (or beamline). As stated in section 2.2, the CXRS emission is the entire region of the beam-chord intersection. In the core, the density and temperature are approximately flux functions[24], so the points on the chord can be identified with points on the midplane intersecting the same flux surface. Since each chord passes through many flux surfaces, the emission can be interpreted as

[24]This assumption breaks down with a large anisotropic fast ion population

being smeared out over a range of radii. Therefore, the finite width of the beam directly translates into a loss of spatial resolution for the diagnostic. In addition, the chords have a finite diameter, which increases the flux surface range.

These effects are treated numerically by casting rays through each viewing chord, and stepping through each ray, and mapping the emission contribution from this point to the flux surface it intersects. The emission depends on the beam density and impurity density at each point. The finite diameter of the chord is treated by using 49 rays per chord, arranged in a 7 point hexagonal pattern at the periscope optics cross multiplied by a 7 point hexagonal pattern at the focal point in the plasma (see figure 2.56.

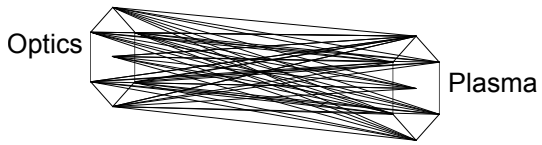

Figure 2.56: Chord approximation by 49 rays

The calculation has been performed for two representative shots for an upper single null (USN) configuration and a lower signal null (LSN) configuration (see figure 1.8). Figure 2.57 shows the results for USN and figure 2.58 shows the results for LSN. The results are presented as the strength of the contribution from each flux surface for each viewing chord/channel. The hair-like jaggedness in each curve is an artifact of the limited 49 ray calculation.

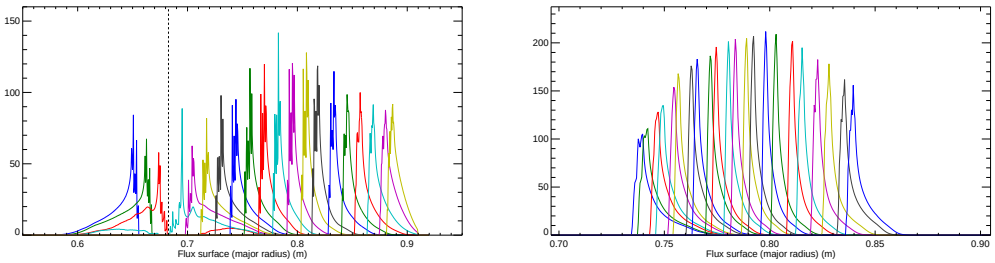

Figure 2.57: Radial localization of channel emission for an USN plasma shot 1110323027. Each overlapping curve is a different channel. *Left*: 20 poloidal channels. *Right*: 22 toroidal channels.

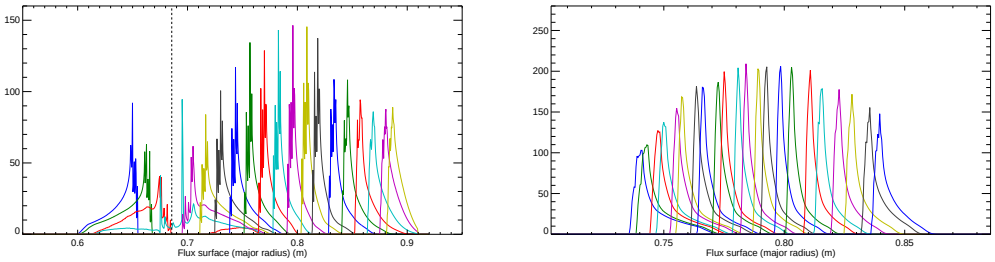

Figure 2.58: Radial localization of channel emission for an LSN plasma shot 1110126006. Each overlapping curve is a different channel. *Left*: 20 poloidal channels. *Right*: 22 toroidal channels.

A 129×129 point standard EFIT calculation is used to construct the flux mapping. The magnetic axis is near 0.68 m, marked by a vertical dotted line. Near the magnetic axis, some grid quantization artifacts are visible in the calculation. Although the high field side and low field side can both be mapped to the same flux surface, the contributions from the high field side have been left separate in the calculation, and mapped to the inner midplane intersection radius, so the inner chords can be clearly distinguished.

Using the results of the calculation, we can assign a centroid radius

to each channel, based on the major radius associated with the centroid of the distribution function. This centroid radius is shifted outward relative to the center of the chord at the midplane because of the contribution from flux surfaces the chord must pass through before and after reaching the midplane. We can also assign a radial bounds of the channel such that 80 % of the channel signal come from inside the bounds. Inner channels are more spread out because the chords must pass through a greater number of flux surfaces. In addition, innermost channels have the greatest shift between between the the centroid radius and the chord center, up to 8 cm for poloidal channel 1 (chord center $R = 0.6516\,\mathrm{m}$, centroid radius $R = 0.7315\,\mathrm{m}$)! The shift is less than 1 cm for chord center $R > 0.74\,\mathrm{m}$. Clearly, this effect poses a large difficulty for plasma core measurements.

2.6.1.5 Intensity calibration error (systematic)

The variation in results of 2.5.2.5 indicate that uncertainty in the optical throughput is a serious source of error in the density measurement. After installation of the aperture on the poloidal optics after the 2011 campaign, the variation in poloidal throughput was strongly reduced, but intensity errors could be on the order of 30 %.

Chapter 3

Light Impurity Transport

3.1 Introduction

Transport is the bulk motion of energy, particles, or momentum from one region of the plasma to another. The goal of magnetic confinement is, at the simplest level, an effort to minimize the transport on a global scale, which will remove energy from the plasma and make it more difficult to reach thermonuclear temperatures. The full story is much more complex, as some level of helium transport is desirable for ash removal, inward transport can aid in the core reaction rate, and momentum transport is linked to plasma rotation which seems to be important for turbulence reduction. Tokamaks have been observed to undergo dramatic changes in transport as they switch into different so-called confinement regimes, which appear to have a global character. A complete understanding of confinement and transport is one of the forefront challenges facing the fusion community.

Transport, along with sources and sinks, control the shape of plasma profiles such as densities, temperatures, and momenta of each species. Since parallel transport is usually fast compared to plasma dynamics, these profiles

are typically near equilibrium within a flux surface[1]. The transport across different flux surfaces is much slower, so the plasma values can vary greatly across the span of flux surfaces. Therefore, many plasma profiles can be accurately treated as a flux function—that is, the local value depends only on the flux surface it intersects. So transport not only influences the shape but the dimensionality of the plasma profile, reducing many parameters to 1D.

Transport in tokamaks is described in terms of neoclassical and anomalous contributions. Neoclassical transport is collisional transport, taking into account the shape of the particle orbits in the plasma. It is a refinement of the classical transport, which describes the collisional transport in a uniform plasma without complicated orbits. Early experiments found transport was much higher than predicted by neoclassical theory. The term anomalous transport was used to describe all the non-neoclassical contributions to transport. The general consensus is that anomalous transport is due to plasma turbulence, and much progress has been made in the last 20 years, particularly in gyrokinetic theory of turbulent transport. Much of the progress is due to the increase in computing power available for gyrokinetic simulations. Turbulent transport theory has successfully explained some of the instabilities and trends that have been seen in experimental measurements, but the physics has not yet reached a point where there is solid quantitative agreement between simulations and experiment.

[1]This is less true at the edge, where sources and sinks are large and poloidal angle dependent and collisions shrink the gap between parallel and perpendicular transport.

Discussions of transport in fusion experiments usually distinguish between transport of three different quantities: particle transport, momentum transport, and energy transport. Ultimately, energy and momentum are carried by the particles, but they need not transport at the same rate. The particle flux, momentum flux, and energy flux correspond to the first, second, and third moments of the kinetic equation. This thesis is primarily concerned with particle transport, since this is the most easily measured with the CXRS diagnostic. The analysis of momentum and thermal transport is more difficult because these quantities can be traded between different species.

The transport of light impurities deserves some special mention because light impurities, that is, low Z ions which are not the main fuel, may dilute the plasma and slow down the fusion reaction. In a thermonuclear plasma, light impurities are fully ionized in the core and therefore their core transport is mainly controlled by just two numbers, the mass A and the charge Z. It is useful to study different species of impurities in order to establish scaling relationships for these numbers.

At the low end of A and Z are helium-3 and helium-4. Helium is inevitably present in substantial quantities in a fusion reactor based on the D-T reaction. Helium-4 is a product of the main reaction, and helium-3 is also produced in the D-D reactions. Helium is also desorbed from the metal vessel components during discharge and readily recycles from the walls, so it is always present to some degree in a tokamak experiment. In a fusion reactor, helium-4 begins its life as a 3.5 MeV fast ion, but eventually thermalizes and

becomes helium "ash", which ought to be removed from the plasma. Helium-3 is also important because it is frequently injected as a minority species for use in ICRF minority heating. This particular application is discussed more fully in chapter 4.

The basic equation governing transport is the continuity equation,

$$\frac{\partial n(\mathbf{r},t)}{\partial t} + \nabla \cdot \mathbf{\Gamma}(\mathbf{r},t) = g(\mathbf{r},t) \tag{3.1}$$

Here, n is any conserved quantity (using the notation for density), $\mathbf{\Gamma}$ is a flux of the quantity, and g is a local rate of generation of the quantity. If the quantity is carried by a fluid, then $\mathbf{\Gamma}$ can be rewritten as $n\mathbf{v}$, but equation 3.1 doesn't require the existence of a fluid velocity $\mathbf{v}$. A more general expression for the flux includes a fluid-like convective term and a diffusive term:

$$\mathbf{\Gamma}(\mathbf{r},t) = -D(\mathbf{r},\xi)\nabla n(\mathbf{r},t) + \mathbf{v}(\mathbf{r},\xi)n(\mathbf{r},t) \tag{3.2}$$

This form is typically used as an ansatz for the transport flux, where D and $\mathbf{v}$ are transport coefficients that must be solved. These values depend on the plasma state, ξ, which may be varying in time. $D\nabla n$ is the diffusion which is due to random walk processes from collisions and certain types of turbulence. $\mathbf{v}n$ is a convective (or pinch) term due to a bias in the diffusive processes due to geometry or thermodynamic effects. This form suggests that the flux is linear in n and ∇n. In general, the transport can be nonlinear, and v must be taken as a function of n, and D as a function of n and ∇n.

When the dependence of D on ∇n is small, a plot of Γ/n versus $\frac{\partial n}{\partial r}$ is approximately linear, and the slope gives the diffusion coefficient D, and

the y-intercept gives the convective velocity v. Linear gyrokinetic simulations (discussed later) show that the curve is indeed quite linear even in cases where the helium is not a trace impurity, as long as there is no transition in the dominant turbulent mode. Figure 3.1 shows simulated flux curves for helium-3 impurity at two different concentrations.

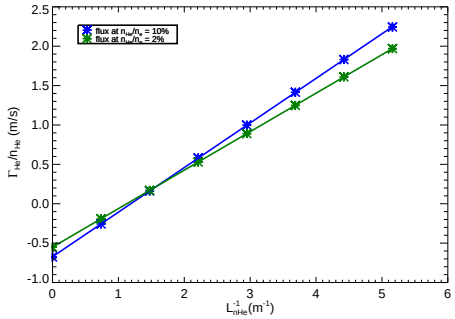

Figure 3.1: Simulated helium-3 flux curves for realistic C-Mod plasma conditions. The blue case has plasma composition $n_{\mathrm{He}}/n_e = 0.1$ and the green case has $n_{\mathrm{He}}/n_e = 0.02$ with the remainder as deuterium.

For cases where the impurity flux is not linear with respect to $\frac{\partial n}{\partial r}$, we must be careful in how we define D and v. The most useful approach is to linearize the curve around the equilibrium point[2]. At equilibrium, D is given by the slope of the line tangent to this point, and v is given by the y-intercept of the tangent line. The advantage of this definition is that equation 3.14 gives the correct equilibrium relationship even outside the trace limit.

[2]The equilibrium occurs where the flux is zero, at the x-intercept

3.1.1 Flux averaging of transport

We are concerned with 1D transport of flux-averaged quantities, since density is approximately a flux function. It is important to take into account that for transport from a larger flux surface to a smaller one, the density decrease in the larger flux surface ought to be smaller than the density increase in the smaller one. We follow the method outlined in the STRAHL manual[46] for constructing the flux surface average of 3.1. The steps are reproduced below. Integrating 3.1 over the volume interior to a flux surface gives

$$\frac{\mathrm{d}}{\mathrm{d}t}\int n\,\mathrm{d}V = -\oint \mathbf{\Gamma}\cdot\mathrm{d}\mathbf{S} + \int g\,\mathrm{d}V \tag{3.3}$$

Let ρ be a flux label which behaves like a minor radius. Assume that the flux surface geometry is independent of time. Then the flux density integral becomes

$$\oint \mathbf{\Gamma}\cdot\mathrm{d}\mathbf{S} = \oint \mathbf{\Gamma}\cdot\frac{\nabla\rho\,\mathrm{d}S}{|\nabla\rho|} = \oint \mathit{\Gamma}^{\rho}\frac{\mathrm{d}S}{|\nabla\rho|} \tag{3.4}$$

where Γ^{ρ} is the radial contravariant component of the flux of the quantity,

$$\mathit{\Gamma}^{\rho} = \mathbf{\Gamma}\cdot\nabla\rho = -D(\rho,\theta)|\nabla\rho|^2\frac{\partial n}{\partial\rho} + \mathbf{v}(\rho,\theta)\cdot(\nabla\rho)\,n \tag{3.5}$$

The flux surface average is an average over the area of the flux surface. However, the area elements must be weighted by $\frac{1}{|\nabla\rho|}$ which acts like an infinitesmal width of each area element, such that the "thicker" parts of the flux surface receive more weight. Therefore, the flux surface average of a quantity $\mathcal{F}$ is

$$\langle F\rangle = \left(\frac{\partial V}{\partial\rho}\right)^{-1}\oint F\frac{\mathrm{d}S}{|\nabla\rho|} \tag{3.6}$$

Taking the flux average of 3.3 gives

$$\frac{\partial}{\partial t}\int_0^\rho \mathrm{d}\rho \frac{\partial V}{\partial \rho}\left\langle n\right\rangle = -\frac{\partial V}{\partial \rho}\left\langle \Gamma^\rho\right\rangle + \int_0^\rho \mathrm{d}\rho \frac{\partial V}{\partial \rho}\left\langle q\right\rangle \tag{3.7}$$

Differentiating by ρ and dividing by "area" gives

$$\frac{\partial \left\langle n\right\rangle}{\partial t} = -\left(\frac{\partial V}{\partial \rho}\right)^{-1}\frac{\partial}{\partial \rho}\left(\frac{\partial V}{\partial \rho}\left\langle \Gamma^\rho\right\rangle\right) + \left\langle g\right\rangle \tag{3.8}$$

If we choose the flux label r, which is calculated as the radius of a cylinder with equal volume to the volume enclosed by a flux surface:

$$r = \sqrt{\frac{V}{2\pi^2 R_{\mathrm{axis}}}} \tag{3.9}$$

then we get the cylindrical particle conservation equation

$$\frac{\partial \left\langle n\right\rangle}{\partial t} = -\frac{1}{r}\frac{\partial}{\partial r} r\left\langle \Gamma^r\right\rangle + \left\langle g\right\rangle \tag{3.10}$$

The flux averaged transport parameters written in terms of r are

$$D^r(r) = \left\langle D(r,\theta)|\nabla r|^2\right\rangle = \frac{1}{4\pi^2 R_{\mathrm{axis}} r}\int_0^{2\pi} D(r,\theta)|\nabla r|\,\frac{\mathrm{d}S}{\mathrm{d}\theta}\,\mathrm{d}\theta \tag{3.11}$$

$$v^r(r) = \left\langle v^r(r,\theta)\right\rangle = \frac{1}{4\pi^2 R_{\mathrm{axis}} r}\int_0^{2\pi} v(r,\theta)\,\frac{\mathrm{d}S}{\mathrm{d}\theta}\,\mathrm{d}\theta \tag{3.12}$$

so that

$$\left\langle \Gamma^r\right\rangle = -D^r(r)\frac{\partial n(r)}{\partial r} + v^r(r)n(r) \tag{3.13}$$

Superscripts indicate the contravariant index and not exponentiation.

However, when dealing with experimental values from diagnostics, the flux label R_{mid}, defined as the major radius where the flux surface intersects the midplane on the low field side of the tokamak, is often used. In this case, a flux coordinate transformation to must be performed.

3.1.2 Equilibrium transport

In a particle equilibrium, in the absence of sources or sinks, we can set $\frac{\partial\langle n\rangle}{\partial t} = \frac{\partial}{\partial t}\frac{\partial\langle n\rangle}{\partial r} = \langle g\rangle = 0$ and therefore Γ is also be equal to 0. When this is the case, we can derive a simple relationship between v, D, and the density inverse scale length.

$$0 = -D^r(r)\frac{\partial n(r)}{\partial r} + v^r(r)n(r)$$

$$\frac{v^r(r)}{D^r(r)} = \frac{1}{n(r)}\frac{\partial n(r)}{\partial r} \equiv -L_n^{-1} \tag{3.14}$$

This type of situation often arises for light impurity transport in the core of the plasma during the flat top of a steady discharge. There is ample time for an intrinsic impurity such as boron to reach steady state. The equilibrium point is a stable equilibrium because the diffusion coefficient D is always positive, driven by the thermodynamic free energy of the particle gradient.

However, for impurity puffing experiments such as when helium is puffed at the edge, helium is not in steady state. The helium density increases during puffing and steadily decreases after the puff (figure 3.2). Even so, it is still appropriate to use equation 3.14 if the time scales of the transport processes are much shorter than the time scales of the decline in impurity density. We shall see that this is indeed the case.

We have a helium disappearance time $\tau_{\text{loss}} \sim 200\,\text{ms}$ which an upper bound to the core confinement time τ_{nHe}. But, the increase in helium density after the puff is much more rapid than the decline, which suggests that the

timescale for the helium loss is governed by the wall recycling efficiency and not the core transport processes. This is confirmed by measuring the edge helium density during the short puff experiment (section 3.5.3). We find that the core confinement time is on the order of 10 ms, which is much shorter than the disappearance time. In this situation, the helium population is in a quasi-steady state, with lost helium balanced by helium reflecting from the wall, and 3.14 is approximately correct.

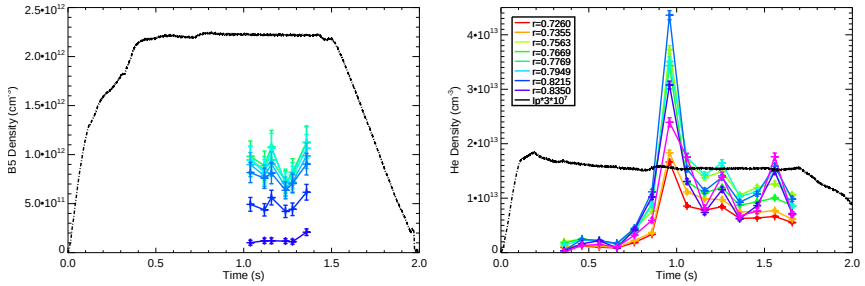

Figure 3.2: Boron and helium time traces. Left: boron in shot 1101209004. Right: helium in shot 1120914007. The plasma current is shown by a dotted line to serve as a reference for the flat top of the plasma.

When far from equilibrium, there is little use for the transport coefficients D and v, and the transport should be characterized by the particle flux, which is not zero outside of equilibrium.

3.2 Classical transport and drifts

As an introduction, we consider a simpler case of classical transport, which is collisional transport in a plasma with straight magnetic field lines. As stated in section 1.2, the particle orbits are helices around the magnetic

field lines, with gyroradius given by

$$\rho_s = \frac{m_s v_\perp}{|q_s|\, B} \approx \frac{\sqrt{2 m_s T_s}}{|q_s|\, B} \tag{3.15}$$

A heuristic argument can be used to get an approximately correct result. Each collision randomizes the phase of the gyro-orbit, so after each collision the guiding center position is shifted by a random distance on average of one gyroradius. Assuming collisions are much rarer than the cyclotron frequency, the gyrating particle executes a random walk across field lines, so the perpendicular diffusion is

$$D_{\perp \mathrm{CL}} \approx \frac{\rho_e^2}{\tau_e} \tag{3.16}$$

The collision time is given by[111]

$$\tau_e = 3\,(2\pi)^{3/2}\, \frac{\epsilon_0^2 m_e^{1/2} T_e^{3/2}}{n_i Z^2 e^4 \ln \Lambda} \tag{3.17}$$

These heuristic random walk arguments predict an ion transport greater than the electron transport. Since the plasma is neutral, an electric field will form in such a manner to force the electron and ion fluxes to be equal[61]. For an impurity, the situation is more complex, and it is better to use a more rigorous calculation.

A more rigorous way to compute the classical transport[111] is by using Ohm's law

$$\mathbf{E} + \mathbf{v} \times \mathbf{B} = \eta \mathbf{j} \tag{3.18}$$

where η is the resistivity and the pressure balance equation

$$\mathbf{j} \times \mathbf{B} = \nabla p \tag{3.19}$$

Taking the cross product of 3.18 by $\mathbf{B}$ and substituting 3.19 gives

$$v_\perp = \frac{\mathbf{E}\times\mathbf{B}}{B^2} - \eta_\perp \frac{\nabla p}{B^2} \tag{3.20}$$

In the plasma rest frame[3], the first term disappears. The second term is

$$v_\perp = \eta_\perp \frac{T(\nabla n) + n(\nabla T)}{B^2} \tag{3.21}$$

$nv_\perp$ is the same as the transport flux Γ^r. We can see that the flux contains a diffusive part (proportional to ∇n) and a thermodiffusive part (proportional to ∇T). The perpendicular resistivity is[111] $\eta_\perp = m_e/ne^2\tau_e$. Therefore, the diffusivity is

$$D = n\eta_\perp \frac{T}{B^2} = n\frac{m_e}{ne^2\tau_e}\frac{m_e v_{th}^2}{2B^2} \sim \frac{\rho_e^2}{\tau_e} \tag{3.22}$$

We see that it is the electron gyroradius that drives the transport.

The particles also experience drifts which contribute to the v transport parameter. These drifts are derived from the guiding center equations of motion of a single particle in a field[156]. These drifts are perpendicular to the magnetic field because parallel motion on the magnetic field line is completely unconstrained. The E-cross-B drift is

$$\mathbf{v}_E = \frac{\mathbf{E}\times\mathbf{B}}{B^2} \tag{3.23}$$

This drift is independent of species. Sometimes the term "plasma rest frame" is used to indicate a frame co-moving with $\mathbf{v}_E$. This drift is particularly important because it acts as an underlying mechanism to more complicated

[3]defined by the condition that $\mathbf{E}\times\mathbf{B} = 0$

transport processes such as Pfirsch-Schlüter transport, the Ware pinch, and drift wave turbulence.

The grad-B drift is

$$v_{\nabla B} = \frac{v_\perp^2}{2\Omega} \frac{\mathbf{B} \times \nabla B}{B^2} \tag{3.24}$$

where $\Omega = q/m$ is the Larmor frequency of the particle, where the sign of the charge is specifically maintained. Therefore, the ion drift exceeds the electron drift and is in the opposite direction.

The inertial drift is

$$v_{\text{inertia}} = \frac{v_\parallel}{\Omega} \mathbf{b} \times \frac{\mathrm{d}\mathbf{b}}{\mathrm{d}t} \tag{3.25}$$

In the limit of constant magnetic field and weak electric field, this reduces to the curvature drift

$$v_{\text{curv}} = \frac{v_\parallel^2}{\Omega} \mathbf{b} \times (\mathbf{b} \cdot \nabla)\, \mathbf{b} \tag{3.26}$$

In a cylindrical geometry or a tokamak, the curvature drift and grad-B drift point in the same direction and can be combined into

$$v_{ds} = \frac{v_\parallel^2 + \frac{1}{2} v_\perp^2}{\Omega_s} \frac{\mathbf{B} \times \nabla B}{B^2} \tag{3.27}$$

The polarization drift is

$$v_{pol} = \frac{\mathbf{b}}{\Omega} \times \frac{\mathrm{d}\mathbf{v}_E}{\mathrm{d}t} \tag{3.28}$$

This is a drift due to changing electric fields, and plays a role in electrostatic turbulence as well as plasma startup.

3.3 Neoclassical transport

Neoclassical transport is transport due to Coulomb collisions between charged particle species and drifts, taking into account the effects of the curved and twisted magnetic geometry (which is responsible for bounded particle orbits). It might also include the classical drift terms as they appear in a curved geometery. Major milestones in the development of neoclassical transport occurred with the development of the Pfirsch-Schlüter regime in 1962[149] and banana-enhanced transport in 1968[61]. Hinton and Hazeltine[78] have written an informative review of neoclassical transport, and Hirshman and Sigmar[80] have done a comprehensive analysis and review of neoclassical impurity transport in a general tokamak equilibrium.

In most cases, turbulent transport greatly exceeds neoclassical. However, there have been cases in which the turbulence is suppressed inside a transport barrier, and the transport reaches neoclassical levels[48, 175], especially in tokamak experiments with reversed shear in the core. Neoclassical transport acts as a lower bound to the transport, and it remains relevant in current and future high performing devices[47].

Neoclassical transport in a tokamak-like geometry has three different limiting forms depending on the collisional regime that the plasma is in (figure 3.3. When the collision rate is lower than the bounce frequency, it is the banana regime, because collisional steps between banana orbits are responsible for the majority of the diffusive flux. At high collision rates, the orbits are completely destroyed, and it is in the Pfirsch-Schlüter regime. In an intermediate collision

frequency, the diffusion rate is independent of collision frequency and it is the plateau regime. The distinction between the banana regime and plateau regime is very blurred at lower aspect ratios[80], and the plateau regime is hardly discernable at an aspect ratio of 4. Hirshman and Sigmar[80] group them together into a single flux term, called the banana-plateau regime. The neoclassical flux can be written $\Gamma^{\text{neo}} = \Gamma^{\text{CL}} + \Gamma^{\text{BP}} + \Gamma^{\text{PS}} + \Gamma^{\text{ES}}$, where the RHS terms are the classical, banana-plateau, Pfirsch-Schlüter, and electrostatic[4] contributions.

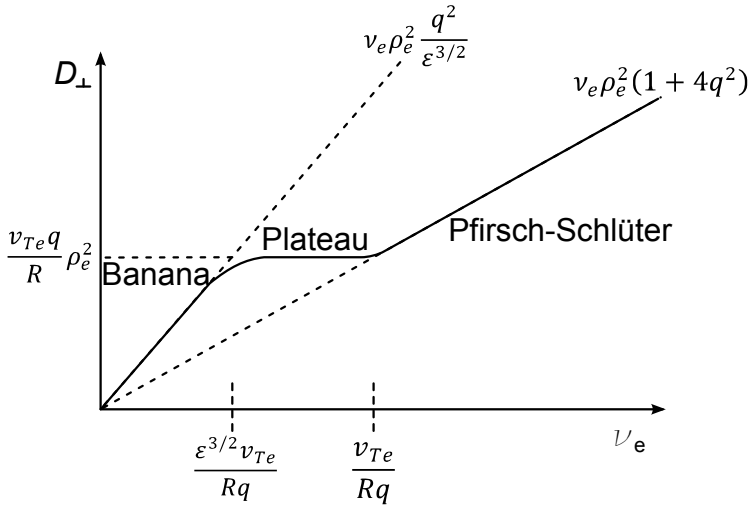

Figure 3.3: Neoclassical regimes for a high aspect ratio device

Analogous to the classical case, there is a heuristic random walk argument for transport in the banana regime. The difference is that the step size is given by the banana width, approximately given by

$$w_{be} \sim \frac{q}{\varepsilon^{1/2}}\rho_e \tag{3.29}$$

[4]radial$\mathbf{E}\times\mathbf{B}$ drift from a poloidal electric field

Therefore, the perpendicular transport is increased by a factor of $q/\varepsilon^{1/2}$, where q is the safety factor and ε is the local inverse aspect ratio.

The bounce frequency is

$$\omega_b \sim \varepsilon^{3/2} v_T / qR \tag{3.30}$$

At higher collision frequencies, the orbits break down. The Pfirsch-Schlüter transport is due to an $\mathbf{E} \times \mathbf{B}$ drift that arises from a parallel Pfirsch-Schlüter current. The Pfirsch-Schlüter current arises from the pressure balance equation which requires a $\mathbf{j} \times \mathbf{B}$ force to balance the pressure gradient. In the large-aspect-ratio approximation, the diffusion is[111]

$$\frac{\langle v_\perp R \rangle}{R_0} = -\frac{1}{B^2} \frac{\mathrm{d}p}{\mathrm{d}r} \left(\eta_\perp + 2q^2 \eta_\parallel \right) - \frac{E_\phi B_\theta}{B^2} \tag{3.31}$$

The magnetic curvature also generates a inward drift term known as the Ware pinch[189]. The effect scales with toroidal electric field, which is generated by the external transformer in order to generate the plasma Ohmic current.

$$v_{\mathrm{Ware}} = c \frac{E_\phi}{B_\theta} \tag{3.32}$$

The cross-field neoclassical particle and heat fluxes are[80]

$$\Gamma_{s\perp} = n_s \frac{c\mathbf{E} \times \mathbf{B}}{B^2} + \frac{\mathbf{b} \times \nabla \cdot \overleftrightarrow{p_s}}{m_s \Omega_s} + \frac{\mathbf{F}_{a1} \times \mathbf{b}}{m_s \Omega_s} \tag{3.33}$$

and

$$q_{s\perp} \equiv \mathbf{Q}_{s\perp} - \frac{5}{2} T_s \Gamma_{s\perp} \quad = \frac{\mathbf{b} \times \left(\nabla \cdot \overleftrightarrow{r_s} - \frac{5}{2} \frac{T_s}{m_s} \nabla \cdot \overleftrightarrow{p} \right)}{\Omega_s} + \frac{T_s \mathbf{F}_{s2} \times \mathbf{b}}{m_s \Omega_s} \tag{3.34}$$

where $\mathbf{F}_{a1} = \int m_s \mathbf{v} C_s(f_s)\,\mathrm{d}\mathbf{v}$ and $\mathbf{F}_{a2} = \int m_s \mathbf{v} \left(\frac{m_s v^2}{2T_s} - \frac{5}{2}\right) C_s\,\mathrm{d}\mathbf{v}$ are friction forces, $\overleftrightarrow{p_s}$ is the pressure tensor, and $\overleftrightarrow{r_s}$ is an energy weighted stress tensor

$$\overleftrightarrow{r}_s = \int \left(\frac{1}{2} m_s v^2 \mathbf{v}\mathbf{v}\right) f_s\,\mathrm{d}\mathbf{v} \tag{3.35}$$

They were derived from the first (force balance) and third moments (heat flow balance) of the Fokker-Planck equation. The result depends on friction forces and higher level constituent relations for each pair of species. The derivation of these, from the underlying kinetic theory, is beyond the scope of this thesis, but see 4.1–4.3 of [80].

The results of the neoclassical theory are very complex for an arbitrary number of species, so numerical codes are needed. But for the simpler case of a single impurity (two ion species) plasma, some approximate forms exist which are based on an ambipolarity heuristic. The rate of ion-impurity collision rate exceeds the ion-electron collision rate by approximately a factor of $\left(m_i/m_e\right)^{1/2} \sim 40$. Therefore, collisions between ion species will tend to give rise to an ambipolar flux in order to satisfy quasineutrality.

$$\Gamma_Z^r = -\frac{Z_i}{Z_Z} \Gamma_i^r \tag{3.36}$$

From [190],

$$\Gamma_Z^{\mathrm{CL}} = \frac{\rho_i^2 \nu_{iZ} n_i}{2Z_Z} \left(\frac{1}{n_i} \frac{\partial n_i}{\partial r} - \frac{Z_i T_Z}{Z_Z T_i n_Z} \frac{\partial n_Z}{\partial r} - \frac{1}{2T_i} \frac{\partial T_i}{\partial r} - \frac{Z_i}{Z_Z T_i} \frac{\partial T_Z}{\partial r} \right) \tag{3.37}$$

$$\begin{aligned} \Gamma_Z^{\mathrm{BP}} = {} & \frac{3c^2 T_i}{2e^2 B_T^2 R^2 Z_i Z_Z^2} \frac{1}{1/K_{11}^i + 1/K_{11}^Z} \\ & \times \left[Z_Z \left(\frac{1}{n_i} \frac{\partial n_i}{\partial r} - \frac{3}{2T_i} \frac{\partial T_i}{\partial r} \right) - Z_i \left(\frac{1}{n_Z} \frac{\partial n_Z}{\partial r} - \frac{3}{2T_Z} \frac{\partial T_Z}{\partial r} \right) \right. \\ & \left. + \left(\frac{Z_Z K_{12}^i}{K_{11}^i} - \frac{Z_i K_{12}^Z}{K_{11}^Z} \right) \frac{1}{T_i} \frac{\partial T_i}{\partial r} \right] \end{aligned} \tag{3.38}$$

$$\Gamma_Z^{\mathrm{PS}} = \frac{q^2 n_i \rho_i^2 \nu_{iZ}}{Z_Z} \left[K \left(\frac{1}{n_i} \frac{\partial n_i}{\partial r} - \frac{Z_i}{Z_Z} \frac{1}{n_Z} \frac{\partial n_Z}{\partial r} \right) + H \frac{1}{T_i} \frac{\partial T_i}{\partial r} \right] \tag{3.39}$$

where the subscripts i and Z refer to the main ion and impurity, respectively. K_{11}^i, K_{12}^i, K_{11}^Z, and K_{12}^Z are viscosity matrix elements, which have dimensions of mass$\times$length$^-1\times$time$^-1$, which are given in [190] but can also be calculated by NCLASS (see below). The K and H constants are

$$K = 1 - \frac{0.52}{0.59 + \alpha + 1.34 g^{-2}} \tag{3.40}$$

$$H = -0.5 + \frac{0.29 + 0.68\alpha}{0.59 + \alpha + 1.34 g^{-20}} \tag{3.41}$$

where $\alpha \equiv n_Z Z_Z^2 / n_i Z_i^2$ and g is the working ion collisionality parameter, $g \equiv \omega_{Ti} \tau_{ii} = \varepsilon^{3/2} \nu_*$.

The fluxes above can be decomposed into diffusive and convective components[5]. Assuming $T_i = T_Z = T$, the impurity D and v components are

[5] All terms proportional to $-\frac{\partial n_Z}{\partial r}$ are treated as diffusive part (which is allowed to depend on n_Z and therefore isn't a true diffusion) and the remaining flux terms is treated as a convection.

$$D_Z^{\mathrm{CL}} = \frac{\rho_i^2 \nu_{iZ} n_i Z_i}{2 n_Z Z_Z^2} \tag{3.42}$$

$$v_Z^{\mathrm{CL}} = D_Z^{\mathrm{CL}} \frac{Z_Z}{Z_i} \left(\frac{1}{n_i} \frac{\partial n_i}{\partial r} - \frac{Z_Z + 2Z_i}{2 Z_Z T} \frac{\partial T}{\partial r} \right) \tag{3.43}$$

$$D_Z^{\mathrm{BP}} = \frac{3c^2 T}{2e^2 B_T^2 R^2 Z_Z^2} \frac{1}{1/K_{11}^i + 1/K_{11}^Z} \frac{1}{n_Z} \tag{3.44}$$

$$\begin{aligned} v_Z^{\mathrm{BP}} = \frac{D_Z^{\mathrm{BP}}}{Z_i} \Bigg[& Z_Z \left(\frac{1}{n_i} \frac{\partial n_i}{\partial r} - \frac{3}{2T} \frac{\partial T}{\partial r} \right) + Z_i \left(\frac{3}{2T} \frac{\partial T}{\partial r} \right) \\ & + \left(\frac{Z_Z K_{12}^i}{K_{11}^i} - \frac{Z_i K_{12}^Z}{K_{11}^Z} \right) \frac{1}{T} \frac{\partial T}{\partial r} \Bigg] \end{aligned} \tag{3.45}$$

$$D_Z^{\mathrm{PS}} = \frac{q^2 n_i \rho_i^2 \nu_{iZ} Z_i}{n_Z Z_Z^2} K \tag{3.46}$$

$$v_Z^{\mathrm{PS}} = D_Z^{\mathrm{PS}} \frac{Z_Z}{Z_i} \left(\frac{1}{n_i} \frac{\partial n_i}{\partial r} + \frac{H}{K} \frac{1}{T} \frac{\partial T}{\partial r} \right) \tag{3.47}$$

In Alcator C-Mod, the main ions and the helium ions are in the banana regime for most of the plasma (see figure 3.4). The v/D ratio is then[158]

$$v_Z / D_Z = \frac{Z_Z}{Z_i} \left(\frac{1}{n_i} \frac{\partial n_i}{\partial r} + \mathcal{K} \frac{1}{T} \frac{\partial T}{\partial r} \right) \tag{3.48}$$

where

$$\mathcal{K} = -\frac{3}{2} + \frac{K_{12}^i}{K_{11}^i} + \frac{Z_i}{Z_Z} \left(\frac{3}{2} - \frac{K_{12}^Z}{K_{11}^Z} \right) \tag{3.49}$$

The thermoconvection coefficient $\mathcal{K}$ varies with plasma conditions and position, but it is generally a smaller effect than the main ion density gradient

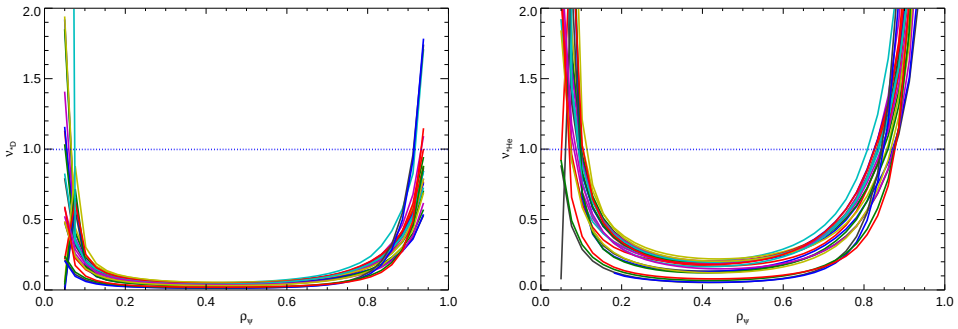

Figure 3.4: Collision frequency to bounce frequency ratio for various C-Mod shots. The dotted line marks an upper threshold for the banana regime. Left is for main ions, right is for helium-4.

dependence. The dependence on Z_i/Z_Z agrees with the ambipolarity heuristic mentioned earlier.

In the banana regime, collisional trapping and detrapping of particles gives rise to a non-Ohmic toroidal current, called the bootstrap current[60, 20]. The asymmetry comes from the fact that the inner and outer sides of a banana orbit are traveling in different directions, so a density gradient will exert a torque on the plasma.

$$j_{\mathrm{BS}} = -\left(\frac{r}{R}\right)^{1/2} \frac{1}{B_\theta} \frac{\partial p}{\partial r} \tag{3.50}$$

The bootstrap current had gathered a lot of attention as a possible source of current in a steady-state advanced tokamak. However, the bootstrap current becomes small as the plasma reaches thermonuclear temperatures, so it appears that external sources of momentum such as neutral beams and electromagnetic current drives will be needed.

3.3.1 NCLASS code

The NCLASS code[85] is a multi-species neoclassical transport code, written in FORTRAN, which solves the momentum and heat flux balance equations (1st and 3rd velocity moments of the Fokker-Planck equation) in a simplified equilibrium geometry with elliptical flux surfaces, for an arbitrary number of impurities. It closely follows the techniques in the Hirshman and Sigmar review[80], but with a more advanced numerical calculation of viscosities.

The code takes as input temperature and density profiles for each species and radial derivatives of temperature and density, q profile, and axial magnetic field, and computes as output, for each species, the flux profiles, the D and v coefficients, the friction coefficients, viscosities, parallel and poloidal flows, heat fluxes, thermal diffusivities, and bootstrap current. The fluxes are broken down by contributing term: banana-plateau, Pfirsh-Schlüter, classical, and electrostatic. The code is fast, running a single 1D plasma scenario in less than a second on a modern workstation.

In order to produce the input for the code, the experimental profiles have been averaged over a time interval of about 0.36 seconds and smoothed using a cubic smoothing spline algorithm from [42] which minimizes the second derivative of a fitting spline while keeping the weighted mean squared residuals beneath a given value. The argon density was not measured for these shots and instead was inferred from the value of Z_{eff}, which was obtained from the `z_neo_profile` code mentioned on page 111. Although the CXRS diagnostic

provides a measurement of the the ion temperature, the electron temperature, measured by the Thomson Scattering diagnostic, was used as a proxy for the ion temperature here, because electron temperature measurement has lower noise and can provide a more accurate temperature derivative[6]. Some input for run case 1 is shown in figure 3.5.

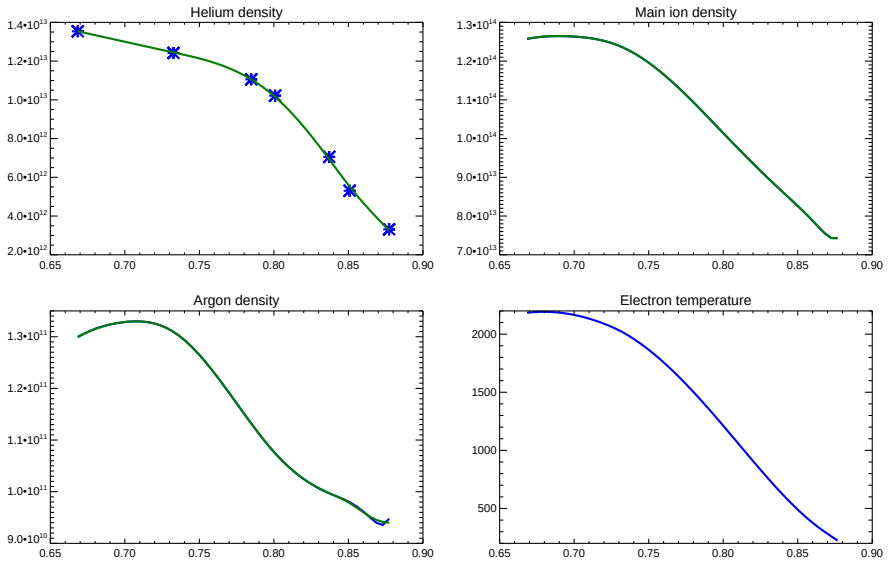

Figure 3.5: Some NCLASS input profiles from shot 1110323006. The data have been smoothed by cubic splines, and unsmoothed data points are shown for the helium density profile. Densities are in cm^{-3} and temperature in keV.

Results are shown for four scenarios. D(^{3}He)(Ar) indicates a D majority, ^{3}He and Ar minority plasma composition. The four scenarios are:

1. D(^{3}He)(Ar) plasma, ICRF-heated L-mode, shot 1110323006

[6]In Alcator C-Mod L-mode plasmas, the electron and ion temperatures are generally collisionally coupled and have the same value.

2. D(^{3}He)(Ar) plasma, ICRF-heated H-mode, shot 1110323026
3. ^{4}He(D)(Ar) plasma, ICRF-heated L-mode, shot 1110323032
4. ^{4}He(D)(Ar) plasma, ICRF-heated H-mode, shot 1110323032

The diffusion and convection coefficients are shown in figure 3.6. The ratio of v/D is compared with the measured density gradient $\frac{1}{n_{He}}\frac{\mathrm{d}n_{He}}{\mathrm{d}r}$ in figure 3.7. We don't actually expect the experimental results to match neoclassical predictions, but for many shot conditions, neoclassical predictions predict a similar peaking factor $-v/D$ to the experimental value. On the other hand, the values for v and D separately don't agree with experiment (section 3.5.3).

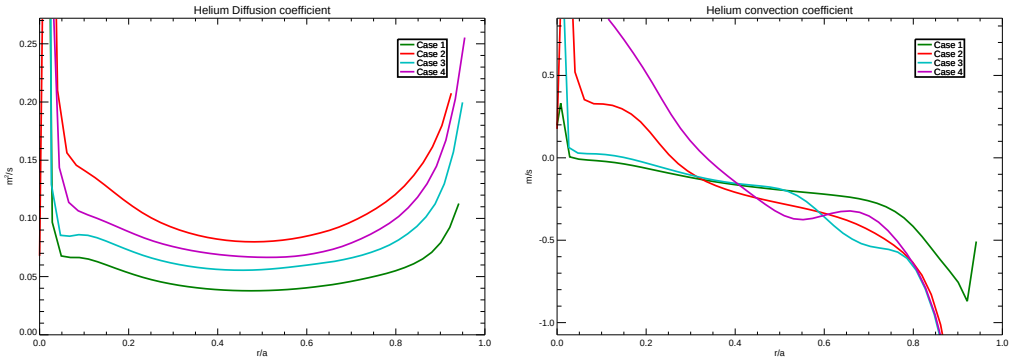

Figure 3.6: Neoclassical diffusion and convection coefficients from NCLASS for test cases

A front-end was developed for running NCLASS over a large set of test cases, drawing input directly from the MDSplus shot database. In figure 3.8, experimental values for L_{nHe}^{-1} are compared to the NCLASS prediction of v_{neo}/D_{neo} for many shots. When looking at a small subset of shots, there appears to be some agreement between L_{nHe}^{-1} and v_{neo}/D_{neo}, but the agreement

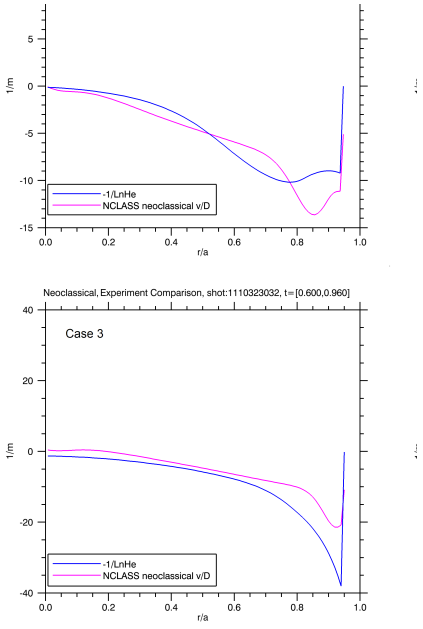

Figure 3.7: Comparison between neoclassical v/D and experimental density gradient

does not hold up when looking at a larger population of shots. The agreement is fairly poor for both species of helium, corroborating the statement that helium transport is not neoclassical.

The neoclassical helium convection velocities are calculated to be in the ballpark of $0.0\,\mathrm{m/s}$ to $-1.0\,\mathrm{m/s}$, and the helium diffusion coefficients are in the ballpark of $0.04\,\mathrm{m^2/s}$ to $0.1\,\mathrm{m^2/s}$. A very rough estimate of helium confinement time can be obtained from the diffusion $\tau_{\mathrm{neo}} \sim a^2/D \sim 1\,\mathrm{s}$. This estimate is considerably longer than what we measure for the helium disappearance time (see figure 3.2), so the helium transport on Alcator C-Mod cannot be governed

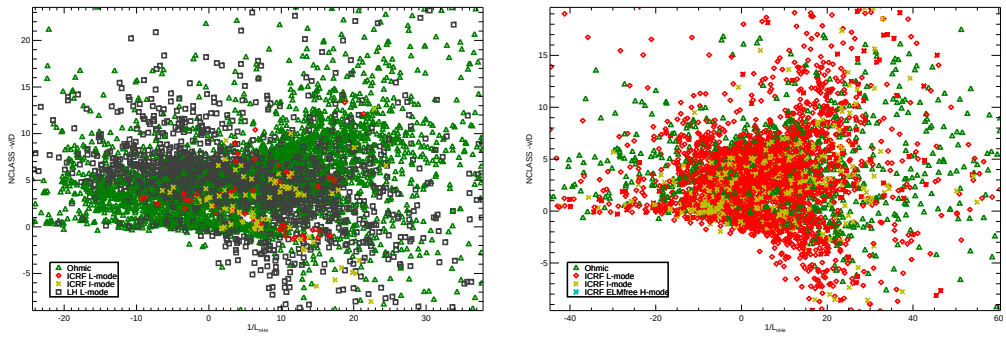

Figure 3.8: Inverse helium density scale length vs NCLASS -v/D over many shots/times, in m^{-1}. *Left*: Helium-4 impurity. *Right*: Helium-3 inpurity.

by neoclassical effects, but rather something faster.

Figure 3.9 shows that that neoclassical diffusivity increases with collision frequency, when viewed across many shot conditions, as expected. The neoclassical convection also increases in magnitude with collision frequency.

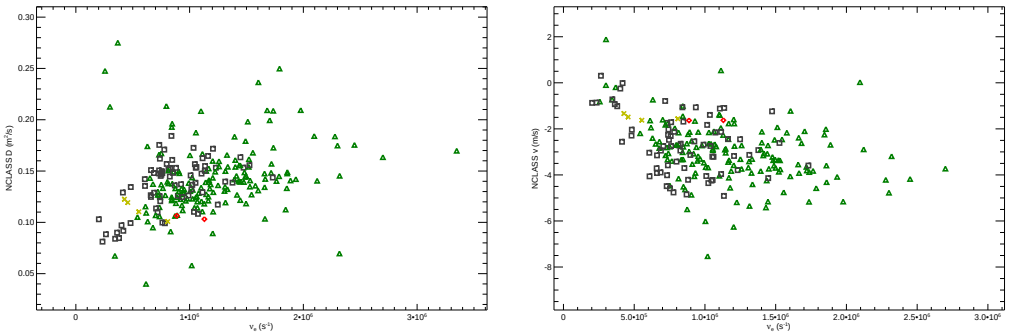

Figure 3.9: NCLASS calculated radial diffusivity versus ν_e from experimental plasma conditions with ^{4}He impurity, at $\rho_{\mathrm{tor}} = 0.6$

Neoclassical theory predicts that impurities are more sharply peaked than the main ion species. If the temperature gradient dependence $\mathcal{K}$ is ne-

glected in equation 3.48, we get $R_0/L_{nHe} \sim 2R_0/L_{ni}$, where the major radius was inserted to obtain a dimensionless value. This relationship is tested in figure 3.10, where the electron density was used as a proxy for the main ion (deuterium) density. Although there is quite a lot of scatter, the overall trend seems to be that the helium-4 is correlated to the electron peaking, with a slope of about 2, as predicted by neoclassical theory.

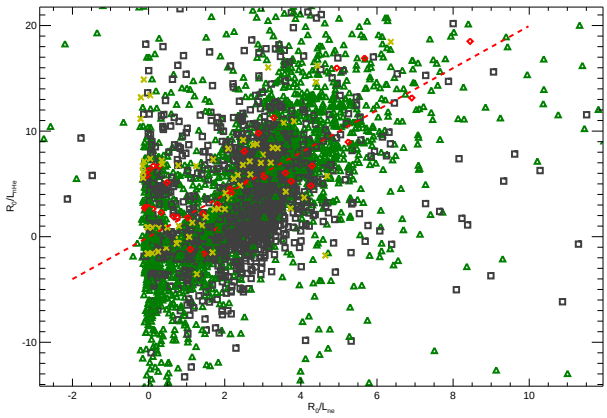

Figure 3.10: Normalized helium-4 inverse scale length vs normalized electron inverse scale length. The red dashed line has a slope of 2, corresponding to a heuristic Z scaling.

3.4 Turbulent transport

The fusion plasma in a tokamak necessarily contains large temperature and density gradients between the hot interior and the cold walls. These gradients act as a source of free energy for a wide variety of linear and nonlinear microinstabilities. These microinstabilities are fluctuations in electromagnetic fields and particle distributions which appear spontaneously. In the case of

linear instabilities, the plasma behavior can be decomposed into a set of unstable modes which grow or shrink in time. In practice, these modes saturate at a low amplitude ($\sim$1 % in the core to $\sim$10 % at the edge) due to nonlinear effects which couple the modes together. The result is a low-level chaotic fluctuation of many of the plasma fields, so the plasma is never truly in a steady state. Electrostatic fluctuations (fluctuations of the electric potential and electric field) cause particles to $\mathbf{E} \times \mathbf{B}$ drift in random directions in the plasma. The net effect of these random motions, known as drift wave turbulence, can give rise to transport.

Tokamak transport is usually dominated by electrostatic turbulence driven transport, which is usually one or two orders of magnitude larger than neoclassical transport except in cases of turbulence suppression or highly collisional plasmas. Fluctuations in the magnetic field can also contribute to transport through magnetic chaos or $\mathbf{E} \times \mathbf{B}$ drift, but these are relatively small at small values of beta[7], since the majority of the magnetic field comes from the magnetic coils which are unaffected by the plasma turbulence.

The net transport flux arising from the drift wave turbulence can be calculated from the correlation between the density fluctuations and the drift velocity fluctuation,

$$\Gamma = \langle \tilde{n}_s \tilde{v}_E \rangle \tag{3.51}$$

This flux is usually expressed as a sum over Fourier modes. The phase differ-

[7]beta is the ratio of plasma pressure to magnetic pressure and is around 1 % in a tokamak

ence between the density and drift fluctuations in the dominant modes determines the direction of the transport.

$$\Gamma = \sum \tilde{n}^*_{s\mathbf{k}} \tilde{v}_{E\mathbf{k}} \tag{3.52}$$

Here, $\tilde{n}_{s\mathbf{k}}$ and $\tilde{v}_{E\mathbf{k}}$ are complex quantities encoding the relative phase of the fluctuations. For an electrostatic fluctuation, the basic fluctuating parameter is the electric potential

$$\Gamma = \sum \tilde{n}^*_{s\mathbf{k}} \frac{\tilde{\mathbf{E}}_{\mathbf{k}} \times \mathbf{B}}{B^2} = \sum \tilde{n}^*_{s\mathbf{k}} \frac{-i\mathbf{k}\tilde{\Phi}_{\mathbf{k}} \times \mathbf{B}}{B^2} \tag{3.53}$$

The shapes of the modes are not trivial because of the curved magnetic geometry. Typically, the Fourier decomposition is not done in Cartesian or cylindrical space but in a field aligned coordinate system. This choice of coordinates is computationally advantageous because the turbulent eddies are much longer in the field parallel direction than the perpendicular direction. But the boundaries of the Fourier decomposition are much more complicated because the field lines do not close on themselves (except for those in a countable number of rational surfaces) and any geometrically possible perturbation must couple many modes. Generally, even computing appropriate eigenmodes for turbulence analysis requires numerical computation.

Direct turbulence measurements in tokamaks is possible using beam emission spectroscopy or phase contrast imaging. BES measurements on TFTR[55] have found that the turbulence spectrum has a peak around $k_\perp \rho_i \approx$ 0.1—0.3. This scale is typically associated with ITG turbulence (see below).

Typical values associated with turbulence in the core are as follows[67]: $\tilde{n}/n \sim 1\,\%$, $k_r\rho_i \sim k_\theta\rho_i \sim$0.1—0.2, $k_\parallel \lesssim 1/qR \ll k_\perp$, and $\omega - \mathbf{k}\cdot\mathbf{v}_E \sim \Delta\omega \sim \omega_*$, where ω_* is the diamagnetic drift frequency and ω and $\mathbf{k}$ are typical frequencies and wavenumbers for the turbulence. At the edge, the fluctuation amplitude $\tilde{n}/n$ may be greater than $10\,\%$. The turbulent eddies are greatly extended in the parallel direction.

Turbulent transport literature identifies four different types of electrostatic instabilities which give rise to turbulence: ion temperature gradient (ITG) modes[8], electron temperature gradient (ETG) modes, trapped ion modes (TIM), and trapped electron modes (TEM). The temperature gradient modes (ITG and ETG) are destabilized by a temperature gradient and bad curvature[9] or negative compressibility. The trapped particle modes (TIM and TEM) are driven by pressure gradients and are associated with the precession of trapped particle orbits or collisions between trapped and passing ions. The dominant turbulent modes in tokamaks seem to be either ITG or TEM, depending on the plasma parameters[10]. Some properties of the classes of instabilities are shown in table 3.1.

Impurity measurements are indispensable tools for the understanding of the turbulent transport. The presence of three or more particle species

[8]also called η_i modes, where $\eta_i \equiv L_{ni}/L_{Ti}$

[9]Bad (or unfavorable) curvature refers to a convex region of higher pressure, so the centrifugal force drives interchange instabilities (figure 3.11). Bad curvature exists on the low field side and good curvature on the high field side of a tokamak.

[10]Actually, the labeling of the modes as ITG or TEM becomes unclear in certain parts of parameter space because they can continuously transform into each other[112].

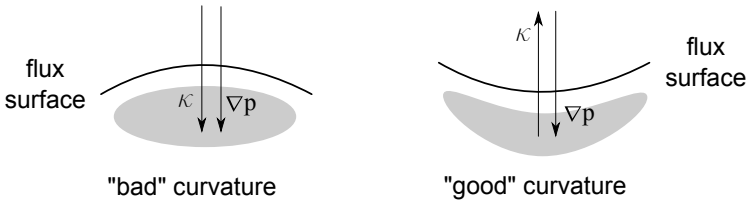

Figure 3.11: Bad and good curvature

Table 3.1: Electrostatic instabilities

classification	free energy	wavelength scale	frequency scale[a]
TIM	n, T_e, T_i	$\sim \rho_\theta$	ω_{*e}
TEM	n, T_e	$\sim \rho_i$	$< \omega_{*e}$
ITG	T_i	$> \rho_i$	$< \omega_{*pi}$
ETG	T_e	$> \rho_e$	$< \omega_{*pe}$

[a] $\omega_{*e} = k_\theta \rho_s c_s / L_{ne}$ is the electron diamagnetic drift frequency defined with the density gradient scale length. $\omega_{*pe} = k_\theta \rho_s c_s / (L_{ne} + L_{Te})$ is the electron diamagnetic drift frequency defined with the pressure gradient scale length.

means that the quasineutrality constraint no longer fully locks the electron and ion density profiles. The shape of the impurity profile provides a wealth of extra information. In addition, impurities can be injected in controlled time intervals to directly watch the transport unfold.

For trace amounts of impurities, the impurities can be treated as tracer particles which respond to the electromagnetic field, but do not significantly alter the field by their presence. On the other hand, if the impurities are a substantial fraction of the the ion population, the dynamics of the system are more complicated. For example, accumulation of impurities at the edge can destabilize the ITG.[35, 177].

3.4.1 Transport dependencies on plasma parameters

The quasilinear flux resulting from gyrokinetic theory can be written as[45, 63, 30]

$$\Gamma_Z^{\mathrm{QL}} = D^{\mathrm{QL}} \left[-\frac{\partial n_Z}{\partial r} + C_c(\hat{s})\frac{2}{R} n_Z + C_{\nabla T}(\omega)\frac{1}{T}\frac{\partial T}{\partial r} n_Z + C_{\parallel}(\omega_{\parallel}) n_Z + C_u(u)\frac{\partial u_s}{\partial r} n_Z \right] \tag{3.54}$$

where the term proportional to $\frac{\partial n_Z}{\partial r}$ is the turbulent diffusion, $C_c(s)$ is the curvature pinch coefficient, $C_{\nabla T}(\omega)$ is the thermodiffusion pinch coefficient, $C_{\parallel}(\omega_{\parallel})$ is the parallel compression pinch coefficient, and C_u is the rotodiffusion pinch coefficient.

The curvature pinch[95, 195, 64] is proportional to $\frac{1}{4} + \frac{2}{3}\langle \hat{s} \rangle \sim \frac{\nabla q}{q}$. It depends only on magnetic geometry and is species independent. In a toroidal system with monotonically increasing q, the curvature pinch is often the most important pinch, giving rise to a density profile which is peaked in the core.

The curvature pinch can be understood in terms of the simpler turbulent equipartition (TEP) model[195, 95], on the basis that the adiabatic invariant J is approximately conserved, which is satisfied when the collision frequency is lower than the transit frequency. In this model, the underlying mechanics of the drift waves is not analyzed, but the turbulence is assumed to relax the plasma toward a state of equipartition, which means an equal distribution of density across ψ space. In the large aspect ratio limit, this means a relaxation to $n(\psi)q(\psi) = \text{const}$. The advantage of the TEP model is that it predicts an equilibrium profile (in the limit that the temperature gradient can

be neglected) which can be easily compared to experiment.

The thermodiffusion pinch[36, 69, 45] has a $1/Z$ species scaling. It can be understood in the following way: consider a positive temperature perturbation on the low field side of the tokamak. Since the drift velocity scales with temperature, the temperature perturbation will induce an ion density perturbation which will induce a $\mathbf{E} \times \mathbf{B}$ drift that convects hotter plasma into the hotter region, causing the instability to grow. Because of the charge dependence, it has an oppositely directed flux for electrons and ions/impurities. For impurities, it is inward for TEM and ETG dominated turbulence and outward for ITG dominated turbulence[3].

The parallel compression term[69, 45] is proportional to Z/A. It can in principle be used to separate the helium isotopes, but it is a very small effect and often neglected in quasilinear expansion. Larger effects can be seen by unrealistically setting $Z/A = 10$ in simulation[45]. In linear analysis, it produces a flux in the opposite direction of the thermodiffusion pinch.

The rotodiffusion term[28, 30] is proportional to A/Z and therefore should have some isotope dependence. It produces an outward flux for the ITG case and inward for the TEM case.

Figure 3.12 shows a comparison of 27 CXRS measured profiles with TEP predictions. The deviations (visible as an upward trend between $0.5 < \rho_{\mathrm{tor}} < 1$) appear to be in a direction consistent with ITG dominant thermodiffusion, which generates an outward impurity flux. The logarithmic temper-

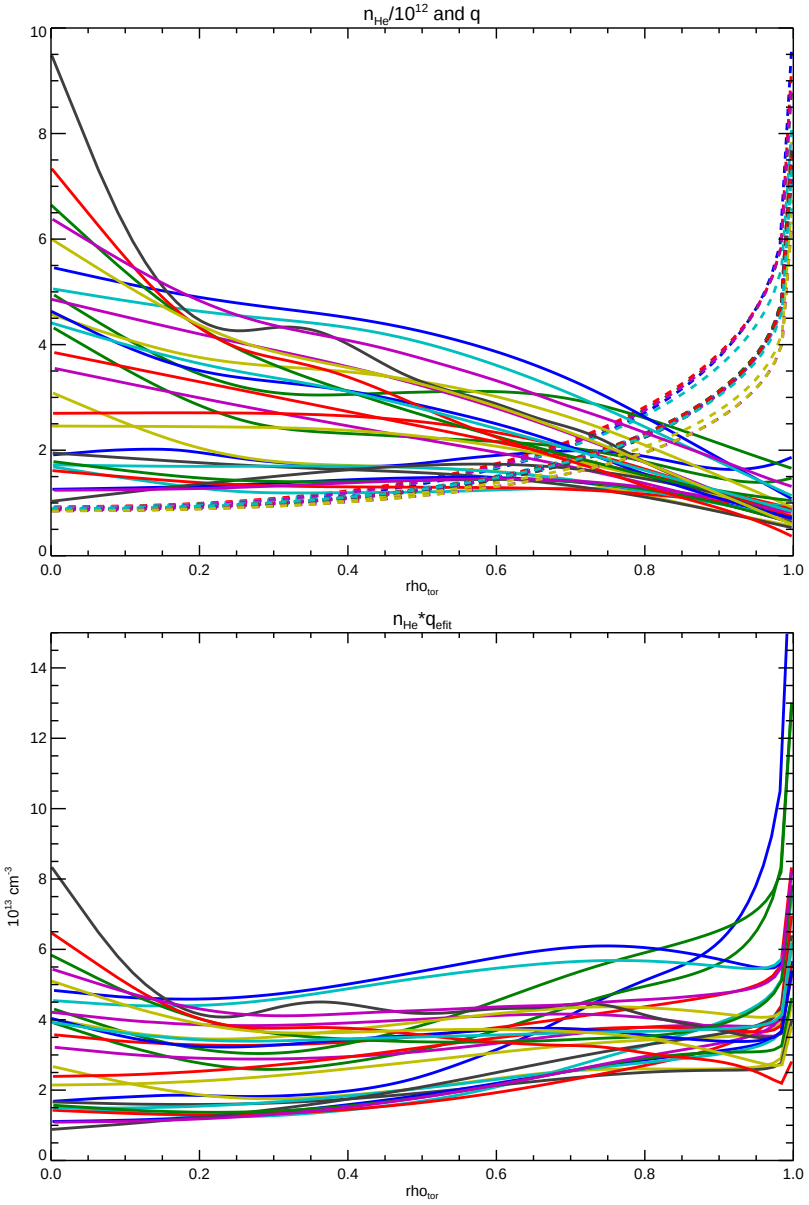

Figure 3.12: Comparison of CXRS helium density profiles and large aspect ratio turbulent equipartition model for 27 shots. Top: density profiles are solid, q profiles (from EFIT are dashed). Bottom: $n_{\mathrm{He}}q$.

ature gradient is larger in the outer annulus of the plasma than the core, so the deviation is greater in this region.

3.4.2 Gyrokinetic equation

The gyrokinetic equation is a guiding center transport equation which is applicable to the study of plasma instabilities. The species populations f_s are written as functions of the gyro-center $\mathbf{X}$, the magnetic moment μ, and the energy U. The dependence on the gyro-phase has been averaged over, reducing the number of phase space dimensions to 5. The gyrokinetic equation separates the electromagnetic field into two parts: a stationary equilibrium field that is slowly varying in space, and a time-varying field associated with an instability which is allowed to vary in space at the gyroradius scale. This time-varying field represents some perturbation or instability in the plasma, and is assumed to be small compared to the equilibrium fields.

The equilibrium quantities are labeled with the subscript 0, and the perturbed quantities with the subscript 1. The scale orderings for gyrokinetics are summarized below.[73]

$$\frac{\rho}{L} \equiv \delta \ll 1$$

$$\nabla Y_1 \sim \frac{Y_1}{\rho} \qquad\qquad \nabla Y_0 \sim \frac{Y_0}{L}$$

$$\frac{Y_1}{Y_0} \sim \Delta \ll 1$$

where Y stands for an arbitrary field or distribution function.

The most common form of the gyrokinetic equation is[73]

$$\frac{\partial \bar{f}_1}{\partial t} + \mathbf{V}_0 \cdot \frac{\partial \bar{f}_1}{\partial \mathbf{X}} + C\bar{f}_1 = i\omega q_s \left[J_0(k_\perp \rho) \left(\Phi_A - \frac{u}{c} A_{\|A} \right) + \frac{s}{ck_\perp} J_1(k_\perp \rho) B_{\|A} \right] \cdot \left[\frac{\partial f_0}{\partial U} + \frac{c}{q_s B_0} \mathbf{k} \times \mathbf{b} \cdot \nabla f_0 \right] \tag{3.55}$$

where $\bar{f}_1$ is the gyro-phase independent part of the perturbed distribution function. $\mathbf{V}_0$ is the guiding center parallel velocity and perpendicular drift, given by

$$\mathbf{V}_0 = \mathbf{u} + \mathbf{v}_{E0} + \mathbf{v} \times (\mathbf{v} \cdot \nabla)(\mathbf{b})\,\Omega + \rho \frac{(\mathbf{v} \cdot \nabla) B_0}{B_0} \tag{3.56}$$

C is a linearized collision operator[11]

The derivation of the gyrokinetic equation starts from a kinetic equation, which is a transport equation in phase space.

$$\frac{\partial f}{\partial t} + \frac{\mathrm{d}\mathbf{X}}{\mathrm{d}t} \cdot \frac{\partial f}{\partial \mathbf{X}} + \frac{\mathrm{d}\mu}{\mathrm{d}t} \frac{\partial f}{\partial \mu} + \frac{\mathrm{d}U}{\mathrm{d}t} \frac{\partial f}{\partial U} + \frac{\mathrm{d}\gamma}{\mathrm{d}t} \frac{\partial f}{\partial \gamma} = C \tag{3.57}$$

Here, γ is the gyro-phase, which hasn't been averaged over yet. Following the derivation of [73], we take gyro-phase averages, and neglect the gyro-phase dependent part of the distribution function. In other words, we make the approximation that

$$\left\langle \frac{\mathrm{d}y^i}{\mathrm{d}t} \frac{\partial f}{\partial y^i} \right\rangle \approx \left\langle \frac{\mathrm{d}y^i}{\mathrm{d}t} \right\rangle \frac{\mathrm{d}\bar{f}}{\partial y^i} \tag{3.58}$$

[11] In many applications, the collision operator can be set to 0. Neoclassical theory already accounts for collisions in the equilibrium distribution, and the perturbation is small compared to the equilibrium distribution, so the electrostatic effects are dominant

for a generic parameter y^i. This is valid as long as f_0 is not strongly anisotropic. Then 3.57 becomes

$$\frac{\partial \bar{f}}{\partial t} + \langle V_0 + V_1 \rangle \cdot \frac{\partial \bar{f}}{\partial \mathbf{X}} + \left\langle \frac{\mathrm{d}\mu}{\mathrm{d}t} \right\rangle \frac{\partial \bar{f}}{\partial \mu} + \left\langle \frac{\mathrm{d}U}{\mathrm{d}t} \right\rangle \frac{\partial \bar{f}}{\partial U} = \langle C \rangle \tag{3.59}$$

The distribution function is split into equilibrium and perturbed parts $\bar{f} = f_0 + f_1$, and lower order terms are dropped. Then the equation is reorganized into

$$\frac{\partial f_1}{\partial t} + \langle \mathbf{V}_0 \rangle \cdot \frac{\partial f_1}{\partial \mathbf{X}} = - \langle \mathbf{V}_1 \rangle \cdot \frac{\partial f_0}{\partial \mathbf{X}} - \left\langle \frac{\partial U}{\partial t} \right\rangle \frac{\partial f_0}{\partial U} \tag{3.60}$$

The gyroaverages $\langle \mathbf{V}_1 \rangle$ and $\left\langle \frac{\partial U}{\partial t} \right\rangle$ are tricky because they involve gyro-averaged perturbed fields.

$$\langle \mathbf{V}_1 \rangle = \frac{c}{B_0} \langle \mathbf{E}_1 \rangle \times \mathbf{b} + \frac{u}{B_0} \langle \mathbf{B}_{1\perp} \rangle - \frac{1}{B_0} \left\langle B_{1\parallel} \mathbf{v}_\perp \right\rangle \tag{3.61}$$

$$\left\langle \frac{\mathrm{d}U}{\mathrm{d}t} \right\rangle = q_s \left[\left\langle \frac{\partial \Phi_1}{\partial t} \right\rangle - \frac{1}{c} \left\langle \mathbf{v} \cdot \frac{\partial \mathbf{A}_1}{\partial t} \right\rangle \right] \tag{3.62}$$

The gyro-averaged fields have a non-local dependence on the electromagnetic fluctuation, and cannot in general be expressed in closed form. A common simplification called the "eikonal approximation" is to assume that the fluctuation has a sinusoidal form near every guiding center point $\mathbf{X}$

$$Y_1(\mathbf{x}) = Y_A^*(\mathbf{X}) e^{i\mathbf{k}_\perp \cdot \mathbf{x}} \tag{3.63}$$

where Y_A^* and $\mathbf{k}_\perp$ vary slowly in space. If Y_A^* and $\mathbf{k}_\perp$ do not vary in space, then the eikonal approximation is essentially the same as choosing a Fourier mode.

With this choice of fluctuation structure, the integrations over sinusoidal fields produce Bessel functions. Finally, we get

$$\langle \mathbf{V}_1 \rangle = i\frac{c}{B_0} J_0(k_\perp \rho) \left(\Phi_A - \frac{u}{c} A_{\|A} \right) \mathbf{k}_\perp \times \mathbf{b} \tag{3.64}$$

$$\left\langle \frac{\mathrm{d}U}{\mathrm{d}t} \right\rangle = -i\omega e \left[J_0(k_\perp \rho) \left(\Phi_A - \frac{u}{c} A_{\|A} \right) + J_1(k_\perp \rho) \frac{s}{c k_\perp} B\| \; A \right] \tag{3.65}$$

3.5 Experimental characterization of helium transport

3.5.1 Profile shapes

In L-mode, the electron and main ion densities are monotonically decreasing from the core to the edge. In the D and v framework, there must be a nearly universal inward pinch on the electrons and ions to support such a density gradient. However, in H-mode, the electron density profile is nearly flat in the core, with a sharp decrease at the edge, in a region known as the pedestal. On the other hand, for light impurities helium and boron, flat, hollow, and peaked profiles have been observed. The turbulent pinch for impurities may be inward or outward, depending on plasma parameters.

The shape of the impurity profile shows a lot more variation than seen in the electron density. See figure 3.13. Since the impurity is a relatively small fraction of the total ion population, the impurity profile shape is not tightly constrained to the electron density by the quasineutrality requirement.

Measurements of velocity component along viewing chord are shown for different confinement modes in figure 3.14, but the uncertainties are too large to observe a velocity dependence on the confinement mode.

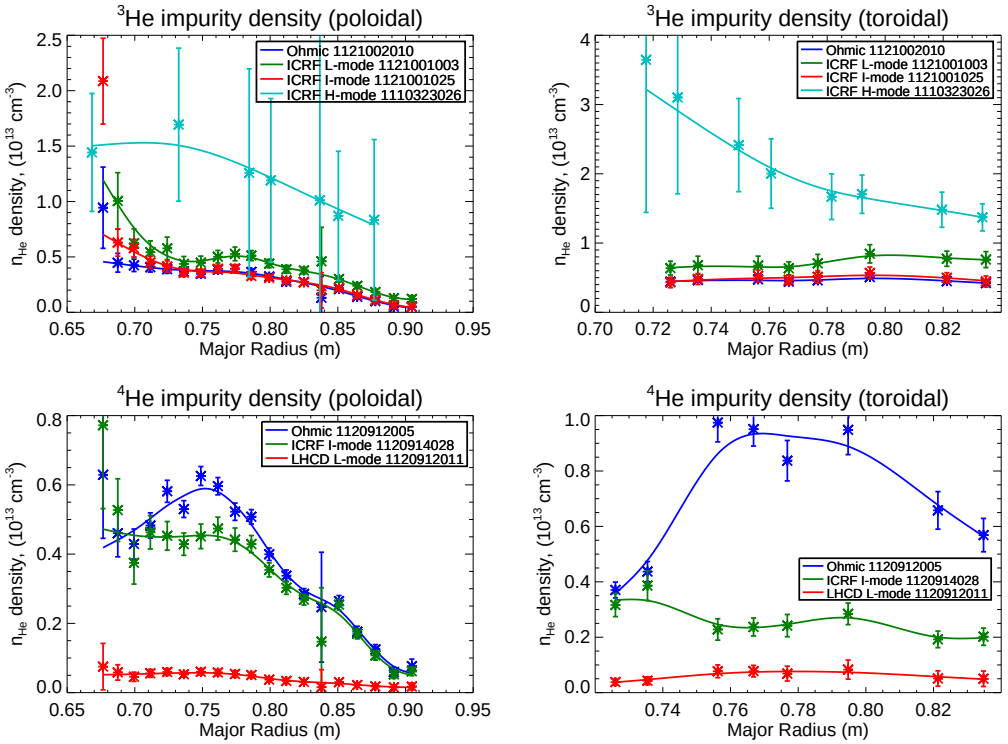

Figure 3.13: Helium density profiles measured in a variety of confinement modes

The temperature measurements are generally monotonically decreasing from the center (figure 3.15), due to central heating. The impurity temperature is usually very similar to the electron temperature, but can show some significant differences during electron or ion heating.

3.5.2 Parameter sensitivities

Several Alcator C-Mod experiments have been conducted in which certain plasma parameters have been varied while other parameters have been

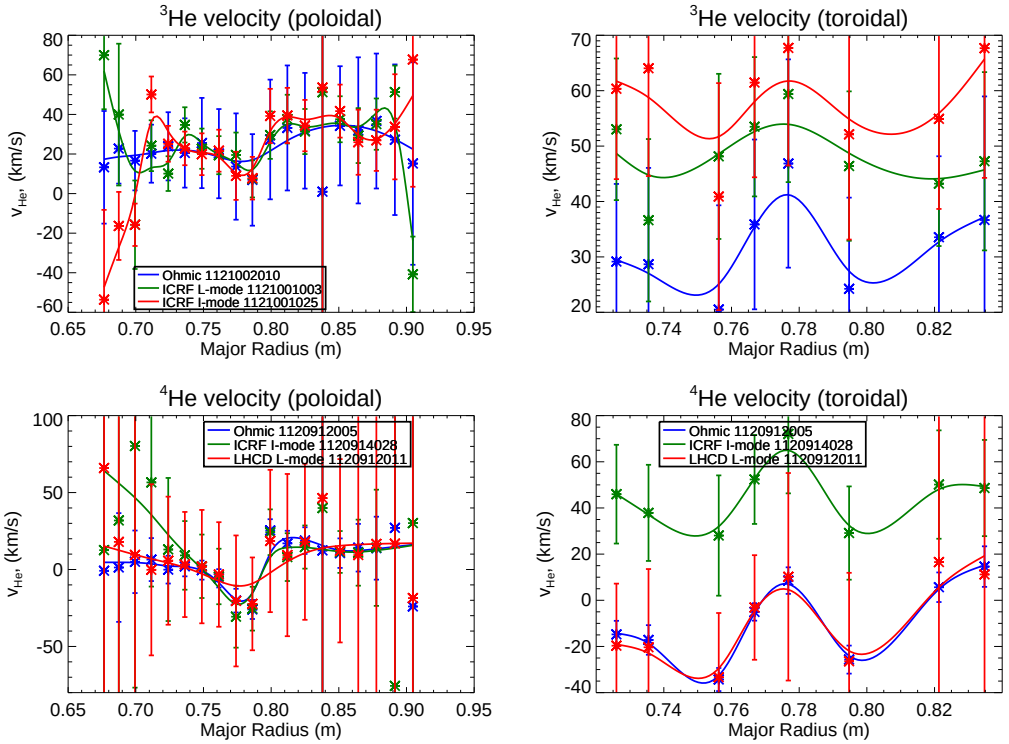

Figure 3.14: Helium velocity profiles measured in a variety of confinement modes

kept fixed (to the extent possible). If it can be assumed that the other plasma parameters have not changed and the transport varies smoothly with the parameter, the impurity measurements can be used to obtain various kinds of transport coefficients.

The curvature pinch plays a dominant role in impurity transport, so we expect a large sensitivity of the transport to the magnetic shear $\langle \hat{s} \rangle$. The q profile is related to the plasma current by[111, p. 121]

$$q(r) = \frac{2\pi r^2 B_\phi}{\mu_0 I(r) R} \tag{3.66}$$

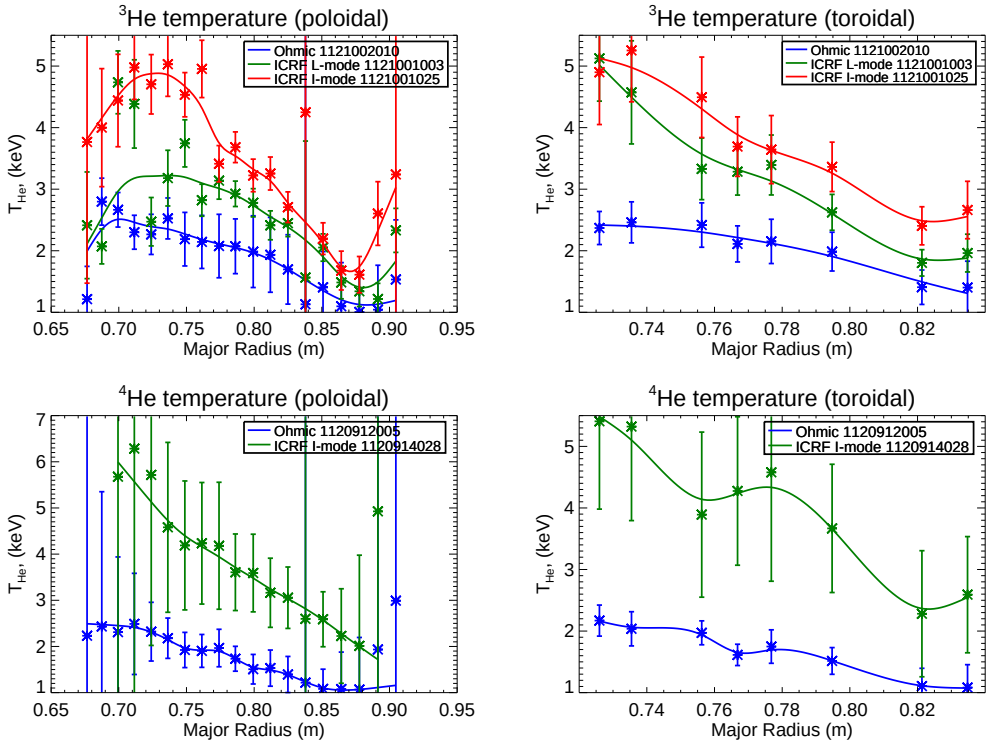

Figure 3.15: Helium temperature profiles measured in a variety of confinement modes

where

$$I(r) = 2\pi \int_0^r j(r')r' \, \mathrm{d}r' \tag{3.67}$$

is the current inside r. Therefore,

$$\hat{s}(r) = \frac{\nabla q}{q} = \frac{2}{r} - \frac{2\pi j(r)}{I(r)} \tag{3.68}$$

The magnetic shear can be varied by changing the total plasma current (which can be manipulated by the main transformer). Unfortunately, increasing the plasma current also increases the Ohmic heating of the plasma, so the effect of curvature pinch cannot be fully isolated.

Profiles across some values of plasma current are shown for both helium-3 and helium-4 in figure 3.16. As the current is increased, the helium profile becomes more peaked in the core, consistent with an increased inward curvature pinch. In addition, more helium is being taken into the plasma at higher plasma current. This could be due to a higher inward pinch at the edge or due to increased ionization.

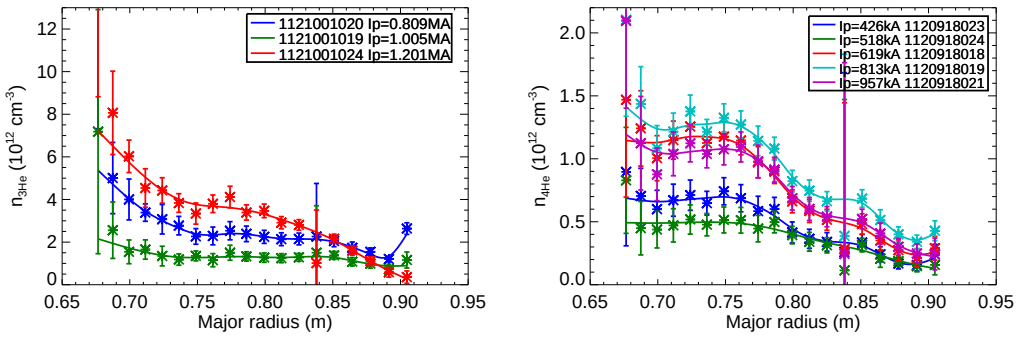

Figure 3.16: Left: ^{3}He profiles for 3 different values of plasma current. Right: ^{4}He profiles for 4 different values of plasma current.

The shear for the helium-4 case is shown in figure 3.17. The shear globally decreases with total plasma current.

The curvature pinch coefficient C_c can be estimated by taking the slope of $L_{n_{\mathrm{He}}}$ versus $\frac{2\hat{s}}{R}$, with data taken from points with different plasma current. For ^{4}He, the process gives an estimate of $C_c \approx -0.14\hat{s}$, at radius of $\rho_{\mathrm{tor}} = 0.5$. This is shown in 3.17. However, the deviation from the linear model suggests a large uncertainty in the fit.

The helium density was measured for three values of magnetic field

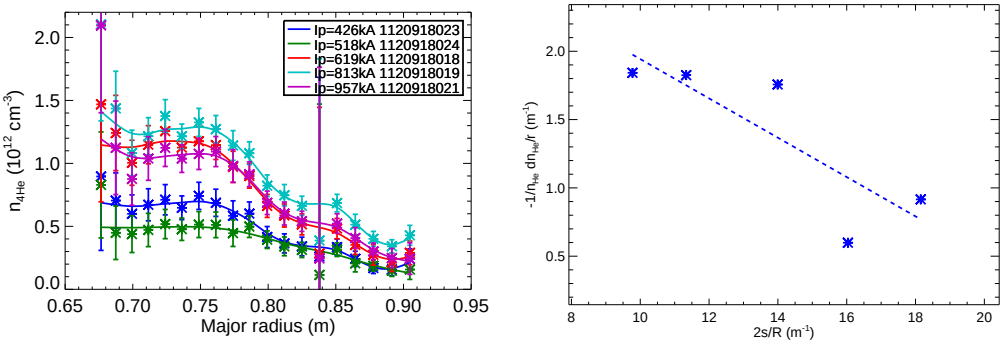

Figure 3.17: Left: ^{4}He profiles for four different values of plasma current, estimated from equilibrium fit code EFIT. Right: Helium density scale length versus $2\hat{s}/R$ for $\rho_{\rm tor} = 0.5$

(figure 3.18). However, the scan range was too small to have a clear effect on $\hat{s}$, and the effect on the helium density too small to verify within the errors of the experiment.

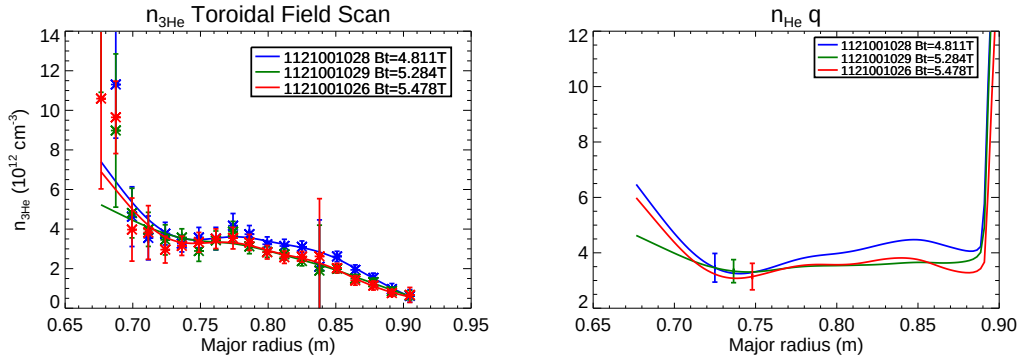

Figure 3.18: Left: ^{3}He profiles for 3 different values of toroidal field. Right: $n_{\rm 3He}q$ for these shots

Helium-3 and helium-4 density profiles were measured over a limited range of electron densities (figure 3.19 while fixing most other parameters.

Line-averaged electron densities are measured by the two color interferometry (TCI) diagnostic. Collisionality ν_* increases with electron density, and $\nu_* \gtrsim 1$ will stabilize the TEM instability. No clear dependence was visible within the errors of the experiment.

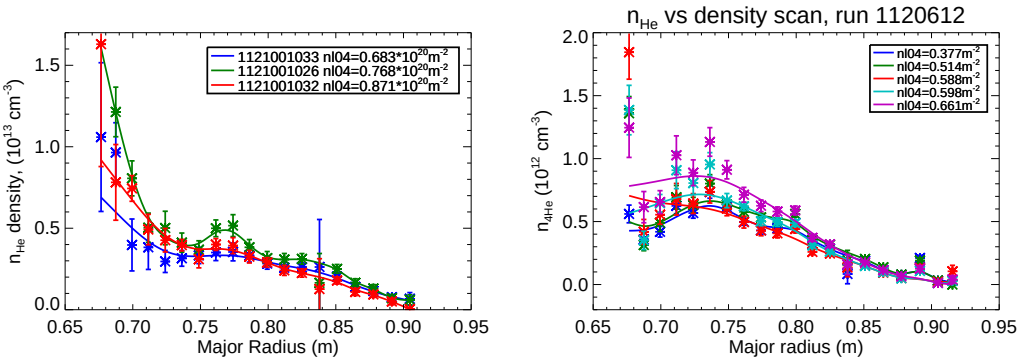

Figure 3.19: Left: ^{3}He profiles for 3 different values of electron density. Right: ^{4}He profiles for 5 different values of electron density. nl04 is the midplane TCI channel.

Helium densities have been measured in the background of several lower hybrid (LH) heating experiments. There is no observed dependence of helium-4 density profile on LH power or phase (figure 3.20). LH has been used for current drive experiments and have some subtle effects on q.

Several helium experiments with ICRF heating have also been done. These will be the focus of chapter 4.

3.5.3 D and v measurements with short puff experiment

While valuable information can be obtained from the equilibrium impurity density profiles, they are not sufficient for determining the particle flux

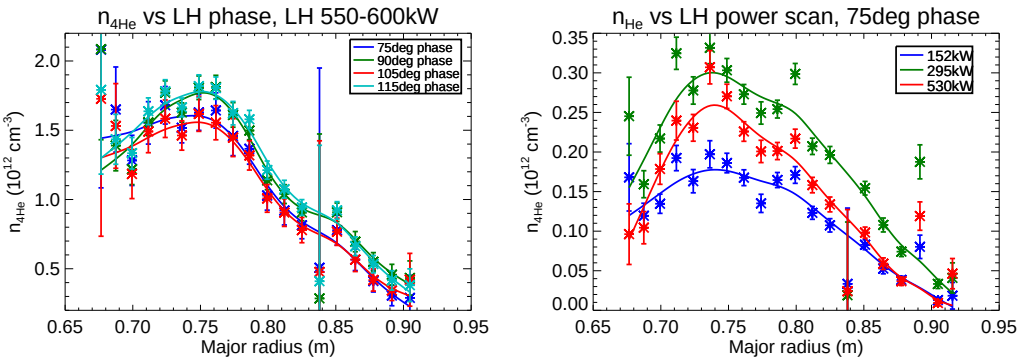

Figure 3.20: Left: ^{4}He profiles taken during LH heating with different phases, showing good reproducibility. Right: ^{4}He profiles at different LH input power.

and for determining the D and v transport coefficients independently. In order to measure these quantities, it is necessary to follow the time dependence of the impurity density profile when the impurity is introduced. This can be achieved by puffing helium at the edge and taking high speed measurements.

Combining 3.10 and 3.13 and dropping the notational brackets, we get the flux averaged transport equation,

$$\frac{\partial n_Z}{\partial t} = \frac{1}{r}\frac{\partial}{\partial r} r \left(D(r,\xi)\frac{\partial n_Z}{\partial r} - v(r,\xi) n_Z \right) + Q_Z \tag{3.69}$$

The source Q_Z for He^{2+} is zero except at the edge, where He^{2+} is formed from ionization of He^{+}. In general, the transport coefficients change when impurity is introduced[65], due to changes to the plasma temperatures, densities, and corresponding gradients. If D and v are allowed to vary in time, then the equation is underconstrained, with $N_r N_t$ equations and $2N_r N_t$ unknowns. A usual simplification is to assume that the impurity puff is nonperturbative and the impurity is passively transported by the background plasma, so that the

transport coefficients is constant in time. Then there are $2N_r$ unknowns which can be solved for using a best fit. This assumption is only valid for a trace level of impurity. Simulations suggest that this trace assumption is reasonable for this case (see section 3.6.3.

The measurement puts some difficult constraints on the required time resolution, since the time resolution must be high enough to capture changes on the transport time scale. Experimental measurements of helium transport on other machines (see table 3.2) put the diffusion coefficient at around $1\,\mathrm{m}^2/\mathrm{s}$. For C-Mod, $a \approx 0.22\,\mathrm{m}$, which establishes a rough transport time scale of 50 ms. In the CXRS measurement, the time resolution is limited by the beam modulation interval, which is limited to periods of about 80 ms or higher (see 2.6). Therefore, special tricks, described below, are needed to obtain measurements at a higher time resolution of 10 ms.

The idea of the experiment is to obtain a steady state discharge (flat top) and puff a small amount of helium into the plasma over a short duration. Neutral helium is introduced at the edge through a tube controlled by a piezoelectric valve, and the helium is ionized and drawn into the plasma at the edge. A layer of singly ionized helium forms at the edge and acts as a source for the fully ionized helium which is present in the core (see figure 3.21). The edge density provides the necessary information about the helium recycling from the walls. The measurement of He^+ is described in section 3.5.3.2. The helium plasma fraction is kept $\lesssim 1\,\%$ in order to minimize the time variation of D and v. The experiment was conducted for a set of Ohmic heated L-mode

plasma discharges.

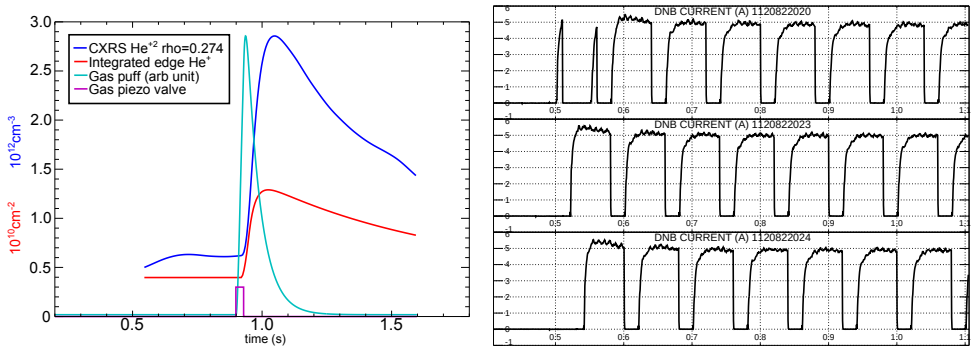

Figure 3.21: Left: Plot of the time evolution of core He^{2+} density, edge He^{+} density, edge He puffing, after opening the piezo valve. Vertical scale for gas puff is arbitrary. Right: Plot of staggered beam timings for three shots

To increase the time resolution of the measurement, we repeated the shot discharge conditions several times, temporally displacing the neutral beam pulses so that data points can be taken at intervening points. Care was taken to ensure that the repeated shots had identical plasma parameters. Scope traces for these shots are shown in figure 3.22. By combining data points from three shots, the time resolution was increased to about 10 ms. Figure 3.23 shows the frame data from three shots overlaid, with the timing of the puff synchronized between shots. Some scaling was necessary to get the intensities of the three shots to line up.

The background subtraction is done differently for this experiment compared to a steady state discharge. In a steady state discharge, background frames are chosen before and after each beam pulse. However, in this scenario, the background and foreground signals are evolving quickly during a

beam pulse. For each channel, a smooth curve was fit through the intensities of the background frames, so the background for each time point could be interpolated using data from all three shots. The density is proportional to the difference between the combined foreground frames and background frames.

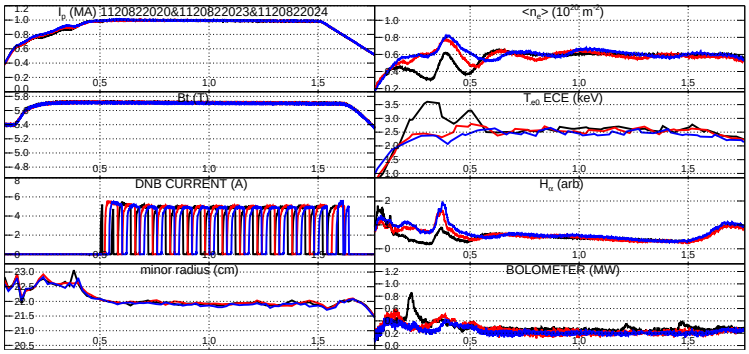

Figure 3.22: Scope traces for "identical" shots 1120822020, 1120822022, 1120822023.

Table 3.2: Helium transport coefficients in different machines

Machine	Mode	Ref	He pumping	D m^2/s	C_v [a]
TFTR	L	[172, 77]	no	10.0	[1]
JT-60	L	[139, 77]	no	1.0	1.0–1.5
PDX	ohmic	[56, 77]	no	2.1	0.80
TEXTOR	L	[76, 77]	no	1.0	1.50
TEXTOR	L	[76, 77]	yes	1.0	0.65
TEXTOR	L	[77]	yes	1.0	0.80
TEXTOR	H	[77]	yes	1.0	1.15
DIII-D	L	[77]	no	1.0	0.95
DIII-D	L	[77]	no	1.0	0.95
C-Mod	L	[120]	no	0.8	1.24

[a] C_v is defined by $vn_e = C_v D \frac{\mathrm{d}n_e}{\mathrm{d}r}$
[1] The pinch velocity is 20 m/s to 30 m/s near the plasma edge

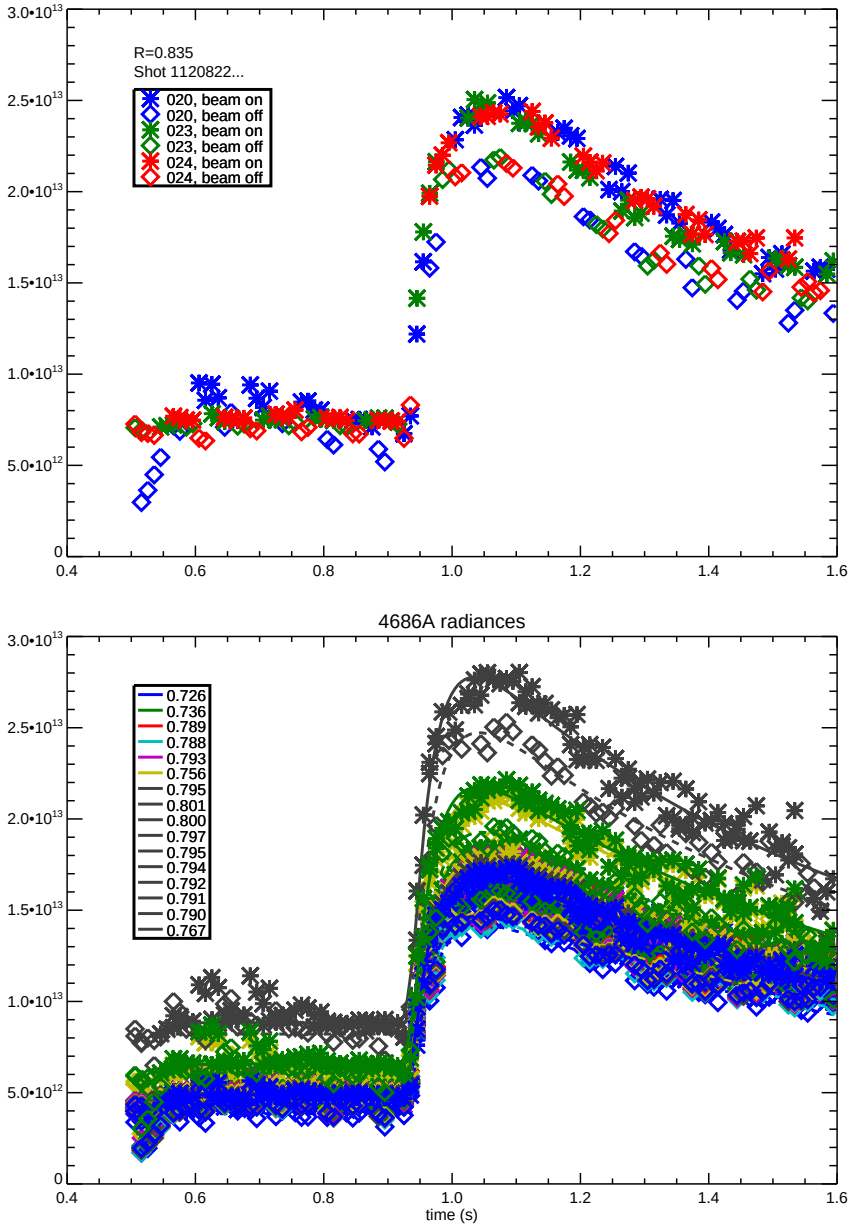

Figure 3.23: Shots 1120822020, 022, 023 combined. Top: a single channel is shown, color coded to show the source shot. Bottom many channels are shown, color coded by channel. In addtion, fits of the beam on and beam off intensity curves are shown.

3.5.3.1 Fitting D and v using STRAHL

Although the transport equation 3.69 is not complicated, it requires proper treatment of the numerical grids to avoid incorrect answers.

STRAHL[10, 46] is a 1D transport code which solves the transport equation as an initial value problem for a numerical flux surface geometry and an arbitrary number of ion species and charge states. It contains a simple model for treating the recycling at the scrape off layer, where a 1D description of the plasma is not adequate. It uses the Crank-Nicolson scheme[37] for integration.

The code takes D and v parameters as the input, and provides the time varying density profiles as the output. Since we wish to solve the inverse problem, it is necessary to run STRAHL iteratively, adjusting the input D and v parameters until the output converges to the measured profiles. For this purpose, I have written a wrapper code which calls STRAHL and solves for best fit D and v coefficients using a process of simulated annealing. Best fit is defined as minimization of the squared residuals between measured densities and predicted densities (scaled to remove the residuals in the averages). More specifically, the goodness of fit (to be minimized) is

$$G\big[D(r), v(r)\big] = \sum_{i}^{N_r} \sum_{j}^{N_t} \left(n_{\text{meas}}(r_i, t_j) - \frac{\langle n_{\text{meas}} \rangle}{\langle n_{\text{pred}} \rangle} n_{\text{pred}}(r_i, t_j) \right)^2 \tag{3.70}$$

The averages are taken over all r, t. The reason for scaling by the ratio of averages is because the overall scaling of the predicted density profiles depends on scrape off layer and pedestal dynamics (which determine the edge generation

rate) which are not very well known. We measure the edge He^+ population which gives the temporal evolution of the He^{2+} generation rate, but the generation scaling depends too sensitively on edge parameters to be adequately predicted by a collisional-radiative model. Nevertheless, the D and v coefficients in the plasma do not depend on this overall scaling, so the scaling is removed from the goodness of fit.

The wrapper code executes the following steps:

1. Run STRAHL
2. Compute Goodness of Fit
3. Generate a new $D(r)$ and $v(r)$ profile by adding random noise to the best fit found so far ($D(r)$ and $v(r)$ with the lowest G so far)
4. If a lower goodness of fit is found, reduce the size of the random noise

At first, the spatial grid was set to 10 radial points. The initial settings of $D_0 = 0.8\,\mathrm{m}^2/\mathrm{s}, v_0 = -3.2\,\mathrm{m/s}$ were obtained by trial and error. The initial noise scaling was $\Delta D = 0.4\,\mathrm{m}^2/\mathrm{s}, \Delta v = 1.6\,\mathrm{m/s}$ and this was scaled by 0.94 every time a better match was found. Figure 3.24 shows the evolution of the goodness of fit over 1000 iterations and the final D and v profiles. The CXRS data from shots 1120822020–023 was limited to the range $0.26 \leq \rho_{\mathrm{pol}} \leq 0.82$, so D and v profiles outside this range are invalid.

The code was rerun using a higher resolution (19 point) grid, using the solution to the lower resolution run as a starting point. The initial noise scaling for this run was $\Delta(\log D) = 0.2, \Delta v = 0.4$ and the noise scale was

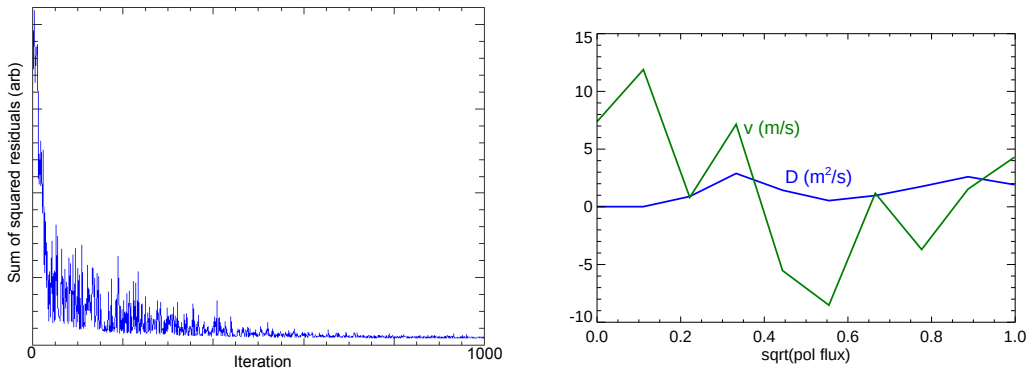

Figure 3.24: Left: Goodness of fit over 1000 iterations. Right: Solution after 1000 iterations.

multiplied by 0.94–0.97 each time a better match was found. Figure 3.25 shows the goodness of fit and solution after 915 iterations. Near iteration 160, I manually increased the randomization to test the effect on the convergence rate, and I reduced it again near iteration 210. Interestingly, it did not have a large effect on the convergence.

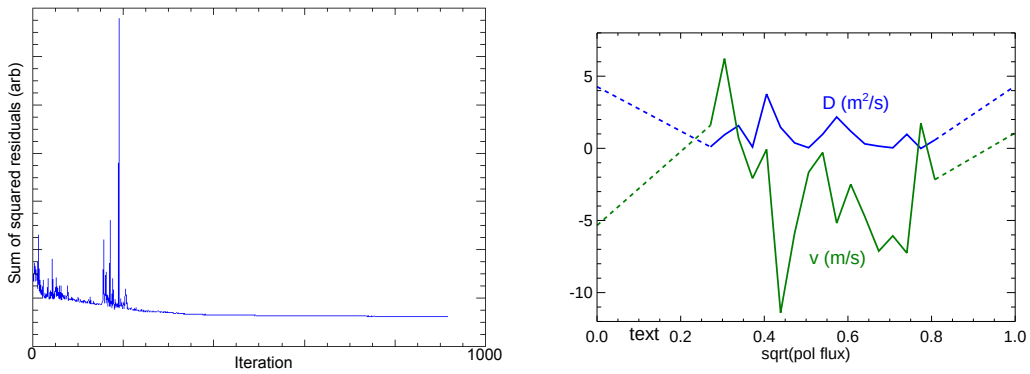

Figure 3.25: Left: Goodness of fit over 915 iterations. Right: Solution after 915 iterations.

Figure 3.26 shows the CXRS measured and best fit STRAHL density profiles after iteration. The temporal characteristics cannot be exactly matched without a time-dependent transport.

The results of STRAHL fitting give a solution with a lot of small scale variation in the transport. This is almost certainly due to overfitting the experimental noise. To account for this, I smoothed the D and v profiles by various amounts and checked how well the STRAHL computed profiles still match the CXRS data. Strong smoothing can be applied to the D and v profiles without a large change in the profiles, due to the integrating nature of the transport. I looked for a high level of smoothing which still gave profiles consistent with the experimental errors in the measured densities. Figure 3.27 shows the results of this smoothing. The D and v profiles were smoothed using an error scaling of $\Delta D = 0.6\,\mathrm{m}^2/\mathrm{s}$ and $\Delta v = 2\,\mathrm{m/s}$.

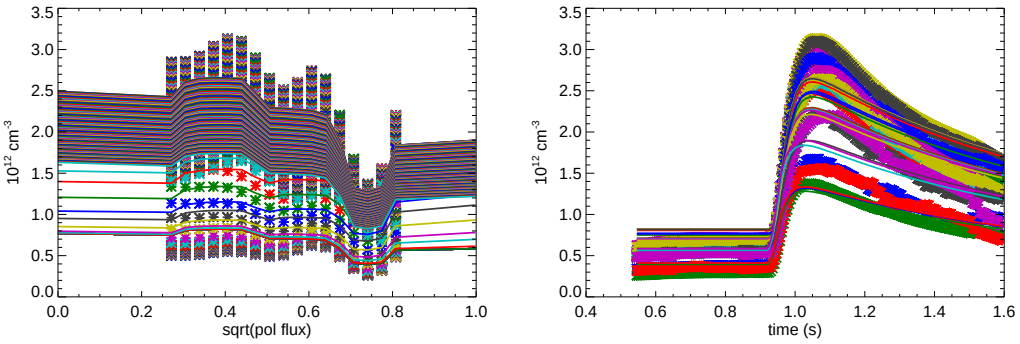

Figure 3.26: STRAHL (lines) and CXRS (asterisks) density profiles. Left: radial domain. Right: temporal domain.

From the results of fitting, we get $D \approx 0.8\,\mathrm{m}^2/\mathrm{s}$ and $v \approx -4.5\,\mathrm{m/s}$,

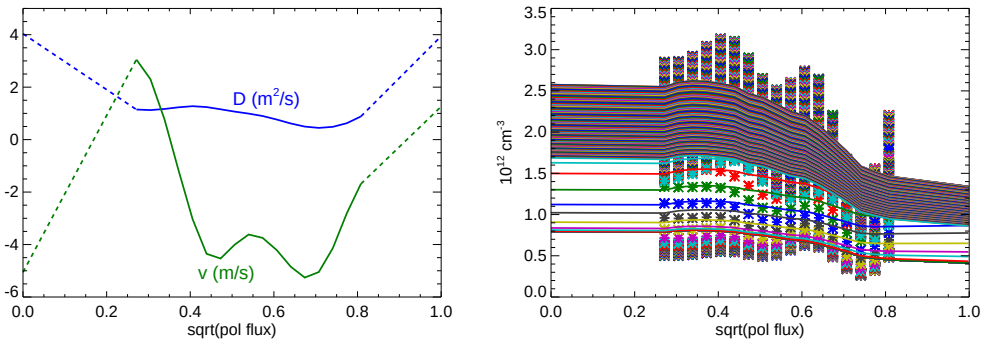

Figure 3.27: Left: Smoothed D and v profiles. Right: Comparison of STRAHL density profiles using smoothed parameters to CXRS measurement.

with v increasing in magnitude toward the edge.

3.5.3.2 Edge Helium II Spectroscopy

The background emission of the CXRS measurement gives a measurement of the He^+ population at the edge of the plasma. This population is generated by passive charge exchange and recombination at the edge, and excited through collisions[12]. Each of the channels of the CXRS system passes through the edge in two positions. For the purpose of this measurement, we assume the edge He^+ density to be flux function, so each channel provides a redundant measure of the edge density. The channel radiances are given by

$$I = \sum_{i \in \{\text{in,out}\}} \sigma_{\text{He}^+} f_{n=4}(T_e, n_e) A_{43} \sec \xi_i \tag{3.71}$$

where σ_{He^+} is the surface helium density at the edge (equal to the density integrated over a path normal to the edge), $f(n = 4)$ is the excitation fraction

[12]Some rough calculations put the width of the emission layer to be about 4 mm

for the $n = 4$ state, and ξ_i is the angle between the viewing chord and the normal to the flux surface at the edge.

$f_{n=4}$ is calculated using a collisional-radiative model, ADAS 205[168]. The excitation fraction is highly sensitive to the electron density and temperature at the edge, which is provided by the Edge Thomson Scattering diagnostic. However, the uncertainties in the edge measurements can easily create errors in $f_{n=4}$ of an order of magnitude or more, so the edge spectroscopy shouldn't be relied on for anything more than a rough measurement of the relative time variation of the He^+ population. For example,

$$f_{n=4}(50\,\mathrm{keV}, 4 \times 10^{13}\,\mathrm{cm}^{-3}) = 1.67 \times 10^{-5}$$
$$f_{n=4}(50\,\mathrm{keV}, 7 \times 10^{12}\,\mathrm{cm}^{-3}) = 3.10 \times 10^{-6}$$
$$f_{n=4}(20\,\mathrm{keV}, 4 \times 10^{13}\,\mathrm{cm}^{-3}) = 5.04 \times 10^{-6}$$

The estimated edge He^+ is obtained by taking a weighted average over each channel. The result can be seen in figure 3.21.

3.5.4 Correlation studies of transport

In a complex tokamak plasma, the transport is governed by nonlinear processes and various plasma parameters are coupled unexpected ways. Therefore, it is not always possible to conduct an experiment in which a parameter is varied in a controlled manner, while fixing other parameters. In addition, lack of dedicated experimental time means that transport studies must include measurement data from a diverse set of experimental conditions, including dif-

ferent confinement regimes. So, it is often necessary to use correlation studies, based on large sets of experimental measurements, to measure turbulent transport sensitivities to plasma parameters. These efforts are guided by turbulent transport theories and in turn guide the theories.

The quasilinear flux equation (3.54) can be separated into D and v components:

$$D = D^{\mathrm{QL}} \tag{3.72}$$

$$v = D^{\mathrm{QL}} \left(C_c(s)\frac{2}{R} + C_{\nabla T}(\omega)\frac{1}{T_Z}\frac{\partial T_Z}{\partial r} + C_{\parallel}(\omega_{\parallel}) + C_u(u)\frac{\partial u}{\partial r} \right) \tag{3.73}$$

The pinch contributions are conveniently written in terms of the diffusion, so the equilibrium inverse scale length is simply

$$-\frac{1}{L_{nZ}} = \frac{v}{D} = C_c(s)\frac{2}{R} + C_{\nabla T}(\omega)\frac{1}{T_Z}\frac{\partial T_Z}{\partial r} + C_{\parallel}(\omega_{\parallel}) + C_u(u)\frac{\partial u}{\partial r} \tag{3.74}$$

An ITG instability exists when $\eta_i \equiv L_{ni}/L_{Ti}$ exceeds a critical value[67]. Kadomtsev and Pogutse[67] give the condition:

$$\eta_i \geq \frac{2}{1 + 2k_\perp^2\rho_i^2\left(1 - \frac{I_1(k_\perp^2\rho_i^2)}{I_0(k_\perp^2\rho_i^2)}\right)} \tag{3.75}$$

where I_0 and I_1 are modified Bessel functions. This function is shown in figure 3.28. It has a minimum of near 0.9 at $k_\perp\rho \sim 1.7$, so modes with wavelength near the ion gyroradius scale are most easily excited by the ion temperature gradient. Horton and Varma[83] provide another criterion $\eta_i \geq 2/3$ based on the maximum work that can be extracted from a Carnot cycle operating across the temperature gradient.

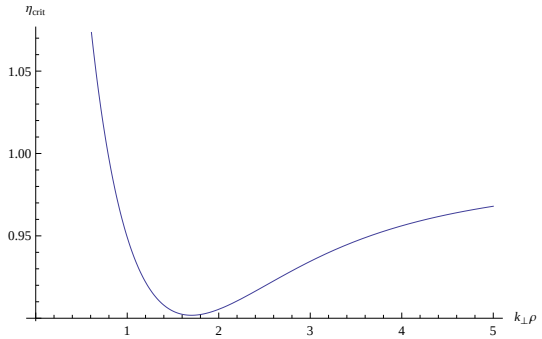

Figure 3.28: ITG η_i threshold

Figure 3.29 shows scatter plots of $1/L_{nZ}$ versus $1/L_{Te}$ for helium-3 and helium-4, across all radii. The electron temperature from the Thomson Scattering diagnostic is used as a proxy for the helium temperature. There is a positive correlation but I suspect that it is due to a correlation with minor radius. Figure 3.30 shows some scatter plots restricted to single radial points. Indeed, in this case, the correlations are negative. For helium-3, the slope inferred pinch coefficients are $C_T = \{-1.2, -1.5, -1.0\}$ for $\rho = \{0.2, 0.5, 0.8\}$. The helium-3 data show more correlation than the helium-4 data because the helium-3 database contains mainly ICRF heated plasmas with many different values of auxiliary heating. The helium-4 database contains a large proportion of Ohmic or lower hybrid heated plasmas, and show a greater diversity in plasma parameters. In other words, the helium-3 database is closer to a controlled experiment, with fewer changes between shots besides the applied power.

Figure 3.31 shows scatter plots of $1/L_{nZ}$ versus rotation shear $\frac{\partial u}{\partial r}$. The data is too scattered to make any conclusion for C_u.

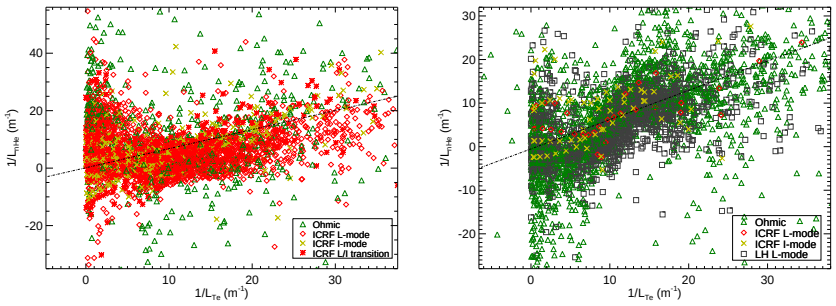

Figure 3.29: Scatter plot of $1/L_{nZ}$ vs $1/L_{TZ}$ for (left) helium-3 and (right) helium-4. Below the dash-dotted lines shows the approximate region for ITG instability based on the η_i criterion.

The Alcator C-Mod measurements have been contributed to a growing database of measurements, spanning many devices. This database is part of an international effort, one of the International Tokamak Physics Activities (ITPA)[13], to study transport and confinement in fusion plasmas.

3.6 GENE gyrokinetic simulations

The Gyrokinetic Electromagnetic Numerical Experiment (GENE) code[110, 109] is a highly parallelized numerical code that obtains linear or nonlinear solutions to the gyrokinetic Vlasov equation. GENE has been developed by a team of people, led by F. Jenko (IPP Garching). The equation is solved as an initial value problem, and the time evolution of a fluctuation is evolved using a fourth-order Runge-Kutta[116] method on a discretized grid. An eigenvalue solver is also present and is invoked as part of the initialization. Usually,

[13] `http://www.iter.org/org/team/fst/itpa/itpacharter`

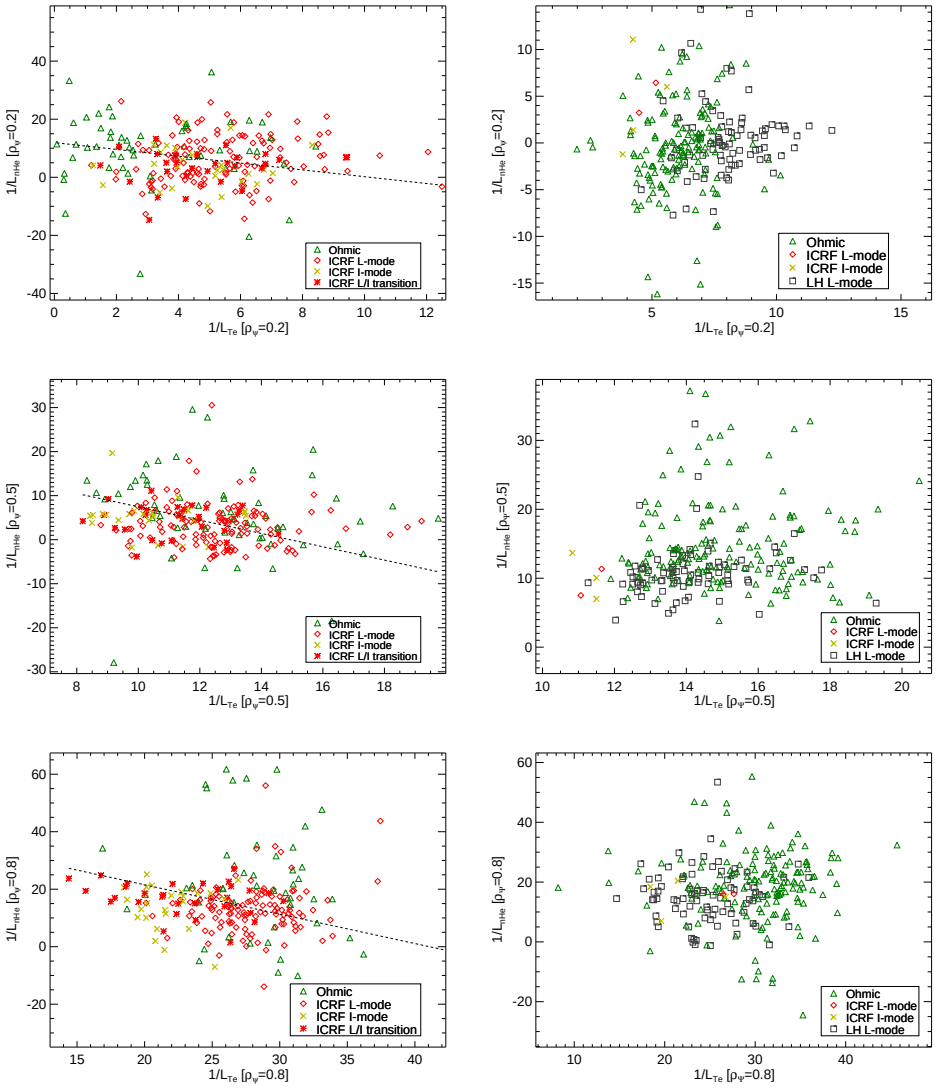

Figure 3.30: Scatter plot of $1/L_{nZ}$ vs $1/L_{Te}$ for (left) helium-3 and (right) helium-4. First row: $\rho_\psi = 0.2$, second row: $\rho_\psi = 0.5$, third row: $\rho_\psi = 0.8$

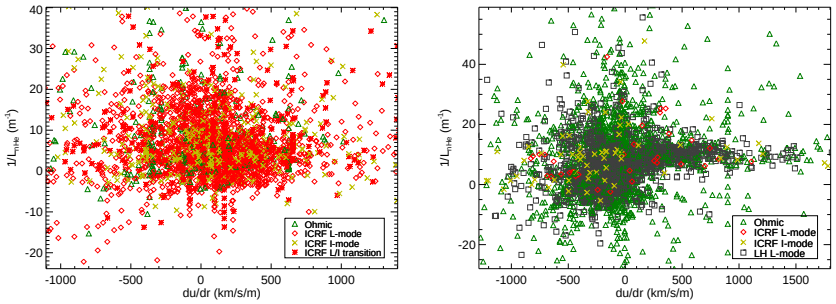

Figure 3.31: Scatter plot of $1/L_{nZ}$ vs $\frac{\mathrm{d}u}{\mathrm{d}r}$ for (left) helium-3 and (right) helium-4.

the grid domain is a flux tube, and the solution only depends on the local plasma parameters in the neighborhood of the tube. GENE can also run a global simulation spanning a large region of the tokamak, at the cost of enormous computation time. The solver itself is written in Fortran 90/95, but the distribution includes a data visualization and analysis tool written in IDL.

The size of state space is 5D + time + species, and the state variables are

- the perturbed distribution function for each species, $f_s(\mathbf{R}, v_\parallel, \mu, t)$
- the electrostatic potential, $\phi(\mathbf{x}, t)$
- the parallel component of the vector potential, $A_\parallel$

Moments of the distribution function (n, $T_\parallel$, $T_\perp$, ...) are also state variables.

GENE uses a field-aligned coordinate system (c.f. [9]) where x is a flux label (approximately radial), z is parallel to the field, and y is orthogonal to x and z (binormal to $\mathbf{B}$). The metric is chosen such that z is equal to the

poloidal angle. (See [73] for more information on field-aligned coordinates.)

$$x = \frac{q_0}{B_0 r_0}(\psi - \psi_0) \tag{3.76}$$

$$y = -\frac{r_0}{q_0}(\alpha - \alpha_0) \tag{3.77}$$

$$\alpha = \zeta - q(\psi)\theta \tag{3.78}$$

$$z = \theta \tag{3.79}$$

Because of the poloidal and toroidal periodicity, the k_x and k_y modes are not independent. The ballooning representation[34, 73] gives a condition for how the k_x and k_y modes are connected:

$$\Phi(k_x, k_y, z + 2\pi) = \Phi(k_x + 2\pi\hat{s}k_y, k_y, z) \tag{3.80}$$

In other words, if k_x follows the quantization condition $\Delta k_x = 2\pi\hat{s}k_y$, the k_x grid can be used to extend the mode structure in the z direction past the ends of the box (chosen at $\pm\pi$). In essence, this is unraveling a 2D grid in kx, z into a long 1D grid in z_{ext}. GENE uses this k_x quantization by default when looking for a linear solution.

GENE can treat a problem as linear or nonlinear. The linear problem is a reduced model which neglects higher order fluctuation terms in the gyrokinetic equation, keeping only terms linear in the fluctuation amplitude. Analysis of the linear problem gives fluctuation eigenmodes which grow (or shrink) in time forever. This information allows us to identify instability thresholds for different classes of turbulence, but it doesn't contain enough physics to predict the final transport. Nevertheless, the linear problem lets

us identify major contributions which exist in the full nonlinear system which would otherwise be obscured by the complexity.

In the linear problem, GENE computes the fastest growing eigenmode within the calculation domain, and computes the growth rate and frequency of the mode. The fastest growing mode of a given k_y is some linear combination of k_x and k_z modes. The eigenmode is a linear combination of fluctuations in each of the state variables above. In a fluctuation eigenmode, each state variable fluctuates with the same frequency and growth rate. On the other hand, the phase and amplitudes can vary across the state variables. GENE also calculates the particle and heat flux for each species from the density and potential fluctuations. These fluxes also grow in time at twice the growth rate.

In the nonlinear case, the fluctuation amplitude does not grow forever but reaches some nonlinear saturation. All Fourier modes are coupled, so the simulation must include all modes simultaneously. The fluctuation does not reach a steady state, but rather follows a bounded chaotic trajectory. The trajectory is very sensitive to initial conditions and can only be expected to agree with an experiment in a statistical sense. The transport is obtained by averaging over some interval which is long compared to the chaotic time scale. Unfortunately, this requires a significant computational effort by today's standards. A nonlinear run may take on the order of 10^5 cpu-hours, limiting us to a few runs, whereas linear runs can be completed in 10^2 cpu-hours. Therefore, these results use a few nonlinear runs to supplement mainly linear runs.

The form of the equation solved by GENE can be found in 2.3.1 of [152].

For the studies of impurity transport on Alcator C-Mod, version 11 of the GENE code was run on the Stampede supercomputer in the Texas Advanced Computing Center (TACC)[14] The focus of the study was on shot 1120822020, for which D and v transport coefficients were available from the short puff experiment.

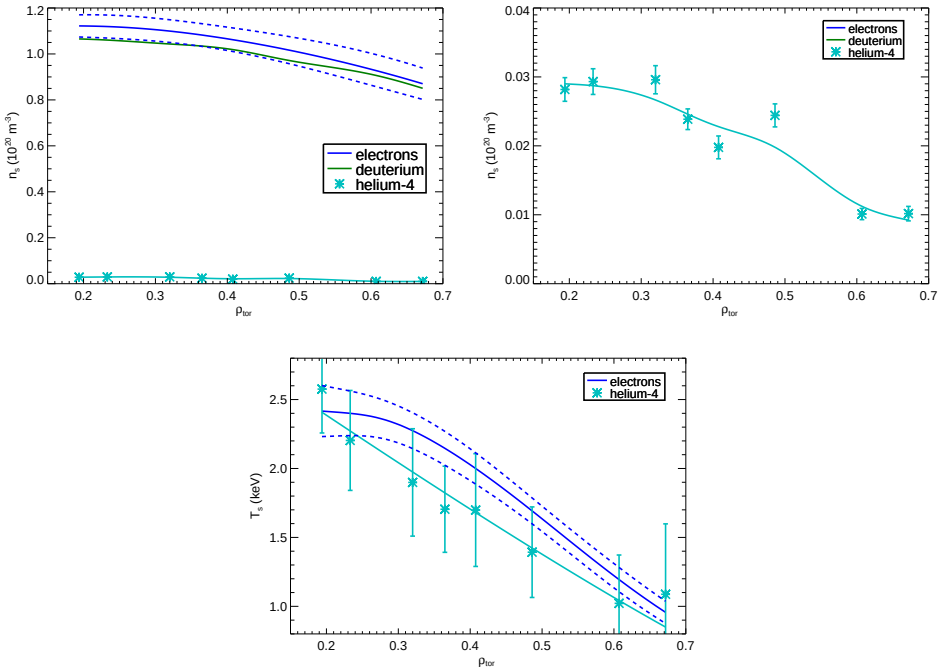

Figure 3.32: GENE input profiles from 1120822020 (1.161 s to 1.201 s). n_e and T_e are obtained from the Thomson Scattering diagnostic. n_D is inferred from quasineutrality. The upper right plot is a zoom of the upper left.

[14]Stampede is a 6400 node, 102400 core, Dell PowerEdge C8220 Cluster with Intel Xeon Phi coprocessors. `http://www.tacc.utexas.edu/resources/hpc/stampede`

Figure 3.32 shows profiles from 1120822020 which were used as input to several GENE runs. In this shot, ^{4}He was puffed to about 2.6 % of n_e. The profiles were fitted with smoothing splines to allow calculation of the density and temperature gradients which are needed for gyrokinetic analysis. The logarithmic gradients of the densities and temperatures are shown in figure 3.33. The uncertainty in derivative is estimated using the technique described in [49] (see remarks below). We can see that the gradients are larger at larger minor radius, and the plasma is generally more unstable at outer minor radii.

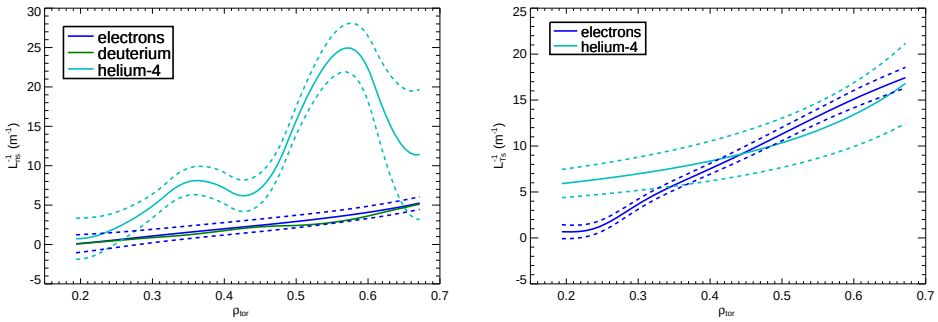

Figure 3.33: Inverse scale lengths from shot 1120822020 (1.161 s to 1.201 s). $L_a \equiv -\frac{\mathrm{d}\log a}{\mathrm{d}r}$. Left: density. Right: temperature.

When running a numerical simulation, it is important to check if the resolution and box size are large enough to not introduce large numerical errors. This was tested by running a few linear base cases under several choices of parameters with increased resolution. The maximum linear growth rate and frequency are relatively unchanged between runs, which suggests that the resolution is adequate. The final resolution and box parameters are `nx=8,nz0=16,nv0=32,nw0=8,lv=3,lw=9`, which is close to the values obtained

in [38]. The optimal parameters do depend on plasma conditions to some degree.

The eigenmodes can be visualized on a toroidal slice by converting the coordinates. Figures 3.34 and 3.35 show the electric potential and density fluctuations for two local simulations. There is a discontinuity at the inner midplane where the flux tube has been cut. The fluctuation structure in the z direction is obscured in this view. Another view is the ballooning representation. Figure 3.36 shows some ballooning representation views. The structure of the mode along the z direction is clearly visible, but the perpendicular structure is obscured in this view. The most unstable modes are extended in the z (parallel) direction, covering the entire poloidal transit in a single oscillation. These "ballooning modes" are heavily damped for $|z| > \pi$.

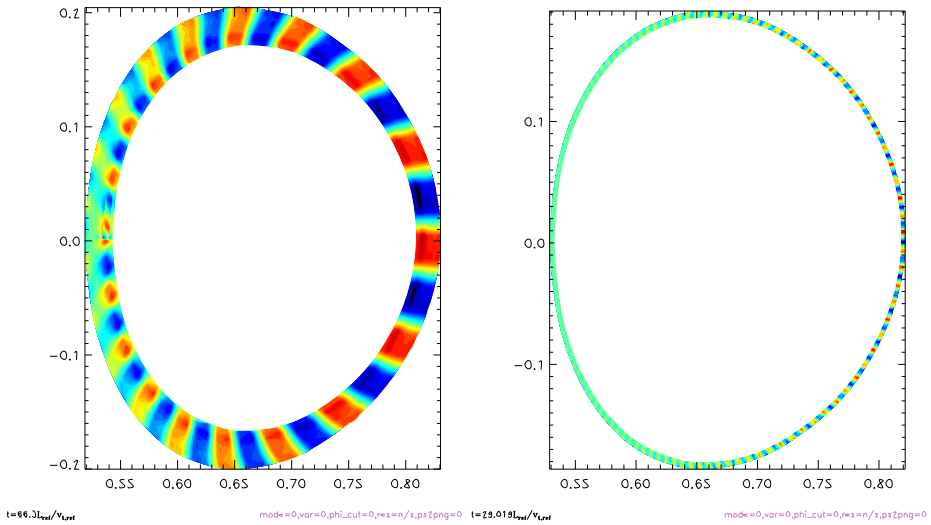

Figure 3.34: Torus representation of Φ in the fastest growing eigenmode for a flux tube at $\rho_{tor} = 0.6$ for: (left) $k_y\rho_D = 0.1$, (right) $k_y\rho_D = 0.6\rho_D$.

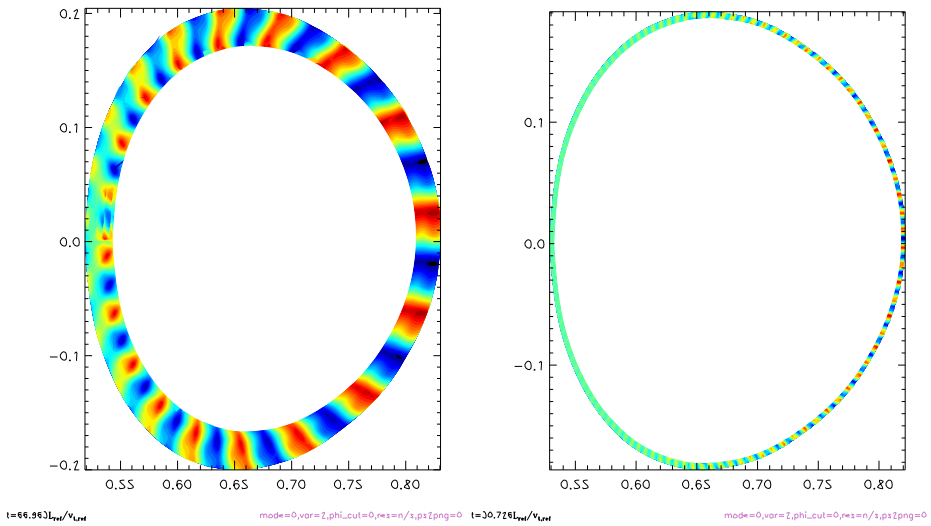

Figure 3.35: Torus representation of n_{He} in the fastest growing eigenmode for a flux tube at $\rho_{tor} = 0.6$ for: (left) $k_y\rho_D = 0.1$, (right) $k_y\rho_D = 0.6$.

Figure 3.37 shows the results of a set of local linear simulations, showing the growth rate and frequency of the fastest growing turbulent mode with a parameter scan over k_y ($0.1 \leq k_y\rho_D \leq 8$) and minor radius ($0.2 \leq \rho_{\mathrm{tor}} \leq 0.65$) . The instability growth rates are larger at higher minor radius, where magnetic shear and thermodynamic gradients are larger, and there is a higher fraction of trapped particles. There is a discontinuity in the frequency and direction of the fastest growing mode between $k_y\rho_D = 1.0$ and $k_y\rho_D = 1.25$. This is due to a switch in the fastest growing mode from ITG to ETG. For the ITG dominated range $k_y\rho_D \lesssim 1.0$, there is a maximum growth rate near $k_y\rho_D \sim 0.7$. This simulation domain doesn't reach the maximum ETG growth rate, which occurs at higher spatial frequencies.

In linear simulations, the final magnitude of a state variable is not

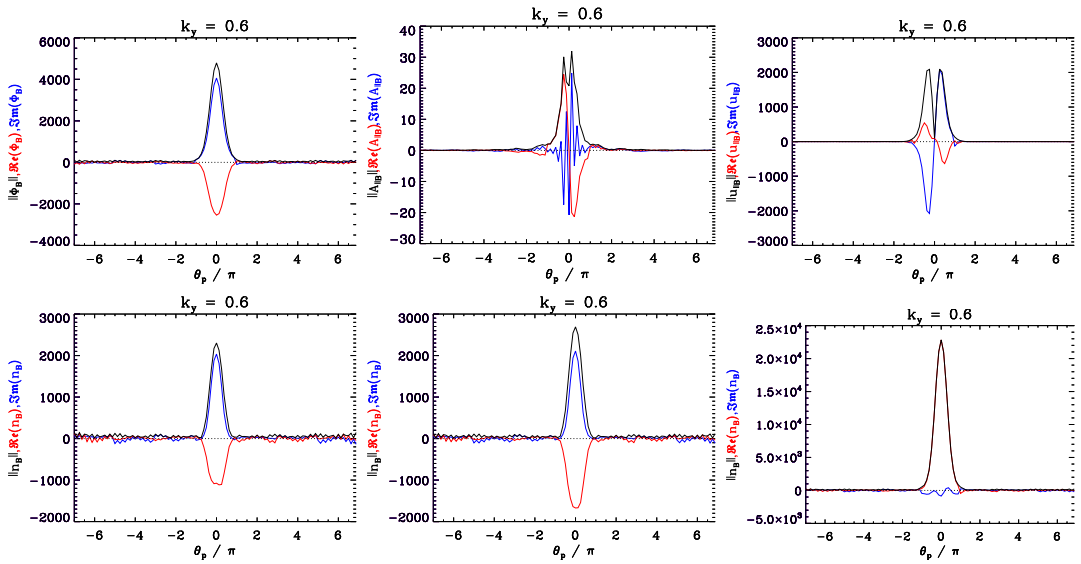

Figure 3.36: Ballooning mode representation of state variable fluctuations for $k_y\rho_D = 0.6$, $\rho_{tor} = 0.6$. First row: Φ; $A_\parallel$; $u_{\parallel i}$. Second row: n_e; n_i; n_{He}

meaningful because they are all growing in time (from an arbitrary starting perturbation). Nevertheless, the ratios between state variables are meaningful, since the growth rates cancel out. We are interested in the particle flux $\langle \tilde{n}_s \tilde{v}_E \rangle$ which is proportional to the fluctuation amplitude squared, so we must normalize by an appropriate quantity such as $\left\langle \left| \tilde{n}^2 \right| \right\rangle$ or $\left\langle \left| \tilde{\Phi}^2 \right| \right\rangle$. Figure 3.38 shows these results. Or, we can plot the ratio between fluxes of different species (Figure 3.39).

We can see that for some modes, particularly in the ion-scale turbulence range ($k_y\rho_D \sim 0.6$), the helium flux is larger than the main ion flux. This is somewhat surprising since the equilibrium helium density is just 2.5 % of the ion density in this scenario. This shows that helium cannot be treated

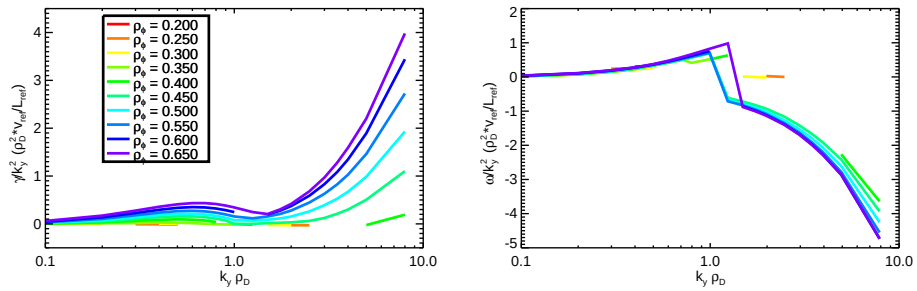

Figure 3.37: GENE linear (left) growth rates and (right) frequencies for shot 1120822020. Positive (negative) frequencies indicate mode propagation in the ion (electron) diamagnetic drift direction. The vertical scale is in normalized units $v_{\mathrm{ref}}/L_{\mathrm{ref}} = 1.2508 \times 10^6\,\mathrm{s}^{-1}$.

as a passive trace impurity. For these modes, the helium drives a significant amount of ion transport in order to maintain quasineutrality. For higher spatial frequency modes, $k_y\rho_D \gtrsim 1.25$, the helium flux is relatively small. GENE has the option of treating a species as passive—that is, not contributing to the electromagnetic field. If this option is turned on for helium, the electron flux is considerably modified.

We can see some general features in the linear scan results. For the electrons and ions, the transport increases with minor radius, but for helium-4, the transport reaches a maximum around $rho_{\mathrm{tor}} \sim 0.55$, where the input density gradient is largest (see figure 3.33). For electrons and ions, the predicted flux is outward for larger scale ITG ($k_y\rho_D \lesssim 0.6$) and inward for ETG and shorter scale ITG ($k_y\rho_D \gtrsim 0.8$). It is expected that outward and inward fluxes largely cancel for a plasma near equilibrium. For helium-4, the transport spectrum is somewhat similar but strongly biased in the outward direction. For minor

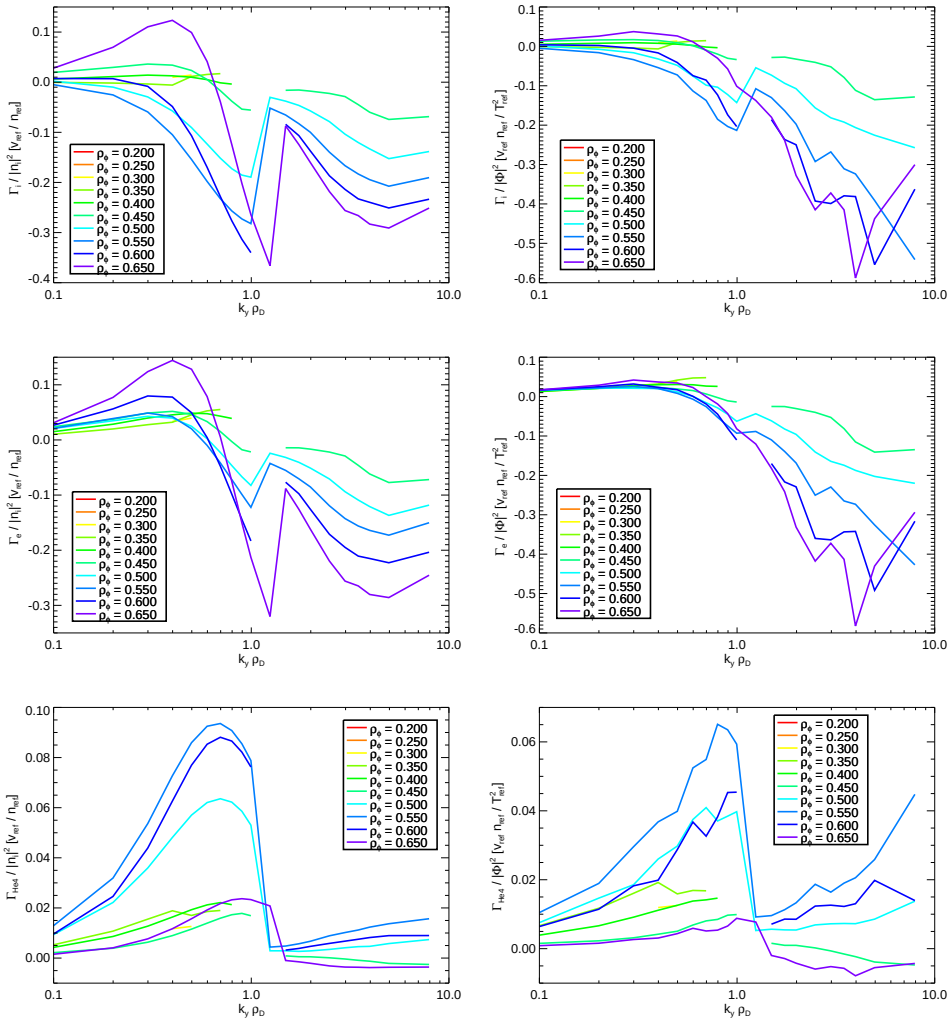

Figure 3.38: Normalized fluxes for turbulent modes. The left column gives flux of each species normalized by $|n_i|^2$ in the units $v_{\rm ref}/n_{\rm ref} = 2.49 \times 10^{-15}\,{\rm m}^4\ {\rm s}^{-1}$. The right column gives flux of each species normalized by $|e\Phi|^2$ in the units $v_{\rm ref} n_{\rm ref}/T_{\rm ref}^2 = 1.85 \times 10^{19}\,{\rm m}^{-2}\ {\rm s}^{-1}\ {\rm eV}^{-2}$. Top: deuterium. Mid: electrons. Bottom: ^{4}He

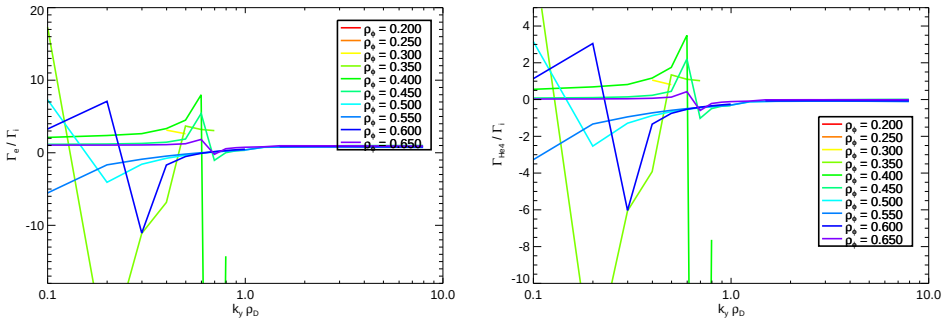

Figure 3.39: Flux ratios for turbulent modes. Left: ratio of electron flux to deuterium flux. Right: ratio of helium-4 flux to deuterium flux.

radii near $\rho_{\mathrm{tor}} \sim 0.55$, the direction is outward for all simulated modes, which implies that the density profile cannot be in quasi-equilibrium[15]. The bump in the density gradient is due to a high value in a single CXRS channel and may be an artifact.

3.6.1 Quasilinear transport

The quasilinear transport is obtained by summing over the transport from each linear eigenmode, which must be scaled using a model for the saturated value for the fluctuating potential spectrum. The linear calculation by itself gives the ratio $\mathit{\Gamma}_{\mathrm{He},k_y}/|\tilde{\phi}_{k_y}|^2$ for the fastest growing modes, but the value of $|\tilde{\phi}_{k_y}|^2$ is yet unknown. The quasilinear transport model uses a heuristic mixing length estimate: $D \sim |\tilde{\phi}_{k_y}|^2 \sim \gamma/k_\perp^2$, which has been relatively successful at reproducing the saturated potential spectrum[109, 29]. This estimate is

[15]In shot 1120822020, t=1.181 s, helium is gradually leaving the plasma; however, the time-scale is expected to be slow compared to the transport

based around an assumption that the turbulent diffusion has a random walk character. Therefore, the quasilinear particle flux is computed by[109]

$$\Gamma = \sum_{k_y} \mathcal{C}(k_y) \frac{\gamma}{\langle k_\perp^2 \rangle} \frac{\Gamma_{k_y}}{|\tilde{\phi}_{k_y}|^2} \tag{3.81}$$

where $\mathcal{C}(k_y)$ is a correction factor which needs to be chosen to match results from nonlinear simulations. The average perpendicular wavenumber $\langle k_\perp^2 \rangle$ for a given k_y is calculated using

$$\langle k_\perp^2 \rangle = \frac{\sum_{k_x} \int \left(k_x^2 g_{xx}(z) + 2k_x k_y g_{xy}(z) + k_y^2 g_{yy}(z) \right) \left(\phi(k_x, k_y, z) \right)^2 J \, \mathrm{d}z}{\sum_{k_x} \int \left(\phi(k_x, k_y, z) \right)^2 J \, \mathrm{d}z} \tag{3.82}$$

The inverse $\langle k_\perp^2 \rangle$ scaling strongly weights the transport toward the larger wavelength modes. For values of $k_y \rho_D \gtrsim 0.2$, the binormal component k_y is the dominant contribution to $\langle k_\perp^2 \rangle$, but at smaller values of k_y, the k_x contribution is important. Figure 3.40 shows $\langle k_\perp^2 \rangle$ from 3.82 and the quasilinear spectral weighting function $\gamma / \langle k_\perp^2 \rangle$. If we compare figure 3.40 to figure 3.37, we can see that although the growth rate for the ETG modes ($k_y \rho_D \gtrsim 1$) is substantially larger than that of the ITG modes, they saturate at much lower amplitude and ITG modes are the dominant contribution to the transport. We observe that the dominant modes have $k_y \rho_D \sim 0.2, 0.3$, and the contribution drops rapidly moving away from these modes.

3.6.1.1 Nonlinear saturation

The time traces of some state variables in a nonlinear run are shown in figure 3.41. The initial part of the time evolution shows an exponential growth

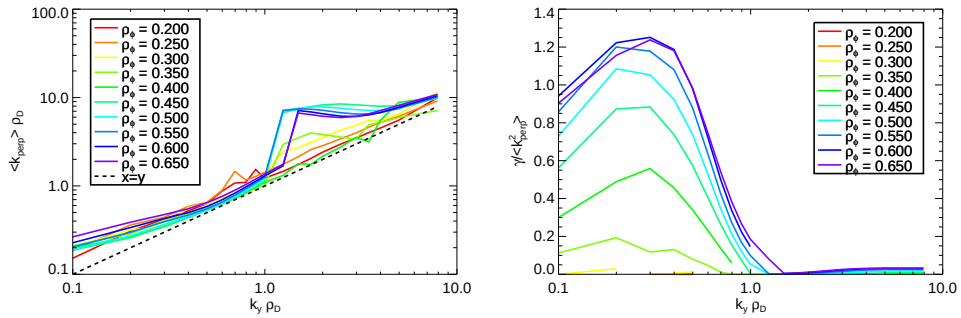

Figure 3.40: Left: Average perpendicular wavenumber for each k_y mode at several radii in shot 1120822020. Right: quasilinear spectral weighting function for k_y at several radii in shot 1120822020.

in all fluctuations, followed by saturation and chaotic turbulence. The time scale is in normalized units, $L_{\mathrm{ref}}/v_{\mathrm{ref}} = 0.96\,\mu\mathrm{s}$. The saturated density fluctuation for helium is very large in this case. It can be seen that the saturation does not occur at a fixed point in phase space but occupies a strange attractor, which appears to have a period on the order of hundreds of microseconds. We are interested in transport behavior on much longer time scales, so it is necessary to average the mode structure over many cycle periods to obtain a reliable answer. Typically, there is a trade-off between computation time and convergence.

By averaging over the nonlinear oscillation, the nonlinear simulation can give the power spectrum of k_y modes in saturation. This can be used to estimate the scaling parameter for quasilinear transport. It should be noted that the nonlinear mode structure is not simply a linear combination of fastest growing linear eigenmodes, because there are also contributions from subdom-

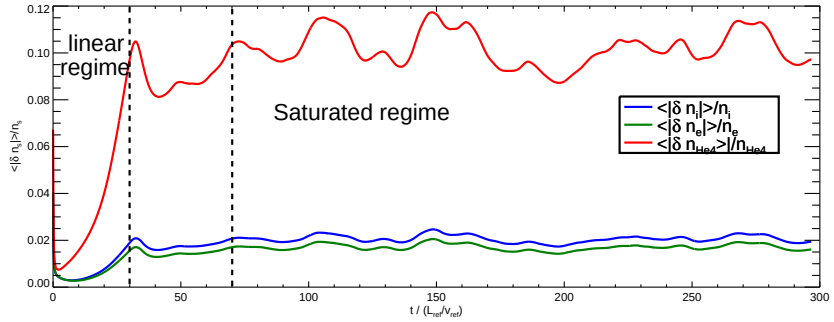

Figure 3.41: Nonlinear simulation for 1120822020 at $\rho_{\text{tor}} = 0.5$, showing normalized density fluctuation amplitude.

inant modes. That is, both ITG and TEM contribute to the nonlinear flux, especially if the growth rates are similar. Nevertheless, the best way to proceed is to simply equate the nonlinear power spectrum to the quasilinear saturated amplitudes.

Figure 3.42 compares the nonlinear saturated amplitudes for two state variables to the heuristic scaling, $\gamma / \langle k_\perp^2 \rangle$. The ratio gives the scaling parameter $\mathcal{C}$. We obtain a different parameter $\mathcal{C}$ for each choice of state variable. The $\langle |\phi|^2 \rangle$ dependence will be used in the following analyses. The peak saturated amplitudes occur at $k_y \rho_D = 0.3$, which is typical for ITG turbulence. The nonlinear simulation across $k_y \rho_D \leq 1.75$ did not show ETG modes. The slope of the nonlinear saturation spectrum for $k_y \rho_D \gtrsim 1$ closely matches a $k_y^{-7/3}$ power law, which is consistent with the critical balance scaling law given in [6].

Combining the quasilinear transport model with the nonlinear scaling $\mathcal{C}$ gives the quasilinear flux spectrum, which can be compared to the nonlinear

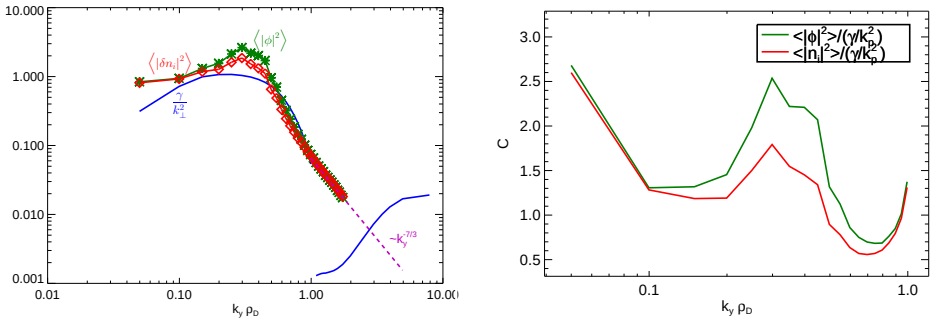

Figure 3.42: Left: quasilinear heuristic scaling and nonlinear power spectra for k_y modes. Right: Ratio between nonlinear power spectra and quasilinear heuristic scaling.

flux spectrum. This is shown in figure 3.43. The quasilinear results are similar to the full nonlinear; however, the nonlinear spectra is about 30 % larger in some places. The nonlinear flux shows a smooth transition from the ITG to ETG scale turbulence, while the quasilinear model has a break near $k_y \rho_D \sim 1$.

The nonlinear simulation was computed only for a single radial point, and the scaling parameter $\mathcal{C}$ evaluated for this point is reused for other radial points to save computation time. The total flux is obtained by summing over modes. The resulting flux profile is shown in figure 3.44. The main ion and helium fluxes are in opposite directions and mostly agree with the ambipolarity heuristic used earlier. In the region of space where the helium-4 density gradient is outward and large ($\rho_{\text{tor}} \sim 0.55$), GENE predicts a strong outward helium flux and inward ion flux.

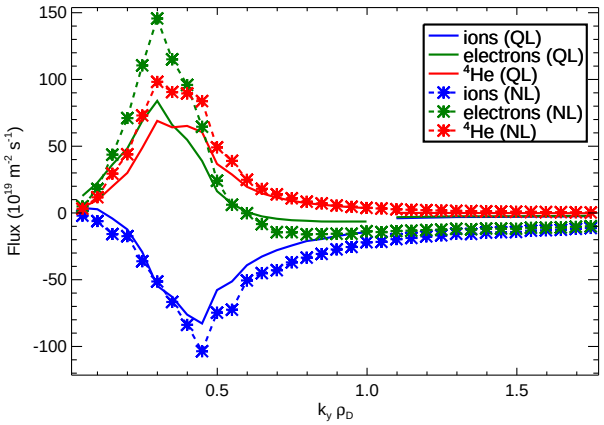

Figure 3.43: Nonlinear and quasilinear flux spectra for shot 1120822020, $\rho_{\text{tor}} = 0.5$. The solid lines show results of quasilinear fluxes scaled by $\mathcal{C}$, and the dashed line with stars shows the nonlinear result.

3.6.1.2 Obtaining transport coefficients

GENE does not directly output the transport coefficients (D_s, v_s). In order to obtain these values (for each species), it is necessary to run a set of simulations in which the densities and gradients of each species is varied over a small region of parameter space. A sensitivity scan over the input profiles includes these runs and also gives the sensitivity of the calculation to errors in the input parameters.

When the impurity under measurement can be treated as trace passive species (meaning that contribution of the impurity density fluctuations to the potential fluctuations can be neglected), the impurity flux is linear in the impurity gradients[3, 30] and the impurity flux can be written as

$$\Gamma_Z = -D_Z(\boldsymbol{\xi})\frac{\partial n_Z}{\partial r} + v_Z(\boldsymbol{\xi})n_Z \tag{3.83}$$

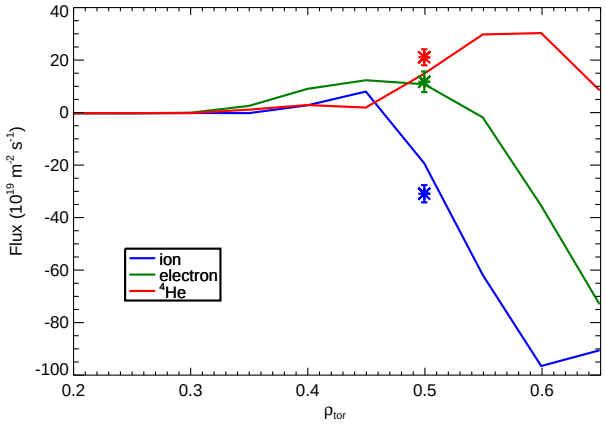

Figure 3.44: Quasilinear fluxes for shot 1120822020, with weighted contributions from k_y modes. The nonlinear flux for $\rho_{\rm tor} = 0.5$ is also shown.

where ξ stands for the plasma state but does not include a dependence on the impurity Z. However, we have already seen that helium can *not* in general be treated as a trace passive species (see figure 3.39). The gyrokinetic transport varies nonlinearly with respect to helium density and gradient, even for the linear problem[16]. In this situation, the definition of $D_{\rm He}$ and $v_{\rm He}$ must be clarified. We observe that the variation in the flux is linear with respect to sufficiently small changes in the input profiles. We can generate a Taylor series expansion

$$\Gamma_Z(\boldsymbol{\xi}) = \Gamma_Z(\boldsymbol{\xi}_0) + \sum_i \left[\frac{\partial \Gamma_Z(\boldsymbol{\xi}_0)}{\partial \xi_i} (\xi_i - \xi_{i0}) \right] + \sum_{i,j} \left[\frac{\partial^2 \Gamma_Z(\boldsymbol{\xi}_0)}{\partial \xi_i \partial \xi_j} \frac{(\xi_i - \xi_{i0})(\xi_j - \xi_{j0})}{2!} \right] + \dots \tag{3.84}$$

where $\boldsymbol{\xi} = (n_e, n_{\rm He}, T_i, T_e, T_{\rm He}, \omega_{ne}, \omega_{n\rm He}, \omega_{Ti}, \omega_{Te}, \omega_{T\rm He})$, where $\omega_{ns} \equiv -\frac{1}{n_s}\frac{\partial n_s}{\partial r}$

[16]The linear gyrokinetic equation is linearized with respect to the rapidly fluctuating variables, but is still nonlinear with respect to equilibrium variables.

and $\omega_{Ts} \equiv -\frac{1}{T_s}\frac{\partial T_s}{\partial r}$.

Let us rewrite 3.54 in the following form, neglecting the parallel diffusion and rotodiffusion terms.

$$\Gamma_Z = D_Z n_Z \left[\omega_{nZ} + C_c(s)\frac{2}{R} - C_{\nabla T}(\omega)\omega_{TZ}\right] \tag{3.85}$$

Let us also rewrite the first order Taylor expansion of the flux as

$$\begin{aligned}\Gamma_Z = \Gamma_{Z0} &+ \tfrac{\partial \Gamma_Z}{\partial \omega_{nZ}}\omega_{nZ} + \tfrac{\partial \Gamma_Z}{\partial \omega_{ne}}\omega_{ne} + \tfrac{\partial \Gamma_Z}{\partial n_Z}n_Z + \tfrac{\partial \Gamma_Z}{\partial n_e}n_e + \tfrac{\partial \Gamma_Z}{\partial n_e}n_e \\ &+ \tfrac{\partial \Gamma_Z}{\partial \omega_{TZ}}\omega_{TZ} + \tfrac{\partial \Gamma_Z}{\partial \omega_{Te}}\omega_{Te} + \tfrac{\partial \Gamma_Z}{\partial \omega_{Ti}}\omega_{Ti} + \tfrac{\partial \Gamma_Z}{\partial T_Z}T_Z + \tfrac{\partial \Gamma_Z}{\partial T_e}T_e + \tfrac{\partial \Gamma_Z}{\partial T_i}T_i\end{aligned} \tag{3.86}$$

If we compare 3.86 to 3.54, we can equate terms to define some transport coefficients for helium. We can subdivide the thermodiffusion pinch by species. We get

$$D_{\mathrm{He}} = \frac{1}{n_{\mathrm{He}}}\frac{\partial \Gamma_{\mathrm{He}}}{\partial \omega_{n\mathrm{He}}} \tag{3.87}$$

$$C_{\nabla T_{\mathrm{He}}} = -\frac{1}{n_{\mathrm{He}} D_{\mathrm{He}}}\frac{\partial \Gamma_{\mathrm{He}}}{\partial \omega_{T_{\mathrm{He}}}} \tag{3.88}$$

$$C_{\nabla T_e} = -\frac{1}{n_{\mathrm{He}} D_{\mathrm{He}}}\frac{\partial \Gamma_{\mathrm{He}}}{\partial \omega_{T_e}} \tag{3.89}$$

$$C_{\nabla T_i} = -\frac{1}{n_{\mathrm{He}} D_{\mathrm{He}}}\frac{\partial \Gamma_{\mathrm{He}}}{\partial \omega_{T_i}} \tag{3.90}$$

$$C_c = -\frac{1}{n_{\mathrm{He}} D_{\mathrm{He}}}\frac{\partial \Gamma_{\mathrm{He}}}{\partial \hat{s}}\frac{\hat{s}R}{2} \tag{3.91}$$

There are two ways to define v. The first is by fitting

$$v_{\mathrm{He}}^{(I)} = \frac{\partial \Gamma_{\mathrm{He}}}{\partial n_{\mathrm{He}}} \tag{3.92}$$

The second is by subtracting the diffusive part from the total flux

$$v_{\mathrm{He}}^{(II)} = \frac{\Gamma_{\mathrm{He}}}{n_{\mathrm{He}}} - (-D\omega_{\mathrm{He}}) \tag{3.93}$$

For a linear trace impurity these are equal, but need not be for a general nonlinear species. For the case of zero flux, the second definition is more useful because it gives a relationship $v/D = -L_n^{-1}$ which can be compared to experiment.

Figures 3.45, 3.46, and 3.47 show results of a sensitivity scan performed on shot 1120822020 at $\rho_{\mathrm{tor}} = 0.5$. The plots show the effect on the species fluxes when each of the following parameters are varied in turn: T_i, T_e, T_{He4}, ω_{Ti}, ω_{Te}, ω_{THe4}, n_e, n_{He4}, ω_{ne}, $\omega_{n\mathrm{He4}}$, $\hat{s}$, and q. Each parameter was varied from 80 % to 120 % of the base value over five points, shown along a single x-axis as an input variation from 0.8 to 1.2, and the quasilinear weighted flux is shown. At an input variation of 1.0, the parameters all take the base (measured) values, so all curves intersect, with the exception of $\hat{s}$ and q (see below). For most cases, the flux of each species varies almost linearly with changes in the input value, but some quadratic behavior is clearly visible (especially for variation of ω_{Te} and ω_{Ti}), so a quadratic fit has been performed on each of the flux sensitivities.

Table 3.3: Normalized units in GENE calculations

$\Gamma_s/\lvert\tilde{\phi}^2\rvert$	$1.85 \times 10^{19}\,\mathrm{m}^{-2}\ \mathrm{s}^{-1}\ \mathrm{eV}^{-2}$
T	$1639.7316\,\mathrm{eV}$
n	$1.010\,402\,5 \times 10^{20}\,\mathrm{m}^{-3}$
ω_T and ω_n	$3.675\,607\,77\,\mathrm{m}^{-1}$

In order to evaluate the sensitivity of the model to the safety factor q or the magnetic shear $\hat{s} = \frac{r}{q}\frac{\partial q}{\partial r}$, it is necessary to run the simulation using

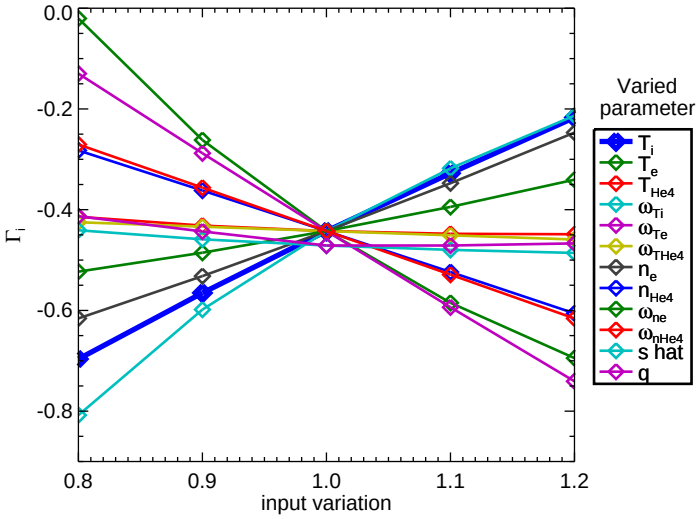

Figure 3.45: Quasilinear ion flux from linear gyrokinetics, in normalized units, versus changes in input profiles.

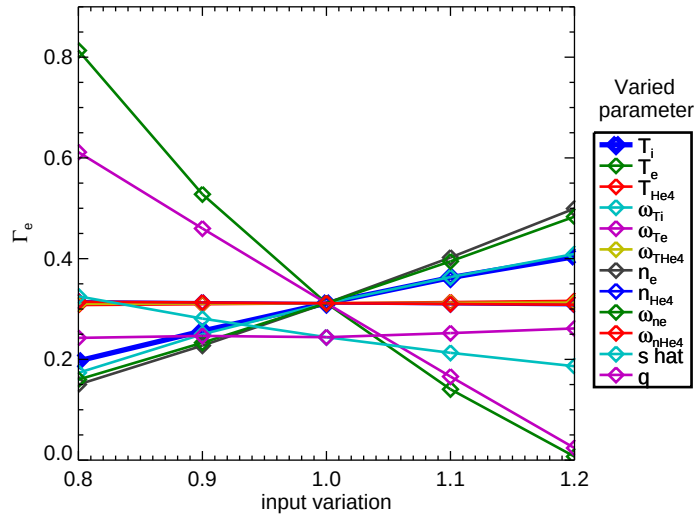

Figure 3.46: Quasilinear electron flux from linear gyrokinetics, in normalized units, versus changes in input profiles.

a simplified form of the geometry, where q and $\hat{s}$ are given as parameters. GENE can accept a generalized Miller equilibrium[181], in which the geometry is given by the safety factor q, magnetic shear $\hat{s}$, Shafronov shift, elongation κ, triangularity δ, squareness ζ, major radius, and minor radius. GENE also includes a tool for extracting Miller parameters from an EFIT file. Figure 3.48 compares some results of simulating with both geometric models. The Miller geometry is a very good approximation of the geometry for flux surfaces not too close to the separatrix. The Miller geometry can be used to extract the curvature pinch contribution of the transport, which depends on $\hat{s}$.

Transport coefficients obtained from simulations are summarized in 3.4. The propagated uncertainties from the input profiles are also shown. The diffusivity for helium from the simulation is substantially higher than the experimental value of $D_{\mathrm{He}} \approx 0.8\,\mathrm{m}^2/\mathrm{s}$. On the other hand, the main ion and electron diffusivities are close to the experimental value of D_{He}. As expected, the curvature pinch is inward for all species. A possible source of the discrepancy is measurement error in the input density profiles used in the simulation. In figure 3.47, we note that the helium flux is quite sensitive to errors in ion temperature and ion temperature gradient, which are only coarsely measured.

The propagated uncertainty in the simulation results can be obtained by combining the input profile uncertainties and the results of the sensitivity scan. For shot 1120822020, I have included the estimated errors in electron and helium density and temperature. Deuterium temperature has been assumed to equal helium temperature, and helium is assumed to be the only impurity.

Table 3.4: Transport simulation results for 1120822020 at $\rho_{\text{tor}} = 0.5$. δ labels the uncertainty

species	Γ $10^{19}\,\text{m}^{-2}/\text{s}$	D m^2/s	v_1 m/s	v_2 m/s	v/D m^{-1}	C_T 1	C_c 1
D	-18.4	0.76	3.57	-3.40	-4.48	-0.009	-0.25
δD	21.2	0.88	4.14	3.94	7.33	0.01	0.29
e	9.56	1.29	3.38	-2.19	-1.69	-0.26	-0.44
δe	14.5	1.96	5.12	3.31	3.61	0.40	0.66
^{4}He	14.0	6.47	77.8	-13.4	-2.07	-1.316	-1.50
δ^4He	6.47	3.00	36.0	6.19	1.35	0.613	0.70

The uncertainties in the CXRS have been discussed earlier in 2.6.1. The uncertainty in the smoothing spline fit is generally lower than the uncertainty in the pointwise measurements because the smoothing applies a low pass filter to the random noise. Smoothing is necessary to obtain a usable result for first derivatives because the uncertainty in the basic discrete derivative is too high. However, smoothing is a delicate matter. Increasing the smoothing decreases the computed uncertainty because the noise is filtered out, but smoothing too much will increase the true error (which cannot be measured) as features are lost. A basic rule of thumb, which is used here, is to look for the smoothest curve (smallest second derivatives) within a 1 σ confidence interval of the measurement, based on the measurement errors[49].

The resulting uncertainties are shown in 3.4. The uncertainties in safety factor q and magnetic shear $\hat{s}$ have been neglected in the calculation.

3.6.2 Turbulence regimes

Gyrokinetic simulations and theory predict a change in the dominant turbulent mode, depending on plasma conditions. The characteristics of the impurity transport change depending on the dominant mode (see 3.4).

The ITG growth rate grows rapidly as the ITG instability threshold (equation 3.75) is exceeded. Therefore, ITG modes are dominant for large values of $\eta_i \equiv L_{ni}/L_{Ti}$ and TEM modes are dominant at smaller values of η_i. This fact can be clearly seen in figure 3.49. Figure 3.49 is a color plot of the frequency of the dominant turbulence mode over a set of linear GENE simulations in which the temperature scale length and and density scale length have been varied. In GENE, a positive frequency indicates mode propagation in the ion diamagnetic direction. The frequencies pass through zero where the dominant mode changes from propagation in the ion diamagnetic direction to propagation in the electron diamagnetic direction. The ion and electron temperatures have been varied together in this scan.

When the temperature profiles are more sharply peaked than the density profiles ($L_T^{-1} > L_n^{-1}$), the instability is ITG dominant. This is typically the case in the Alcator C-Mod plasma. The case of shot 1120822020 at $\rho_{\mathrm{tor}} = 0.5$ is shown on the plot. If neither the temperature nor density profiles are sufficiently peaked, the simulations predict a stable region for oscillations in this set of wavenumbers.

3.6.3 Trace impurity threshold

As the helium impurity density increases from a fraction of a percent to a majority of the plasma density, at some point, the helium can no longer be treated as a trace impurity. Up till now, I have been vague in my definition of what a trace impurity is. Here are some characteristics of a trace impurity: For a sufficiently small amount of an impurity, the plasma should behave identical to having no impurity. Therefore, a trace impurity has no effect on the turbulent mode frequencies and growth rates, which are determined by the parameters of the major plasma constituents. In the drift wave turbulence model, the trace impurity has negligible effect on the electric potential perturbations. Therefore, the trace impurity has no effect of the transport of any other species, and the trace impurity transport is determined by the correlation between the impurity density fluctuations and the potential perturbations. Another aspect of a trace impurity is that the impurity flux is proportional to the impurity density. If twice as much impurity is put into the same background plasma, the flux should be doubled because the trace impurity is carried by the plasma and does not influence it. I have run some simulations to determine the situations in which this trace condition can hold.

A set of linear GENE simulations were run for a helium-3 and deuterium plasma. The helium-3 and deuterium concentrations were varied over a large range, leaving the electron density fixed. Other parameters were based on a typical ITG dominated helium-3 minority plasma. Under these conditions, the characteristics of the turbulence varied smoothly with helium concenta-

tion across the entire scan. The unstable growth rates increased with helium concentration, and the most unstable k_y mode shifted toward smaller wavelength (see figure 3.50). The mode frequencies dropped with increasing helium concentration. If we look at the particle fluxes, we see that the electron flux is relatively insensitive to the ion composition as long as other plasma parameters remain fixed. The helium and deuterium fluxes primarily move in opposite directions. The fluxes are shown in figure 3.51, scaled by charge to show the ambipolar relationship. For small helium concentrations, the helium flux scales with with helium density. But at high concentrations, the helium flux begins to decrease, because the deuterium flux begins to decrease as deuterium density becomes small.

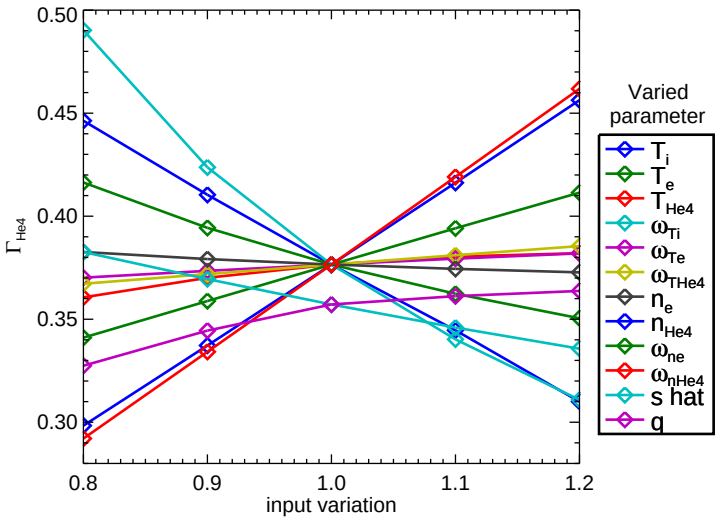

Figure 3.47: Quasilinear helium-4 flux from linear gyrokinetics, in normalized units, versus changes in input profiles.

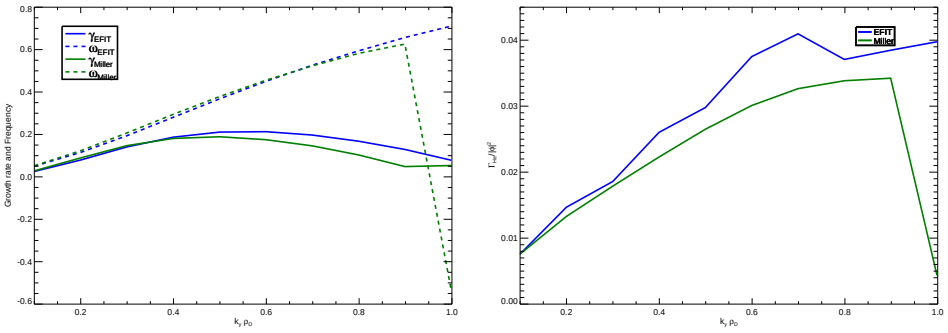

Figure 3.48: Left: Growth rates and frequencies of various k_y modes for 1120822020, $\rho_{\text{tor}} = 0.5$, using EFIT and Miller geometries. Right: Flux ratios for various k_y modes, using EFIT and Miller geometries.

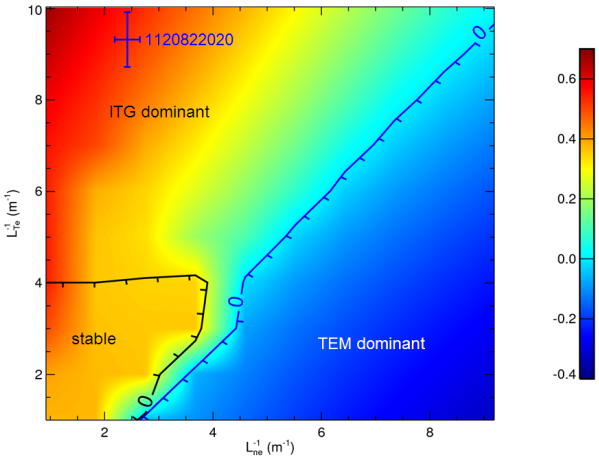

Figure 3.49: Turbulent mode ITG and TEM threshold

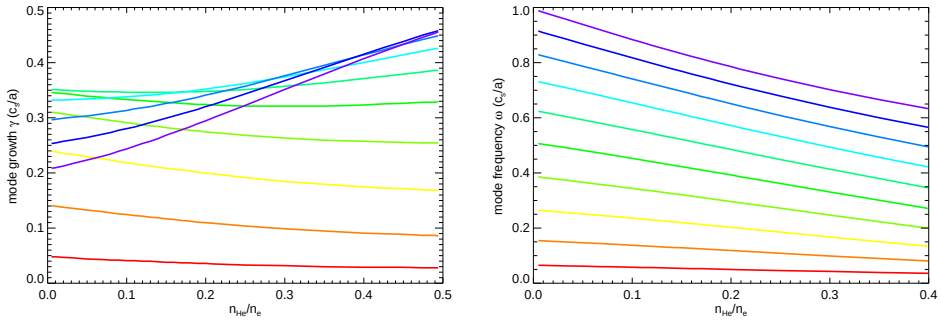

Figure 3.50: Left: Growth rates of the fastest growing k_y modes, in normalized units, as a function of helium fraction. Right: Frequencies of the fastest growing k_y modes, in normalized units, as a function of helium fraction.

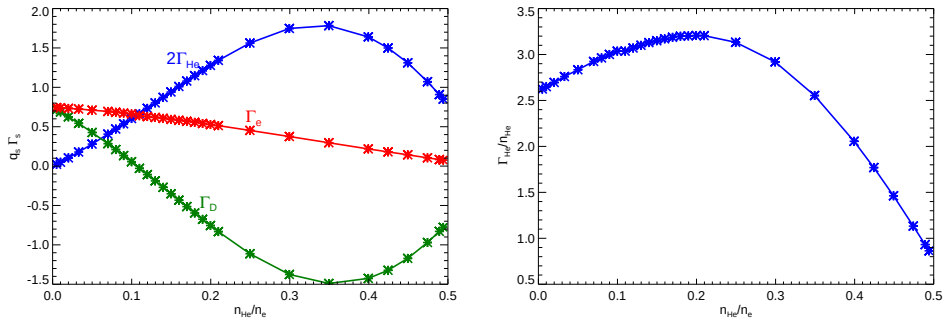

Figure 3.51: Left: Helium, deuterium, and electron fluxes (scaled by charge) versus helium concentration, in normalized units. Right: Helium flux divided by helium density versus helium concentration, in normalized units

Chapter 4

Minority Ion Profile Effects on ICRF Heating

4.1 Introduction

Injection of electromagnetic waves in the ion cyclotron range of frequencies (ICRF) is frequently used in many tokamak devices, and ion cyclotron resonance heating (ICRH) is the primary auxiliary heating method on Alcator C-Mod. ICRH refers to electromagnetic waves injected into the plasma at frequency which matches a multiple of an ion cyclotron frequency somewhere in the plasma, and is either directly accelerates the ions or undergoes mode conversion and is absorbed mainly by electrons through various mechanisms. ICRH allows reaching electron and ion temperatures significantly higher than Ohmic heating alone, and is needed to achieve top performing plasmas on C-Mod. ICRH can also provide an external drive for plasma current[145] or plasma rotation[123], which could be useful in attaining steady-state advanced tokamak operation or for reducing plasma turbulence by controlling flow shear.

Ion cyclotron resonances occur when the wave frequency reaches a multiple of the cyclotron frequency, which is given by

$$\omega_{cj}(\mathbf{r}) = \frac{q_j B(\mathbf{r})}{m_j} \tag{4.1}$$

where q_j is the charge, B is the amplitude of the magnetic field, and m_j is the mass. For convenience, the sign of the charge is kept, so the sign of ω_{cj} tells the direction of gyration (positive=left-handed). When a passing wave matches the cyclotron frequency, and the polarization of the wave matches the direction of the particle's gyration, energy can be resonantly transfered between the wave and particles. Due to the high entropy of particle motion, this usually results in wave absorption by the plasma. In a tokamak, the magnetic field scales approximately as $1/R$, where R is the major radius, so, for a fixed frequency of input electromagnetic waves, the cyclotron resonances occur at nearly vertical band-like regions in the plasma (figure 4.1).

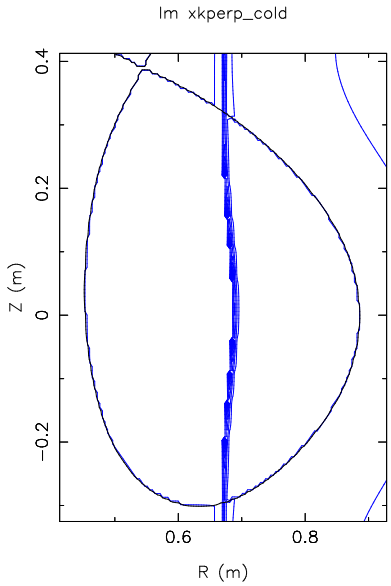

Figure 4.1: ICRF ^{3}He minority resonance for shot 1110323025, based on cold plasma dispersion relation.

When multiple ion species are present in the plasma, the ion density

distributions have crucial effects on the wave propagation and absorption dynamics. The most important ICRF heating mechanism, called minority heating, utilizes a two ion species plasma in which the concentration of one species, the minority ion, is a few percent of the concentration of the main ion[166]. In this case, the minority species acts as an impurity and the minority distribution is governed by impurity transport. At higher concentrations of the minority ion, mode conversion becomes the dominant heating mechanism.

On C-Mod, up to 5 MW of ICRF power is injected into the fast magnetosonic wave (fast wave) by three ICRF antennas[194] (see figure 1.6). The D-port antenna and E-port antenna each contain two current straps and operate at 80.5 MHz and 80 MHz. The J-port antenna contains four current straps which allows for a flexible phasing configuration and can operate over a range of frequencies.

The most common heating scenario on Alcator C-Mod uses first harmonic heating of H and second harmonic heating of D in a D(H) plasma[1], where the ratio of H to H+D is about 5 %. For this scenario, with $B_T = 5.4\,\mathrm{T}$, an ICRF frequency of 80 MHz puts the first harmonic H and second harmonic D resonances in the center of the plasma. ICRF experiments are also performed on C-Mod for D(^{3}He) plasma. In this case, options include setting $B_T = 8\,\mathrm{T}$ and $\omega = 80\,\mathrm{MHz}$ or $B_T = 5.4\,\mathrm{T}$ and $\omega = 50\,\mathrm{MHz}$ to put the minority resonance

[1]In a mixed plasma, the notations D(H) or (H)D both refer to a plasma composition where the majority of ions are deuterium and a small fraction are hydrogen. There can be more than one minority ion, e.g. (^{3}He)(H)D.

near the center of the plasma. One advantage of ^{3}He experiments is that the lower cyclotron absorption efficiency allows better study of mode conversion physics. Another advantage is that He CXRS can be used to directly measure the minority species, which can give us useful insight into the power deposition mechanism and generation of fast ions.

This chapter will focus on the helium minority measurements and simulations of the helium effects on power deposition.

4.2 ICRF Waves in Plasmas

The study of electromagnetic waves in magnetized plasmas is complex due to the anisotropy imposed by the magnetic field and the large number of solutions. A full treatment of waves in plasma is beyond the scope of this work, but background relevant to minority heating and mode conversion heating will be given.

The electromagnetic wave equation is

$$\nabla \times \nabla \times \mathbf{E} = -\frac{1}{c^2}\left(\frac{\partial^2 \mathbf{E}}{\partial t^2} + 4\pi \frac{\mathbf{J}}{\partial t}\right) \tag{4.2}$$

All of the wave physics are contained within this seemingly simple equation. However, the current $\mathbf{J}$ has a very complicated dependence on $\mathbf{E}$, which makes closure of these equations very difficult. In principle, the current can be exactly solved from the equations of motion for charged particles under the Lorentz force. However, the Lorentz force depends an electromagnetic field distribution which depends on the microscopic charge distribution, and solving for

these quantities self-consistently is a formidable task. To solve the equations, approximate forms for the current are needed, even for numerical simulations.

Generally, ICRF waves are sufficiently low amplitude that we can treat the plasma as a linear medium, and we can try to decompose the wave into Fourier modes. Then equation 4.2 can be written as

$$\mathbf{k} \times \mathbf{k} \times \mathbf{E}(\mathbf{k}, \omega) = -\frac{1}{c^2} \overleftrightarrow{\mathbf{K}}(\mathbf{k}, \omega) \cdot \omega^2 \mathbf{E}(\mathbf{k}, \omega) \tag{4.3}$$

where $\overleftrightarrow{\mathbf{K}}$ is known as the dielectric permittivity tensor. It is a second rank tensor which contains a directional dependence from the magnetic field. $\overleftrightarrow{\mathbf{K}}$ depends on the global properties of the entire plasma. In many situations, the plasma can be treated as slowly-varying[2], in which case Wentzel-Kramers-Brillouin (WKB) methods can be used, in which the homogeneous plasma solutions are assumed to apply locally (but see section 4.5.2).

The cold plasma approximation is frequently used to characterize ICRF waves due to the relative simplicity of the dispersion relation. The approximation assumes that the phase velocity of the wave is much greater than the thermal velocity, i.e.

$$\frac{\omega}{k_\parallel} \gg v_{th} \sim \sqrt{\frac{2T}{m_e}} \tag{4.4}$$

$$k_\perp \rho_i \ll 1 \tag{4.5}$$

It is fairly accurate in describing fast wave behavior far from the resonances, but is not adequate for treating the behavior near resonances, where k goes to

[2]Using the limit $|k^{-2}||\nabla k| \ll 1$

0. Nevertheless, it can be used find the locations of the resonances where the behavior must be examined more closely.

If the cold dielectric permittivity tensor is written out in terms of a special set of orthogonal basis vectors (right-handed circularly polarized perpendicular to **B**, left-handed circularly polarized perpendicular to **B**, linearly polarized parallel to **B**), the tensor is diagonal:[167]

$$\overleftrightarrow{\mathbf{K}}_{\text{cold}} = \begin{pmatrix} R & 0 & 0 \\ 0 & L & 0 \\ 0 & 0 & P \end{pmatrix} \tag{4.6}$$

where R, L, and P are the permittivities for waves with right-handed circular polarization, left-handed circular polarization, and linear polarization, typically called Stix parameters. In the Cartesian basis, letting $z = \hat{\mathbf{b}}$, $\overleftrightarrow{\mathbf{K}}_{\text{cold}}$ is given by

$$\overleftrightarrow{\mathbf{K}} = \begin{pmatrix} S & -iD & 0 \\ iD & S & 0 \\ 0 & 0 & P \end{pmatrix} \tag{4.7}$$

where

$$R = 1 - \sum_s \frac{\omega_{ps}^2}{\omega^2} \frac{\omega}{\omega + \omega_{cs}} \tag{4.8}$$

$$L = 1 - \sum_s \frac{\omega_{ps}^2}{\omega^2} \frac{\omega}{\omega - \omega_{cs}} \tag{4.9}$$

$$P = 1 - \sum_s \frac{\omega_{ps}^2}{\omega^2} \tag{4.10}$$

$$S = \frac{R + L}{2} \tag{4.11}$$

$$D = \frac{R - L}{2} \tag{4.12}$$

The summation is over all species. ω_{cs} is given in 4.1 and $\omega_{ps}^2 = \frac{n_s q_s^2}{\epsilon_0 m_s}$ is the plasma frequency. Figure 4.2 shows the values for the Stix parameters for a midplane cross section of a D(^{3}He) Alcator C-Mod plasma, with $n_{\mathrm{He3}}/n_e \approx 0.027$. Note that L and S contain poles at the ion cyclotron resonances.

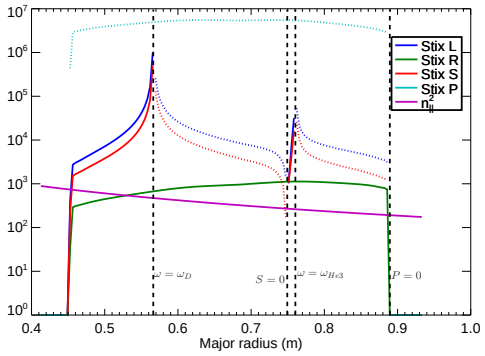

Figure 4.2: Cross sectional view of the Stix parameters L, R, and S at the midplane, shown on a logarithmic vertical axis. Positive parameter values are shown in solid lines and negative parameter values are shown inverted, with dotted lines. One possible choice of $n_\parallel$ is also shown, calculated for a toroidal mode $n_\phi = 13$. ^{3}He and D ion cyclotron resonances are also shown.

The wave equation 4.3 can be written[170]

$$\begin{pmatrix} S - n^2\cos^2\theta & -iD & n^2\cos\theta\sin\theta \\ iD & S - n^2 & 0 \\ n^2\cos\theta\sin\theta & 0 & P - n^2\sin^2\theta \end{pmatrix} \cdot \mathbf{E} = \mathbf{0} \tag{4.13}$$

where $n = \frac{kc}{\omega}$ is the index of refraction and θ is the wave propagation angle with respect to the magnetic field. The solutions (eigenvalues) for n^2 are given by the dispersion relation obtained by setting the determinant to zero:

$$An^4 - Bn^2 + C = 0 \tag{4.14}$$

where

$$A = S\sin^2\theta + P\cos^2\theta \tag{4.15}$$

$$B = RL\sin^2\theta + PS\left(1+\cos^2\theta\right) \tag{4.16}$$

$$C = PRL \tag{4.17}$$

This dispersion relation is often called the Appleton-Hartree equation.

Equation 4.14 can also be put into the compact form:[170, 156]

$$\tan^2\theta = -\frac{P\left(n^2-R\right)\left(n^2-L\right)}{\left(Sn^2-RL\right)\left(n^2-P\right)} \tag{4.18}$$

The cold plasma equations are quadratic in n^2 and admit two solutions:

$$n^2 = \frac{B \pm \sqrt{4AC}}{2A} \tag{4.19}$$

The two solutions have different phase velocities and are labeled the fast wave and the slow wave accordingly. In the zero electron mass limit, the (cold) fast wave solution can also be written as[167]

$$n_\perp^2 = -\frac{(n_\parallel^2-R)(n_\parallel^2-L)}{n_\parallel^2-S} \tag{4.20}$$

For waves travelling parallel or perpendicular to the magnetic field, the two solutions are also labeled according to the electric field polarization. For the parallel direction, there are R and L waves for right- and left-handed circular polarization. For the perpendicular direction, the solutions are labeled the ordinary (O) wave or the extraordinary (X) wave. Adopting the labeling of Allis, the O wave is unaffected by the magnetic field, and the X wave is affected.

The polarization of a solution is given by

$$\frac{iE_x}{E_y} = \frac{n^2 - S}{D} \tag{4.21}$$

4.2.1 Cutoffs and resonances

Cutoffs occur when the phase velocity goes to infinity, i.e. when n^2 goes through zero. Wave reflection occurs at cutoffs. In the eikonal approximation, a ray gradually approaching a cutoff plane at an acute incidence angle will bend away from the cutoff and never reach the cutoff plane, so cutoffs are barriers to propagation. In cold plasma theory, resonances occur where the phase velocity goes to zero i.e. when n^2 goes to infinity. Resonances are places where the cold plasma approximation breaks down. The behavior at resonances requires a more detailed theory, but typically results in absorption of the wave. The sign of n^2 changes at each cutoff and resonance, and the wave is evanescent in the region where $n^2 < 0$ which lies between a cutoff and resonance.

According to equation 4.18, cutoffs occur when $P = 0$, $R = 0$, or $L = 0$. For frequencies in the ICRF range (10s to 100s of MHz), there is a $P = 0$ cutoff at the edge of the plasma where the plasma density is very low. The ICRF antennas are located just outside the edge, so the wave energy must pass through the cutoff. This can be achieved by placing the antenna close to the plasma edge so that most of the ICRF power can tunnel through the cutoff and couple to the fast wave in the denser plasma. Close is defined relative to

the wavelength of the fast wave: $\Delta_{\text{ant}} k_\perp < 1$, where $\Delta_{\text{ant}} \sim 1\,\text{cm}$ is the gap distance and $|k_\perp| \sim 0.1\,\text{cm}^{-1}$.

Resonances do have an angular dependence. By taking the limit of 4.19 as $n^2 \to \infty$, we obtain the resonance condition

$$\tan^2\theta = -\frac{P}{S} \tag{4.22}$$

For waves traveling parallel to the magnetic field, the resonance occurs when $S \to \infty$. This occurs at either electron resonance ($R \to \infty$) or ion cyclotron resonances ($L \to \infty$). For waves traveling exactly perpendicular to the field, resonance occurs at $S = 0$. These latter resonances are called hybrid resonances. For plasmas with multiple ion species with different charge to mass ratios, there are ion-ion hybrid resonances (IIH) between adjacent ion cyclotron resonances. For a two-ion plasma, the IIH occurs at[26]

$$\omega_{ij}^2 = \omega_{ci}\omega_{cj} Z_i Z_j \left(\frac{m_i X_i + m_j X_j}{m_j Z_i^2 X_i + m_i Z_j^2 X_j} \right) \tag{4.23}$$

where m, Z, and X refer to the mass, charge, and density fraction of ions i and j. For a plasma with a minority and majority species, the ion-ion hybrid resonance appears close to the minority ion cyclotron resonance and moves toward the majority ion cyclotron resonance as the minority fraction is increased. This has important implications for ICRH. Figure 4.3 shows the Stix parameters with similar circumstances to figure 4.2 except that $n_{\text{He3}}/n_e \approx 0.145$ near the IIH. The $S = 0$ surface has moved significantly inward. At oblique angles, the resonance occurs between the ion cyclotron resonance and the IIH, where $n_\parallel^2 = S$.

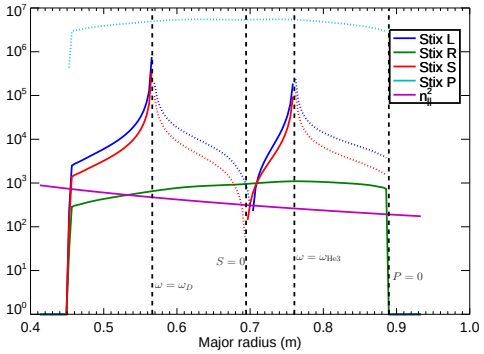

Figure 4.3: Cross sectional view of the Stix parameters L, R, and S at the midplane, shown on a logarithmic vertical axis. Positive parameter values are shown in solid lines and negative parameter values are shown inverted, with dotted lines. One possible choice of $n_\parallel$ is also shown, calculated for a toroidal mode $n_\phi = 13$. ^{3}He and D ion cyclotron resonances are also shown.

It should be noted that resonances, defined by $k \to 0$, don't really exist in the hot plasma framework, and are replaced by regions where $\mathfrak{Im}\{k\} > \mathfrak{Re}\{k\}$.

4.3 Hot plasma dispersion relation

Kinetic theory can be used to obtain the wave solutions when thermal velocity is not negligible or when the particles are not in a thermal distribution. In hot plasmas, collisions can typically be neglected, so the basic equation for kinetic theory is the Vlasov equation:

$$\frac{\partial f_s}{\partial t} + \mathbf{v}_s \cdot \nabla f_s + \frac{q_s}{m_s}\left(\mathbf{E} + \frac{1}{c}(\mathbf{v} \times \mathbf{B})\right) \cdot \nabla_{\mathbf{v}} f_s = 0 \tag{4.24}$$

where $f_s \equiv f_s(\mathbf{r}, \mathbf{v}, t)$ is the distribution function for species s.

The derivation of the hot plasma dispersion relation is lengthy and I

will simply give the result. For a Maxwellian equilibrium distribution function with zero mean velocity, the dielectric permittivity tensor can be written[170]

$$K_{xx} = 1 + \sum_s \frac{\omega_{ps}^2}{\omega^2} \frac{e^{-\lambda_s}}{\lambda_s} \xi_{0s} \sum_{n=-\infty}^{\infty} n^2 I_n(\lambda_s) Z(\xi_{ns}) \tag{4.25}$$

$$K_{xy} = -K_{yx} = i \sum_s \frac{q}{|q|} \frac{\omega_{ps}^2}{\omega^2} e^{-\lambda_s} \xi_{0s} \sum_{n=-\infty}^{\infty} n \left(I_n(\lambda_s) - I_n'(\lambda_s) \right) Z(\xi_{ns}) \tag{4.26}$$

$$K_{xz} = K_{zx} = \sum_s \frac{\omega_{ps}^2}{\omega^2} \frac{e^{-\lambda_s}}{\sqrt{2\lambda_s}} \xi_{0s} \sum_{n=-\infty}^{\infty} n I_n(\lambda_s) Z'(\xi_{ns}) \tag{4.27}$$

$$K_{yy} = 1 + \sum_s \frac{\omega_{ps}^2}{\omega^2} \frac{e^{-\lambda_s}}{\lambda_s} \xi_{0s} \sum_{n=-\infty}^{\infty} \left(n^2 I_n(\lambda_s) + 2\lambda_s^2 \left[I_n(\lambda_s) - I_n'(\lambda_s) \right] \right) Z(\xi_{ns}) \tag{4.28}$$

$$K_{yz} = -K_{zy} = -i \sum_s \frac{q}{|q|} \frac{\omega_{ps}^2}{\omega^2} \sqrt{\frac{\lambda_s}{2}} e^{-\lambda_s} \xi_{0s} \sum_{n=-\infty}^{\infty} \left(I_n(\lambda_s) - I_n'(\lambda_s) \right) Z'(\xi_{ns}) \tag{4.29}$$

$$K_{zz} = 1 - \sum_s \frac{\omega_{ps}^2}{\omega^2} e^{-\lambda_s} \xi_{0s} \sum_{n=-\infty}^{\infty} I_n(\lambda_s) \xi_{ns} Z'(\xi_{ns}) \tag{4.30}$$

where $I_n(\lambda_s)$ is the modified Bessel function of order n,

$$\lambda_s = \frac{T_s k_\perp^2}{m_s \omega_{cs}^2} \tag{4.31}$$

and $Z(\xi_{ns})$ is the Fried-Conte dispersion function[170]

$$Z(\xi_{ns}) = \pi^{-1/2} \int_{-\infty}^{\infty} \frac{e^{-t^2}}{t - \xi_{ns}} \, \mathrm{d}t \tag{4.32}$$

$$\xi_{ns} = \frac{\omega - n\omega_{cs}}{k_\parallel v_{Ts}} \tag{4.33}$$

More general forms (non-zero flow, non-Maxwellian) can be found in [170].

The wave equation takes the form

$$\begin{pmatrix} \kappa_{xx} - k_z^2 - k_y^2 & \kappa_{xy} + k_x k_y & \kappa_{xz} + k_x k_z \\ \kappa_{yx} + k_y k_x & \kappa_{yy} - k_x^2 - k_z^2 & \kappa_{yz} + k_y k_z \\ \kappa_{zx} + k_z k_x & \kappa_{zy} - k_z k_y & \kappa_{zz} + k_\perp^2 \end{pmatrix} \begin{pmatrix} E_x \\ E_y \\ E_z \end{pmatrix} = 0 \tag{4.34}$$

where $\overleftrightarrow{\kappa} = \frac{\omega^2}{c^2}\overleftrightarrow{K}$ and the dispersion relation is

$$\begin{aligned} 0 = \left[\left(k_\parallel^2 - \kappa_{xx}\right)\left(k^2 - \kappa_{yy}\right)\right]\kappa_{zz} + k_\perp^2\left[\left(k^2 - \kappa_{yy}\right)\kappa_{xx} - \kappa_{xy}^2\right] \\ +\kappa_{xy}\left(k^2 - \kappa_{yy}\right)\left(2k_\perp k_\parallel + \kappa_{xz}\right) - \kappa_{yz}\left[\left(k_z^2 - \kappa_{xx}\right)\kappa_{yz} + 2\kappa_{xy}\left(k_\perp k_\parallel + \kappa_{xz}\right)\right] \end{aligned} \tag{4.35}$$

The hot dispersion relation has two pairs of roots in the ion cyclotron range of frequencies. These roots can be called the fast and slow waves, and come in pairs because they can travel in either direction. The fast wave (FW) is essentially the same as the fast wave in the cold plasma approximation, with slight modification near the resonances. The slow wave is very different from the cold plasma slow wave, and it comes in two different flavors, depending on the local plasma parameters. The slow wave is called the Ion Bernstein Wave (IBW) or the Ion Cyclotron Wave (ICW) depending on which side of the resonance region it propagates on. Figure 4.4 shows the hot dispersion roots near the IIH for one set of parameters. The IBW is a mainly electrostatic that propagates on the high field side of the IIH. As the IIH is approached from the high field side, the IBW and FW come together and intersect. When the IBW exists, the slow wave on the low field side is purely imaginary.

For different parameters, the slow wave is imaginary on the high field side and mostly real on the low field side. In this case, it is called the Ion

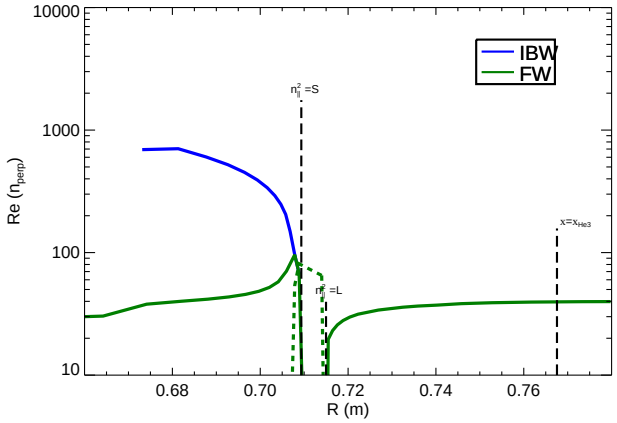

Figure 4.4: Hot dispersion relation near the ion-ion hybrid resonance for shot 1110323006 along the midplane. The dashed line indicates the imaginary part of the dispersion root.

Cyclotron Wave (ICW). The ICW connects to the FW near the high field side of the IIH but branches out on the low field side. The IBW primarily appears near the midplane, while the ICW appears above and below the midplane[180].

A significant difference between cold and hot plasma solutions is that the hot plasma solutions are complex valued. The imaginary part of the wavevector indicates damping (or possibly amplification). The greatest damping occurs near the IIH, but the slow waves have significant damping everywhere. Literature identifies several kinds of damping that can occur in the absence of collisions (which are not included in hot plasma theory based on the Vlasov equation).

Landau damping[117] occurs when the longitudinal electric field of a wave resonantly interacts with a particle species. Wave energy is absorbed

when the velocity space distribution function has a negative gradient (in the direction of propagation) in the vicinity of the phase speed. Amplification can occur with a positive gradient, which can be induced by a beam. It is associated with $\mathfrak{Im}\{K_{zz}\}$.

Transit time magnetic pumping (TTMP)[14] is a related phenomenon in which the transverse magnetic field of a wave resonates with the particle orbits and can be thought of as a magnetic analog to Landau damping. It is associated with $\mathfrak{Im}\left\{K_{yy}\right\}$.

The hot plasma dielectric function also contains a cross term associated with $\mathfrak{Im}\left\{K_{yz}\right\}$ which may also provide damping[150].

Collisionless cyclotron damping occurs near harmonics of the cyclotron resonances. When a suitably polarized wave moves past a particle which is gyrating at close to the wave frequency, energy can be exchanged between the wave and particle. If the distribution function is decreasing with perpendicular velocity, then, on average, wave energy is transferred to perpendicular kinetic energy. It is associated with $\mathfrak{Im}\left\{K_{yz}\right\}$.

4.4 Toroidal modes and antenna phasing

As the electromagnetic waves propagate through the plasma, the propagation angle may change, but the toroidal mode is a constant of motion. This is a consequence of the toroidal symmetry of the tokamak, which is a good approximation at ICRF scales. This fact allows the waves in each toroidal

mode to be analyzed independently (in the linear limit), which eases the computation. The toroidal mode number enters into the expression for the parallel index of refraction:

$$n_{\|} = \frac{c}{\omega}\left(\frac{n_\phi}{R} - \frac{mB_\theta}{rB_\phi}\right) \tag{4.36}$$

where m is the poloidal mode number of a particular wave solution. Since, in a tokamak, the toroidal field is dominant, it can be convenient to neglect the poloidal field term and obtain the simple equation:

$$n_{\|} \approx \frac{cn_\phi}{\omega R} \tag{4.37}$$

This is a good approximation for fast waves, but less appropriate for waves with high m, such as the IBW and ICW. In ICRF lingo, the poloidal mode correction to $n_{\|}$ or $k_{\|}$ is known as the *upshift*.

When the ICRF antennas couple to the system, the wave energy is divided among all possible toroidal modes, with a distribution that depends on the geometry of the antenna straps and the phasing of the currents that is applied to them. The intensity available to the toroidal modes is given by the spatial power spectrum of the antenna current (with complex phase) summed over all straps. [3]

The J antenna on C-mod has four straps which allows several different phasing options, useful for exciting different toroidal modes. The main configurations are: $[0, \pi, 0, \pi]$ (heating), $[0, \pi, \pi, 0]$, $[0, 0, \pi, \pi]$ (dipole), $\left[0, \frac{\pi}{2}, \pi, \frac{3\pi}{2}\right]$

[3]Not all available antenna power makes it into the plasma. The edge cutoff acts as a filter for high $k_{\|}$ (which tend to be reflected), but this effect depends on detailed plasma geometry so the intensity available from the antenna, truncated at some $k_{\|}$, is often used.

(90°), and $\left[0, \frac{3\pi}{2}, \pi, \frac{\pi}{2}\right]$ $(-90°)$. The $[0, 0, 0, 0]$ (monopole) phasing has been tried a few times but appears to generate a lot of sputtering and negligible heating. Figures 4.5 and 4.6 show power spectra for the J-port antenna with various phasing configurations. The first set of configurations shows symmetric phasing configuations, and the second set shows two assymmetric phasings. The assymmetric configurations provide torque to the plasma and are used in some flow drive experiments.

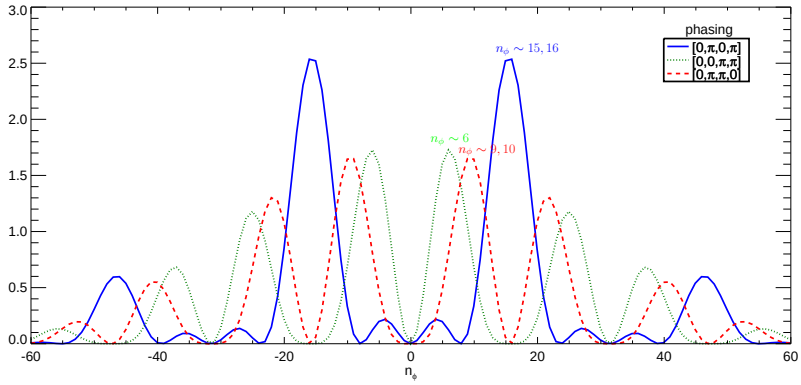

Figure 4.5: Toroidal power spectra from J-port antenna, symmetric phasing.

Although a full spectrum consist of many toroidal modes, approximate behavior can be obtained by analyzing a few toroidal modes or even a single mode at the peak of the power spectrum. This is done in numerical simulations to reduce computation time. For example, with heating phasing, $[0, \pi, 0, \pi]$, the general resonance structure can be obtained by setting $n_\phi = 15$ and $k_\parallel \sim 15/R$.

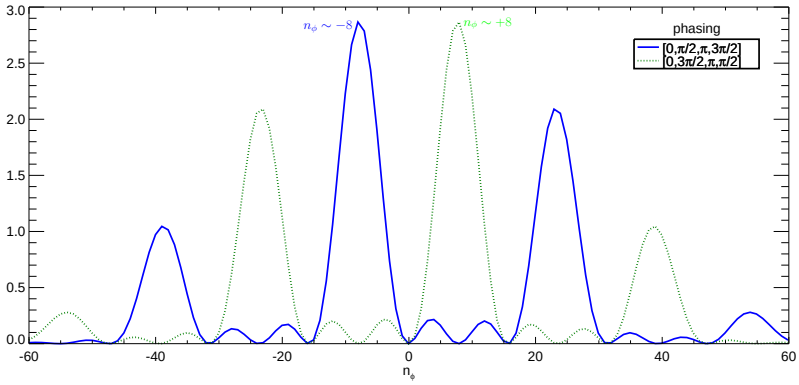

Figure 4.6: Toroidal power spectra from J-port antenna, assymmetric phasing.

4.5 Heating by ICRF Waves

Ion cyclotron heating is advantageous in the fact that it heats ions directly. One benefit is that this can lead to a population of fast ions which can increase the fusion reactivity beyond that of a thermal plasma.

The simplest scheme envisionable for ICRF heating is to launch waves which will resonate with the main ions at the first harmonic, known as ion cyclotron resonance heating. However, an analysis of the cold plasma equations will show that this will not work. A short explanation follows.

Figure 4.7 is a CMA diagram (named after Clemmow, Mullaly, and Allis)[32, 1], which shows the topology of cold plasma wave solutions spanning a range of magnetic field strengths and densities. For a fixed wave frequency, the magnetic field increases along the y-axis, and density increases along the x-axis. Approximate locations of the antenna and the tokamak plasma core are indicated, so wave energy must traverse the regions indicated by the broken red

line. Note that the antenna frequency has been chosen such that the tokamak core is at the ion cyclotron resonance, where $L \to \infty$.

We can see two problems here. The first is that the antennas are located in a low density region on the opposite side of the $P = 0$ surface which is a cutoff. The solution to the first problem is to place the antennas as close as practical to the plasma edge. The wave energy can tunnel through the short space between the antenna and the dense plasma region. The second problem is that the slow wave (which is the L wave when propagating parallel to the field) can not propagate in the region between the antenna and resonance layer, and it is the left-polarized L wave which can heat ions through cyclotron damping. Only the fast wave has accessibility to the core plasma at ICRF frequencies. But the fast wave cannot heat the main ions because it has no left-handed circularly polarized component at the cyclotron resonance.

Let us look more closely at the polarization fraction of the fast wave solution. The second row of 4.13 can be rearranged into

$$E_x + iE_y = \frac{R - n^2}{D} iE_y \tag{4.38}$$

Therefore, the polarization ratio $|E_+/E_y|$ is given by

$$\left|\frac{E_+}{E_y}\right| \equiv \left|\frac{E_x + iE_y}{E_y}\right| = \left|\frac{R - n^2}{D}\right| = \left|\frac{n_\perp^2 + n_\parallel^2 - R}{D}\right| \tag{4.39}$$

Plugging in the fast wave solution for $n_\perp^2$ from 4.20 gives

$$\left|\frac{E_+}{E_y}\right| = \left|\frac{(n_\parallel^2 - R)(n_\parallel^2 - L)}{(n_\parallel^2 - S)D} + \frac{n_\parallel^2 - R}{D}\right| \tag{4.40}$$

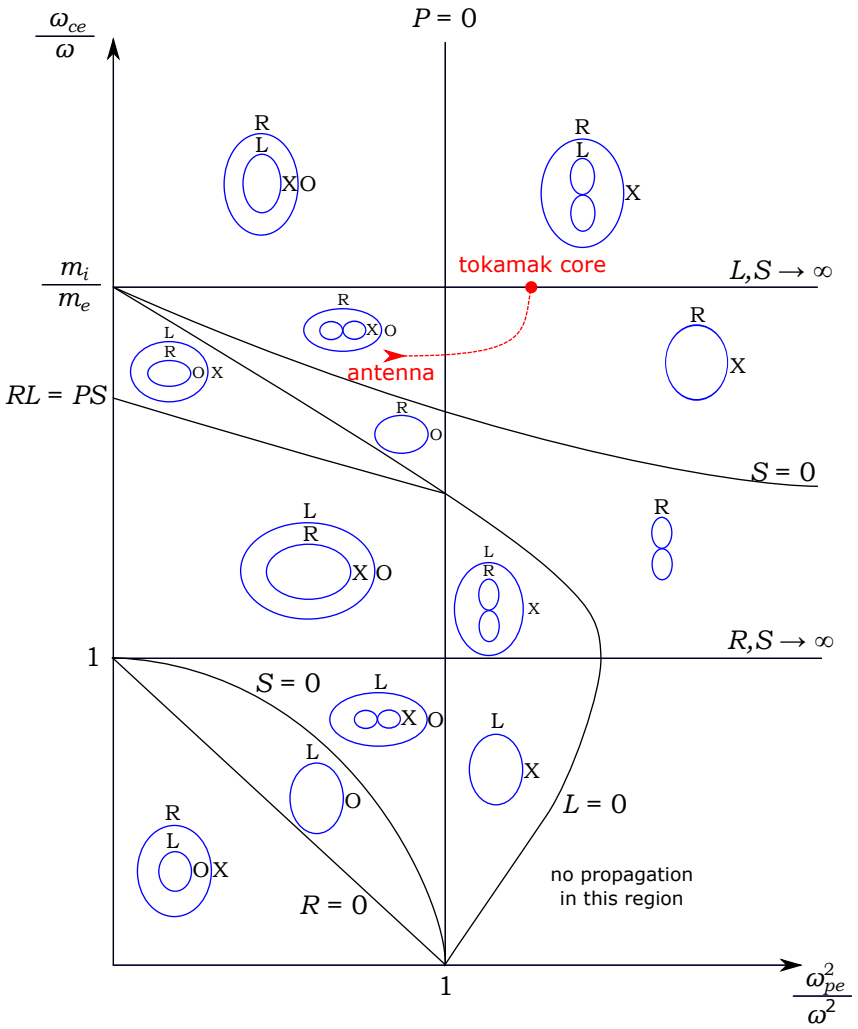

Figure 4.7: CMA diagram for a single ion plasma (not to scale). Black lines show region boundaries. Blue circles and lemniscoids show wave normal surfaces for wave solutions within each region. The wave normal surfaces are labeled R, L, X, and O. When one wave normal surface is drawn within another, the outer and inner surface represent the fast and slow waves, respectfully.

The following appoximation[150] is valid close to the main ion cyclotron resonance:

$$\left|\frac{E_+}{E_y}\right|^2 = \frac{(\omega/\omega_{ci}-1)^2(\omega/\omega_{ci}-\cos^2\theta)^2}{|\omega/\omega_{ci}(1+\cos^2\theta)|^2} \tag{4.41}$$

When hot plasma effects are included, the polarization ratio result is modified, and is given by[150]

$$\frac{|E_1^+|}{|E_y|^2} = \frac{1}{1+\sigma_1^2} \tag{4.42}$$

where

$$\sigma_1^2 = \frac{\pi}{4}\left(\frac{n_2 m_1 Z_2^2}{n_1 m_2 Z_1^2}\right)^2 \left(1-\frac{\omega_{c1}^2}{\omega}\right)^2 \left(\frac{\omega}{k_\parallel v_{Ti}}\right)^2 \tag{4.43}$$

The cold plasma fast wave polarization ratio along the midplane is plotted in figure 4.8 for a D(^{3}He) plasma. The fast wave is completely right-circularly polarized at the main ion cyclotron resonance, hence its association with the R wave.

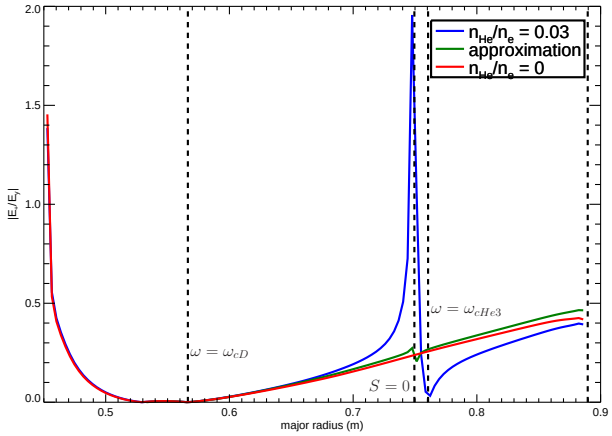

Figure 4.8: Fast wave polarization ratio $|E_+/E_y|$ for a deuterium plasma with about 3 % ^{3}He, approximation 4.41, and a pure deuterium plasma.

Early experiments attempted to circumvent this issue by utilizing the second harmonic ion cyclotron resonance for fast wave heating. This is a relatively weak effect arising from finite Larmor radius effects in the hot plasma dispersion relation.

The density fraction of the minority species plays a key role in determining the relative importance of different heating avenues and the primary heating mode[150].

In (^{3}He)D plasmas with a small helium fraction, $X[^3\mathrm{He}] \equiv n_{^3\mathrm{He}}/n_e \lesssim 6\,\%$, minority heating is the dominant heating mechanism. When the helium fraction is greater, $X[^3\mathrm{He}] \gtrsim 10\,\%$, mode conversion heating becomes the dominant mechanism. As the minority concentration is increased, the ion-ion hybrid resonance moves inward, increasing the gap δ between the ion-ion hybrid resonance and the minority cyclotron resonance.

4.5.1 Minority Heating

In early ICRF experiments plasmas, it was observed[105, 148] that there is another absorption mechanism for fast waves other than direct absorption at the ion cyclotron resonance. The fast waves can be mode converted to shorter wavelength modes and absorbed primarily by electrons through Landau damping or TTMP. This mechanism is frequently utilized in ^{3}He minority experiments on C-Mod. The ICRF absorption physics are convered in more depth in section 4.5.

Minority heating was originally envisioned for a tritium majority, deu-

terium minority plasma, as a way to achieve efficient heating of the deuterium[166]. In early ICRF experiments, attempts were made to heat the plasma using 2nd harmonic heating of deuterium on ATC[173] and T-4[104]. These found anomalously high ICRF absorption efficiencies as well as the presence of high energy protons during heating. These effects were attributed to the presence of a small amount of hydrogen impurity in the deuterium plasma, which absorbed strongly at the first harmonic.

Figure 4.9 shows a poloidal cross section diagram of the fast wave propagation areas.

In figure 4.8, we see that the cold plasma polarization ratio drops to zero at both ion cyclotron resonances, and reaches a peak near the ion-ion hybrid resonance. When the density fraction of the minority ion is small, the ion-ion hybrid resonance is very close to the minority resonance. Although the left polarization fraction is zero at the cyclotron resonance, cyclotron damping can still occur due to hot plasma effects. A heuristic argument follows: there is a finite width to the cyclotron resonance layer due to parallel Doppler broadening of the ions, and the small scale polarization features near the minority resonance are washed out over the width of the resonance, so the hot plasma polarization curve tends to the single ion solution in 4.8.

The power absorbed by the minority ion is given by[150]

$$P_2 = \frac{\omega_{p2}}{16\pi^{1/2}} \frac{|E_+|^2}{k_\parallel v_{T2}} \exp\left[-\frac{(\omega - \omega_{c2})^2)}{k_\parallel^2 v_{T2}^2} \right] \tag{4.44}$$

where subscripts 1 and 2 refers to the majority and minority species. The

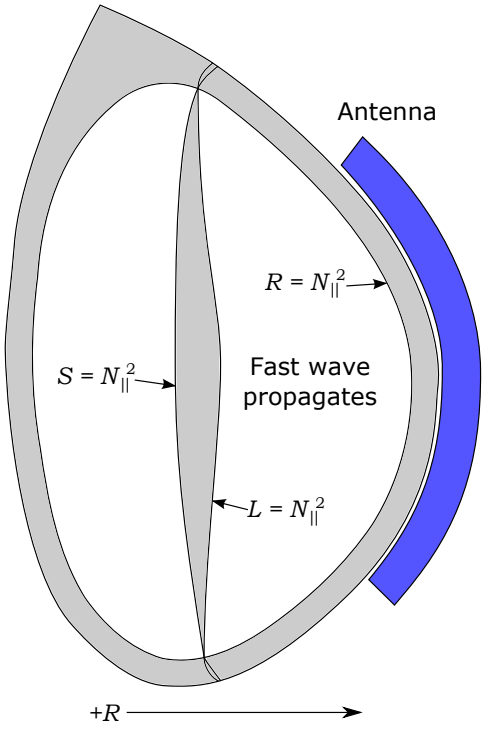

Figure 4.9: Fast wave resonances, cutoffs, and propagation volumes for a two ion species plasma (not to scale). Grey areas are areas where the fast wave is evanescent.

damping coefficient is obtained by integrating the absorption across the resonance layer and dividing by the Poynting flux $(c/8\pi)n_\perp|E_y|^2$, giving[150]

$$2\eta = \frac{\pi}{2}\frac{\omega_{p1}}{c}\frac{n_2}{n_1}\frac{Z_2}{Z_1}R\left|\frac{E_+}{E_y}\right|^2 \tag{4.45}$$

where R is the major radius.

In the limit that $\sigma_1^2 \ll 1$, minority heating is effective and scales with minority density. When $\sigma_1^2 \gg 1$, minority heating is ineffective. Figure 4.10 shows the value of σ_1^2 as a function of helium fraction and the damping coefficient.

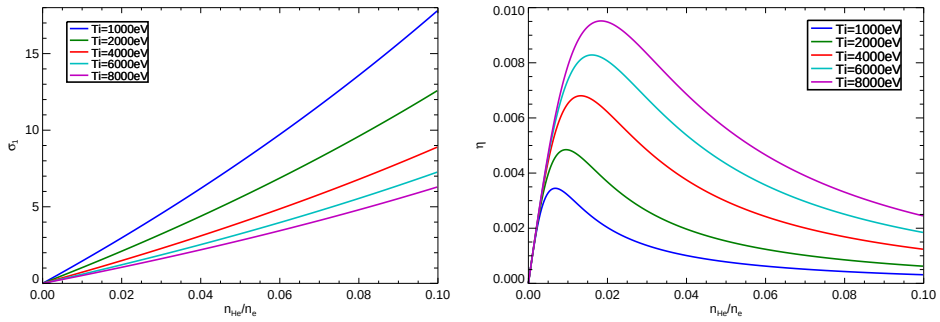

Figure 4.10: σ_1 from equation 4.43 and η from equation 4.45 for C-Mod conditions.

4.5.1.1 Width of resonance layer

Oblique fast waves traveling through the plasma will encounter ions with some spread of velocities in the parallel direction. The moving ions will experience a Doppler shifted frequency, which will broaden the region for resonant absorption.

A simple estimate of the width of the resonance layer, based on Doppler shift, is

$$\Delta = \frac{k_{\|} v_{Ti\|} R}{\sqrt{2}\omega} \tag{4.46}$$

For fast waves on Alcator C-mod, rough values are $k_{\|} \sim 16\,\mathrm{m}^{-1}$, $v_{Ti\|} \sim 3 \times 10^5\,\mathrm{m/s}$, $R \sim 0.7$, $\omega \sim 2\pi \times 50\,\mathrm{MHz}$, $\Delta \sim 0.007\,\mathrm{m}$.

The power spread in toroidal modes contributes to the power deposition width because the resonance position depends on $n_{\|}^2$. For $[0, \pi, 0, \pi]$ phasing, the approximate range of n_ϕ is $10 \ldots 22$, with an associated $n_{\|}^2 = S$ range of $180 \ldots 900$. For D(^{3}He), with $n_{He}/n_e = 0.03$, we get $\delta x \approx 0.002\,\mathrm{m}$.

For effective minority heating, the width of the resonance layer must exceed the distance between the IC resonance and the IIH, i.e.

$$\Delta > \delta = \sqrt{\omega_{c1} Z_1 Z_2 \left(\frac{m_1 X_1 + m_2 X_2}{m_2 Z_1^2 X_1 + m_1 Z_2^2 X_2} \right)} - 1 \tag{4.47}$$

4.5.1.2 Generation of Fast Ions

With minority heating, energy is resonantly transferred to perpendicular motion of the minority ions. The minority ion velocity distribution function is controlled by a competition between the perpendicular heating, collisions, which induce pitch angle scattering and slowing down of particles, synchrotron emission, and also particle loss. The result is a non-Maxwellian ion distribution with an excess of particles with high perpendicular velocity. The high energy particles are called fast ions or energetic particles. The fast ions can have energies much higher than the ion temperature, up to many MeV. However, fast ions are not well confined, which limits the attainable energy.

Analysis of the minority ion velocity distribution function was originally done by Stix in 1975[166]. Starting from the Fokker-Planck equation

$$\frac{\partial f}{\partial t} = -\nabla_v \cdot \left(\langle \Delta \mathbf{v} \rangle \, f \right) + \frac{1}{2} \nabla_v \cdot \left[\nabla_v \cdot \left(\langle \Delta \mathbf{v} \Delta \mathbf{v} \rangle \, f \right) \right] \tag{4.48}$$

the analysis includes the effects of heating through the quasilinear diffusion coefficient of Kennel and Engelmann, and the Coulomb collision operator of Chandrasekhar and Spitzer. It uses some simplifying assumptions: homogenous plasma, no transport effects are included, and analytic solution is only obtainable for the angle-averaged speed distribution function.

The isotropized (angle-averaged) distribution function is given by:

$$\ln f(v) = -\frac{E}{T_e(1+\xi)}\left[1 + \frac{R_j(T_e - T_1 + \xi T_e)}{T_1(1+R_1+\xi)} H\left(\frac{E}{E_1}\right)\right] \tag{4.49}$$

where

$$E = \frac{1}{2}mv^2 \tag{4.50}$$

$$R_1 \equiv \frac{n_1 Z_1^2 v_{Te}}{n_e v_{T1}} \tag{4.51}$$

$$\xi = \frac{m\langle P\rangle}{8\pi^{1/2} n_e n_2 Z^2 e^4 \ln\Lambda} v_{Te} \tag{4.52}$$

$$E_1(\xi) = \frac{m_2 T_1}{m_j}\left[\frac{1+R_1+\xi}{2\epsilon(1+\xi)}\right]^{2/3} \tag{4.53}$$

$$H(x) = \frac{1}{9x}\left[\sqrt{3}\pi + 6\sqrt{3}\arctan\left(\frac{2\sqrt{x}-1}{\sqrt{3}}\right) + 3\ln\left(\frac{1-\sqrt{x}+x}{1+2\sqrt{x}+x}\right)\right] \tag{4.54}$$

m_1 and m_2 are the majority and minority ion masses, T_1 is the majority ion temperature, v_{Te} and v_{T1} are the electron and majority ion thermal velocities. ξ is a parameter which relates to the average wave power density in the resonance layer. For the following set of parameters: $n_e = 1\times10^{14}\,\mathrm{cm}^{-3}$, $n_{\mathrm{He3}} = 2\times10^{12}\,\mathrm{cm}^{-3}$, $T_e = 2500\,\mathrm{eV}$, $\langle P\rangle = 2\,\mathrm{W/cm}^{-3}$; $\xi = 31$. The function must be normalized, e.g.

$$f_{\mathrm{norm}}(v) = n_1 f(v) / \int_0^\infty 4\pi v^2 f(v)\,\mathrm{d}v \tag{4.55}$$

The normalized Stix distribution is shown in figure 4.11 for several values of the wave power parameter. With no wave energy ($\xi = 0$), the result is Maxwellian. As ξ is increased, a larger fraction of the population occupies

the tails. For high energies, ($E \gg E_j$), the tail effective temperature asymtotes to $(1+\xi)T_e$.

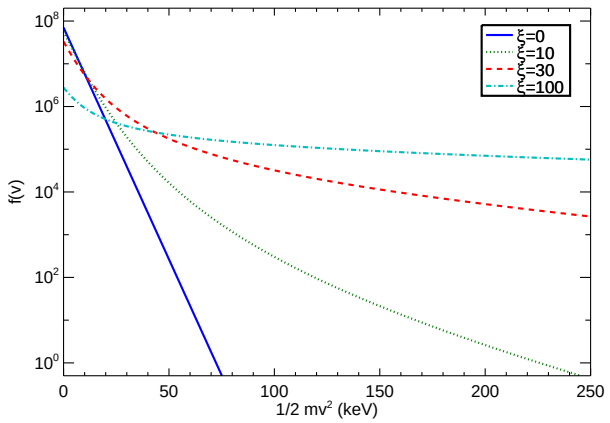

Figure 4.11: Minority ion isotropic speed distribution based on equation 4.49. $T_e = T_i = 4000\,\mathrm{eV}$, $Z_{eff} = 2$.

The full 2D distribution function is highly anisotropic because the heating is directed in the perpendicular direction. However, the peak in the angular distribution are shifted from the perpendicular direction due to the influence of banana orbits. Since the magnetic moment is an adiabatic invariant, the pitch angle of each particle changes as it follows an orbit. In the banana collisional regime, it is not useful to parameterize the distribution function by the instantaneous position and velocity of each particle but rather by the minor radius, speed, and pitch angle of the particle as it crosses the midplane.

From the conservation of magnetic moment, the turning points of a banana orbit are given by:

$$\frac{B(\mathbf{r}_{\mathrm{mid}})}{B(\mathbf{r}_{\mathrm{turn}})} = \sin^2\theta_0 \tag{4.56}$$

In a flux surface which crosses the midplane on the LFS of the ICRF resonance band, some banana orbits will never reach the resonance band. Only the orbits whose turning points intersect the resonance band or are on the HFS can receive heating. Therefore, there is a spread of pitch angles about perpendicular which receive no heating, with a half-angle given by

$$\alpha_c = \sqrt{1 - B_{mid}/B_{res}} \tag{4.57}$$

where B_{mid} is the minimum magnetic field amplitude on the particle's orbit and B_{res} is the magnetic field for cyclotron resonance. This half-angle becomes larger as we move to flux surfaces at larger radii, and disappears when the flux surface intersects the resonance layer at the midplane.

These analytical distributions require great simplifying assumptions and cannot properly handle the effects of transport, fast ion losses, finite deposition width, and magnetic geometry effects. The result also depends on a power deposition parameter ξ which is difficult to estimate. It seems that numerical simulations are required to address these limitations and hopefully achieve quantitively accurate results. Numerical simulations utilizing the CQL3D Fokker-Planck code, used in conjunction with AORSA wave solver, will be described in section 4.6.

Although simulations predict a generation of a large fraction of fast ions, fast ions are difficult to measure using CXRS because the background emission is high and the time-slice background subtraction technique allows low frequency noise through. Even in optimal conditions of low electron density

and low impurity content, direct observation of the fast ion signal is barely visible. Figure 4.12 shows the raw spectrometer signal at 4697.05 Å, equivalent to a Doppler energy of 7620 eV. The high resolution x-ray diagnostic (HIREX) has measured the argon ion temperature to be 2600 eV. If the helium-3 ions had a thermal distribution of the same temperature, the beam enhancement at this energy would be 0.05 % of the beam enhancement at the wavelength center. At 7620 eV Doppler energy, the beam enhancement is roughly 50 counts. The noise level is about $\sqrt{600} = 25$ counts. If the population is Maxwellian, we expect about 940 counts of enhancement at the wavelength center. This should be easily visible on the left plot of the figure, but the actual enhancement seems much less–very difficult to quantify because of the noise, but < 400 counts.

Unfortunately, it seems the fast ion visibility is too low for successful automated analysis. Section 4.6.5 will more carefully evaluate the visibility threshold. I have attempted to experimentally fit fast ions using a non-Gaussian model function, but the results were proven to be unreliable using Monte Carlo techniques.

4.5.2 Mode Conversion Heating

When a wave goes meets a resonance region, several things can happen to the energy of a wave. If the evanescent region is thin enough, the wave can tunnel through the barrier. It can be reflected, or absorbed, or also undergo mode conversion. Obtaining the fraction of power transmitted, re-

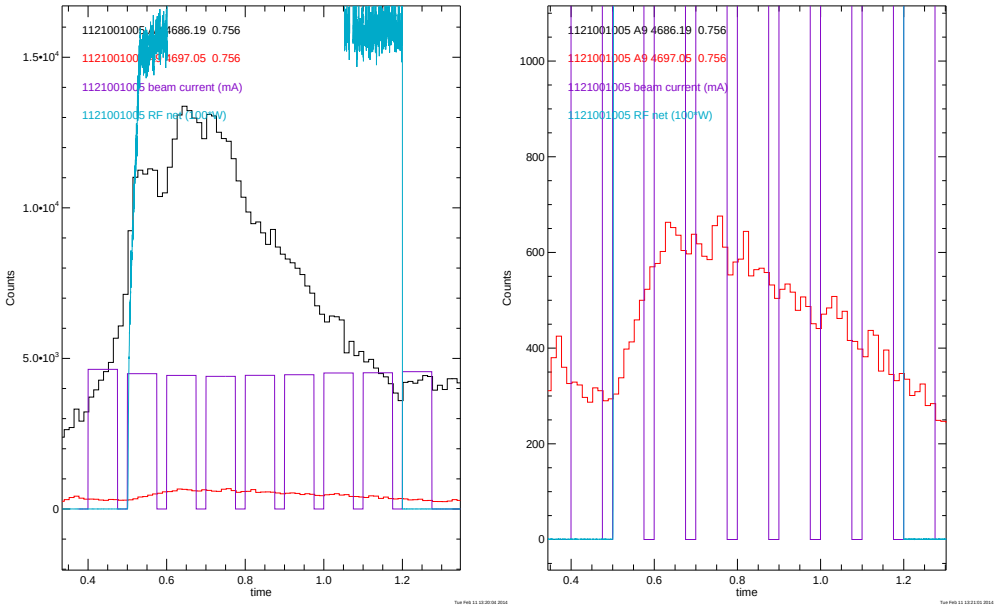

Figure 4.12: Raw spectrometer signal as a function of time for a toroidal channel passing $R_{\text{mid}} = 0.756\,\text{m}$ at 4686.19 Å and 4697.05 Å. Beam timing and ICRF envelope are also shown. RIght: zoom

flected, absorbed, or converted is a primary goal of mode conversion analysis. The scattering parameters, $\mathcal{T}, \mathcal{R}, \mathcal{A}, \mathcal{C}$ will refer to the amplitude ($\propto \sqrt{\text{power}}$) of the transmitted, reflected, absorbed, or converted wave.

In a multi-ion species plasma, a resonance/cutoff pair exists near the ion-ion hybrid resonance and minority cyclotron resonance. In the hot dispersion relation, the fast wave and another root come together at two points. This opens the opportunity for mode conversion to a nearby ion Bernstein wave or an ion cyclotron wave. Both waves are heavily Landau damped on electrons, so this type of mode conversion heating may be called mode conversion electron heating (MCEH). MCEH has been demonstrated on TFTR[128], Tore-

Supra[160], ASDEX-Upgrade[142], Alcator C-Mod[23, 124], and JET[130].

The tunneling factor η is defined as an optical depth for transmission: $\mathcal{T} = e^{-\eta}$. It is obtained by integrating the imaginary part of the k vector across the absorption region:

$$\eta = \int_{x_0}^{x_1} \mathfrak{Im}\left\{k(x)\right\} \mathrm{d}x \tag{4.58}$$

The power that is not transmitted is somehow split among absorption, reflection, and mode conversion. Calculating these scattering amplitudes is harder than calculating the tunneling factor, probably needing numerical analysis. But in the limit that absorption can be neglected, $\mathcal{R}$ and $\mathcal{C}$ can be computed.

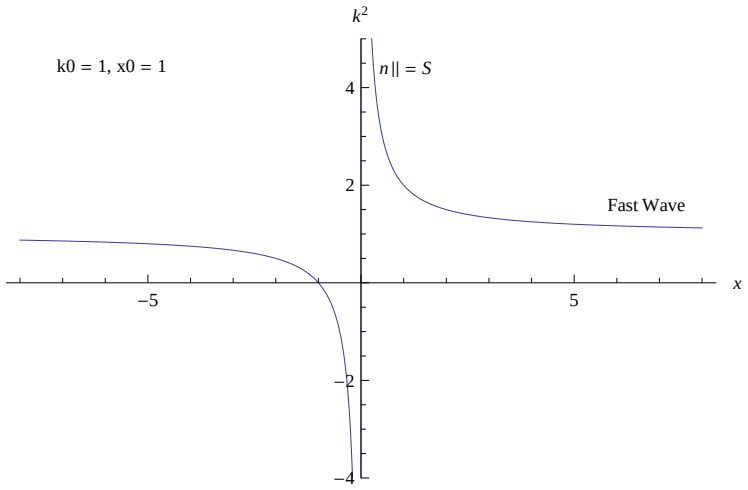

Figure 4.13: Budden equation 4.59 for $k_0 = 1$, $x_0 = 1$, modeling a fast-wave resonance.

Analytical treatment of the wave behavior near a resonance typically involves solving a model function which is topologically equivalent to the wave

equation in the vicinity of the resonance. An early 1D model for the resonance is the Budden equation[171],

$$k^2(x) = k_0^2 \left(1 + \frac{x_0}{x}\right) \tag{4.59}$$

which is plotted in figure 4.13. We can see that the Budden equation closely resembles the cold fast wave resonance, but it does not include the hot plasma solutions, which are an important feature of mode conversion. Analysis of the Budden equation produces a good estimate for the tunneling factor, but does not correctly handle what happens to energy not transmitted; energy is not conserved. The Budden equation has been superseded by tunneling equations which include additional roots and the possibility of mode conversion. The standard form for the tunneling equation is[171]

$$f^{(iv)} + \lambda^2 z f'' + (\lambda^2 z + \gamma) f = 0 \tag{4.60}$$

which is equivalent to the characteristic equation

$$k^4 - \lambda^2 z k^2 + \lambda^2 z + \gamma = 0 \tag{4.61}$$

This equation is plotted in figure 4.14, with the analogous hot dispersion roots labeled. Note that the low field side is on the left of this plot. The ion cyclotron wave is not included in this model. The tunneling factor can be calculated exactly for this model function[171]:

$$\eta = \frac{\pi}{2} \left| \frac{1 + \gamma}{\lambda^2} \right| \tag{4.62}$$

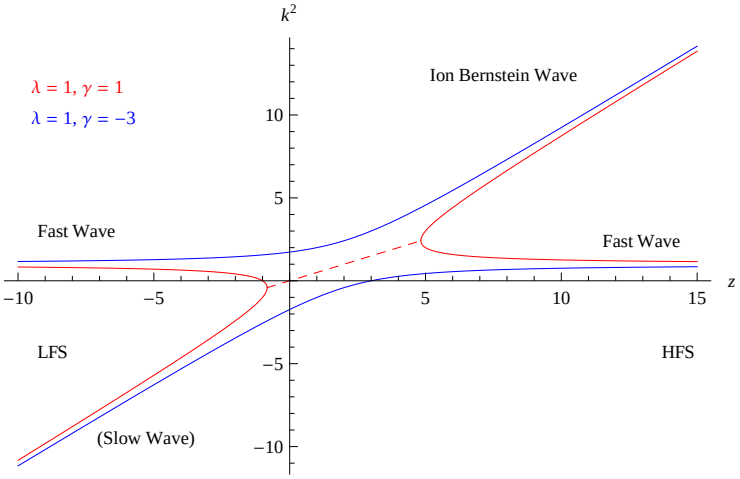

Figure 4.14: Tunneling equation 4.61 with two different parameter values. Solid lines indicate real solutions, and the dashed line indicates the real part of a complex solution.

The parameters λ, γ, and z are used to asymptotically match the model to the real dispersion relation at the IIH. This procedure requires an analytic expansion for the dispersion relation about the IIH resonance. This was performed by Swanson[171], assuming Maxwellian distributions and taking the distance to the resonance x, and $\lambda_j = \frac{1}{2}k_\perp^2\rho_{Lj}^2$ to be small. The matching

coefficients are

$$\lambda^2 = \frac{8c}{\omega_{p1} L \beta_1} \frac{\mu(\mu+\alpha)^{7/2}}{\alpha\delta(\mu^2-1)(\mu-1)^3(\mu\theta-1)(1_g)} \left[\frac{2\mu}{\delta f}\right]^{\frac{1}{2}} \tag{4.63}$$

$$\gamma = \frac{8\mu(\mu+\alpha)^3}{\beta_1\delta^2(\mu^2-1)(\mu-1)^2(\mu\theta-1)(1+g)} \tag{4.64}$$

$$\kappa = \frac{\omega_{p1}}{c}\left[\frac{(\mu-1)^2 f\delta}{2\mu(\mu+\alpha)}\right]^{\frac{1}{2}} \tag{4.65}$$

$$\beta_1 = 2\mu_0 n_1 \kappa T_1 / B_0^2 \tag{4.66}$$

$$f = \frac{1+\mu\alpha}{\mu+\alpha} \tag{4.67}$$

$$g = \frac{(\mu^2-1)[4-\mu f+\mu\alpha\theta(4\mu-f)]}{(\mu\theta-1)(\mu+\alpha)(4\mu-f)(4-\mu f)} \tag{4.68}$$

$$\delta = \frac{4\mu(1+\alpha)(\mu+\alpha)}{\alpha(\mu^2-1)(\mu-1)} - 2 \tag{4.69}$$

$$\alpha = \frac{q_2 n_2}{q_1 n_1} \tag{4.70}$$

$$\mu = \frac{q_1 m_2}{q_2 m_1} = \frac{\omega_{c1}}{\omega_{c2}} \tag{4.71}$$

$$\theta = \frac{q_1 T_2}{q_2 T_1} \tag{4.72}$$

where L is the magnetic field scaling: $B(x) = B_0(1 + x/L)$, so $L \approx R_{\mathrm{maj,IIH}}$. The tunneling equation, scaled for C-Mod D(^{3}He) plasma conditions, is shown in figure 4.15. We can see that the width of the domain where k^2 is complex closely matches the Doppler width of the resonance calculated heuristically in section 4.5.1.1.

In the limit of no absorption (no minority heating), the scattering pa-

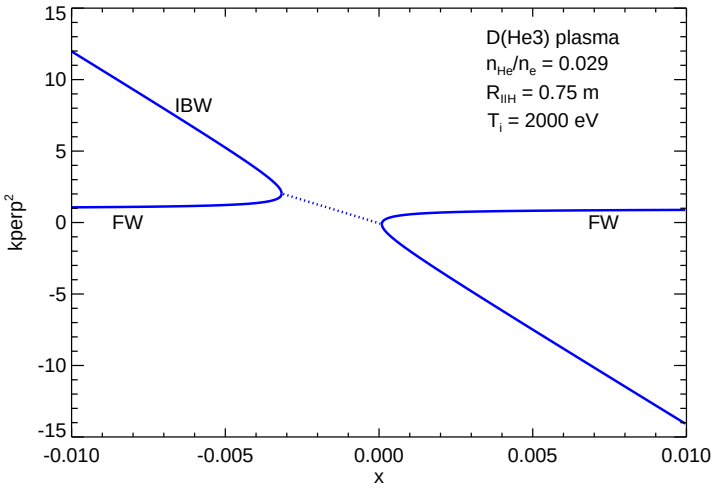

Figure 4.15: Tunneling equation scaled to match C-Mod plasma dispersion relation.

rameters for the tunneling equation for low field side launch are[150, 169]:

$$|\mathcal{T}|^2 = e^{-2\eta} \tag{4.73}$$

$$|\mathcal{R}|^2 = (1 - e^{-2\eta})^2 \tag{4.74}$$

$$|\mathcal{C}|^2 = e^{-2\eta}(1 - e^{-2\eta}) \tag{4.75}$$

This limit is applicable when distance between the IC resonance and IIH resonance is large and minority heating is weak. Apparently, single-pass mode conversion cannot exceed 0.25 of the input power, so boundary conditions and standing wave patterns could affect the final absorption, but these effects can only be treated in simulation. When absorption is included, the analytical results become very difficult.

In the case of D(^{3}He) plasma, both minority heating and mode conver-

sion heating contribute to the total heating.

It is apparent that the primary controlling parameter which determines the dominant heating mechanism is the ratio δ/Δ, where δ is the distance between the IC resonance and ion-ion hybrid resonance layers, and $\Delta \propto k_{\|} v_{Ti} R/\omega$ is the Doppler width of the IC resonance layer[122]. When the ratio is small, minority heating is the dominant heating mechanism. When the ratio is large, mode conversion is the dominant heating mechanism. Since the ion-ion hybrid resonance location depends on the minority ion fractions, this means that the minority density profile is a key factor in the power deposition analysis. For C-Mod D(^{3}He) plasmas, minority heating is dominant at $[^3\mathrm{He}] \lesssim 6\,\%$ and mode conversion is dominant at $[^3\mathrm{He}] \gtrsim 10\,\%$.

From a operational point of view, the main difference between minority heating and mode conversion heating is that minority heating directly heats the minority ions and generates fast ions, while mode conversion heating primarily heats electrons, which is useful for current drive due to the low mass of electrons.

4.6 Simulation of ICRF heating with AORSA and CQL3D

Many simplifying assumptions have been made for analytical treatment of ICRH. The dispersion functions given above are only strictly valid in infinite homogeneous plasmas and are approximately correct for plasmas which are spatially slowly varying. This approximation is not so good for a compact machine such as Alcator C-Mod, because the wavelength of the fast waves

($\sim 0.1\,\mathrm{m}$) is actually quite close to the tokamak dimensions ($a \approx 0.23\,\mathrm{m}$). The analysis is typically limited to asymptotic treatment of resonance layers in 1D, using Maxwellian or simpler ion distribution functions.

Numerical simulations allows the study of ICRH with realistic plasma geometry, in 2D or even 3D. Full-wave simulations can calculate situations where the eikonal treatment is inadequate. Much like a microwave oven, there can be hot and cold spots associated with antinode and node patterns.

4.6.1 All Orders Spectral Algorithm (AORSA)

AORSA[106] solves the inhomogeneous wave equation

$$-\nabla\times\nabla\times\mathbf{E}+\frac{\omega^2}{c^2}\left(\mathbf{E}+\frac{i}{\omega\epsilon_0}\mathbf{J}_p\right)=-i\omega\mu_0 J_{\mathrm{ant}} \tag{4.76}$$

and the nonlocal current equation

$$\mathbf{J}_p(\mathbf{r},t)=\sum_s\int_\infty^t \mathrm{d}t'\int \mathrm{d}^3\,r'\boldsymbol{\sigma}_s(f_s(E),\mathbf{r},\mathbf{r}',t,t')\mathbf{E}(\mathbf{r}',t) \tag{4.77}$$

where $\sigma(f_s(E),\mathbf{r},\mathbf{r}',t,t')$ is the plasma conductivity kernel. The kernel is evaluated to all orders in $\mathbf{k}\rho_s$ for an arbitrary minority distribution function f_2. The code includes a basic model for the antenna current, and calculates the electromagnetic field and quasi-linear diffusion coefficients for the minority ion[4] on the spatial grid. AORSA's algorithms are written to run on massively parallelized computing clusters with distributed memory, which allows higher resolution simulations than otherwise attainable.

[4]The diffusion coefficients give the rate of change in the ion distribution function induced by electromagnetic forcing.

Rather than solving the analytic approximations for the wave dispersion function, the wave equation is evolved directly. There is no finite Larmor radius approximation or Bessel function expansion, so the model is good to all orders in $k_\perp \rho$. This is important for properly handling mode conversion behavior near resonances, where long wavelength approximations break down. However, the computing time is quite long for an AORSA simulation, requiring about 2400 CPU-hours for a 400×256 grid resolution run on 4096 processors.

For an arbitrary non-Maxwellian species, the conductivity kernel is $\boldsymbol{\sigma}_s = -i\omega\epsilon_0 \boldsymbol{\chi}_s$, where the susceptibility tensor in normalized units[5] is[106]

$$\boldsymbol{\chi}_s = 2\pi \frac{\omega_{ps}^2}{\omega^2} \left[\sum_{l=-\infty}^{\infty} \int \frac{\mathrm{d}u_\parallel}{1 - (n_\parallel u_\parallel c/v_{\mathrm{norm}} - (l\omega_{cs}/\omega)} \int \mathrm{d}u_\perp U S_l \right. \\ \left. + \hat{\mathbf{e}}_\parallel \hat{\mathbf{e}}_\parallel \int \mathrm{d}u_\parallel \int \mathrm{d}u_\perp u_\parallel \left(u_\perp \frac{\partial f}{\partial u_\parallel} - u_\parallel \frac{\partial f}{\partial u_\perp} \right) \right] \tag{4.78}$$

where

$$U = \frac{\partial f}{\partial u_\perp} - \frac{n_\parallel c}{v_{\mathrm{norm}}} \left(u_\parallel \frac{\partial f}{\partial u_\perp} - u_\perp \frac{\partial f}{\partial u_\parallel} \right) \tag{4.79}$$

$$S_l = \begin{pmatrix} \frac{1}{2} u_\perp^2 J_{l+1}^2 & \frac{1}{2} u_\perp^2 J_{l+1} J_{l-1} & \frac{1}{\sqrt{2}} u_\perp u_\parallel J_{l+1} J_l \\ \frac{1}{2} u_\perp^2 J_{l+1} J_{l-1} & \frac{1}{2} u_\perp^2 J_{l-1}^2 & \frac{1}{\sqrt{2}} u_\perp u_\parallel J_{l-1} J_l \\ \frac{1}{\sqrt{2}} u_\perp u_\parallel J_{l+1} J_l & \frac{1}{\sqrt{2}} u_\perp u_\parallel J_{l-1} J_l & u_\parallel^2 J_l^2 \end{pmatrix} \tag{4.80}$$

where the argument to the Bessel functions J_n is $\xi = k_\perp v_\perp / \omega_{cs} = k_\perp u_\perp v_{\mathrm{norm}} / \omega_{cs}$.

AORSA assumes linear waves. The 2D version uses a rectangular grid on a poloidal cross section, and the main calculation is done on the Fourier

[5] velocities are normalized to $v_{\mathrm{norm}} = \sqrt{2E_{\mathrm{norm}}/m}$; f is normalized to n/v_{norm}^3, where n is the density

transformed grid. Since toroidal modes are uncoupled, a 3D calculation can be performed by looping over n_ϕ, at the cost of large computation time.

The current equation depends on the particle distribution functions. For ICRH simulation, each non-minority species is assumed to be Maxwellian, with density and temperature based on experiment. But the minority ion (^{3}He) is allowed to have a general 2D distribution. Section 4.5.1.2 describes how a non-Maxwellian population can form during ICRH. However, in this case, we can use numerical calculations for the minority distribution function as input to AORSA. These are provided from another code, CQL3D, described below.

Alcator C-Mod currently has three ICRF antennas operating at different frequencies, but AORSA is only capable of simulating a single frequency source at a time. The effect of multiple antennas can be obtained by summing the results of multiple simulations, due to the superposition principle, but this happens to be unnecessary for the experiments presented here, because only the J-port antenna is capable of running at 50 MHz. The D(^{3}He) experiments which will be simulated here use a magnetic field of 5.0 T to 5.7 T, which puts the minority resonance at 50 MHz near the center of the plasma. The D and E port antennas are frequently also running during the experiment, but they heat the hydrogen minority, which isn't the focus here. Their effects are passively included into the temperature profiles of the plasma used as input to the code.

The electric field is computed in a local magnetic coordinate system

which is defined by three orthogonal basis vectors, $\hat{\mathbf{e}}_\alpha$, $\hat{\mathbf{e}}_\beta$, and $\hat{\mathbf{e}}_b$. $\hat{\mathbf{e}}_\alpha$ is the part of the x unit vector that is perpendicular to $\hat{\mathbf{e}}_b$:

$$\hat{\mathbf{e}}_\alpha \propto \hat{\mathbf{e}}_x - (\hat{\mathbf{e}}_x \cdot \hat{\mathbf{e}}_b)\hat{\mathbf{e}}_b \tag{4.81}$$

$\hat{\mathbf{e}}_\beta$ is the remaining direction, $\hat{\mathbf{e}}_\beta = \hat{\mathbf{e}}_b \times \hat{\mathbf{e}}_\alpha$. These correspond to the lab frame $(\hat{\mathbf{e}}_x, \hat{\mathbf{e}}_y, \hat{\mathbf{e}}_z)$ when the poloidal field is zero.

The computed quasi-linear diffusion coefficients, $B_0(u_0, \theta_0, \rho)$, $C_0(u_0, \theta_0, \rho)$, $E_0(u_0, \theta_0, \rho)$, and $F_0(u_0, \theta_0, \rho)$ are four parts of the orbit-averaged diffusion operator $Q(\mathbf{E}, f_0)$:[106]

$$Q(f_0, \mathbf{E}) = \frac{1}{u_0^2}\frac{\partial}{\partial u_0}\left(B_0\frac{\partial f_0}{\partial u_0} + C_0\frac{\partial f_0}{\partial \theta_0}\right) + \frac{1}{u_0^2 \sin\theta_0}\frac{\partial}{\partial \theta_0}\left(B_0\frac{\partial f_0}{\partial u_0} + C_0\frac{\partial f_0}{\partial \theta_0}\right) \tag{4.82}$$

The equations for B, C, E, and F are in [106]. The total change in energy in the distribution function is equal to the flux-averaged energy loss by the wave.

I have used version `04-28-2010_AORSA_SIMPLE_LOAD_20_mod`, which contains N. Tsujii's modifications for 4-strap antenna phasing.

4.6.2 Collisional QuasiLinear 3D (CQL3D)

CQL3D[71] solves the Fokker-Planck equation,

$$\frac{\mathrm{d}f_0}{\mathrm{d}t} = Q(\mathbf{E}, f_0) + C(f_0) + S(\mathbf{x}, \mathbf{v}) \tag{4.83}$$

for the orbit-averaged distribution function $f_0(u, \theta_0, x, t)$, where $Q(\mathbf{E}, f_0)$ is the diffusion operator, $C(f_0)$ is a collision operator (which relaxes the distribution towards Maxwellian), and $S(\mathbf{x}, \mathbf{v})$ is a particle source (which is zero in our

case). The distribution function is a 3D function of velocity (u, θ_0), where θ_0 is the velocity pitch angle at the midplane and flux surface label x.

The code uses a zero-banana width (ZBW) approximation and zero electrostatic forces approximation and up-down symmetric flux surfaces. The ZBW approximation is a pretty severe limitation of the code, as fast ions can have very large orbits, and the orbit width is likely to play some role in the width of the power deposition region. The code allows for radial transport via radial diffusion and pinch operators, but for the purposes of ICRH simulation, the radial transport is turned off, so the density profile remains fixed to the experimental input values.

For a single species, with no sources and transport turned off, $150 \times 100 \times 64$ point resolution for (velocity, pitch angle, flux surfaces), runtime is about 3 minutes on a single processor.

4.6.3 AORSA + CQL3D

When the heating power is sufficient to distort the initially Maxwellian distribution of ions, the wave mechanics are affected. This poses a difficulty for simulation: the full wave solution depends on the ion distribution functions which depend in turn on the full wave solution. To obtain a numerical solution, AORSA and CQL3D are run iteratively until convergence. This method is described in [106]. We start by running AORSA with Maxwellian distribution functions for all ions to calculate diffusion coefficients. These are used to calculate a first-pass minority distribution function using CQL3D. Then AORSA

is called again, using the new distribution function. This is repeated until the distribution functions converge. This takes about 4-5 calls to AORSA. The computation time is dominated by the AORSA calls; therefore, the total computational cost is multiplied by 5.

Shot number 1121001003 is a test case for ^{3}He minority heating. Table 4.1 gives some experimental parameters for the shot.

Figures 4.16 – 4.20 show different aspects of the simulated electric field, for a single toroidal mode $n_\phi = 10$. Note that the scale for the electric field in the $\hat{\mathbf{e}}_b$ direction is much smaller than the others, since the primary propagating wave, FW, is perpendicularly polarized. Although ^{3}He minority heating is the dominant mechanism for this set of parameters, we can see that mode conversion still occurs to some degree, evident from the appearance of the short wavelength IBW just inside the IIH. The single pass absorption is low, and FW is present on both sides of the barrier. The IBW is primarily longitudinal, so it appears on E_α since it is propagating inward, perpendicular to the field. The real and imaginary parts of the electric field give snapshots of the wave at different points in the oscillation.

The amplitude squared plots show that the wave intensity is very nonuniform over the plasma. There are clear hot spots and voids. The exact position of the hot spots is unlikely to be correct, due to sensitive dependence on the plasma geometry and boundary conditions, but we can expect features of similar size to exist on C-Mod. Note that the hot spot locations are shifted for different toroidal modes, so averaging over the toroidal direction

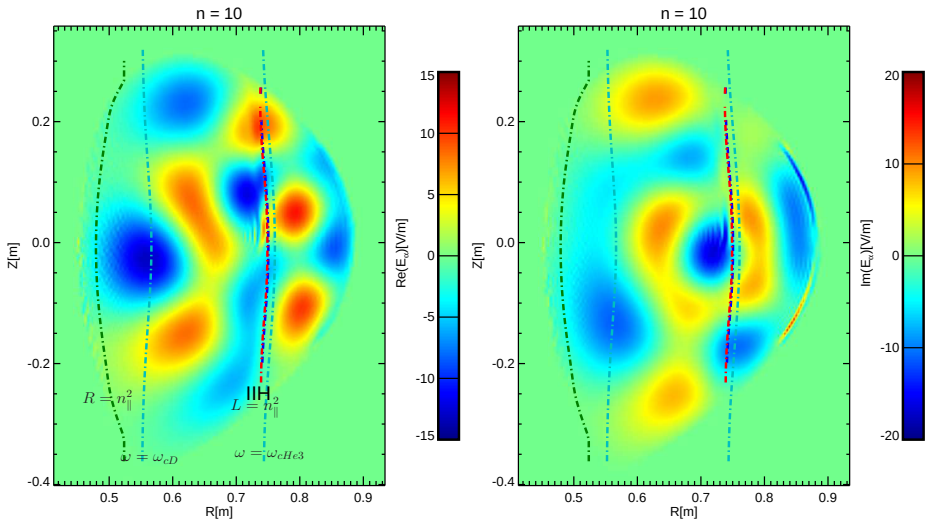

Figure 4.16: Simulated E_α for shot 1121001003

does produce a substantially more uniform power distribution.

The power deposition is calculated in two ways by AORSA. The Joule heating is given by

$$P_{\mathrm{J}} = \frac{1}{2}\mathfrak{Re}\left\{\mathbf{E}^* \cdot \mathbf{J}\right\} \tag{4.84}$$

It is only approximately correct as it assumes all charge acceleration is converted to heat. Plasma waves comprise of fields and collective particle motion, so part of the wave energy is stored in the kinetic energy of the particles, the so-called kinetic flux term[165]. The kinetic flux term is mainly important for slow electrostatic waves in the hot plasma. AORSA keeps track of the contribution to current from each species separately, so species heating fractions can be estimated. Figure 4.21 shows the total Joule heating in 2D, and the contributions to each species in a reduced 1D plot.

A more general form for the wave heating subtracts off the local change

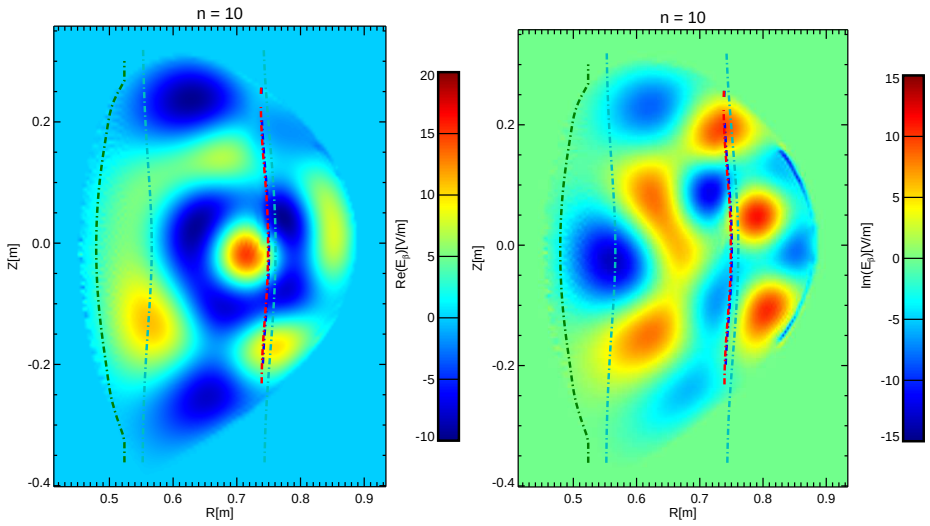

Figure 4.17: Simulated E_β for shot 1121001003

in kinetic flux, $\mathbf{S}$:

$$P_{\mathrm{RF}} = \frac{1}{2}\mathfrak{Re}\left\{\mathbf{E}^* \cdot \mathbf{J}\right\} - \nabla \cdot \mathbf{S} \tag{4.85}$$

This can be calculated by[106]

$$P_{\mathrm{RF}} = \frac{1}{2}\mathfrak{Re}\left\{\frac{\epsilon_0 \omega}{i} \sum_{\mathbf{k}_1,\mathbf{k}_2} e^{i(\mathbf{k}_1-\mathbf{k}_2)\cdot\mathbf{r}} \mathbf{E}^*_{\mathbf{k}_2} \cdot \mathbf{W}_l \cdot \mathbf{E}_{k_1}\right\} \tag{4.86}$$

where

$$\mathbf{W}_l = 2\pi\frac{\omega_{ps}^2}{\omega^2}\sum_{l=-\infty}^{\infty} e^{il(\beta_1-\beta_2)}\mathbf{C}^{-1}(\beta_2)\cdot\left[\int_{-\infty}^{\infty}\frac{\mathrm{d}u_\parallel}{1-(n_\parallel u_\parallel/\sqrt{\mu})-(l\omega_{cs}/\omega)}\int_0^{\infty}\mathrm{d}u_\perp U\mathbf{S}'\right]\cdot\mathbf{C}(\beta_1) \tag{4.87}$$

This can be rewritten as[106]

$$P_{RF} = -\frac{\pi}{2}\frac{\epsilon_0\omega_{ps}^2}{\omega}\mathfrak{Re}\left\{\int_0^{\infty}\mathrm{d}u_\perp\sum_{l=-\infty}^{\infty}\left(\sum_{k_2}\epsilon_{k_2}^{*T}\cdot\mathbf{a}_l^{(2)T}\right)\left(\sum_{k_1}\pi U\frac{v_{\mathrm{norm}}}{|n_\parallel c}\mathbf{a}_l(1)\cdot\epsilon_{k_1}\right)\Bigg|_{u_{\parallel,\mathrm{res}}}\right\} \tag{4.88}$$

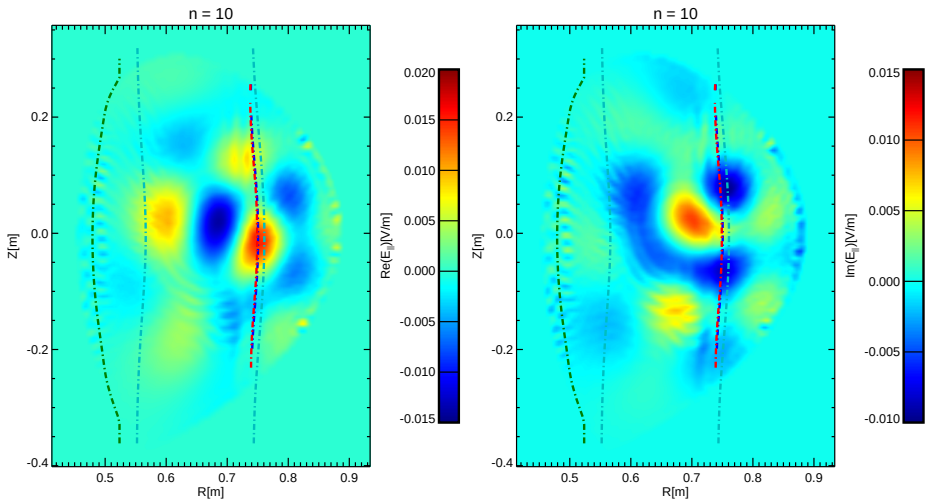

Figure 4.18: Simulated E_b for shot 1121001003

where the resonance condition $u_{\parallel,\mathrm{res}}$ is given by

$$1 - (n_\parallel u_{\parallel,\mathrm{res}} v_{\mathrm{norm}}/c) - (l\omega_{cs}/\omega) = 0 \tag{4.89}$$

and

$$\mathbf{a}_l \equiv \left(u_\perp J_{l+1}, \quad u_\perp J_{l-1}, \quad \sqrt{2} u_\parallel J_l \right) \tag{4.90}$$

$$\epsilon_{\mathbf{k}} \equiv \begin{pmatrix} \frac{1}{\sqrt{2}}(E_\alpha - iE_\beta) e^{i\left[\mathbf{k}\cdot\mathbf{r} + (l+1)\beta\right]} \\ \frac{1}{\sqrt{2}}(E_\alpha + iE_\beta) e^{i\left[\mathbf{k}\cdot\mathbf{r} + (l-1)\beta\right]} \\ E_\parallel e^{i[\mathbf{k}\cdot\mathbf{r} + l\beta]} \end{pmatrix} \tag{4.91}$$

where β is the angle between $k_\perp$ and $\hat{\mathbf{e}}_\alpha$.

Figure 4.22 shows the heating calculated by this other method.

Simulated helium-3 distribution functions are shown in figures 4.24 – 4.26 for shot 1121001003 for three different flux surfaces, which are shown in figure 4.23 to provide heating context. The inner flux surface at 0.70 m mostly misses the ^{3}He resonance band and receives little minority heating.

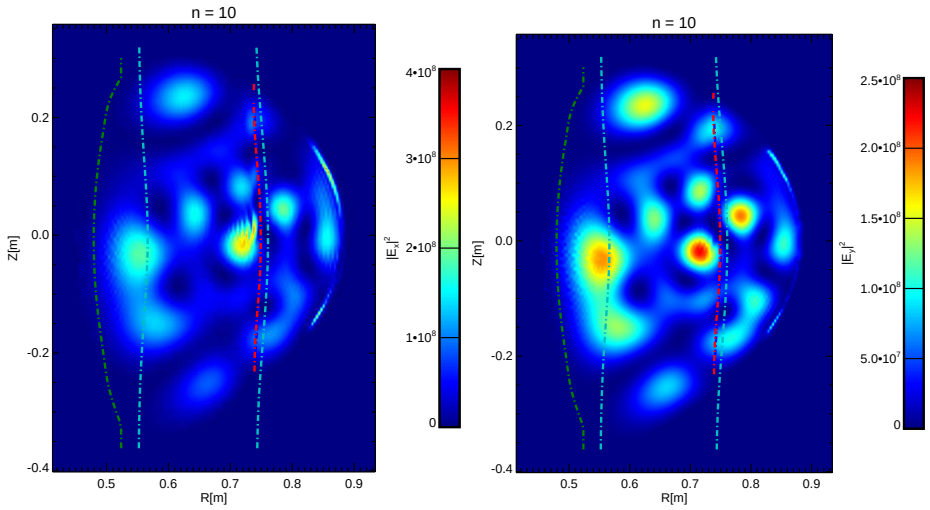

Figure 4.19: Simulated $|E_x|^2$ and $|E_y|^2$ for shot 1121001003

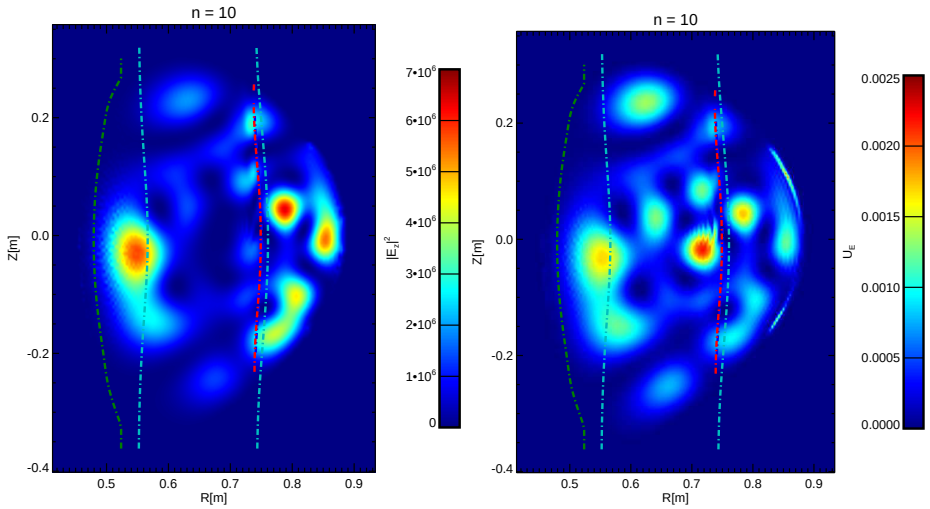

Figure 4.20: Simulated $|E_z|^2$ and $U_E = \epsilon_0(|E_x|^2 + |E_y|^2 + |E_z|^2)$ for shot 1121001003

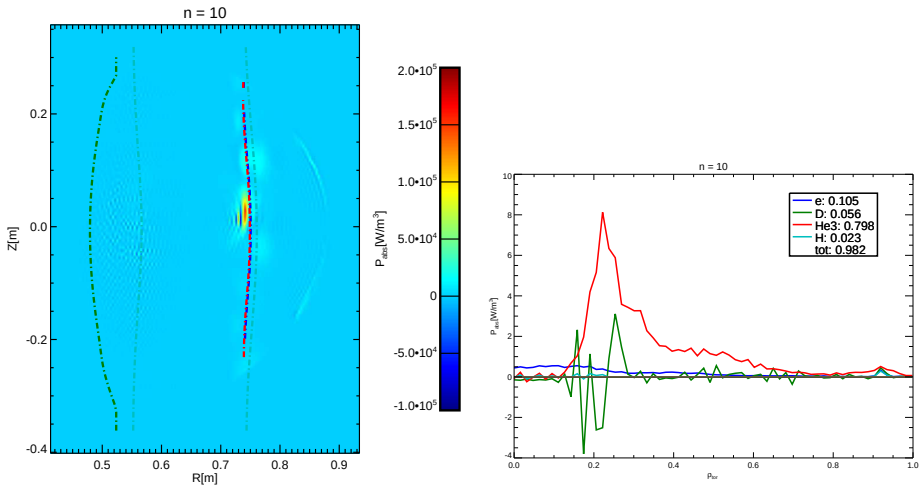

Figure 4.21: Left: Joule heating ($\mathfrak{Re}\{\mathbf{E}^* \cdot \mathbf{J}\}$) summed over all species for $n_\phi = 10$. Right: Joule heating for each species, plotted against normalized square root of toroidal flux.

There is some asymmetry in the circulating particles at high energies, but the asymmetry disappears for $|v_\parallel| \lesssim 500\sqrt{2\text{keV}/m_{\text{He3}}}$. Asymmetry could arise from the fact that the two circulation directions have opposite Doppler shifts. The Doppler shift of thermal particles is too small to reach the resonance band, but for the fast ions, the Doppler shift is much larger. The flux surface at 0.75 m intersects the resonance band near the midplane and receives strong heating, and the fast ion content is much higher. The heating is largely focused in the perpendicular direction. In this case, asymmetry in passing particles is less visible. The flux surface at 0.80 m reaches the midplane on the LFS of the resonance band, so it contains a no-heating region given equation 4.57 where the banana orbits do not reach the resonance band. This is reflected in the distribution function, where we see a gap in the fast ions near perpendicular

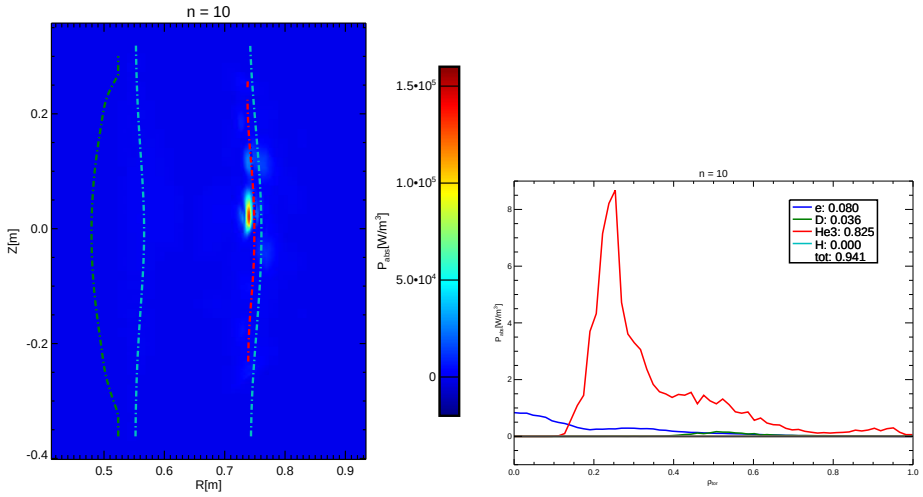

Figure 4.22: Left: Power absorbed, P_{RF} summed over all species for $n_\phi = 10$. Right: Power absorbed for each species, plotted against normalized square root of toroidal flux.

pitch angle. The overall heating is less than at 0.75 m. We see some asymmetry in the circulating particles, but this time in the opposite direction to the 0.70 m case: the co-passing particles are more heated. This makes sense because an opposite Doppler shift is necessary to reach resonance from the LFS compared to the HFS.

Figure 4.27 shows the convergence of the simulation over several iterations of a call to AORSA and CQL3D.

4.6.4 Fast ion induced poloidal asymmetry

In the banana collisional regime, an anisotropy in the ion distribution function generally induces an asymmetry in the ion pressure profile with respect to poloidal angle. In other words, the ion pressure (and density) need

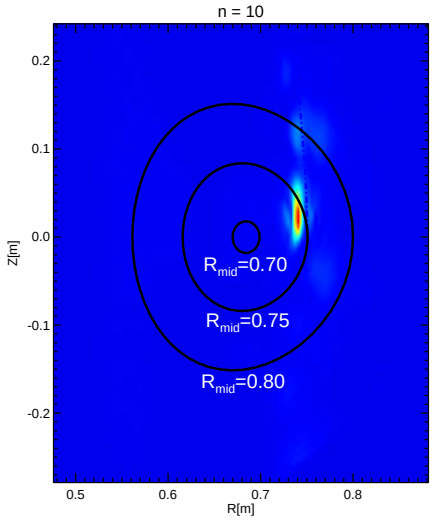

Figure 4.23: Three flux surfaces shown superimposed on simulated power absorption for shot 1121001003.

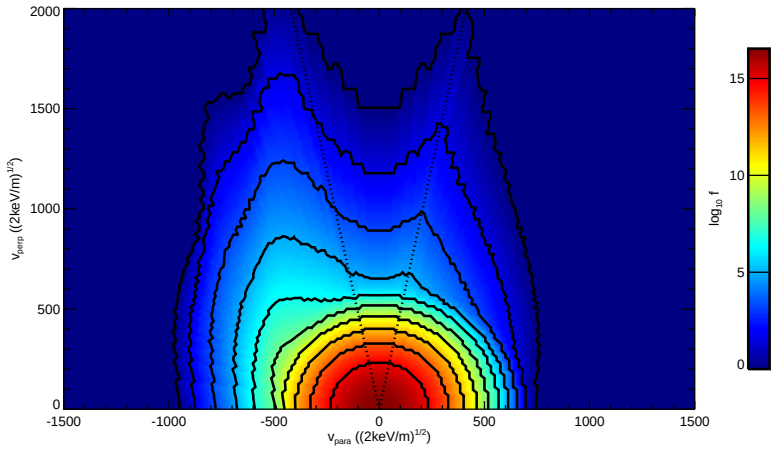

Figure 4.24: Simulated velocity space distribution function at flux surface $R_{\mathrm{mid}} = 0.70\,\mathrm{m}$ for shot 1121001003. The dotted line shows the trapped-passing boundary.

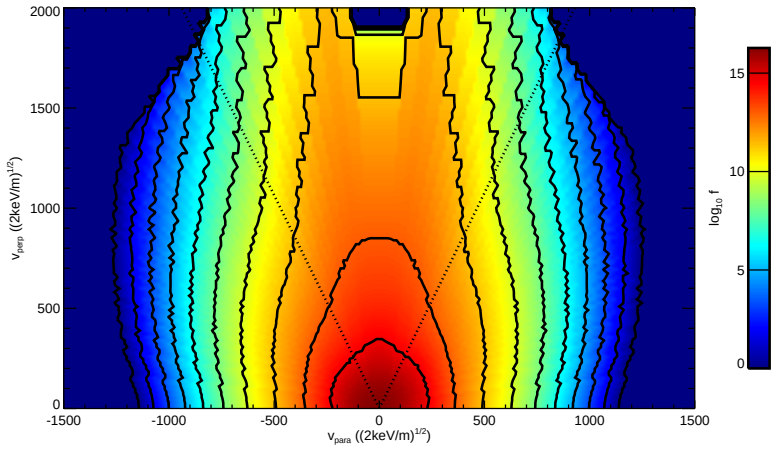

Figure 4.25: Simulated velocity space distribution function at flux surface $R_{\mathrm{mid}} = 0.75\,\mathrm{m}$ for shot 1121001003. The dotted line shows the trapped-passing boundary.

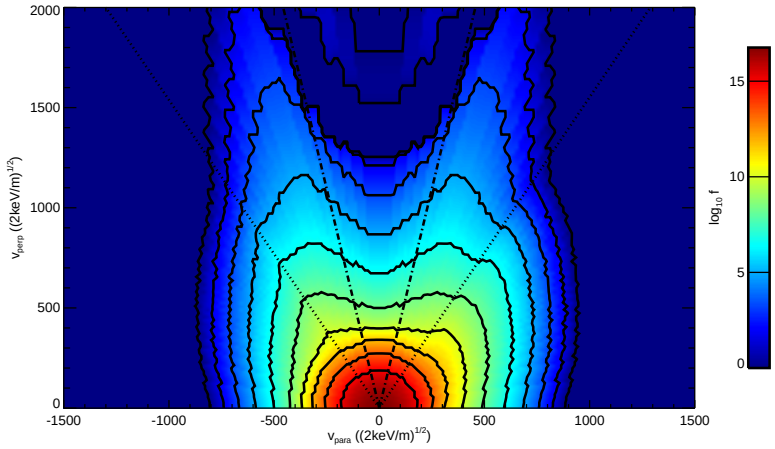

Figure 4.26: Simulated velocity space distribution function at flux surface $R_{\mathrm{mid}} = 0.80\,\mathrm{m}$ for shot 1121001003. The dotted line shows the trapped-passing boundary, and the dot-dash line shows the no-heating region.

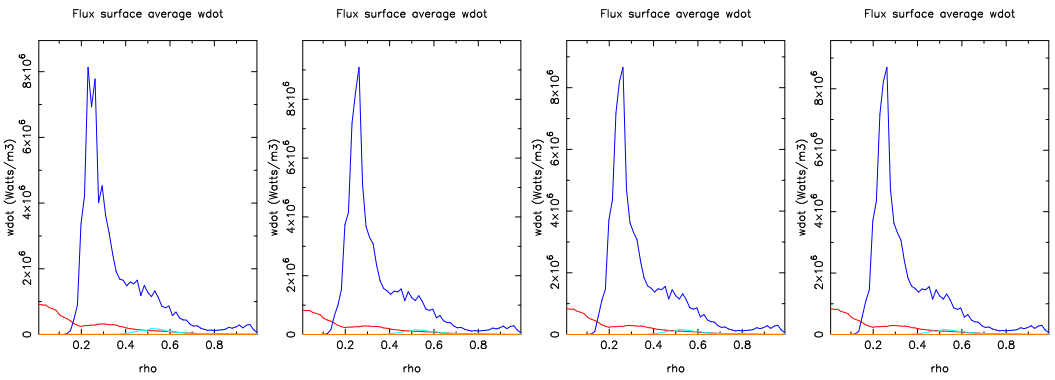

Figure 4.27: From left to right, the plots show output of iterations 1, 2, 3, and 4

not be a flux function. Intuitively, if the perpendicular temperature is high compared to the parallel temperature, then most particles will be trapped, with short banana orbits, so the predominance of particles will be on the low field side.

Consider a single banana orbit. Assuming small banana width, the turning points depend only on the flux surface and the pitch angle of the velocity at the midplane (or some other standard position), given by equation 4.56. The orbit only contributes to density between these turning points. The contribution of this orbit to the local density must be scaled by the fraction of time spent along each portion of the orbit. The orbit weighting function is

$$w(z) = v_{\parallel}(z)^{-1} \left(\tau_{\text{bounce}} \int v_{\parallel}(z')^{-1} \, \mathrm{d}z' \right)^{-1} \tag{4.92}$$

where z is the arc distance along the orbit.

$$v_{\parallel}(z) = v \sqrt{1 - \frac{B(\mathbf{r})}{B_{\text{mid}}(\rho)} \sin^2 \theta} \tag{4.93}$$

Figure 4.28 shows turning points and contribution weighting for three different orbits (in the zero width approximation). The particle spends much of its time near the turning points where its parallel velocity is low.

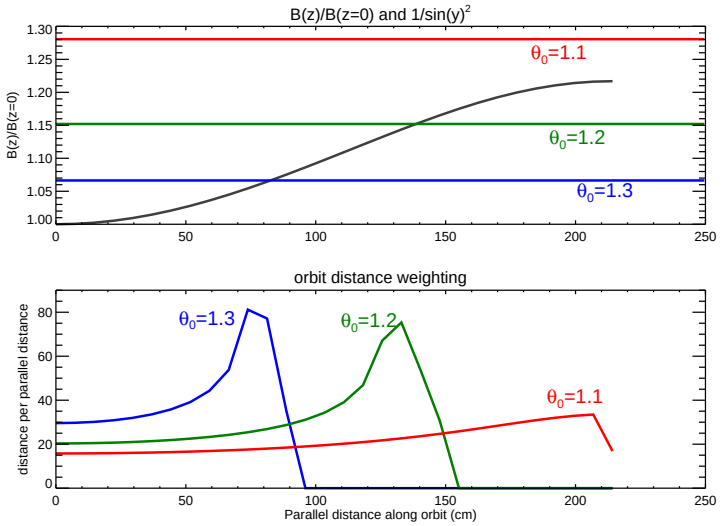

Figure 4.28: Top: Magnetic field ratio along an orbit for a flux surface at $R_{\mathrm{mid}} = 0.75\,\mathrm{m}$ for shot 1121001003. Intersections with horizontal lines indicates turning points for three pitch angles. Bottom: Density weighting functions for two banana orbits and a circulating orbit on the same flux surface.

From the ion distribution function computed by CQL3D, it is straightforward to calculate the density as a function of poloidal angle. This is done by numerically integrating over the distribution function weighted by the orbit weighting functions. For an isotropic ion distribution, the poloidal density profile becomes flat, owing to an interesting cancellation of the orbit weightings. Figure 4.29 shows some ion poloidal density profiles for a shot with ICRF-induced fast ions. The inner flux surface at 0.70 m misses the ^{3}He resonance band and receives little minority heating, and therefore the density profile is

relatively flat[6]. The flux surface at 0.75 m intersects the resonance band near the midplane and receives strong heating, and therefore shows strong asymmetry. The flux surface at 0.80 m shows less asymmetry than the 0.75 m case.

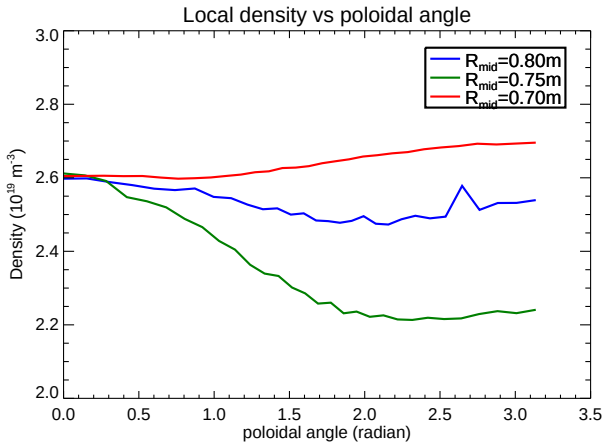

Figure 4.29: Local ^{3}He density as a function of poloidal angle for shot 1121001003, for flux surfaces at $R_{\mathrm{mid}} = \{0.70, 0.75, 0.80\}$ m.

According to the simulation, the asymmetry is very strong, with $n(\theta = 0) > 3n(\theta = \pi)$ in some cases with 1 MW heating. Neglecting this effect would lead to incorrect estimates of the total density. Since the core CXRS system and neutral beam are focused at the low field side midplane, this means that the average ^{3}He density could be lower than the measured value during ICRF heating. Unfortunately, the core CXRS system is not designed to effectively measure the poloidal asymmetry. Since the beam is large, the toroidal and poloidal views have some different levels of contribution from different angles

[6]Interestingly, the angular profile looks slightly less dense along the midplane. This is corroborated with figure 4.24 which shows slightly higher parallel heating than perpendicular

and radii. However, these contributions are not easily separated and the beam does not penetrate to the high field side, where the effect is more pronounced.

Poloidal asymmetry has been studied at the edge[31], where it exists for completely different reasons, due in part to interaction of poloidal flows with the scrape off layer.

4.6.5 Fast ion synthetic diagnostic

The He CXRS spectrum depends on the helium distribution function along the viewing chord. We have seen above that ICRF can induce a strongly non-Maxwellian distribution function. What is the effect on the measured spectra? Can we measure the fast ion content? A synthetic diagnostic, using the non-Maxwellian distribution function simulated by AORSA and CQL3D, was written to answer these questions and test the influences of several other things on the spectrometer signal. Ultimately, the synthetic diagnostic tests the limits of our measurement and guide the development of improvements.

Equation 2.7 can be used in calculating the synthetic diagnostic, using the distribution function simulated by CQL3D. To demonstrate the technique, a few stages of calculation will be shown here.

We have to use the local distribution function in 2.7, which differs from the midplane distribution function due to the effects of orbits. If we neglect orbit width, the local distribution function at (R, Z) is given by

$$f(v, \theta, R, Z) = f_0(v, \theta_0, \rho) w J \tag{4.94}$$

where f_0 is the orbit-averaged distribution function parameterized by the midplane coordinates v, θ_0, ρ, where ρ is the flux surface containing (R, Z) and θ_0 is the pitch angle at the midplane, given by:

$$\sin^2(\theta) = \frac{B(R,Z)}{B_0(\rho)} \sin^2(\theta_0) \tag{4.95}$$

Also,

$$J = \frac{\sin(\theta_0)}{\sin(\theta)} \frac{R_{\text{mid}}}{R} \frac{B_0(\rho) \sin 2\theta}{B(R,Z) \sin 2\theta_0} \tag{4.96}$$

$$w = \frac{v_{\|}^{-1}(R,Z)}{\left\langle v_{\|}^{-1} \right\rangle_{\rho}} \tag{4.97}$$

The first factor of J is due to the $\sin\theta_0$ in the density integral, $n = \iint f v^2 \sin\theta_0 \, \mathrm{d}\theta_0 \, \mathrm{d}v$. The second factor is due to the compression of the volume element with decreasing major radius. The third factor is due to the coordinate transformation. w accounts for density bunching due to the slowing of the parallel velocity.

Figure 4.30 shows parts of local distribution functions for several points calculated from the output of CQL3D. Roughly, the effect of moving away from the midplane is to remove a segment of midplane population near $\theta_0 = \pi/2$ and pinch the distribution function inward to close the gap. The total density decreases when the midplane distribution has a high perpendicular density. This effect is clearly seen at 7.125 keV.

Figure 4.31 shows the spectral emissivity (equation 2.4) calculated using the result of AORSA+CQL3D at a single point. The local distribution function was used in the calculation, but the helium fine structure is neglected

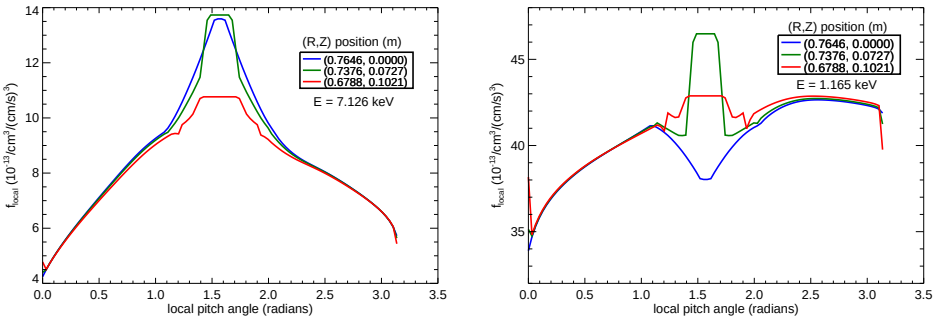

Figure 4.30: Shot 1121001003, three local distribution functions on the same flux surface. Left: $E = 7.126\,\mathrm{keV}$. Right: $E = 1.165\,\mathrm{keV}$.

so far. We see that the emission pattern is slightly skewed and the different components have shifted centers. This is due to the cross section effect (section 2.2.2). The right plot shows the same distribution with the cross section effect turned off[7]. The asymmetry in the spectral pattern is no longer visible.

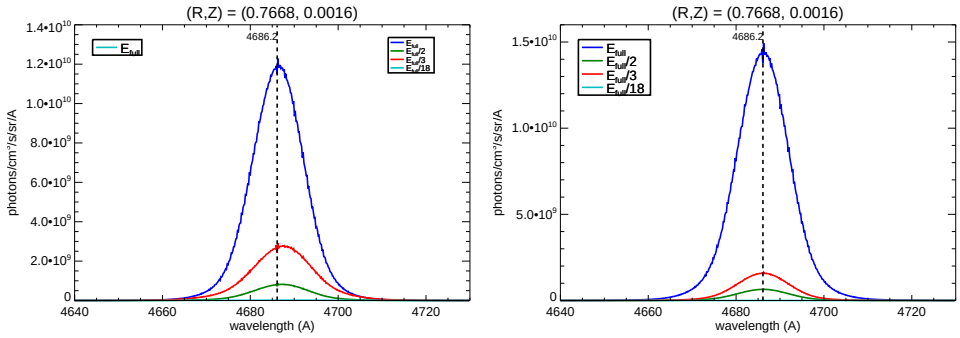

Figure 4.31: Left: Simulated spectral emissivity for 1121001003 at point $(R, Z) = (0.7668, 0.0016)$m for each beam component. Right: Same, but with cross section effects turned off.

In the numerical simulation, we walk along the viewing chord in steps

[7]The ion velocity is not included in the collision velocity

of about 1 cm and compute the spectral emissivity at each position. The emissivities are combined to give the spectral radiance from CXRS emission. Points with negligible beam density are skipped. Figures 4.32 and 4.33 show the emissivity (summed across beam components) at several points along the viewing chord. Of course, the strongest contributions to the radiance are from the points near the midplane.

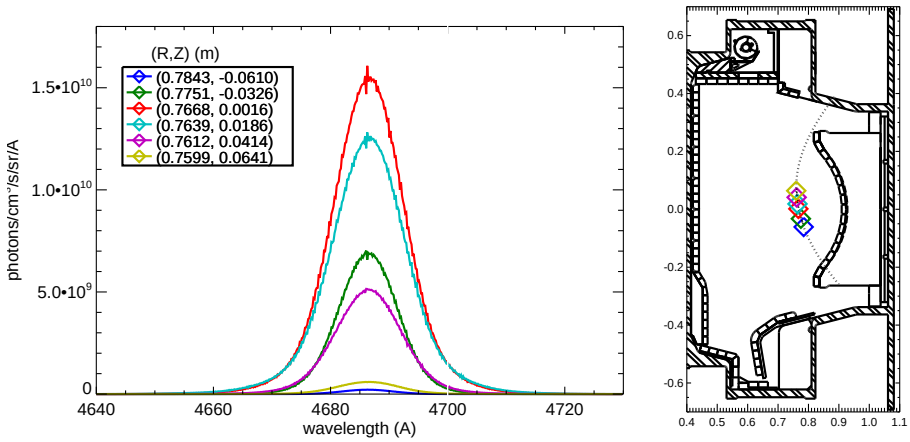

Figure 4.32: Simulated spectral emissivity for 1121001003 at selected points over toroidal chord L2 $R_{\mathrm{mid}} = 0.767\,\mathrm{m}$. The right plot shows the selected points along the chord.

Integrating over the chords gives the spectral radiance shown in figure 4.34. Interestingly, the poloidal channel is predicted to have a much wider spectral pattern than the toroidal channel, even though they both intersect the midplane at about the same major radius. This is expected, because the poloidal chord receives Doppler shift primarily from the perpendicular direction (to the magnetic field), while the toroidal view receives Doppler shift from both perpendicular and parallel directions. So far, all of the noise in the

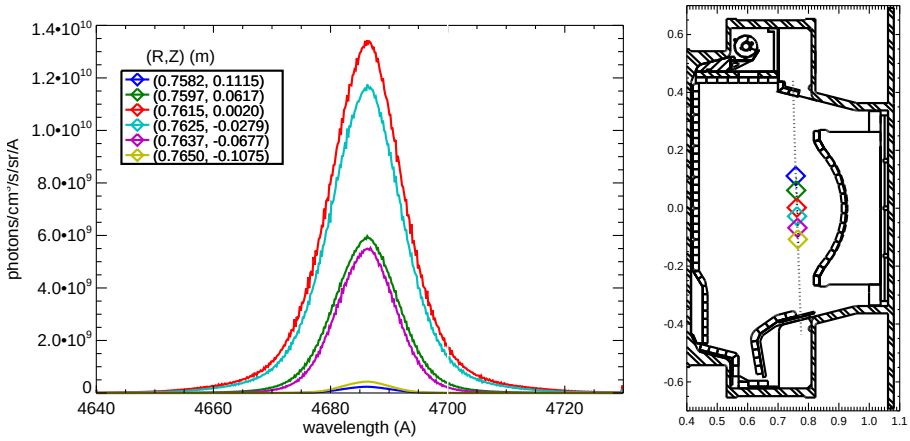

Figure 4.33: Simulated spectral emissivity for 1121001003 at selected points over poloidal chord P1 $R_{\mathrm{mid}} = 0.762\,\mathrm{m}$. The right plot shows the selected points along the chord.

spectrum come from numerical artifacts, as photon shot noise has not been applied yet. The stairstep appearance is due to velocity quantization of the distribution function. The wavelength bins at the edge of the plotting window contains contribution from all the out of bounds part of the spectrum.

The power of the synthetic diagnostic comes from the ability to turn on and off certain influences on the spectrum, in order to compare the strengths of the influences and the deviation from the simple model of a Gaussian spectrum. The major effects that can be toggled are:

I Full distribution (off=Maxwellian)

II Viewing chord integration (off=midplane only)

III Cross section effects

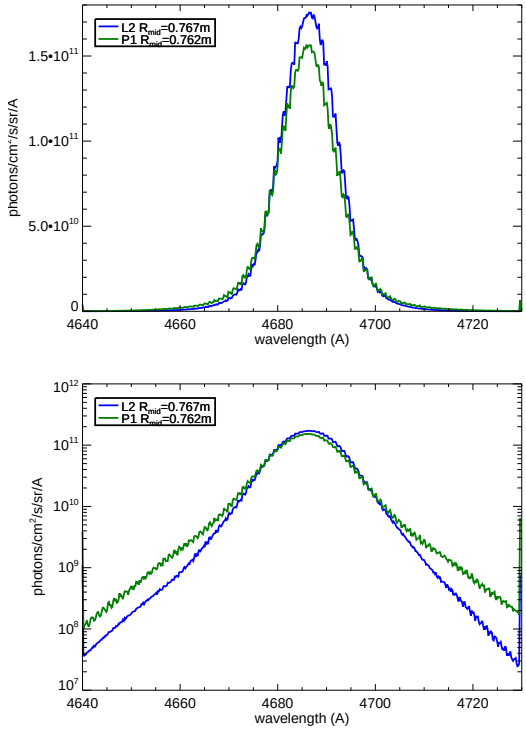

Figure 4.34: Simulated spectral radiance for 1121001003 for two channels, L2 $R_{\mathrm{mid}} = 0.767\,\mathrm{m}$ and P1 $R_{\mathrm{mid}} = 0.762\,\mathrm{m}$.

IV Zeeman and fine structure effect[8]

V Instrument function (width $w = \sqrt{2}\sigma$ is about 2 Å)

Synthetic spectra with several choices of toggled effects are shown in figures 4.35 and 4.36. The effect of the Zeeman effect (IV) and instrument function (V) are both to smooth the spectrum slightly, which slightly increases the width of the line. The difference between the chord-integrated spectrum and the scaled midplane spectrum is actually quite small. The most important

[8]Stark-Zeeman interaction is not included for simplicity

effect is the inclusion of the full distribution function versus a Maxwellian. The differences are difficult to see in the linear plot, but are very clearly seen in the semilog plot in the slopes of the tails. The full-distribution spectra have much higher tail effective temperatures than the Maxwellian spectra, even though the $1/e$ width is about the same.

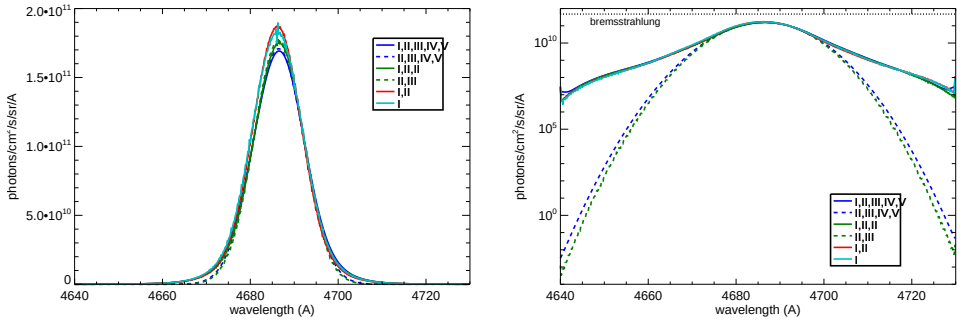

Figure 4.35: Synthetic spectra for shot 1121001003, channel L2 $R_{\mathrm{mid}} = 0.767\,\mathrm{m}$, using different combinations of included effects.

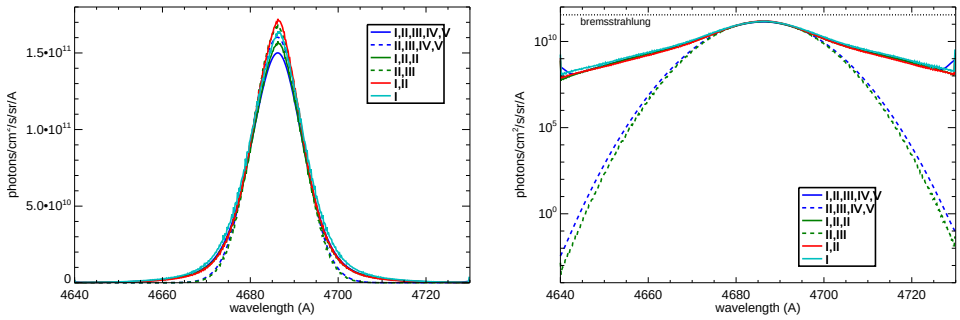

Figure 4.36: Synthetic spectra for shot 1121001003, channel P1 $R_{\mathrm{mid}} = 0.762\,\mathrm{m}$, using different combinations of included effects.

The final step is to convert the spectral radiances to a detector signal. We know the throughput and transmission function from calibrations, so this is

straightforward. The edge emission is simulated by a simple Gaussian which is scaled to the empirically measured value. Poisson noise and dark current noise are added to the result. Figures 4.37 and 4.38 shows the result of the synthetic diagnostic, compared to the actual measurement. The bremsstrahlung model does not include wall reflections and underpredicts the background continuum level somewhat.

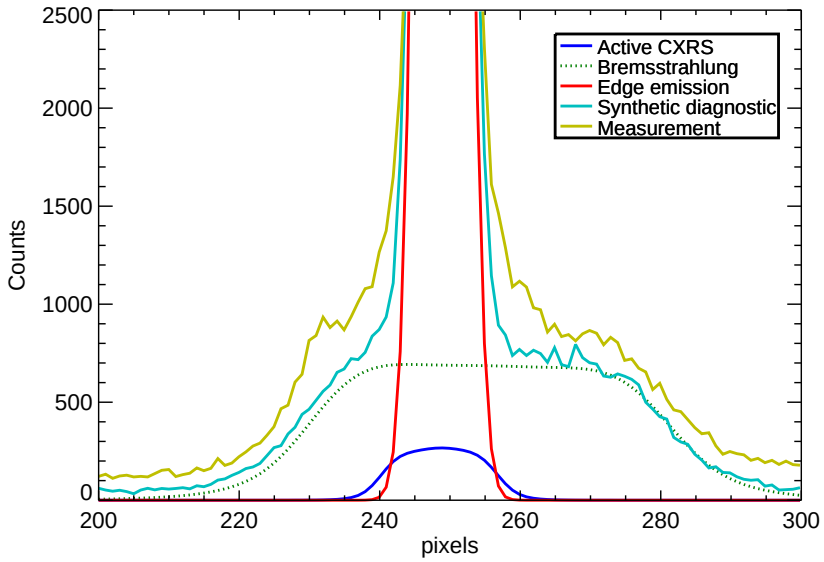

Figure 4.37: Synthetic diagnostic and measurement for shot 1121001003, channel L2 $R_{\mathrm{mid}} = 0.767\,\mathrm{m}$.

One of my initial goals for helium charge exchange was the direct measurement of the fast ions generated by ICRH using CXRS. This effort was deemed FICXS, for Fast Ion Charge Exchange Spectroscopy. Similar experiments have been successfully conducted on D-IIID and NSTX for measuring deuterium fast ions with CXRS. A fundamental difference is that these exper-

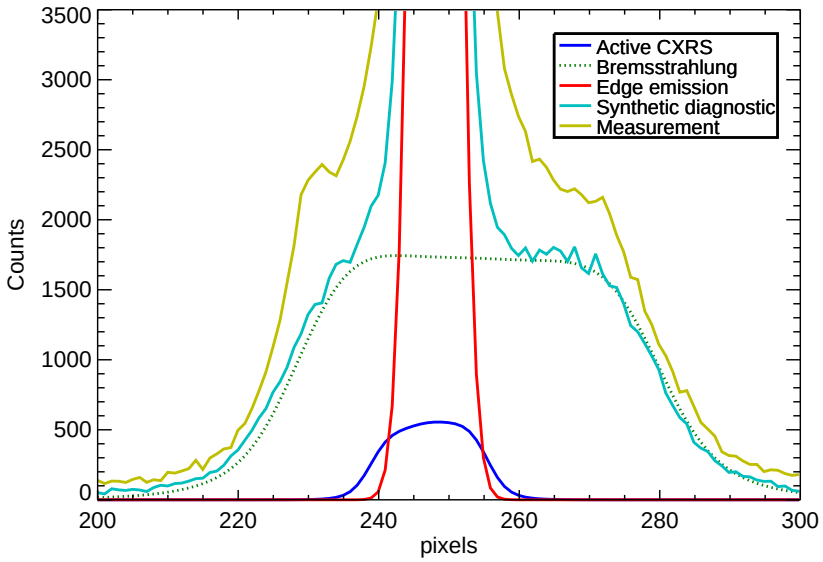

Figure 4.38: Synthetic diagnostic and measurement for shot 1121001003, channel P1 $R_{\mathrm{mid}} = 0.762\,\mathrm{m}$.

iments measured fast ions generated by neutral beam injection instead of fast ions generated by ICRH. The distribution function for neutral beam injected ions contains a separated peak near the beam velocity which is capable of being resolved from the thermal population. On the other hand, the ICRH minority distribution function only contains a single peak and there is no clean separation between thermal and fast particles.

Figure 4.39 shows a comparison between the synthetic spectrum calculated with the full ion distribution function and that calculated with a Maxwellian distribution function. The difference between the two spectra is very small compared to the noise in the spectra. Unfortunately, this means that direct measurement of ICRH-generated fast ions is impossible using the

present system.

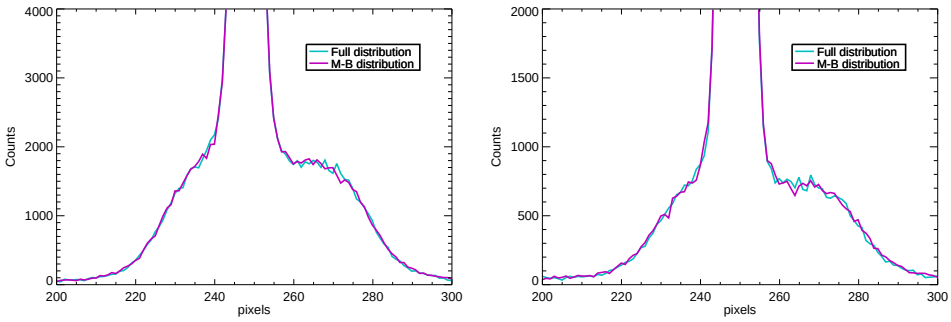

Figure 4.39: Left: Comparison of synthetic spectra for L2 $R_{\mathrm{mid}} = 0.767\,\mathrm{m}$. Right: for P1 $R_{\mathrm{mid}} = 0.762\,\mathrm{m}$.

4.7 Results

4.7.1 Variation of helium concentration

Runs 1110323 and 1121001 were both ICRH experiments in which the helium concentration was varied (in D(^{3}He) plasmas) to explore the region between minority heating dominated and mode conversion heating dominated regimes. Helium CXRS was available for both these runs, and the Phase Contrast Imaging (PCI) diagnostic was available for run 1110323.

The Phase Contrast Imaging (PCI) diagnostic[179] provides a measurement of line-integrated electron density fluctuations sensitive at ICRF wavelengths. The maximum intensity of the mode converted waves occurs near the IIH resonance whose position is sensitive to the minority concentration, so the PCI either provides a rough independent measurement of minority ion concentration or, together with the CXRS measurements of the minority density,

provides a verification of two-ion fast-wave heating theory and simulations. The PCI has a radial array of vertical chords which typically spans the ICRF resonance band. With increasing minority concentration, the peak of the PCI signal moves inward smoothly and monotonically, but the precise functional relationship depends on detailed ICRF physics and must be obtained from full-wave simulations (see figure 5-33 of [179]).

Table 4.1: Run 1110323 parameters

Parameter	value
I_P	0.8 MA
B_T	5.4 T
$\int n_e$	$0.6 \times 10^{20}\,\mathrm{m}^{-2}$ to $1.0 \times 10^{20}\,\mathrm{m}^{-2}$
P_{ICRF}	0.5 MW to 2.5 MW
equilibrium	LSN
V_{beam}	50 keV
I_{beam}	7 A

Some parameters for run 1110323 are shown in table 4.1. Figure 4.40 compares the CXRS/TS measurements and PCI measurements of helium concentration (n_{He}/n_e). The CXRS/TS measurement uses helium density from CXRS and electron density from Thomson Scattering[88], both interpolated to the helium-3 cyclotron resonance radius, $\{R_{\mathrm{He}} \mid \omega = \omega_{c2}(R_{\mathrm{He}}, Z = 0)\}$. Both measurements are in rough agreement, and are also correlated with the helium-3 puff duration, which is the amount of time in each 1.5 s shot that the plenum valve was open to emit helium to the plasma edge.

A difference between the measurements is that the PCI result is based

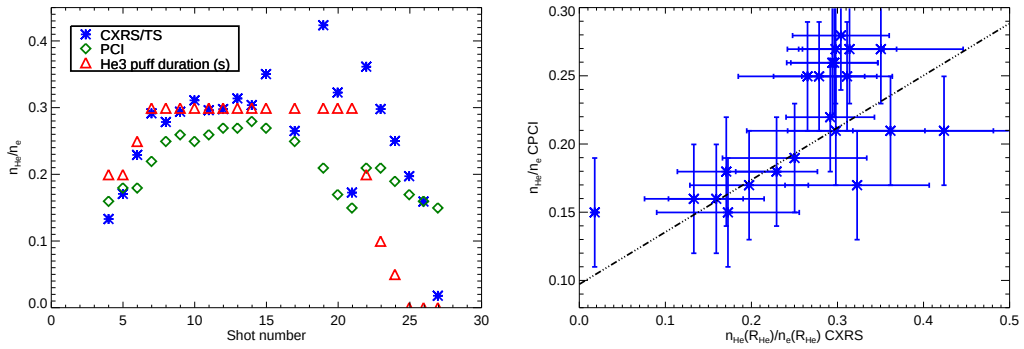

Figure 4.40: Left: Helium concentrations measured by CXRS/TS and PCI versus shot number for run 1110323, with helium puffing overlaid. Right: Helium-3 concentration measured by PCI vs. helium concentration measured by CXRS/TS

on a chord integrated signal and is an average over the vertical resonance region, while the CXRS measurement comes from the midplane. The electron density is actually measured on a vertical chord but mapped to the midplane. Since He CXRS cannot distinguish between the two isotopes of helium, the helium-3 concentration could be overpredicted.

In Alcator C-Mod, the electron and ion temperatures are often collisionally coupled, which makes distinguishing electron heating and ion heating difficult. The thermal equilibration rate for ions on electrons (for $T_i \approx T_e$) is given by[70]

$$\nu_{ei}^{\mathrm{Th}}/n_e = 3.2 \times 10^{-15} \frac{Z^2 \ln \Lambda}{m_i/m_p T^{3/2}} \quad [m^3 s^{-1}] \tag{4.98}$$

For typical C-Mod values, $\nu_{ei}^{\mathrm{Th}} \sim 15 \ldots 300\,\mathrm{s}^{-1}$, or $1/\nu_{ei}^{\mathrm{Th}} \sim 3 \ldots 70\,\mathrm{ms}$. The equilibration rate is lowest for low density plasmas during ICRH, which gives us an opportunity to look for differences in heating. During high ICRH heating,

T_e can differ significantly from T_i (by $\lesssim 30\,\%$).

We can distinguish electron and ion heating by looking at high time resolution temperature data when ICRH is initiated or stopped[9][62]. If there is a change in the slope $\frac{\partial T_e}{\partial t}$ which occurs at a must faster timescale than the equilibration rate, then there must be direct electron heating. The size of the step gives the electron heating power:[119]

$$P(r) \approx \frac{3}{2} n_e \Delta \left[\frac{\partial T_e(r)}{\partial t} \right] \tag{4.99}$$

This type of analysis is called break-in-slope analysis. The FRC Electron Cyclotron Emission[126] diagnostic provides fast electron temperature data. Unfortunately, we cannot do a similar analysis for direct ion heating, since the available ion temperature diagnostics have too low temporal resolution.

Figure 4.41 shows break in slope fits for two shots with different minority concentrations. The fit is a least squares fit of two connected line segments with a knee when ICRF is turned off. A time window of 0.05 s before the step and 0.02 s after the step was used. This time window is long enough to average over several sawteeth, which complicate the analysis, but is shorter than the equilibration time. The electron temperature is measured at the minority resonance radius.

The shots in figure 4.41 have equal ICRF input power, but the electron heating is clearly greater in the shot with higher helium-3 concentration. To

[9]The RF shutoff is nearly instantaneous ($< 10\,\mu s$) in comparison to the equilibration time

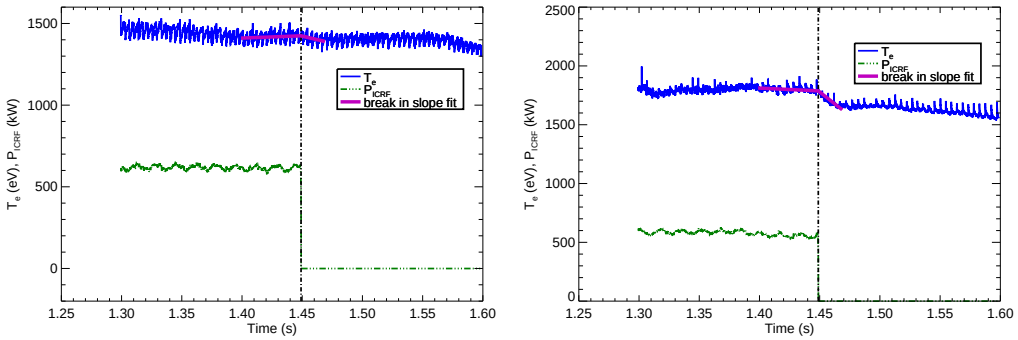

Figure 4.41: Break in slope fits for (left) $n_{\mathrm{He}}/n_e \approx 0.13$ (shot 1110323004) and (right) $n_{\mathrm{He}}/n_e \approx 0.29$ (shot 1110323007).

aid in comparison between shots, I define the dimensionless value

$$H = \frac{P_{\mathrm{BIS}}(R_{\mathrm{res}})V_{\mathrm{plasma}}}{P_{\mathrm{input}}} \tag{4.100}$$

which is representative of the electron heating efficiency. R_{res} is the major radius of the helium-3 resonance. Table 4.2 and figure 4.42 show some results of the analysis. As heating power is increased, the fraction of electron heating goes down because the minority heating width increases with plasma temperature. The "H sim" column shows electron heating efficiency calculated from AORSA-CQL3D simulation, which were run using experimental minority profiles and plasma parameters. The simulation seems to overpredict the electron heating. This may be due to an inadequate model for parasitic edge absorption in AORSA, which could be a significant power sink when single pass absorption is low.

Table 4.2: Electron heating efficiency analysis

Shot	n_{He}/n_e (CXRS/TS)	n_{He}/n_e (PCI)	P_{ICRF} (MW)	H exp	H sim
4	0.13	0.16	0.62	0.13	0.12
5	0.17	0.18	0.62	0.15	0.92
6	0.23	0.18	0.62	0.31	0.96
7	0.29	0.22	0.56	0.44	1.00
8	0.28	0.25	1.19	0.33	
9	0.29	0.26	1.21	0.33	
10	0.31	0.25	1.19	0.38	
11	0.30	0.26	1.24	0.37	

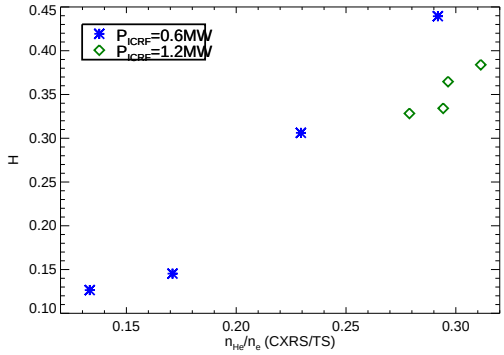

Figure 4.42: Electron heating efficiency versus minority fraction from break in slope analysis.

4.7.2 Effect of minority profile shape on ICRF heating

Although minority and mode conversion heating have been studied since the 1970s, not a lot of attention has been placed on the shape of the minority density profile. Due to a lack of spatially-resolved measurements of the minority species, previous analyses have generally assumed a minority concentration n_{min}/n_e that is constant throughout the plasma. However, we know from direct CXRS measurements that the minority density profile does

not completely follow the electron density. Hollow, flat, and peaked helium profiles have been observed in primarily peaked electron profiles. We would like to know what kind of impact the minority shape has on the deposition.

Since impurity shape cannot be easily controlled in an experiment, this section focuses on simulation results based on idealized input minority density profiles. This frees us to test unrealistic as well as realistic inputs, so any effects can be more pronounced. In addition, all other plasma parameters can be held fixed, while only the minority density is changed between test cases.

The fixed parameters are based upon shot 1121001003, which is a D(^{3}He)(H) plasma, with LSN, reverse field. D and E-port ICRF antennas are operating near 80 MHz at 1 MW each, and the J-port antenna is operating at 50 MHz at 1 MW. The electron density and temperature (from Thomson Scattering) are shown in figure 4.43. The hydrogen density is assumed to be 5 % of n_e and the deuterium density is chosen to be $n_e - n_{\mathrm{H}} - 2n_{\mathrm{He}}$. Each of the simulations was run for just a single toroidal mode, $n_\phi = 10$, except where noted.

The first group of test cases uses a modified inverse tangent shape for ^{3}He density:

$$n_{\mathrm{He}} = A(1 + pz)\tanh(z), \quad z = \frac{a - \rho_{\mathrm{tor}}}{c} \tag{4.101}$$

where shape parameters are chosen: $a = 1$, $c = 0.3$, $p \in -0.3, -0.15, 0.0, 0.15, 0.3$. Parameter p controls the peakedness of the profile in the core, and modifies the slope near the resonance region, which is near $\rho_{\mathrm{tor}} \sim 0.25$. A is chosen

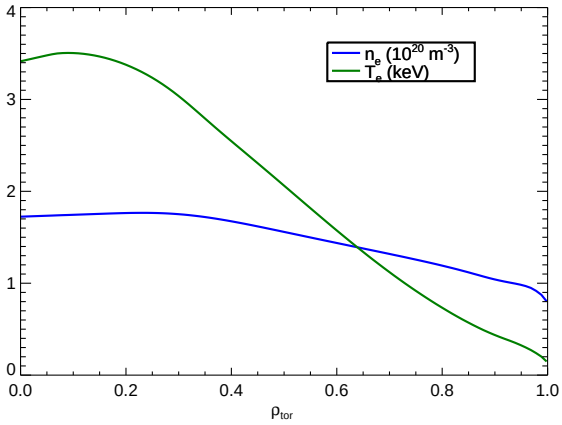

Figure 4.43: Electron density and temperature for model test cases, based on 1121001003.

such that $\langle n_{\mathrm{He}} \rangle_{\mathrm{vol}} = 2 \times 10^{18}\,\mathrm{m}^{-3}$. These are shown in figure 4.44. The density curves cross over at $\rho_{\mathrm{tor}} = 0.595$. In each case, the density fraction is low, $n_{\mathrm{He}}/n_e < 0.03$.

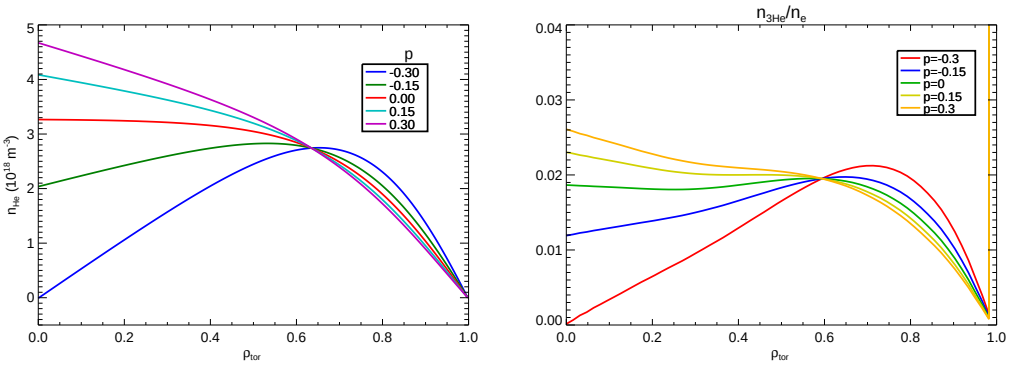

Figure 4.44: Model density profiles using equation 4.101

The simulated flux-averaged power deposition profiles are shown in figure 4.46. The power absorbed by electrons, deuterium, and hydrogen do not change shape much between cases; they merely scale up or down to collect

what has not been absorbed by the helium-3 minority. This is owing to the fact that the single pass absorption is weak (see 4.75). The overall minority heating is strongest for $p = 0.3$ and weakest for $p = -0.3$. It appears that for regions ρtor < 0.5, the peaked profile has greater minority heating, but for regions ρtor > 0.6, the hollow profiles have greater heating. Figure 4.45 shows this more clearly by taking the power absorbed by helium-3 for each case and dividing by the power absorbed by helium-3 for the $p = 0$ case.

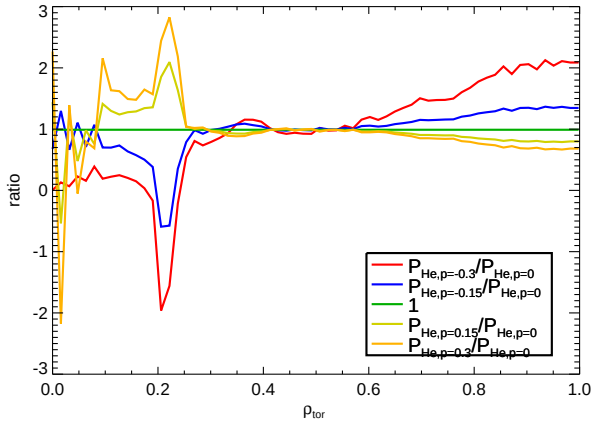

Figure 4.45: Minority heating for each case divided by minority heating for case 3.

The simplest explanation for this is that the power deposition does not depend on the slope of the minority density, and therefore the deposition curves meet at approximately $\rho_{\rm tor} \sim 0.6$, where the input densities match up[10]. Clearly, the minority heating power increases with minority density, so

[10]The crossing position is not exact because the total minority heating power in each case is different, so multiple pass absorption shifts the curves relative to each other.

the peaked profiles receive relatively greater heating in the core and vice versa. In other words, all cases are in the minority heating regime. This seems to be at odds with figure 4.10, which suggests that minority heating should roll off for $X[^3\mathrm{He}] \gtrsim 0.014$.

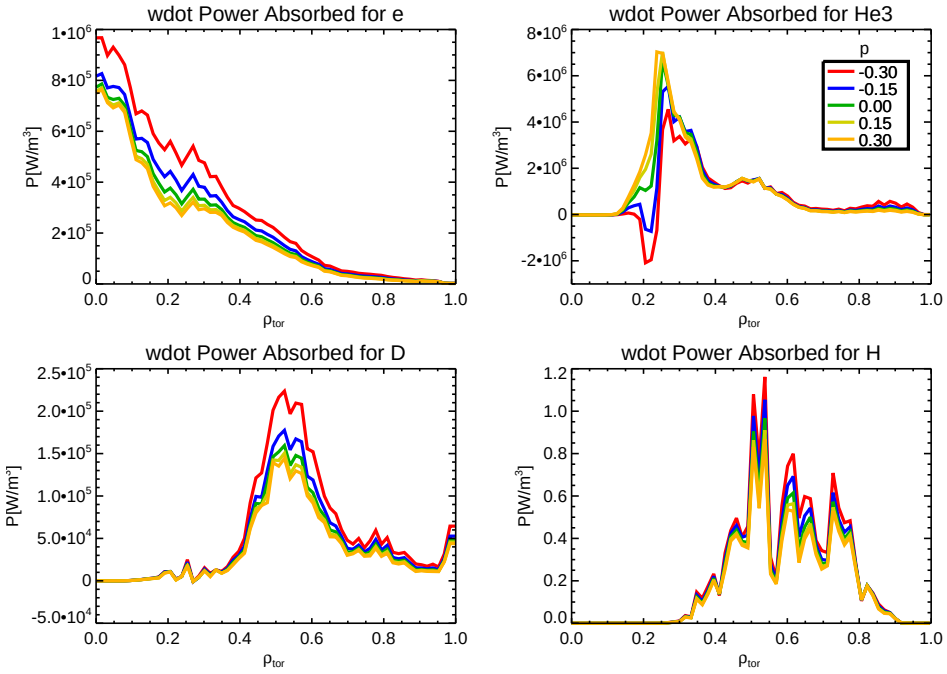

Figure 4.46: Flux-averaged power deposition profiles for test cases using equation 4.101

For some reason, the simulation predicts a negative power absorption for ^{3}He in the region $\rho_{\mathrm{tor}} \sim 0.2$ for the hollow profile cases. These are the cases in which the minority density is low in the resonance region, so there is a large fraction of fast ions generated. This effect goes away if the simulation is run with a Maxwellian distribution function, so it is an effect of high energy particles. I believe this is an artifact of the zero orbit width distribution of

CQL3D. The fast ions at the resonance have large gyroradii which allow them to penetrate to the high field side of the resonance, which creates an apparent population inversion on the high field side which gives up energy to the wave.

The second group of test cases is a scan of the total minority density using the same form 4.101, setting $p = 0$ for all cases, but varying A. The input densities are shown in figure 4.47. The flux-averaged power deposition curves are shown in figure 4.48. The power absorption profile changes dramatically with helium fraction. At moderate minority fractions (0.03 % to 0.08 %), minority heating is strong and the deposition seems to extend farther to the high field side. I believe this is due to broadening of the resonance region by fast ions. At high minority fractions, the electron heating exceeds the minority heating, although the minority heating is still substantial. The deuterium deposition profile scales up as helium heating is reduced, and it changes shape somewhat as the wave hot spots shift around. The power absorbed by hydrogen is negligible.

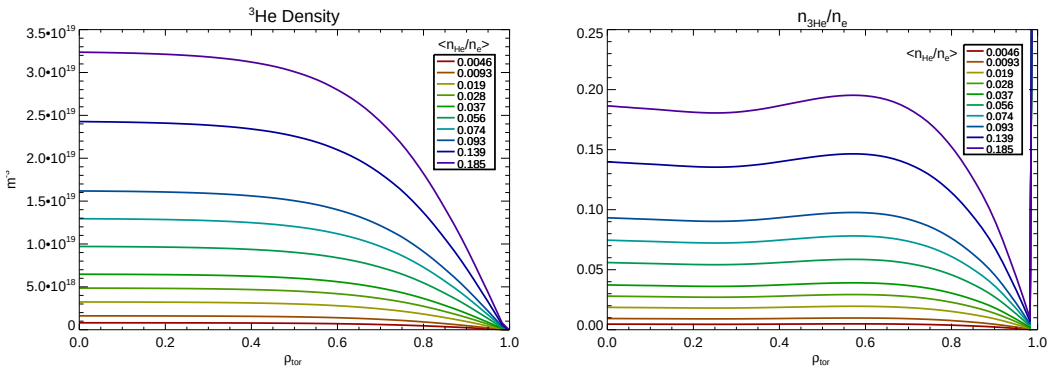

Figure 4.47: Model density profiles for second group of test cases. The legend labels show volume-averaged minority fraction.

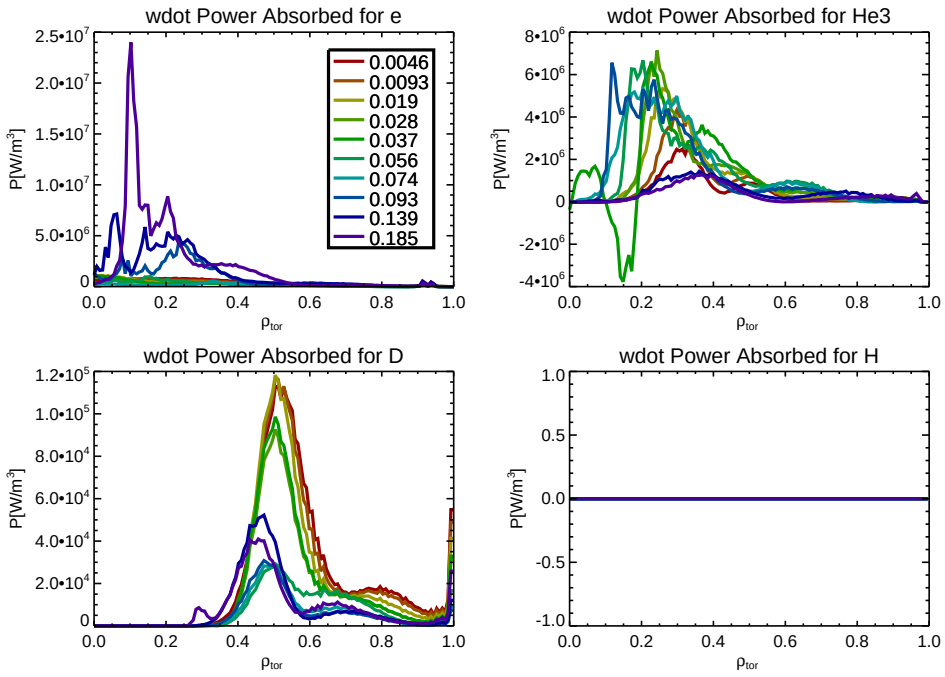

Figure 4.48: Flux-averaged power deposition profiles for second group of test cases

The total power dissection is shown in figure 4.49. Two calculations are shown The minority heating power reaches a maximum at $n_{\mathrm{He}}/n_e \sim 6\,\%$ with a wide peak. The mode conversion electron heating becomes dominant in the vicinity of $n_{\mathrm{He}}/n_e \sim 12\,\%$.

The third group of test cases, a flat minority density profile is compared to three inverse tangent profiles from earlier. The density profiles are shown in figure 4.50. The power deposition is shown in figure 4.51. The inverse tangent profiles are labeled according to the volume averaged helium density. In the core, $\rho_{\mathrm{tor}} < 0.4$, the flat profile is very close to the "`atan 60e11`" case, and the minority power deposition is also very similar in this region. Near $\rho = 0.7$, the

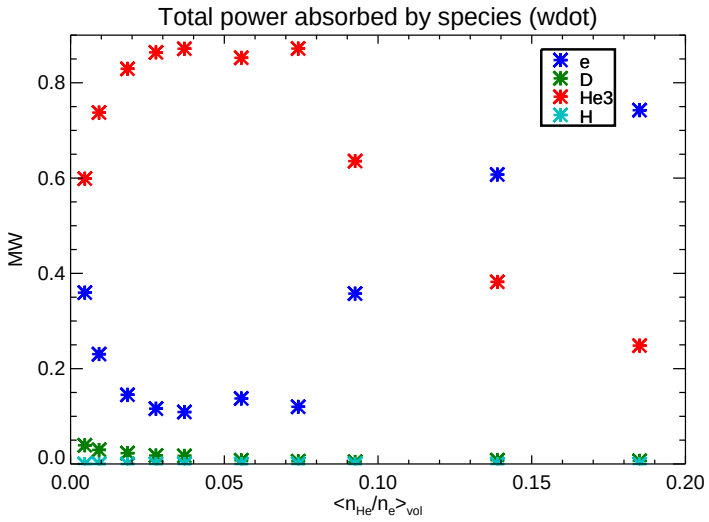

Figure 4.49: Total volume-integrated power deposited to each species for each case, labeled by volume-averaged minority fraction.

flat density profile intersects the "`atan 80e11`" case, and again the minority power deposition is very close. It appears as if the deposition profile can be reasonably explained by dividing the plasma into radial bins and looking only at the local minority density in each region.

To test this idea, the next group of test cases uses a set of minority profiles which are narrow Gaussians with centers shifted across the minor radius, when plotted against ρ_{tor}. Gaussians were used instead of rectangular blocks to reduce artifacts from numerical interpolation. The model functions are shown in figure 4.52. The power deposition curves are shown in figure 4.53.

If we simply add the results, we get something that roughly resembles the results of the flat density input. This is shown in figure 4.54. The sums have been arbitrarily multiplied by 0.25. Of course, we can't expect a good

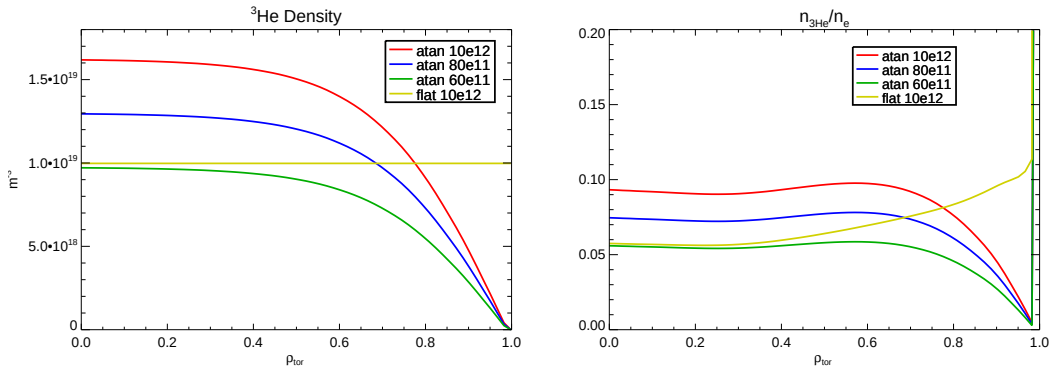

Figure 4.50: Model density profiles comparing a flat minority density to the inverse tangent model.

match because when the single-pass absorption is weaker, there will be more passes before the waves are completely absorbed, so cases with weaker absorption, such as the gaussian at $\rho_{\text{tor}} = 0.8$, have exaggerated impact on the plot. Still, there seems to be a slight difference in the position of the hot and cold spots, which isn't so surprising because the fast wave wavenumber does depend on the minority density.

Another test case looks at a single simulation with several different toroidal modes. The minority profile is the same as the modified inverse tangen $p = -0.3$ case above, but eight toroidal modes $n_\phi \in 5, 6, \ldots, 12$ are computed. The total deposition is weighted by the $[0, \pi, \pi, 0]$ antenna phasing power spectrum shown in figure 4.5. The computation is more correct, but requires eight times the CPU-time. Figure 4.55 compares the result of the simulation with one toroidal mode to 8 mode simulation. The damping factors do not change much between adjacent toroidal modes, but the standing wave patterns are slightly different, so hot and cold spots cancel to some extent. The cold spot

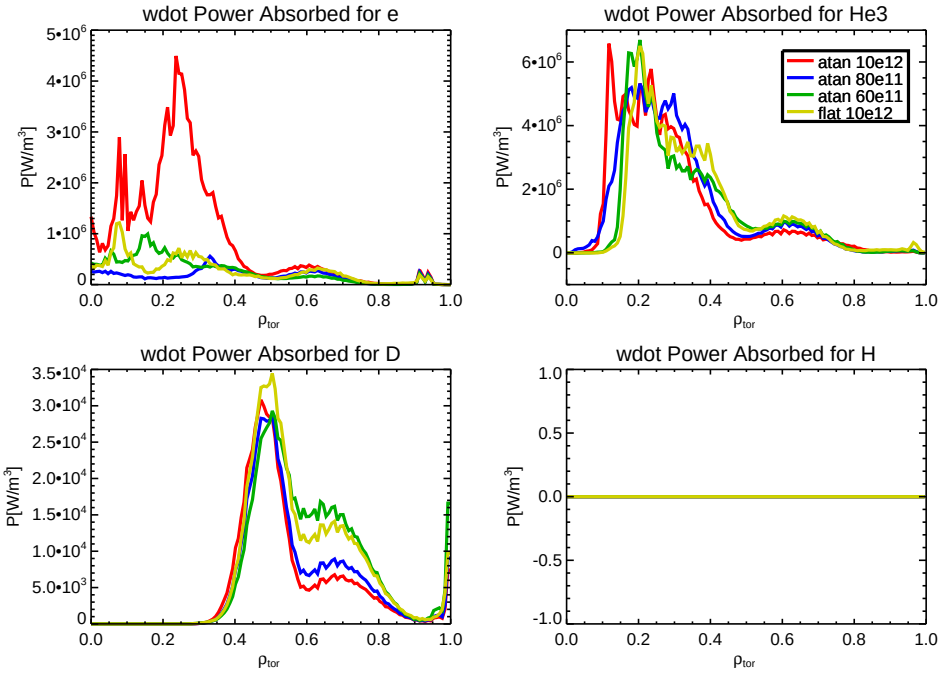

Figure 4.51: Flux-averaged power deposition profiles comparing a flat minority density to the inverse tangent model.

at $\rho_{\rm tor} = 0.4$ has been replaced by a hot spot and the whole deposition curve is smoother.

The conclusion is that the shape of the minority profile has a slight effect on the overall wave deposition and propagation dynamics. The effects are strongest for the minority density in the IC resonance band in the region, $0.2 \lesssim \rho_{\rm tor} \lesssim 0.65$. Outside the region, there is negligible effect of the helium-3 profile unless the helium-3 density is large; and then there can be subtle effects on the positions of the hot and cold spots. The slope of the minority profile seems to have no effect on heating.

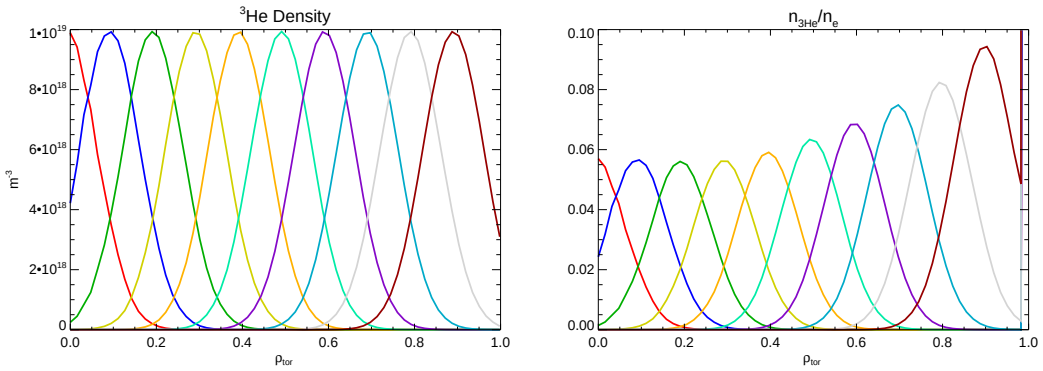

Figure 4.52: Center-shifted gaussians model functions.

A purely local model will miss the effects of hot and cold spots in the plasma. The heating is amplified if a hot spot sits on top of the minority resonance. But these hot spots and cold spots are mostly washed out when multiple toroidal modes are included in the simulation. In real plasmas, the minority density shape will vary less than in these simulations, so the overall effects of the shape can probably be ignored, unless a very accurate calculation is needed.

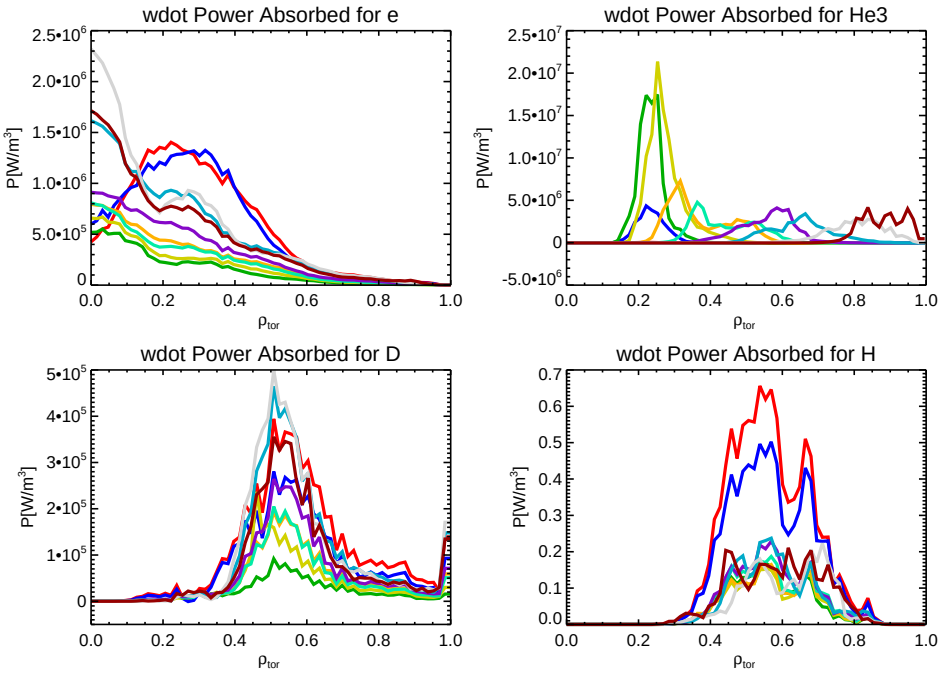

Figure 4.53: Flux-averaged power deposition profiles from minority profiles using gaussian model functions.

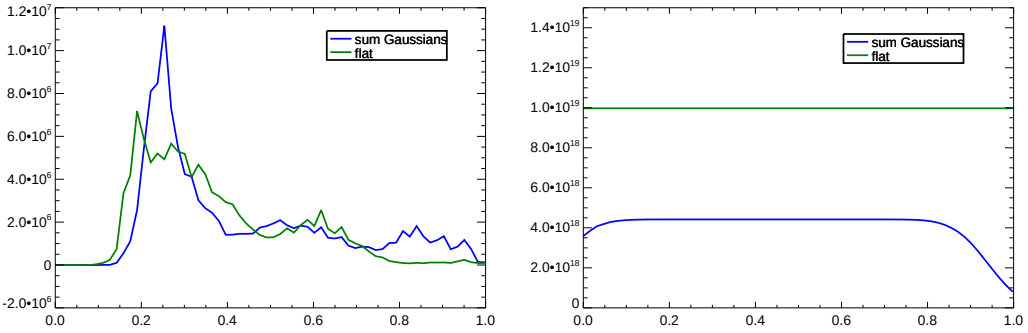

Figure 4.54: Left: Comparison between power deposition obtained by summing results of Gaussian density profiles and power deposition of flat profile. Right: Weighted summation of Gaussian density profiles and flat profile.

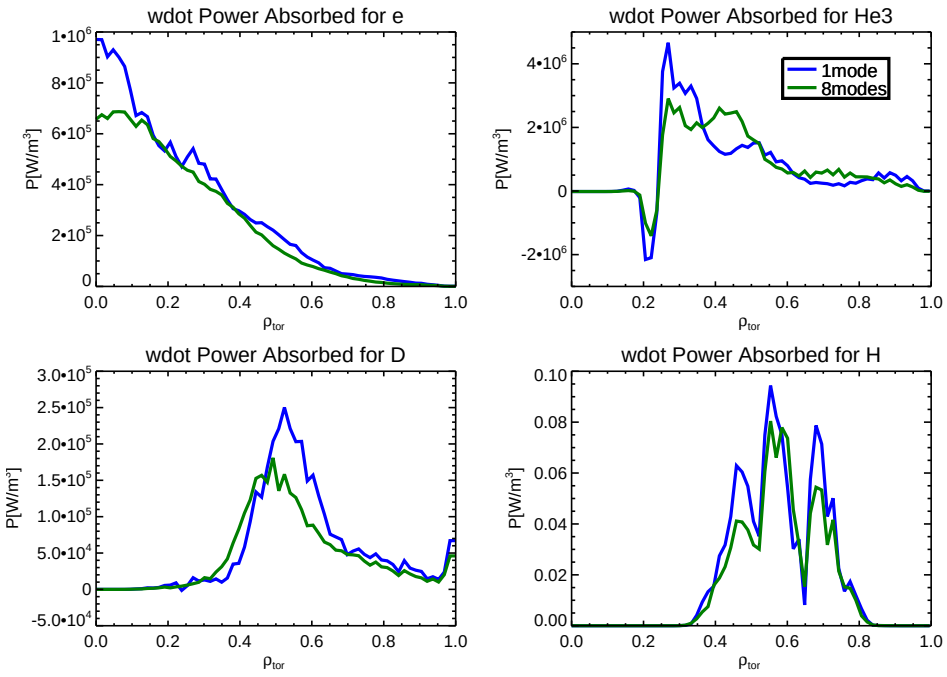

Figure 4.55: Comparison of flux-averaged power deposition between single toroidal mode calculation and weighted sum over 8 modes.

Chapter 5

Conclusion

5.1 Summary

I hope I have demonstrated some of the power of the Charge Exchange Recombination Spectroscopy technique. Helium density, temperature, and velocity measurements were made on Alcator C-Mod in L-mode, H-mode, and I-mode including data from both isotopes. Upgrades to the hardware were made to detect the small signal levels such as the new toroidal optics and poloidal aperture. Significant effort was focused on obtaining the most accurate spectral model possible, accounting for the effective charge exchange cross section, cross section effects, Zeeman effect, halo, bremsstrahlung, edge recombination emission, plume, and the effects of a non-Maxwellian distribution function. Several calibration methods are shown, and different intensity calibrations (with different tradeoffs of availability and accuracy) are compared. This text should serve as useful reference for someone developing a CXRS diagnostic.

The D and v helium transport coefficients were obtained using time dependent measurements puffed helium for an Ohmic discharge. The results ($D \sim 1\,\mathrm{m}^2/\mathrm{s}$, $v \sim -4\,\mathrm{m/s}$) are in reasonable agreement with measurements

on other devices. Pinch contributions were estimated using scalings derived from a database of many shots. The helium transport is shown to be highly non-neoclassical and dominated by turbulence. The measured transport is of similar magnitude to gyrokinetic predictions, but quantitative agreement is difficult to assess due to the large experimental uncertainties.

A set of Alcator C-Mod helium measurements has been submitted to a growing multi-device ITER Physics Activity database to support ongoing helium transport research.

It was initially hoped that the CXRS system on C-Mod could resolve ICRF-generated fast ions, but an exhaustive synthetic diagnostic demonstrated very little sensitivity to the distribution tails. Nevertheless, CXRS measurements of the minority species provides vital information for accurate simulation of the ICRF power deposition. It is well-known that the minority concentration has a large influence on the deposition, but little attention has been placed on the shape of the minority density profile. We observe subtle but minor effects of the profile shape on the deposition.

5.2 Future directions

We don't intend to stop taking measurements. Additional measurements can help bolster the database which is a bit thin in H-mode (particularly EDA and ELMy) and I-mode data. Helium main ion data is also very sparse. Additional data collection and analysis can move us towards obtaining quantitative agreement between experiments and gyrokinetic simulations, or

in finding additional terms which must be included.

The CXRS diagnostic hardware has proven to be very versatile and has found applications for different kinds of measurements which can be made without dismantling the CXRS system. Several applications have already been tested or are being tested now as proofs of concept. An advantage is that most of the calibration is identical and many of the analysis tools can be quickly converted for a new application.

One of these applications is beam emission spectroscopy using an H_α grating ($\sim 6562.8\,\text{Å}$). We have already conducted some experiments with an H_α grating in order to characterize beam performance (looking at beam shape and beam width versus perveance and energy fraction) or observe of a non-statistical nkm-resolved collisional-radiative model on the MSE spectrum[18]. Given the success of the beam measurements, we are investigating the possibility of a spectral MSE diagnostic for C-Mod. This technique has been pioneered on DIII-D[144].

Our group is proposing a BES/CXRS hybrid system[17] for Alcator C-Mod, which combines BES and CXRS measurements taken through the same optical views. The beam emission and charge exchange ion emission occur at separated wavelength ranges, and the light from the two periscopes can be separated using a dichroic filter and sent to two spectrometers (figure 5.1). This allows BES and CXRS emission to be obtained simultaneously using one set of in-vessel optics, but more importantly, the BES system measures the local beam density at each chord which is needed for the CXRS analysis,

supplanting the modeling of beam attenuation which is described in section 2.4.2.1. The beam modeling is a large source of uncertainty in the plasma core because even small errors in the beam stopping cross section may compound into a large error in the predicted beam density where the beam penetration is low. Also, the system automatically adjusts for secular variation in the beam parameters, such as perveance. In addition, the combined system is less sensitive to changes in the optical throughput, since the effects on the beam density measurement and CXRS intensity cancel (in the low beam density limit).

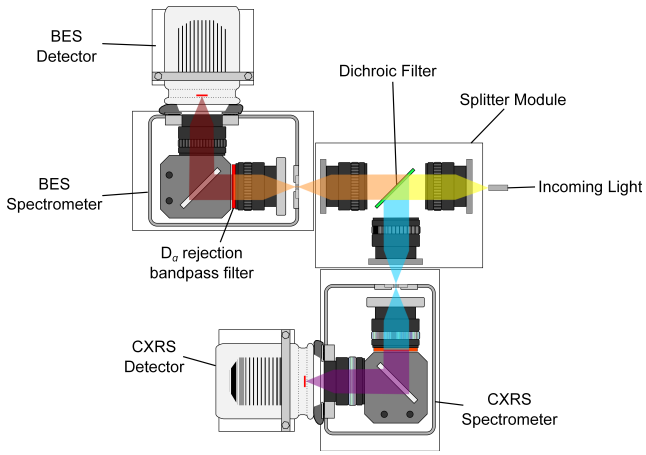

Figure 5.1: BES/CXRS setup, with light splitter module.

Unfortunately, the approach comes at the cost of complexity of optical alignment and the BES/CXRS approach will probably only work for channels in which the beam emission and main ion emission are adequately separated by Doppler shift. This includes channels near the core where the angle between the chord and beam is acute.

Alcator C-Mod has particularly high background signals. The time-slice background subtraction method is not ideal because the plasma can change over the modulation time of the beam, and time resolution is limited by the beam modulation rate. This is a particularly large impediment for puffed impurity experiments. The time resolution and accuracy can potentially be improved with dedicated background periscope views. These are periscopes with congruent geometry to the active beam views, but toroidally displaced so they don't intersect the beam. Therefore, with proper scaling and interpolation, and careful control of edge toroidal asymmetries, full time-resolved background subtraction can be made. This technique has been used on the TII-U[92], JT-60U[114], and MAST[135]. The drawback is that it requires twice the hardware and vessel space, but with improved background subtraction, ICRF-generated fast ion spectroscopy may become feasible.

On the other hand, it may be more fruitful to observe the ICRF-generated fast ion distribution indirectly, by looking at poloidal asymmetries in the minority density. If we want to use CXRS for this purpose, we require a beam that can penetrate to the high field side, or perhaps the data can be obtained from vertically displaced chords that take advantage of the large width of the beam.

5.3 Final word

I believe, in my lifetime, that we will have clean, practical fusion energy. Studies involving CXRS, as a very direct and versatile tool, will continue be

a large part of what gets us there. Finally, after all the technical issues of transport have been solved (though there's always room for improvement), we will still want a way to monitor helium ash concentrations, and helium CXRS will be there, inside the power plants of the future.

Appendices

Appendix A

DNB Diagnostics

The DNB is an essential and complex part of the CXRS diagnostic, and the quality of the beam model used directly affects the accuracy of the measurement. Therefore, I have put some additional effort into new diagnostic measurements for the DNB, including installation of a new spectroscopic view in the beam duct and a spectroscopic view of the neutralizer.

Accurate determination of the local beam density in the plasma is strongly influenced by the beam divergence, which is a function of the perveance of the beam. The perveance of an ion beam is defined by the beam current and voltage by

$$P = \frac{I_{\text{beam}}}{V_{\text{beam}}^{3/2}} \tag{A.1}$$

The beam divergence, and therefore the beam width, reaches a minimum at an optimal of perveance for the beam design, and increases on either side. Minimizing beam divergence is important for maintaining good spatial resolution and localized beam density in the plasma. Unfortunately, the perveance tends to vary from shot to shot, and among modulation pulses. Experimental measurement of the beam divergence versus perveance can be used to improve the beam model used by CXRS and other beam-based diagnostics.

A.1 Duct View

The duct view consists of 11 channels which are oriented in a fan-like pattern to cover the beam cross section, and the channel chords all lie in a plane which is tilted at 65° to the beam, oriented such that the beam emission is red-shifted. The tilt allows separation of the beam energy components, which have differing width functions. The mounting stages are easily adjustable to any angle or for blue-shifted measurement. The hardware consists of 11 ThorLabs SMA220-B (NA=0.25) fiber collimators held in a jig mounted to an open flange beneath a vacuum section between the calorimeter and beam duct. The collimators share the same 400 µm transfer fibers as the Core CXRS system and use the same spectrometer. The design is shown in figure A.1. The coverage of the chords across a typical beam width is shown in figure A.2.

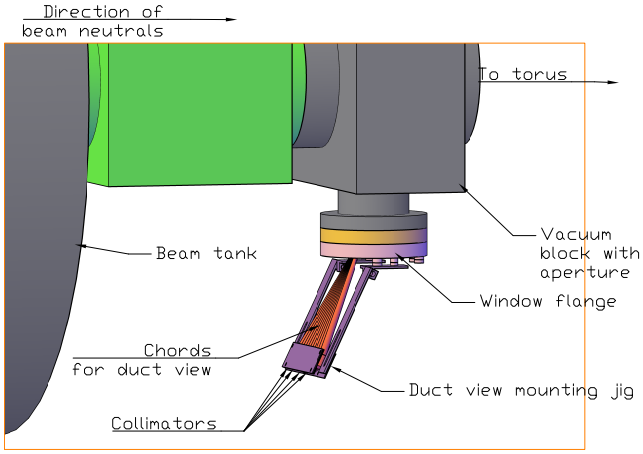

Figure A.1: Drawing of duct view hardware at bottom of aperture vacuum block. Chords are shown as orange solid objects.

The sensitivity of the beam divergence to perveance is experimen-

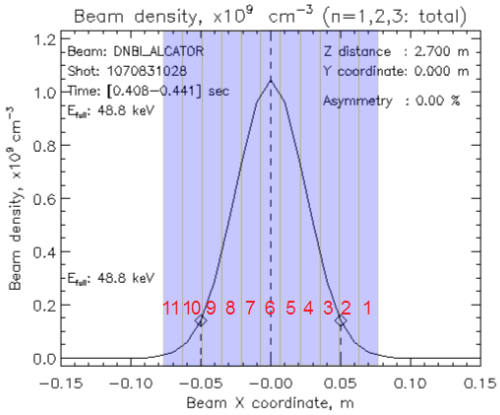

Figure A.2: Duct view coverage shown over a typical beam density cross section. The shaded columns show chord coverage for each of the 11 channels.

tally obtained by measuring beam emission at the red-shifted H_α line using a $\sim 6562.8\,\text{Å}$ grating, and performing a current scan. Eventually, the width measurements will be incorporated into the beam model used for CXRS analysis.

A.2 Neutralizer View

A single channel DNB neutralizer view is also installed on the same port as the 11 channel duct view. The diagnostic is designed to look at the visible emission of the neutralizer gas in order to diagnose the neutralizer gas temperature. It should be possible to obtain the rotational temperature by looking at ratios of Fulcher-α band transition lines for different excitation states of molecular hydrogen[162]. To access the neutralizer, which is located deep within the beam tank, a stainless steel mirror is located within the aperture vacuum block which reflects the light from the neutralizer into a fiber collimator located be-

neath the vacuum window. A 600 µm optical fiber transmits the light to an Ocean Optics USB4000-UV-VIS spectrometer.

Figure A.3 shows a spectrum measured by the neutralizer view during a beam pulse. The brightest signal comes from atomic H_α emission, but the emission spectrum is quite complex and includes emission over a wide range of wavelengths. Results of analysis are not yet available.

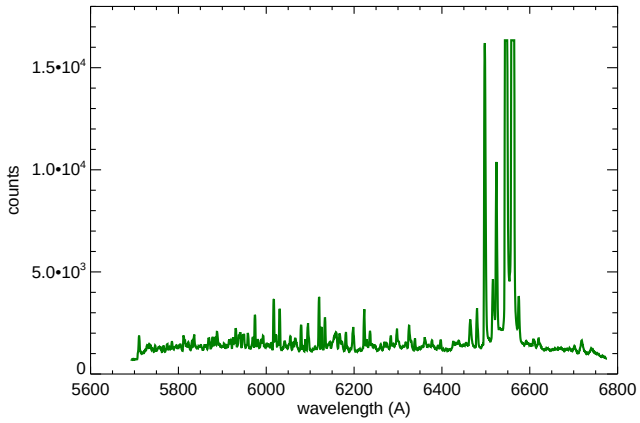

Figure A.3: Spectrum taken from neutralizer emission for a beam into vacuum shot 1131214325.

Bibliography

[1] W. Allis. Waves in a plasma. In *Sherwood Conf. Contr. Fusion, Gatlinburg*, 1959.

[2] H. Anderson, M. von Hellermann, R. Hoekstra, L. Horton, A. Howman, R. Konig, R. Martin, R. Olson, and H. Summers. Neutral beam stopping and emission in fusion plasmas I: deuterium beams. *Plasma physics and controlled fusion*, 42(7):781, 2000.

[3] C. Angioni and A. Peeters. Direction of impurity pinch and auxiliary heating in tokamak plasmas. *Physical review letters*, 96(9):95003, 2006.

[4] S. Atzeni and J. Meyer-ter Vehn. *The Physics of Inertial Fusion: Beam-Plasma Interaction, Hydrodynamics, Hot Dense Matter: Beam-Plasma Interaction, Hydrodynamics, Hot Dense Matter*. Number 125. Clarendon Press, 2004.

[5] R. Aymar, V. Chuyanov, M. Huguet, Y. Shimomura, I. Teams, et al. Overview of ITER-FEAT-The future international burning plasma experiment. *Nuclear Fusion*, 41(10):1301, 2002.

[6] M. Barnes, F. Parra, and A. Schekochihin. Critically balanced ion temperature gradient turbulence in fusion plasmas. *Physical review letters*, 107(11):115003, 2011.

[7] C. Barnett, H. Hunter, M. Kirkpatrick, I. Alvarez, C. Cisneros, and R. Phaneuf. *Atomic Data for Fusion, vol 1.* Oak Ridge National Laboratory, 1990.

[8] D. Beals, R. Granetz, W. Cochran, W. Byford, W. Rowan, A. Ivanov, P. Deichuli, V. Kolmogorov, and G. Shulzhenko. Installation and Operation of New Long Pulse DNB on Alcator C-Mod. In *Fusion Engineering 2005, Twenty-First IEEE/NPS Symposium on*, pages 1–4. IEEE, 2005.

[9] Beer. *Gyrofluid Models of Turbulent Transport in Tokamaks.* PhD thesis, Princeton University, 1995.

[10] K. Behringer. Description of the impurity transport code STRAHL JET-R (87)-08. *JET Joint Undertaking, Culham, UK*, 1987.

[11] D. S. Belkic and R. Janev. Electron capture from hydrogen and helium atoms by fast alpha particles. *Journal of Physics B: Atomic and Molecular Physics*, 6(6):1020, 1973.

[12] R. Bell. Exploiting a transmission grating spectrometer. *Review of scientific instruments*, 75(10):4158–4161, 2004.

[13] R. Bell, L. Dudek, B. Grek, D. Johnson, and R. Palladino. Tokamak fusion test reactor poloidal rotation diagnostic. *Review of scientific instruments*, 70(1):821–826, 1999.

[14] J. Berger, W. Newcomb, J. Dawson, E. Frieman, R. Kulsrud, and A. Lenard. *Phys. Fluids*, 1:301, 1958.

[15] I. Bespamyatnov, W. Rowan, and R. Granetz. Compact, accurate description of diagnostic neutral beam propagation and attenuation in a high temperature plasma for charge exchange recombination spectroscopy analysis. *Review of Scientific Instruments*, 79(10):10F315–10F315, 2008.

[16] I. Bespamyatnov, W. Rowan, and K. Liao. ALCBEAM–Neutral beam formation and propagation code for beam-based plasma diagnostics. *Computer Physics Communications*, 183(3):669–676, 2012.

[17] I. Bespamyatnov, W. Rowan, K. Liao, and R. Granetz. An integrated charge exchange recombination spectroscopy/beam emission spectroscopy diagnostic for Alcator C-Mod tokamak. *Review of Scientific Instruments*, 81:10D709, 2010.

[18] I. Bespamyatnov, W. Rowan, K. Liao, O. Marchuk, Y. Ralchenko, and R. Granetz. Benchmark of collisional-radiative models for ITER beams at the Alcator C-Mod tokamak. *Nuclear Fusion*, 53(12):123010, Dec 2013.

[19] H. A. Bethe and E. E. Salpeter. Quantum mechanics of one-and two-electron systems. In *Atoms I*, pages 88–436. Springer, 1957.

[20] R. Bickerton, J. Connor, and J. Taylor. Diffusion driven plasma currents and bootstrap tokamak. *Nature*, 229:110–112, 1971.

[21] T. Biewer, R. Bell, R. Feder, D. Johnson, and R. Palladino. Edge rotation and temperature diagnostic on the National Spherical Torus Experiment. *Review of scientific instruments*, 75(3):650–654, 2004.

[22] C. Boley, R. Janev, and D. Post. Enhancement of the neutral-beam stopping cross section in fusion plasmas due to multistep collision processes. *Physical review letters*, 52(7):534–537, 1984.

[23] P. T. Bonoli, P. O'Shea, M. Brambilla, S. N. Golovato, A. E. Hubbard, M. Porkolab, Y. Takase, R. L. Boivin, F. Bombarda, C. Christensen, C. L. Fiore, D. Garnier, J. Goetz, R. Granetz, M. Greenwald, S. F. Horne, I. H. Hutchinson, J. Irby, D. Jablonski, B. LaBombard, B. Lipschultz, E. Marmar, M. May, A. Mazurenko, G. McCracken, R. Nachtrieb, A. Niemczewski, H. Ohkawa, D. A. Pappas, J. Reardon, J. Rice, C. Rost, J. Schachter, J. A. Snipes, P. Stek, K. Takase, J. Terry, Y. Wang, R. L. Watterson, B. Welch, and S. M. Wolfe. Electron heating via mode converted ion Bernstein waves in the Alcator C-Mod tokamak. *Phys. Plasmas*, (4):1774, 1997.

[24] H.-S. Bosch and G. Hale. Improved formulas for fusion cross-sections and thermal reactivities. *Nuclear Fusion*, 32(4):611, 1992.

[25] C. Breton, C. D. Michelis, M. Finkenthal, and M. Mattioli. H alpha and H beta spectral profiles from neutral beams and plasmas in high magnetic fields. *Journal of Physics B: Atomic and Molecular Physics*, 13(8):1703–1718, Apr. 1980.

[26] S. J. Buchsbaum. Resonance in a Plasma with Two Ion Species. *Physics of Fluids*, 3(3):418, 1960.

[27] E. Busche, H. Euringer, and R. Jaspers. Measurement of deuterium ion temperature profiles at TEXTOR-94. *Plasma physics and controlled fusion*, 39(9):1327, 1997.

[28] Y. Camenen, A. Peeters, C. Angioni, F. J. Casson, W. Hornsby, A. Snodin, and D. Strintzi. Impact of the background toroidal rotation on particle and heat turbulent transport in tokamak plasmas. *Physics of Plasmas*, 16:012503, 2009.

[29] A. Casati, C. Bourdelle, X. Garbet, F. Imbeaux, J. Candy, F. Clairet, G. Dif Pradalier, G. Falchetto, T. Gerbaud, V. Grandgirard, et al. Validating a quasi-linear transport model versus nonlinear simulations. *Nuclear Fusion*, 49(8):085012, 2009.

[30] F. Casson, R. McDermott, C. Angioni, Y. Camenen, R. Dux, E. Fable, R. Fischer, B. Geiger, P. Manas, L. Menchero, et al. Validation of gyrokinetic modelling of light impurity transport including rotation in ASDEX Upgrade. *Nuclear Fusion*, 53(6):063026, 2013.

[31] M. Churchill. Flux Surface Variation of Impurity Density and Flows in the Pedestal Region. In *55th Annual Meeting of the APS Division of Plasma Physics, Denver, CO*, 2013.

[32] P. Clemmow and R. Mullaly. Dependence of the refractive index in magneto-ionic theory on the direction of the wave normal. *Physics of the Ionosphere: Report of Phys. Soc. Conf. Cavendish Lab. (Phys. Soc. London)*, page 340, 1955.

[33] J. W. Coenen, B. Schweer, M. Clever, S. Freutel, O. Schmitz, H. Stoschus, U. Samm, and B. Unterberg. Charge exchange recombination spectroscopy on a diagnostic hydrogen beammeasuring impurity rotation and radial electric field at the tokamak TEXTOR. *Journal of Physics B: Atomic, Molecular and Optical Physics*, 43(14):144015, 2010.

[34] J. W. Connor, R. J. Hastie, and J. B. Taylor. Shear, Periodicity, and Plasma Ballooning Modes. *Physical Review Letters*, 40(6):396, February 1978.

[35] B. Coppi, H. Furth, M. Rosenbluth, and R. Sagdeev. Drift instability due to impurity ions. *Physical Review Letters*, 17(7):377, 1966.

[36] B. Coppi and C. Spight. Ion-mixing mode and model for density rise in confined plasmas. *Physical Review Letters*, 41(8):551, 1978.

[37] J. Crank and P. Nicolson. A practical method for numerical evaluation of solutions of partial differential equations of the heat-conduction type. *Proc. Camb. Phil. Soc.*, 43:50–67, 1947.

[38] T. Dannert and F. Jenko. Gyrokinetic simulation of collisionless trapped-electron mode turbulence. *Physics of Plasmas*, 12:072309, 2005.

[39] C. G. Darwin. The Zeeman Effect and Spherical Harmonics. *Proceedings of the Royal Society A: Mathematical, Physical and Engineering Sciences*, 115(770):1–19, June 1927.

[40] V. Davydenko, A. Ivanov, S. Korepanov, and I. Kotelnikov. Precise formation of geometrically focused ion beams. *Review of scientific instruments*, 77(3):03B902–03B902, 2006.

[41] V. Davydenko, A. Ivanov, A. Rogozin, and R. Uhlemann. Optimization of an ion-optics system with thick electrodes for the diagnostic neutral beam injector of the TEXTOR tokamak. *Review of scientific instruments*, 68(3):1418–1422, 1997.

[42] C. De Boor. *Applied Mathematical Sciences 27: A practical guide to splines*. Springer, New York, 1978.

[43] P. Deichuli, G. Abdrashitov, A. Ivanov, V. Kolmogorov, V. Mishagin, G. Shul'Zhenko, N. Stupishin, D. Beals, and R. Granetz. Ion source with LaB hollow cathode for a diagnostic neutral beam injector. *Review of scientific instruments*, 77:03B514, 2006.

[44] E. Delabie, M. Brix, C. Giroud, R. Jaspers, O. Marchuk, M. O'Mullane, Y. Ralchenko, E. Surrey, M. von Hellermann, K. Zastrow, et al. Consistency of atomic data for the interpretation of beam emission spectra. *Plasma Physics and Controlled Fusion*, 52(12):125008, 2010.

[45] N. Dubuit, X. Garbet, T. Parisot, R. Guirlet, and C. Bourdelle. Fluid simulations of turbulent impurity transport. *Physics of plasmas*, 14:042301, 2007.

[46] R. Dux. *STRAHL User Manual*. Max-Planck-Institut für Plasmaphysik D-85748 Garching b. München Assoziation EURATOM-IPP, 2006.

[47] R. Dux and A. Peeters. Neoclassical impurity transport in the core of an ignited tokamak plasma. *Nuclear fusion*, 40(10):1721, 2000.

[48] P. Efthimion, S. Von Goeler, W. Houlberg, E. Synakowski, M. Zarnstorff, S. Batha, R. Bell, M. Bitter, C. Bush, F. Levinton, et al. Observation of particle transport barriers in reverse shear plasmas on the Tokamak Fusion Test Reactor. *Physics of Plasmas*, 5:1832, 1998.

[49] I. Enting, C. Trudinger, and D. Etheridge. Propagating data uncertainty through smoothing spline fits. *Tellus B*, 58(4):305–309, 2006.

[50] Ephrem Geert Delabie. *Neutral beam diriven hydrogen spectroscopy in fusion plasmas*. PhD thesis, Universiteitsdrukkerij Technische Universiteit Eindhoven, 2011.

[51] P. T. Farnsworth. Method and apparatus for producing nuclear-fusion reactions, jun 1968.

[52] D. Finkenthal. *The measurement of absolute helium ion density profiles on the DIII-D tokamak using charge exchange recombination spectroscopy.* PhD thesis, University of California at Berkeley, 1994.

[53] C. Fiore, D. Ernst, Y. Podpaly, D. Mikkelsen, N. Howard, J. Lee, M. Reinke, J. Rice, J. Hughes, Y. Ma, et al. Production of internal transport barriers via self-generated mean flows in Alcator C-Mod. *Physics of Plasmas*, 19:056113, 2012.

[54] D. Fitts. *Principles of Quantum Mechanics : as Applied to Chemistry and Chemical Physics.* Cambridge University Press, 2002.

[55] R. Fonck, G. Cosby, R. Durst, S. Paul, N. Bretz, S. Scott, E. Synakowski, and G. Taylor. Long-wavelength density turbulence in the TFTR tokamak. *Physical review letters*, 70(24):3736, 1993.

[56] R. Fonck, D. Darrow, and K. Jaehnig. Determination of plasma-ion velocity distribution via charge-exchange recombination spectroscopy. *Physical Review A*, 29(6):3288, 1984.

[57] M. Foord and E. S. Marmar. Sawtooth oscillations in the visible continuum on Alcator C. *Nuclear fusion*, 25(2):197, 1985.

[58] G. Frieling, R. Hoekstra, E. Smulders, W. Dickson, A. Zinoviev, S. Kuppens, and F. de Heer. Cross sections for l-selective electron capture into the He+ (n = 4) shell in intermediate energy collisions of He2+ with H

and H2. *Journal of Physics B: Atomic, Molecular and Optical Physics*, 25(6):1245, 1992.

[59] W. Fritsch. Calculation of partial electron-transfer cross sections in 1–84 keV/amu $He^{2+} + H$ collisions. *Physical Review A*, 38(5):2664, 1988.

[60] A. Galeev. Diffusion-electrical phenomena in a plasma confined in a tokamak machine. *Sov. Phys. JETP, 3 2*, 752, 1971.

[61] A. Galeev and R. Sagdeev. Transport phenomena in a collisionless plasma in a toroidal magnetic system. *Sov. Phys. JETP*, 26(1):233–240, 1968.

[62] D. Gambier, M. Evrard, J. Adam, A. Becoulet, S. Corti, P. Hennequin, J. Jacquinot, D. Start, K. Thomsen, B. Tubbing, and V. Zanza. ICRF power deposition profile and determination of the electron thermal diffusivity by modulation experiments in JET. *Nuclear Fusion*, 30(1):23, 1990.

[63] X. Garbet, N. Dubuit, E. Asp, Y. Sarazin, C. Bourdelle, P. Ghendrih, and G. Hoang. Turbulent fluxes and entropy production rate. *Physics of plasmas*, 12:082511, 2005.

[64] X. Garbet, L. Garzotti, P. Mantica, H. Nordman, M. Valovic, H. Weisen, and C. Angioni. Turbulent particle transport in magnetized plasmas. *Physical review letters*, 91(3):35001, 2003.

[65] K. Gentle. Dependence of heat pulse propagation on transport mechanisms: Consequences of nonconstant transport coefficients. *Physics of Fluids*, 31(5):1105–1110, 1988.

[66] K. Gentle and H. He. Texas Helimak. *Plasma Science and Technology*, 10(3):284, 2008.

[67] R. Goldston, R. White, T. Hahm, and S. Kaye. Physics of Confinement. In *Fusion Physics*. International Atomic Energy Agency, 2012.

[68] H. Grad and H. Rubin. Hydromagnetic equilibria and force-free fields. *Journal of Nuclear Energy (1954)*, 7(3):284–285, 1958.

[69] R. Guirlet, C. Giroud, T. Parisot, M. Puiatti, C. Bourdelle, L. Carraro, N. Dubuit, X. Garbet, and P. Thomas. Parametric dependences of impurity transport in tokamaks. *Plasma physics and controlled fusion*, 48(12B):B63, 2006.

[70] Z. Hartwig and Y. Podpaly. *Magnetic Fusion Energy Formulary*. MIT, 2011.

[71] R. Harvey and M. McCoy. *The CQL3D Fokker-Planck Code*. General Atomics, 2011. General Atomics Report GA-A20978, 1992.

[72] C. Havener, R. Rejoub, P. Krstić, and A. Smith. Charge transfer in low-energy collisions of He^{2+} with atomic hydrogen. *Physical Review A*, 71(4):042707, 2005.

[73] R. D. Hazeltine and J. D. Meiss. *Plasma confinement*. Courier Dover Publications, 2003.

[74] W. Heidbrink, R. Bell, Y. Luo, and W. Solomon. Fast-ion D-alpha diagnostic for NSTX. *Review of scientific instruments*, 77(10):10F120–10F120, 2006.

[75] W. Heidbrink, K. Burrell, Y. Luo, N. Pablant, and E. Ruskov. Hydrogenic fast-ion diagnostic using Balmer-alpha light. *Plasma physics and controlled fusion*, 46(12):1855, 2004.

[76] D. Hillis, K. Finken, J. Hogan, K. Dippel, R. Moyer, A. Pospieszczyk, D. Rusbüldt, K. Akaishi, R. Conn, H. Euringer, et al. Helium exhaust and transport studies with the ALT-II pump limiter in the TEXTOR tokamak. *Physical review letters*, 65(19):2382–2385, 1990.

[77] D. Hillis, J. Hogan, K. Finken, W. West, R. Weynants, M. Wade, K. Akaishi, W. Baek, J. Boedo, K. Burrell, et al. Helium transport in enhanced confinement regimes on the TEXTOR and DIII-D tokamaks. *Journal of nuclear materials*, 196:35–44, 1992.

[78] F. Hinton and R. Hazeltine. Theory of plasma transport in toroidal confinement systems. *Reviews of Modern Physics*, 48(2):239, 1976.

[79] R. L. Hirsch. Inertial-Electrostatic Confinement of Ionized Fusion Gases. *Journal of Applied Physics*, 38(11):4522–4534, 1967.

[80] S. Hirshman and D. Sigmar. Neoclassical transport of impurities in tokamak plasmas. *Nuclear Fusion*, 21(9):1079, 1981.

[81] R. Hoekstra, F. De Heer, and R. Morgenstern. State-selective electron capture in collisions of He2+ with H. *Journal of Physics B: Atomic, Molecular and Optical Physics*, 24(18):4025, 1991.

[82] E. Hollmann, A. Pigarov, and R. Doerner. Effect of graphite and molybdenum wall tile reflections on visible light diagnostics in tokamak experiments. *Review of scientific instruments*, 74(9):3984–3990, 2003.

[83] C. Horton Jr and R. Varma. Electrostatic Stability Theory of Tokamaks from Two-Component Fluid Equations. *Physics of Fluids*, 15:620, 1972.

[84] G. Hose. Charge exchange, excitation, and ionization in H (1s) + He^{2+} collisions simulated using the multichannel perturbed-stationary-state propagator. *Physical Review A*, 56(2):1364, 1997.

[85] W. Houlberg, K. Shaing, S. Hirshman, and M. Zarnstorff. Bootstrap current and neoclassical transport in tokamaks of arbitrary collisionality and aspect ratio. *Physics of Plasmas*, 4:3230, 1997.

[86] Howard Yuh. *The Motional Stark Effect Diagnostic on Alcator C-Mod*. PhD thesis, MIT, 2005.

[87] J. W. Hughes, D. Mossessian, A. Hubbard, E. Marmar, D. Johnson, and D. Simon. High-resolution edge Thomson scattering measurements

on the Alcator C-Mod tokamak. *Review of Scientific Instruments*, 72(1):1107–1110, 2001.

[88] J. W. Hughes, D. Mossessian, K. Zhurovich, M. DeMaria, K. Jensen, and A. Hubbard. Thomson scattering upgrades on Alcator C-Mod. *Review of scientific instruments*, 74(3):1667–1670, 2003.

[89] C. R. Hull. Farnsworth-Hirsch Fusor. *The Bell Jar*, 6:3–4, 1997.

[90] I. Hutchinson. Excited-state populations in neutral beam emission. *Plasma physics and controlled fusion*, 44(1):71, 2002.

[91] I. H. Hutchinson, R. Boivin, F. Bombarda, P. Bonoli, S. Fairfax, C. Fiore, J. Goetz, S. Golovato, R. Granetz, M. Greenwald, et al. First results from Alcator-C-MOD. *Physics of Plasmas*, 1:1511, 1994.

[92] K. Ida and S. Hidekuma. Space- and time-resolved measurements of ion temperature with the CVI 5292-A charge-exchange recombination line after subtracting background radiation. *Review of Scientific Instruments*, 60(5):867, 1989.

[93] IEA. Key World Energy Statistics. Technical report, International Energy Agency, 2012.

[94] J. Irby, D. Gwinn, W. Beck, B. LaBombard, R. Granetz, and R. Vieira. Alcator C-Mod design, engineering, and disruption research. *Fusion science and technology*, 51(3):460–475, 2007.

[95] M. Isichenko, A. Gruzinov, and P. Diamond. Invariant measure and turbulent pinch in tokamaks. *Physical review letters*, 74(22):4436–4439, 1995.

[96] R. Isler. Profiles and polarizations of the Balmer-α line from high-temperature hydrogen atoms in strong magnetic fields. *Physical Review A*, 14(3):1015, 1976.

[97] R. Isler. Observation of the Reaction $H^0 + O^{8+} \rightarrow H^+ + O^{7+}$ during Neutral-Beam Injection into ORMAK. *Physical Review Letters*, 38(23):1359–1362, 1977.

[98] R. Isler and E. Crume. Charge-Transfer Excitation of Impurity Ions in Tokamaks. *Physical Review Letters*, 41(19):1296–1300, 1978.

[99] R. Isler, L. Murray, S. Kasai, J. Dunlap, S. Bates, P. Edmonds, E. Lazarus, C. Ma, and M. Murakami. Charge-exchange excitation and recombination of oxygen in the ISX-B tokamak. *Physical Review A*, 24(5):2701, 1981.

[100] E. ITER. documentation series No. 24. *ITER technical basis, IAEA, Vienna*, 2002.

[101] `http://www.iter.org/org/team/fst/itpa/tc`.

[102] A. Ivanov, V. Davydenko, P. Deichuli, A. Kreter, V. Mishagin, A. Podminogin, I. Shikhovtsev, B. Schweer, and R. Uhlemann. Radio frequency

ion source for plasma diagnostics in magnetic fusion experiments. *Review of Scientific Instruments*, 71(10):3728–3735, 2000.

[103] A. Ivanov, V. Davydenko, P. Deichuli, G. Shulzhenko, and N. Stupishin. Ion sources with arc-discharge plasma box driven by directly heated LaB electron emitter or cold cathode. *Review of Scientific Instruments*, 79:02C103, 2008.

[104] N. Ivanov, I. Kovan, and I. SOKOLOV. Magnetosonic heating of a two-component plasma in the T-4 tokamak. *JETP Letters*, 24:316–319, 1976.

[105] J. Jacquinot, B. McVey, and J. Scharer. Mode conversion of the fast magnetosonic wave in a deuterium-hydrogen tokamak plasma. *Physical Review Letters*, 39(2):88–91, 1977.

[106] E. Jaeger, R. Harvey, L. Berry, J. Myra, R. Dumont, C. Phillips, D. Smithe, R. Barrett, D. Batchelor, P. Bonoli, et al. Global-wave solutions with self-consistent velocity distributions in ion cyclotron heated plasmas. *Nuclear fusion*, 46(7):S397, 2006.

[107] R. Janev, editor. *Atomic and Plasma-material Interaction Data for Fusion, volume 4*. International Atomic Energy Agency, 1993.

[108] R. Janev, C. Boley, and D. Post. Penetration of energetic neutral beams into fusion plasmas. *Nuclear Fusion*, 29(12):2125, 1989.

[109] F. Jenko, T. Dannert, and C. Angioni. Heat and particle transport in a tokamak: advances in nonlinear gyrokinetics. *Plasma physics and controlled fusion*, 47(12B):B195, 2005.

[110] F. Jenko, W. Dorland, M. Kotschenreuther, and B. Rogers. Electron temperature gradient driven turbulence. *Physics of Plasmas*, 7:1904, 2000.

[111] John Wesson et al. *Tokamaks*. Clarendon Press, Oxford, 3rd edition, 2004.

[112] M. Kammerer, F. Merz, and F. Jenko. Exceptional points in linear gyrokinetics. *Physics of Plasmas*, 15:052102, 2008.

[113] W. Karzas and R. Latter. *The Astrophysical Journal Supplement Series*, 55:167, 1961.

[114] Y. Koide, A. Sakasai, Y. Sakamoto, H. Kubo, and T. Sugie. Multichordal charge exchange recombination spectroscopy on the JT-60U tokamak. *Review of Scientific Instruments*, 72(1):119, 2001.

[115] Kurt Gottfried and Tung-Mow Yan. *Quantum Mechanics: Fundamentals*. Springer, 2nd edition, 2003.

[116] W. Kutta. Beitrag zur näherungweisen Integration totaler Differentialgleichungen. 1901.

[117] L. Landau. *J. Phys*, (10):25, 1946.

[118] L. Lao, H. S. John, R. Stambaugh, A. Kellman, and W. Pfeiffer. Reconstruction of current profile parameters and plasma shapes in tokamaks. *Nuclear fusion*, 25(11):1611, 1985.

[119] E. Lerche, D. Van Eester, et al. Improved break-in-slope analysis of the plasma energy response in tokamaks. *Plasma Physics and Controlled Fusion*, 50(3):035003, 2008.

[120] K. Liao, W. Rowan, I. Bespamyatnov, W. Horton, and X. Fu. Transport of helium as an impurity and as a main ion in Alcator C-Mod. *Bulletin of the American Physical Society*, 57, 2012.

[121] K. Liao, W. Rowan, I. Bespamyatnov, S. Wukitch, Y. Lin, A. Bader, D. Pace, and N. Tsujii. Fast ion charge exchange measurements during minority heating in Alcator C-Mod. *Bulletin of the American Physical Society*, 56, 2011.

[122] Y. Lin, J. Rice, S. Wukitch, M. Greenwald, A. Hubbard, A. Ince Cushman, L. Lin, E. Marmar, M. Porkolab, M. Reinke, et al. Observation of ion cyclotron range of frequencies mode conversion plasma flow drive on Alcator C-Mod. *Physics of Plasmas*, 16:056102, 2009.

[123] Y. Lin, J. Rice, S. Wukitch, M. Reinke, M. Greenwald, A. Hubbard, E. Marmar, Y. Podpaly, M. Porkolab, N. Tsujii, et al. ICRF mode conversion flow drive on Alcator C-Mod. *Nuclear Fusion*, 51(6):063002, 2011.

[124] Y. Lin, S. J. Wukitch, P. T. Bonoli, E. Marmar, D. Mossessian, E. Nelson Melby, P. Phillips, M. Porkolab, G. Schilling, S. Wolfe, and J. Wright. Ion cyclotron range of frequencies mode conversion electron heating in deuterium-hydrogen plasmas in the Alcator C-Mod tokamak. *Plasma Physics and Controlled Fusion*, 45(6):1013, 2003.

[125] Y. Luo. *Fast-ion Dα Measurements and Simulations in DIII-D*. PhD thesis, University of California, 2007.

[126] A. Lynn. *Electron Cyclotron Emission Measurements of Coherent and Broadband Density Fluctuations in the Alcator C-Mod Tokamak*. PhD thesis, University of Texas at Austin, 2004.

[127] A. T. M. Czerny. *Z. Phys*, 61:792, 1930.

[128] R. Majeski, J. Rogers, S. Batha, R. Budny, E. Fredrickson, B. Grek, K. Hill, J. Hosea, B. LeBlanc, F. Levinton, and et al. Mode Conversion Heating and Current Drive Experiments in TFTR. *Physical Review Letters*, 76(5):764–767, Jan 1996.

[129] W. Mandl, R. C. Wolf, M. G. v. Hellermann, and H. P. Summers. Beam emission spectroscopy as a comprehensive plasma diagnostic tool. *Plasma Physics and Controlled Fusion*, 35(10):1373–1394, Oct. 1993.

[130] M. Mantsinen, M. Mayoral, D. Van Eester, B. Alper, R. Barnsley, P. Beaumont, J. Bucalossi, I. Coffey, S. Conroy, M. de Baar, et al. Lo-

calized bulk electron heating with ICRF mode conversion in the JET tokamak. *Nuclear Fusion*, 44(1):33, 2004.

[131] C. Marquardt. Non-Linear Least Squares Fitting in IDL with MPFIT. In P. D. . D. D. D. Bohlender, editor, *Astronomical Data Analysis Software and Systems XVIII*, volume 411 of *ASP Conference Series*, pages 251–254, Quebec, Canada, 2009. Astronomical Society of the Pacific: San Francisco.

[132] `http://www.wolfram.com/mathematica/`.

[133] R. McDermott. *Edge radial electric field studies via charge exchange recombination spectroscopy on the Alcator C-Mod Tokamak.* PhD thesis, Massachusetts Institute of Technology, 2009.

[134] G. McKee, R. Fonck, B. Stratton, R. Bell, R. Budny, C. Bush, B. Grek, D. Johnson, H. Park, A. Ramsey, et al. Confined alpha distribution measurements in a deuterium-tritium tokamak plasma. *Physical review letters*, 75(4):649–652, 1995.

[135] C. A. Michael, N. Conway, B. Crowley, O. Jones, W. W. Heidbrink, S. Pinches, E. Braeken, R. Akers, C. Challis, M. Turnyanskiy, and et al. Dual view FIDA measurements on MAST. *Plasma Physics and Controlled Fusion*, 55(9):095007, Sep 2013.

[136] T. Minami, T. G. Lee, M. S. Pindzola, and D. R. Schultz. Total and state-selective charge transfer in He2++ H collisions. *Journal of Physics*

B: Atomic, Molecular and Optical Physics, 41(13):135201, 2008.

[137] Moré. *Numerical Analysis*, volume 630, chapter The Levenberg-Marquardt Algorithm: Implementation and Theory, page 105. Springer-Verlag: Berlin, 1978.

[138] D. A. Mossessian, A. Hubbard, and J. Irby. Performance of Alcator C-Mod core Thomson scattering system. *Review of scientific instruments*, 70(1):759–762, 1999.

[139] H. Nakamura, T. Hirayama, Y. Koide, K. Tobita, K. Tani, T. Fukuda, H. Kubo, M. Kuriyama, Y. Kusama, A. Sakasai, et al. Helium ash exhaust studies with core fueling by a helium beam: L-mode divertor discharges with neutral-beam heating in the JT-60 tokamak. *Physical review letters*, 67(19):2658–2661, 1991.

[140] `http://www.nist.gov/pml/data/asd.cfm`.

[141] G. Norlén. Wavelengths and energy levels of Ar I and Ar II based on New Interferometric Measurements in the Region 3 400-9 800 å. *Physica Scripta*, 8(6):249, 1973.

[142] J. Noterdaeme, M. Brambilla, B. Brüsehaber, R. Dux, H. Fahrbach, W. Becker, F. Braun, H. Faugel, D. Hartmann, F. Hofmeister, et al. 3He in H, ion cyclotron resonance frequency mode conversion and minority heating experiments in ASDEX Upgrade. In *Proc. 26th Conf. on*

Controlled Fusion and Plasma Phyiscs (Maastricht), volume 23, pages 1561–4, 1999.

[143] R. Olson. Ion-Rydberg atom collision cross sections. *Journal of Physics B: Atomic and Molecular Physics*, 13(3):483, 1980.

[144] N. Pablant, K. Burrell, R. Groebner, D. Kaplan, and C. Holcomb. Measurements of the internal magnetic field on DIII-D using intensity and spacing of the motional Stark multiplet. *Review of Scientific Instruments*, 79(10):10F517–10F517, 2008.

[145] A. Parisot, S. J. Wukitch, P. Bonoli, M. Greenwald, A. Hubbard, Y. Lin, R. Parker, M. Porkolab, A. K. Ram, and J. C. Wright. Sawtooth period changes with mode conversion current drive on Alcator C-Mod. *Plasma Physics and Controlled Fusion*, 49(3):219–235, Mar 2007.

[146] R. Parker. An Alcator Chronicle, or What happened to Alcator B. 2011.

[147] B. Patel and W. Parsons. Operational Beryllium Handling Exeperience at JET. Technical report, European Fusion Development Agreement.

[148] F. Perkins. Heating tokamaks via the ion-cyclotron and ion-ion hybrid resonances. *Nuclear Fusion*, 17(6):1197, 1977.

[149] D. Pfirsch and A. Schlüter. Max-Planck Institute Report MPI. *PA/7i*, 1962.

[150] M. Porkolab. Plasma heating by fast magnetosonic waves in tokamaks. In *AIP Conference Proceedings*, volume 314, page 99, 1994.

[151] R. Post. The magnetic mirror approach to fusion. *Nuclear Fusion*, 27(10):1579, 1987.

[152] M. Püschel. *Electromagnetic Effects in Gyrokinetic Simulations of Plasma Turbulence.* PhD thesis, Westfälischen Wilhelms-Universität Münster, 2009.

[153] G. Racah. On a new type of vector coupling in complex spectra. *Physical Review*, 61(7-8):537, 1942.

[154] F. Ribe. Liˆ{6}(n, α) Hˆ{3} Cross Section as a Function of Neutron Energy. *Physical Review*, 103(3):741, 1956.

[155] J. Rice, M. Greenwald, Y. Podpaly, M. Reinke, P. Diamond, J. Hughes, N. Howard, Y. Ma, I. Cziegler, B. Duval, et al. Ohmic energy confinement saturation and core toroidal rotation reversal in Alcator C-Mod plasmas. *Physics of Plasmas*, 19:056106, 2012.

[156] Richard Fitzpatrick. *The Physics of Plasmas.* Lulu, 2008.

[157] T. H. Rider. A general critique of inertial-electrostatic confinement fusion systems. *Physics of Plasmas*, 2:1853, 1995.

[158] W. Rowan, I. Bespamyatnov, and C. Fiore. Light impurity transport at an internal transport barrier in Alcator C-Mod. *Nuclear Fusion*, 48(10):105005, 2008.

[159] A. Salop. The distribution of excitation resulting from electron capture in stripped-ion-hydrogen-atom collisions. *Journal of Physics B: Atomic and Molecular Physics*, 12(6):919, 1979.

[160] B. Saoutic, A. Bécoulet, T. Hutter, D. Fraboulet, A. K. Ram, and A. Bers. Mode Conversion Heating Experiments on the Tore Supra Tokamak. *Phys. Rev. Lett.*, 76:1647–1650, Mar 1996.

[161] V. Shafranov. Plasma equilibrium in a magnetic field. *Reviews of Plasma Physics*, 2:103, 1966.

[162] T. Shikama, S. Kado, Y. Kuwahara, K. Kurihara, F. Scotti, and S. Tanaka. Fulcher-α Band Spectra in Mixed Hydrogen Isotope Plasmas. *Plasma and Fusion Research*, 2(0):1045–1045, 2007.

[163] T. C. Simonen. Experimental progress in magnetic-mirror fusion research. *Proceedings of the IEEE*, 69(8):935–957, 1981.

[164] J. Skellam. The frequency distribution of the difference between two Poisson variates belonging to different populations. *Journal of the Royal Statistical Society, Series A*, 109:296, 1946.

[165] D. N. Smithe. Local full-wave energy and quasilinear analysis in nonuniform plasmas. *Plasma Physics and Controlled Fusion*, 31(7):1105–1126, Jun 1989.

[166] T. Stix. Fast-wave heating of a two-component plasma. *Nuclear Fusion*, 15(5):737, 1975.

[167] T. Stix. *Waves in plasmas*. Amer Inst of Physics, 1992.

[168] Summers. The ADAS User Manual, version 2.6, 2004.

[169] D. Swanson. Radio frequency heating in the ion-cyclotron range of frequencies. *Physics of Fluids*, 28:2645, 1985.

[170] D. G. Swanson. *Plasma Waves*. Academic Pr, 1989.

[171] D. G. Swanson. *Theory of Mode Conversion and Tunneling in Inhomogeneous Plasmas*. Wiley-VCH, 1998.

[172] E. Synakowski, B. Stratton, P. Efthimion, R. Fonck, R. Hulse, D. Johnson, D. Mansfield, H. Park, S. Scott, and G. Taylor. Measurements of radial profiles of He^{2+} transport coefficients on the TFTR tokamak. *Physical review letters*, 65(18):2255–2258, 1990.

[173] H. Takahashi, C. Daughney, R. Ellis Jr, R. Goldton, H. Hsuan, T. Nagashima, F. Paoloni, A. Sivo, and S. Suckewer. Ion heating in ATC tokamak in the ion-cyclotron range of frequencies. *Physical Review Letters*, 39(1):31–34, 1977.

[174] Takashi Fujimoto. *Plasma Spectroscopy*. Clarendon Press, Oxford, 2004.

[175] H. Takenaga, A. Sakasai, Y. Koide, Y. Sakamoto, H. Kubo, S. Higashijima, T. Oikawa, H. Shirai, T. Fujita, and Y. Kamada. Impurity

Transport in Reversed Shear and ELMy H-Mode Plasmas of JT-60U. 75(8):952–966, 1999.

[176] V. Tang. *Experimental and Numerical Characterization of Ion-Cyclotron Heated Protons on the Alcator C-Mod Tokamak*. PhD thesis, MIT, 2006.

[177] W. Tang, R. White, and P. Guzdar. Impurity effects on ion-drift-wave eigenmodes in a sheared magnetic field. *Physics of Fluids*, 23:167, 1980.

[178] C. Theiler, R. Churchill, A. Hubbard, J. Hughes, B. Lipschultz, E. Marmar, M. Reinke, J. Terry, J. Walk, D. Whyte, et al. Recent edge CXRS measurements in I-mode and ELMy H-mode plasmas on C-Mod. In *54th Annual Meeting of the APS Division of Plasma Physics, Providence, RI*, volume 57. American Physical Society, 2012.

[179] N. Tsujii. *Studies of ICRF Mode Conversion with Phase Contrast Imaging and Full-Wave Simulations in Alcator C-Mod*. PhD thesis, MIT, July 2012.

[180] N. Tsujii, M. Porkolab, P. Bonoli, Y. Lin, J. Wright, S. Wukitch, E. Jaeger, D. Green, and R. Harvey. Measurements of ion cyclotron range of frequencies mode converted wave intensity with phase contrast imaging in Alcator C-Mod and comparison with full-wave simulations. *Physics of Plasmas*, 19(8):082508–082508, 2012.

[181] A. Turnbull, Y. Lin Liu, R. Miller, T. Taylor, and T. Todd. Improved magnetohydrodynamic stability through optimization of higher

order moments in cross-section shape of tokamaks. *Physics of Plasmas*, 6:1113, 1999.

[182] M. Van Hemert, E. Van Dishoeck, J. Van der Hart, and F. Koike. Quantum-mechanical and impact-parameter treatment of He^{2+}-H collisions. *Physical Review A*, 31(4):2227, 1985.

[183] M. Van Zeeland, J. Yu, N. Brooks, W. Heidbrink, K. Burrell, R. Groebner, A. Hyatt, T. Luce, N. Pablant, W. Solomon, et al. Active and passive spectroscopic imaging in the DIII-D tokamak. *Plasma Physics and Controlled Fusion*, 52(4):045006, 2010.

[184] M. Von Hellermann, P. Breger, J. Frieling, R. Konig, W. Mandl, A. Maas, and H. Summers. Analytical approximation of cross-section effects on charge exchange spectra observed in hot fusion plasmas. *Plasma physics and controlled fusion*, 37(2):71, 1995.

[185] M. Von Hellermann, W. Core, J. Frieling, L. Horton, R. Konig, W. Mandl, and H. Summers. Observation of alpha particle slowing-down spectra in JET helium beam fuelling and heating experiments. *Plasma physics and controlled fusion*, 35(7):799, 1993.

[186] M. von Hellermann and H. Summers. Active Beam Spectroscopy at JET. Technical report, JET, 1993. JET-P(93)34.

[187] M. Von Hellermann and H. P. Summers. Active Beam Spectroscopy at JET. *Atomic and Molecular Dat afor Fusion Reactor Technology*, 1993.

[188] F. Wagner, G. Becker, K. Behringer, D. Campbell, A. Eberhagen, W. Engelhardt, G. Fussmann, O. Gehre, J. Gernhardt, and G. Gierke. Regime of improved confinement and high beta in neutral-beam-heated divertor discharges of the ASDEX Tokamak. *Physical Review Letters*, 49(19):1408–1412, 1982.

[189] A. A. Ware. Pinch Effect for Trapped Particles in a Tokamak. *Phys. Rev. Lett.*, 25:15–17, July 1970.

[190] K. Wenzel and D. Sigmar. Neoclassical analysis of impurity transport following transition to improved particle confinement. *Nuclear Fusion*, 30(6):1117, 1990.

[191] D. Whyte, A. Hubbard, J. Hughes, B. Lipschultz, J. Rice, E. Marmar, M. Greenwald, I. Cziegler, A. Dominguez, T. Golfinopoulos, et al. I-mode: an H-mode energy confinement regime with L-mode particle transport in Alcator C-Mod. *Nuclear Fusion*, 50(10):105005, 2010.

[192] I. Williams, J. Geddes, and H. Gilbody. Balmer α emission in collisions of H, H+, H2+ and H3+ with H2. *Journal of Physics B: Atomic and Molecular Physics*, 15(9):1377, 1982.

[193] T. G. Winter and G. J. Hatton. Plane-wave-factor, molecular-state treatment of electron transfer in collisions of He^{2+} ions with H atoms. *Physical Review A*, 21(3):793, 1980.

[194] e. a. Wukitch, S. Field-Aligned ICRF Antenna Characterization and Performance in Alcator C-Mod. In *54th APS DPP Annual Meeting Providence, RI USA October 29-Nov 2, 2012*, 2012.

[195] V. Yankov and J. Nycander. Description of turbulent transport in tokamaks by invariants. *Physics of Plasmas*, 4:2907, 1997.

Vita

Kenneth Teh-Yong Liao was born in Massachusetts, USA in 1981, the second son of Dr. Winston Y.H. Liao and Su-Lin Liao, both immigrants from Taiwan. He received the Bachelor of Arts with a double major in Computer Science and Physics from University of California at Berkeley in 2003. He worked as a test engineer in industry from 2004 to 2007. He left the company to pursue further education in physics. He was accepted by the University of Texas at Austin and began studies in August 2007. He joined the Fusion Research Center (now part of the Institute for Fusion Studies) to do experimental research in fusion science. He did ion spectroscopy measurements on the Texas Helimak, before focusing primarily on the Alcator C-Mod Tokamak.

Email address: kenliao@physics.utexas.edu

This dissertation was typeset with LaTeX[†] by the author.

[†]LaTeX is a document preparation system developed by Leslie Lamport as a special version of Donald Knuth's TeX Program.